

Characterization of Nanoparticles with Optical Fluidic Cavity

Kiana Malmir

University of Oxford

This thesis is submitted to the Materials Department of the University of Oxford, in partial fulfilment of the requirements for the degree of Doctor of Philosophy

Trinity 2022

To the hope as has been the Emerald of my life...

Acknowledgements

I would firstly like to thank Professor Jason Smith. You have been a fantastic supervisor, really supportive, and given brilliant scientific advice throughout my PhD. I can not appreciate enough the opportunity you gave me to join your group. Special thanks goes to Dr. Aurélien Trichet who guided me during all these years. I am really grateful for taking the time to teach me microfabrication and optics in the lab. Your comprehensive and meticulous techniques and great enthusiasm have helped me a lot throughout my PhD. Many thanks for arranging weekly meeting even after you left PNG. With many thanks to Dr. Amit Dhawan who always made me feel confident. I would particularly like to thank your time for having all the conservations that guided me so positively. I truly appreciate your support and constant encouragement that allowed me to reach this point - I am deeply thankful.

I have had the pleasure of working with the great members of the PNG lab, past and present, who have provided such a welcoming and productive environment. Thanks to Andrew, Annabel, Ben, Brandon, Dean, Fred, Jack, Laiyi, Immy, Matt, Matteo, Sam, Sanmi, Shazea, Shannon and William. I have valued spending my time with all of you. Cheers to Shazea for welcoming me really well into the group by making a delicious cake and bringing the group together on birthdays especially my first one in PNG. To Annabel and Brandon, it was a pleasure working directly with you both. You were brilliant students and your contributions to the group were invaluable. I wish you all the best in your career steps. Further thanks goes to William whose coding and laser skills made things in the lab run really efficiently. Many many thanks, of course, to Oxford HighQ for kindly supporting me and providing the funding during my academic career at Oxford. It was really a great opportunity to work with Oxford HighQ memebrs Ben Ash, Claire, Dean, Jeremy, Matteo, and Rob. Thank you so much all.

A very special gratitude goes out to Dr. Adrian Taylor for his never-edning support and assistance and the Materials Department for providing the funding for the last year of my study. Many thanks to Paul for always helping me with my IT problems and rescuing my data backups.

I am also exceptionally grateful to Linacre College and specifically to my college Senior Tutor Dr. Jane Hoverd for her generous, heart-warming, and never-ending support throughout the most difficult stages of my

education. This was, and always will be, invaluable to me. She was always keen to know what I was doing and how I was proceeding. I am extending my wholehearted thanks to her for her friendship, kindness, and understanding. Many many thanks for driving me to be the best I can be. I would not be here without her and I will forever be grateful - thank you so much for everything.

A huge thank you goes to Prof. Dr. Derek Hobbs, his family, and Buddy for their strong support, care, and never-ending love as if I was one of their family members. You have been like my father during my final months in Oxford. You, as well as your constant encouragement in every step, pushed me to where I am right now - I could not have finished this journey without you. I cannot find any word to express how much grateful I am.

I would also like to thank Penny and Martin Wainwright, for their overwhelming generosity. It was a great pleasure to get to know you and I never forget your care and support during those three years of my stay in our beautiful village. I still feel the warmth of the Christmas campfire and your kindness. I am so grateful for organizing the glorious farewell with Dolores for me - truly unforgettable memories with both of you.

There has been a great friend who has provided endless moments of cheer and hope. I have truly enjoyed seeing you Annette in the computer science department every day and will always hold a place in my heart for those memories.

Also, thanks to my best friends Bani, Bardia, Matt, and Zeinab for encouraging me to be strong - thank you so much. Finally, I would like to thank my family for their unconditional love and support. Without all their support throughout my academic career, I never would have made it this far. Thank you for always being there for me.

Abstract

The optical trapping of nanoparticles and biomolecules has recently attracted considerable attention as a means for the manipulation and characterization of target analytes. Nano-particulate pollutants and microbiological organisms, such as viruses, have optical characteristic signatures based on their refractive index, size, and polarizability, as well as spectral signatures. By leveraging these properties, optical sensing and spectroscopy techniques have proven to be powerful tools for detecting and characterizing nanoparticles at the single-particle level. In this work, we show that the confined optical field in a Fabry-Pérot style microcavity resonator can be used as a means for both trapping and measuring nanoparticle characteristics with high resolution. This characterization is performed by recording the spectral shift of the mode wavelength when the particles diffuse through the microcavity. The maximum mode displacement provides an accurate measure of the polarizability of each particle. We illustrate an accurate measurement of the distribution of polarizabilities in a solution containing a mixture of 50 nm, 75 nm, and 100 nm polystyrene particles in water. This work also studies the theory behind the behavior of particles in an optofluidic microcavity based on the particle size, the optical power, and throughput of a given instrument. Based on the developed theory, the dynamic characteristics of particle trapping in an optofluidic microcavity are further investigated by simulating a stochastic model of nanoparticle dynamics. Furthermore, this work introduces a new model for analyzing the dynamics of nanoparticles in fluidic systems and studying the optical trapping potential. This model allows to accurately design an optical microfluidic system for trapping the desired range of particles based on the flow rate and the optical power, and subsequently detect nanoparticles with high resolution. We express the trapping rate of nanoparticles as a function of the flow rate, the optical power, and the size of particles. Thus, the technique proposed in this work provides a deep understanding of the optical trapping of nanoparticles in flowing fluid, which is crucial for trapping and manipulating nanoparticles and biomolecules. We also show that similar-sized particles of different materials can be distinguished as a result of the difference in refractive indexes, which means the introduced method is sensitive to the refractive index. Therefore, it can be a powerful method to analyze nanoparticles in a solution in applications where we need high-resolution measurement at the single-particle level.

Statement of Originality

The contents of this dissertation are partly based on our publications at the *International Conference On Nanomedicine And Nanobiotechnology, 2019* [1], *S3IC 2019* [2] and *Photon, 2020* [3]. At the time of writing, a number of chapters were under review or yet to be submitted for journal publications [4, 5].

Contents

1 Introduction **1**
- 1.1 Nanoparticle Characterization with Microcavities . . . 3
- 1.2 Dissertation Overview . . . 5
- 1.3 Publications by the author . . . 9

2 Literature Review **11**
- 2.1 Introduction . . . 11
- 2.2 Characterization Methods . . . 12
  - 2.2.1 Atomic Force Microscopy (AFM) . . . 14
  - 2.2.2 Scanning Electron Microscopy (SEM) . . . 15
  - 2.2.3 Transmission Electron Microscopy (TEM) . . . 16
  - 2.2.4 Dynamic Light Scattering (DLS) . . . 17
  - 2.2.5 Nanoparticle Tracking Analysis (NTA) . . . 18
  - 2.2.6 Flow Cytometry (FCM) . . . 20
  - 2.2.7 Analytical Ultracentrifugation (AUC) . . . 23
  - 2.2.8 Differential Centrifugal Sedimentation (DCS) . . . 24
- 2.3 Sensors for Nanoparticle Characterization . . . 25
  - 2.3.1 Optical Waveguides . . . 29
    - 2.3.1.1 Antiresonant Reflecting Optical Waveguide (ARROW) . . . 30
    - 2.3.1.2 Slot Waveguides . . . 31
  - 2.3.2 Optical Microcavities . . . 34
    - 2.3.2.1 Ring Resonators . . . 35
    - 2.3.2.2 Photonic Crystals . . . 38
    - 2.3.2.3 Plasmonics . . . 41
    - 2.3.2.4 Fabry-Pérot Microcavities . . . 44
- 2.4 Summary . . . 48

3 Theory **50**
- 3.1 Introduction . . . 50
- 3.2 Open-Access Cavity . . . 50
- 3.3 Gaussian Beam . . . 53
- 3.4 Hermite-Gaussian Beam . . . 56
- 3.5 Optical Modes through the Cavity . . . 59
- 3.6 Optical Mode Shift . . . 64

3.7 Summary . . . 66

4 Experimental Method 67
4.1 Introduction . . . 67
4.2 Requirements for Nanoparticle Characterization . . . 68
4.3 Optical Microcavity . . . 68
4.4 Flow Cell . . . 71
4.5 Optical Set-up . . . 74
4.6 Sample Preparation . . . 81
4.7 Measurement . . . 82
4.8 Summary . . . 88

5 Monte-Carlo Modelling and Simulation 89
5.1 Introduction . . . 89
5.2 Optical Nanoparticle Trapping . . . 90
5.2.1 Optical Force . . . 91
5.2.2 Drag Force . . . 93
5.2.3 Brownian Force . . . 97
5.2.4 Thermophoretic Force . . . 99
5.2.4.1 McNab-Meisen Model . . . 100
5.2.4.2 Duhr-Braun Ionic-shielding Model . . . 104
5.3 Particle Trajectory . . . 105
5.4 Diffusivity Particle . . . 108
5.4.1 RoC Effect . . . 111
5.4.2 Flow Velocity Effect . . . 116
5.4.3 Trap Time Duration . . . 116
5.4.4 Shape of Cavity . . . 119
5.5 Particle Delivery Based on Pressure-driven Method . . . 120
5.6 Summary . . . 129

6 Measurements at Zero Flow Rate 130
6.1 Introduction . . . 130
6.2 Simulation and Experimental Data . . . 131
6.2.1 Homogeneous Particles . . . 138
6.2.2 Trap Time Duration . . . 141
6.3 Summary . . . 143

7 Measurements Using Pressure-Driven Flow 145
7.1 Introduction . . . 145
7.2 CFTA Technique . . . 146
7.2.1 Experiment Results . . . 154
7.2.2 Linear vs Parabolic Flow . . . 166
7.2.3 Time Effect on Trap Rate . . . 169
7.3 CFTA based on Velocity Changes . . . 170
7.4 Effect of Thermophoresis on CFTA . . . 173

7.5 Summary 175

8 Conclusions and Future Work **177**
8.1 Conclusions 177
8.2 Future Work 180
8.2.1 CFTA-Eo 180
8.2.2 Different RoC 181
8.2.3 Sorting Nanoparticles by CFTA 181
8.2.4 Real Nanoparticles 182

Bibliography **182**

List of Figures

1.1 A schematic of open cavity as an optical tweezer to trap nanoparticles [4]. 4

2.1 (a) AFM distribution of 20 nm, and 100 nm polystyrene nanoparticles in an 8:1 mixture. (b) AFM scan of 20 nm, and 100 nm polystyrene nanoparticle mixture, and AFM size distribution data. (c) Three-dimensional AFM image of 20 nm, and 100 nm polystyrene nanoparticle mixture. 20 nm particles can be seen in the background [6]. 14
2.2 Schematic of components of (a) SEM and (b)TEM [7]. 16
2.3 The optical configuration of a typical experimental setup for DLS measurements [8]. 17
2.4 NTA characterization system: (a) schematic diagram; (b) typical micrograph showing bulk nanobubbles [9]. 19
2.5 Size distribution from NTA and DLS measurements of monodisperse polystyrene beads with size of 60 nm and 100 nm. Error bars represent standard deviations obtained from three measurements of the same sample [10]. 20
2.6 Graphical representation of the FCM analysis (NP: nanoparticle) [11]. 21
2.7 Results of Nano-Flow Cytometry (NFCM): (a) silica spherical particles size distribution as an artificial sample (b) particle size distribution for a biological sample [12]. 22
2.8 Normalized light extinction weighted size distributions of the PS NPs as measured by DCS in sedimentation (continuous black line) and flotation (dash grey line) modes [13]. 25
2.9 The layout of an optical tweezer (above) along with a magnification near the beam focus. A transparent sphere settles on the beam axis just beyond the beam focus where the gradient and scattering forces are equal [14]. 28
2.10 Schematic illustration of electromagnetic force in evanescent modes, where the gradient force and scattering force are perpendicular to each other [15]. 30

2.11 (a) Schematic layout of the ARROW optofluidic analysis platform. Inset: Working principle of the particle position sensor showing the illumination during (1) the first and (2) the second half-period of modulation. (b) Solid-core waveguide with overlayed optical mode profile. (c) Same for hollow-core waveguide. (d) Photograph of the actual chip with reservoirs [16]. 31
2.12 (a) Microparticle sorting device. (b) CCD image of the sorting with a guided power of 20 mW. The waveguides are indicated by the gray lines in the first frame. The trapped particles are marked by white arrows with the indicators S and L for the 320 nm and 2 μm particles, respectively. The obstacle particle is marked in the second frame [17]. 32
2.13 (a) SEM image of the double-ring structure, (b) transmission spectrum of a particle storage chain comprised of two microrings with radii of 5 and 10 μm. Dips at 1557.9 nm and 1561.2 nm correspond to the resonance frequencies of small and large microrings, respectively. Lower left inset: CCD image of particles trapped on the small microring at a laser wavelength of 1557.9 nm; Lower right inset: CCD image of particles trapped on the large microring at a laser wavelength of 1561.2 nm. Yellow lines label the positions of micro rings and bus waveguides. The white arrows indicate the trapped particles [18]. 36
2.14 (a) Output power as a function of time when particles are trapped. (b) Output power as a function of time, shown in detail [18]. . . . 37
2.15 Stronger fixed-position traps are achieved with photonic crystal (PC) resonators. A nanoparticle that was transported along a bus waveguide (yellow circles) is trapped at a side-coupled PC resonator (orange circles) before being released and transported along the bus waveguide again [19]. 39
2.16 Schematic illustration of a nanoslot waveguide photonic crystal cavity [20]. 40
2.17 Plasmonic near-field optical trap [21]. 42
2.18 Optofluidic lab-on-a-chip: (a) general view; (b) exploded view: the chip is made of three layers: the plasmonic substrate, the flow layer, and the control layer. (c) SEM image of the fabricated gold plasmonic structures on the dielectric substrate [22]. 43
2.19 Optical plasmonic trapping of yeast cells in a microfluidic channel. The bright structures represent the gold disks with trapped yeast cells on top of them. A free yeast cell is trapped in the bottom right highlighted structure and another cell is trapped by the top highlighted disk about half a minute later [22]. 44
2.20 (a) SEM image: arrays of cavities FIB milled onto a Silicon substrate [23] (b) SEM image of the chip template displaying different RoC microcavities (vertical axis) and repetitions (horizontal axis) [24]. 46

2.21 (a) Transmission scans as a function of time. The top (or bottom) transmission peak is the reference (or trapping) signal. The parameter τ_{diff} gives the time scale of free diffusion of a 200 nm nanoparticle in the cavity volume. (b) Blue dots: experimental mode shifts versus time during a trapping event. The red line is the moving maximum over 80 ms [24]. 47

3.1 A schematic of a simple open microcavity. 51
3.2 The resonant wavelength in terms of FSR and Q factor in a simple Fabry-Pérot resonator. 52
3.3 The intensity distribution of Hermite-Gaussian beams. The order (l, m) is shown in each case and the intensity is propagated in the z direction. 58
3.4 A simulation of an open-access microcavity consists of a concave mirror (with radius of curvature of 4 μm) and a planar mirror to create 7 antinodes (optical modes). 59
3.5 An incident beam is reflected by the mirror in the z direction to form a Gaussian beam. 60
3.6 The laser beam is propagated through the cavity with radius of curvature of 4 μm, generating 7 antinodes in (a) Gaussian (with small divergence) and (b) cylindrical model (without small divergence). 62
3.7 Changing the position of resonance wavelength when a particle is placed through the optical mode. 63

4.1 (a) SEM image of an array of concave mirrors on the plinth along with the different RoC and the depth of the cavities, (b) a schematic of the chip where the microcavities are milled on the plinth (the center squar). 70
4.2 (a) An image of the mould along with the sealant; the mould consists of two parts; part A and B, part A is installed on part B to make the sealant. (b) a schematic of components of the flow cell; (1) the flow cell comprises of patterned mirror on the ridge, sealant, flat mirror, inlet, and outlet tubes (2) the channel shape when the sealant environs the ridge to seal the flow cell and (3) the patterned mirror with the dimension of the ridge (the center rectangular). . . 72
4.3 (a) A top-view of the flow cell (the cavities are placed on the ridge) in the xy direction and (b) a side view along with a cross-section of the flow cell in the xz direction to show how the particles are introduced through the cavity. 73

4.4 (a) Schematic of the optical setup; P:P-Polarizer, M(1-9): PF10-03-P01-protected silver mirror, M8:Flip mirror, HWP: Half-Wave Plate for adjusting the input light intensity, L(1-4): lenses (Thorlabs), L1:LC1060-B - N-BK7, L2:AC254-075-B-ML, L3, L4:AC254-030-A-ML, DM: Dichroic Mirror (DMLP605R-Thorlabs and angled at 45^o with respect to the LED light beam), Objective lens (10X): Nikon, antireflection, the APD (430-Thorlabs) and CCD camera:(340M-USB-Thorlabs). (b) an image of the experimental set-up. 75
4.5 An image of the sensing and reference cavities that are monitored by the CCD camera. 76
4.6 (a) A 3D image of the flow cell with holders to show where the piezo and the mirrors are placed (b) a close up of the flow cell along with more details in the direction of the incident laser, the sealant, fluid inlet, and outlet. 77
4.7 Diagram of locking the cavity by the PID controller. 78
4.8 (a) Steps of cavity stabilization process by fringes, (b) PID controller panel. 79
4.9 (a) Transmission scan of experimental data that includes two signals, the strong signal represents the sensing signal and the weaker signal is related to the reference cavity, (b) an example of wavelength shift when the PMMA particle with diameter or size of 196 ± 4.4 nm is detected by the sensing signal. 83
4.10 An example of raw data from the APD when a solution of PMMA particles with size of 200 nm is introduced through the cavity; the red arrow represents the maximum intensity which indicates that a particle is escaped from the cavity. The events with two-headed arrows indicate that a particle is trapped. 85
4.11 The mode shift of a PMMA particle with size of 200 nm. The maximum mode shift is 700 pm. 87

5.1 A schematic of the flow cell to show flow direction and the propagated laser direction when there is flowing fluid and the cavities are milled on a ridge. 93
5.2 Total potential energy with the intracavity power of $10mW$ and beam waist of 560 μm by considering a polystyrene particle (diameter or size of 100 nm) with no flow (blue curve) and with the flow of 100 $\mu m/s$ velocity in the x direction. Note that the laser wavelength is assumed to be 640 nm in our simulations to match the experimental work (see Section 4.5 of Chapter 4). 94
5.3 Cross-sections of the potential energy versus the position of a 200 nm polystyrene particle which is delivered through the cavity with two different flow rates. The flow profile is assumed to be flat or linear and the optical beam is based on the cylindrical model with the RoC of 25 μm and the intracavity power of 50 mW. 96

5.4 Thermophoretic velocity versus the particle position, where the laser power and the particle diameter are 50 mW and 200 nm, respectively. 101
5.5 Thermophoresis effect on the potential energy (based on cylindrical model) when a polystyrene particle with diameter of 100 nm is in the cavity with RoC of 25 μm. 103
5.6 Thermophoretic velocity versus the position of two different particle sizes of 100 nm and 200 nm when the intracavity of 50 mW is assumed. 104
5.7 The trajectory of a PS spherical particle with diameter or size of 200 nm in an open-access microcavity with the intracavity laser of 20 mW and two flow rates: (a) 1 $\mu m/s$ which the particle is trapped through the antinodes and (b) 50 $\mu m/s$ which the particle has escaped from the cavity, (c) the particle is trapped by increasing the laser power to 50 mW. 106
5.8 The mode shift of a PMMA particle with size or diameter, $2a_{PMMA}$ of 200 nm for two intracavity powers of (a) 2 mW with which the particle is diffused and then escaped from the cavity, and (b) 10 mW under which the particle is trapped through the cavity more than 850 ms. 107
5.9 Maximum mode distribution of PS particles with the size of 200 nm in cylindrical and realistic models when the intracavity power is 20 mW. 109
5.10 Relationship between the optical intensity and the maximum mode shift. The mode shifts of PS particles with the size of 200 nm are calculated here. 110
5.11 Maximum mode distribution simulated for 200 nm PS particles ($D = 2a = 200\ nm$) for different time steps and intracavity powers. 112
5.12 Maximum mode distribution with respect to the intracavity power and the size of the particle when the RoC is 25 μm. 113
5.13 The normalized Maximum mode ($Max - shift_N$) distribution for the intracavity power and particle size when RoC is 5 μm or the beam waist is 693 nm. 115
5.14 Normalized maximum mode shift ($Max - shift_N$) distribution with respect to the flow velocity in the x direction and particle size with RoC 25 μm. 117
5.15 Simulation results of two trap time durations as a filter; particles diffuse in the cavity more than (a): 200 ms and (b): 300 ms. 118
5.16 The normalized maximum mode shift distribution is compared in the flat hat and the concave cavity for PS particles with diameter of 200 nm where the color scale bar denotes the normalized optical intensity for both cavities. 120
5.17 (a) A close-up of the fluidic channel to show the L and $2h$. (b) Profile of parabolic flow according to the length of the cavity when RoC is 25μm and the pressure is around 4 $mbar$. 122

5.18 (a) A COMSOL schematic of the flow cell where the cavities are milled on the ridge and the sealant has sealed the channel, (b) COMSOL simulation with the streamline flow through the channel (c) a slice view of the flow profile through the ridge in COMSOL that proves the parabolic flow through the cavity as the velocity in the center of channel is higher (red color) than the walls (light blue) in the zoomed area. 123
5.19 (a) A side view (top figure) and a top view (bottom figure) of the ridge chip, (b) channel dimension along with the tubes size. 125
5.20 A top view of the flow cell to show the flow distribution through the channel by streamlines in COMSOL. 126
5.21 The top view of velocity (color-scale bar) through the flow cell when the pressure of (a) 100 Pa and (b) 500 Pa are applied through the ridge according to the mentioned dimension in Figure 5.19a. 127

6.1 (a) schematic of flow cell along with the mixture of three different PS particles (red spheres), (b) a close up of an array of the concave mirrors on the plinth. 132
6.2 The measured maximum mode shifts of the mixture of PS particles with nominal sizes of 50, 75 and 100 nm by the microcavity with the RoC of 4 μm or beam waist of 560 nm with the length of cavity of 702 nm; (a) two different maximum mode shifts of 134 pm and 250 pm, (b) more example of mode shifts that are measured by the flow cell. 133
6.3 (a) Histograms of the maximum mode shift by the experimental data, and (b) the simulation data. 135
6.4 Particle size distribution with respect to the mean and the standard deviation from the factory data-sheet for nominal sizes of 50 nm, 75 nm and 100 nm from left to right, respectively. 136
6.5 A comparison between the standard deviation of the three different particles in the measurement and the calculation of the maximum mode shift. 137
6.6 (a) Measured polarizability volume and (b) the measured size distribution with the proposed flow cell. 139
6.7 Maximum mode shift distribution of a homogeneous mixture of PS particles where the diameters of 50 nm, 75 nm, 100 nm are considered in the simulation. 140
6.8 Experimental results of trap events when the trap time duration of 50 ms is set for the mixture of 50 nm, 75 nm, and 100 nm PS particles. 141
6.9 Simulation result of the time effect on the resolution of the characterization method for measuring 150 nm PS particles. 142

7.1 Open-access microcavity with 4 antinodes through the concave (RoC of 4 μm) and flat mirrors along with the direction of flowing fluid (antinodes are simulated based on the cylindrical model). 147
7.2 The trajectory (based on the cylindrical model with 4 μm RoC of the concave mirror) of a sphere PS particle with a diameter of 200 nm in a flow cell with two flow rates (a) the velocity of the particle is 1 $\mu m/s$ with which the particle is trapped through the antinodes. (b) the particle is escaped from the cavity with a flow rate of 60 $\mu m/s$. (c) Probability of trapping with respect to the position of the particle in y and z direction in the microcavity when the flow velocity is 1 $\mu m/s$. 148
7.3 Trapping cross-section as a function of diameter ($D = 2a$) in x axis and velocity of the particle (v) in y axis when RoC or the optical beam waist, the laser power, and the refractive index of the particle is changed. 151
7.4 (a) A schematic of flow cell along with the flat mirror and the ridge that provides infrastructure for the microcavity. (b) side view of the flow cell. 155
7.5 Experimental data of (a) the mode shift when the particle is trapped (b) different laser powers that affect the number of trapping events; the top and the bottom figures represent trap events for 100 % and 35 % of full optical power (20 mW), respectively. 158
7.6 Optical modes based on the realistic model in the cavity along with a parabolic flow distribution to show the dependency of speed value on the position of the cavity with RoC of 25 μm. 160
7.7 Experimental results (a-b) versus simulation results (c-d) when polystyrene nanoparticles with diameters of 140 nm and 175 nm are introduced into the cavity by pressure of 2 $mbar$and when the maximum intracavity power is 20 mW. 162
7.8 Experimental results (a-b) versus simulation results (c-d) when 187 nm PS and 196 nm PMMA nanoparticles are introduced into the cavity by the pressure of 2 $mbar$ and when the maximum intracavity power is 20 mW. 164
7.9 The Gaussian fit is applied to the experimental result to show the resolution of the method. 165
7.10 A comparison between the effect of linear and parabolic flow on the trap rate of PS particles with size of 175 nm in the simulation when the maximum interactivity is 35 mW. 166
7.11 Experimental (left) and simulation (right) results of the trap rate when 175 nm PS particles are delivered to the cavity by the pressure of 4 $mbar$ or the average flow velocity of 108 $\mu m/s$. The maximum intracavity power (100%) is 15 mW. 167

7.12 Experimental results of changing the trap events in two different pressures of 5 $mbar$ or the average flow velocity of 135 $\mu m/s$ and 3 $mbar$ or the average flow velocity of 81 $\mu m/s$ for the PS particle with the diameter of 175 nm when the maximum intracavity power is 20 mW. 169
7.13 Experimental results where particles (more than 800 particles) are delivered throught the cavity with pressure of 4 $mbar$ or the average flow velocity of 108 $\mu m/s$ - Trap rate (left) and the derivative of trap rate (right) for two different filter times of 100 ms and 50 ms when the maximum intracavity power is 20 mW. 170
7.14 Results of (a) the trap rate calculation for two PS particles with diameters of 60 nm and 66 nm (left) and size distribution based on the derivative of trap rate with respect to velocity (right) (b) trap rate calculation for a mixture of two PS particles with sizes of 60 nm and 66 nm (left) size distribution based on the derivative of trap rate with respect to velocity (right). 171
7.15 Nanoparticle trapping cross-section for different velocities against different interactivity powers in (a) McNab-Neisen and Duhr-Braun Models. (b) Thermophoretic effect on trapping nanoparticles in McNab-Meisen (left column), Duhr-Braun (middle column), and no thermophoresis (right column) models when interactivity power and RoC are 1 W and 25 μm, respectively. 174

8.1 CFTA method as a sorting technique by using the cavity, an optical waveguide, and applying an external flow. 182

List of Tables

2.1 Summary of Characterization Techniques 13
2.2 Summary of Optical Sensors for Trapping and Manipulating Particles 29

6.1 Summary of Reference Samples of Phosphorex Polystyrene Particles 131
6.2 Experimental trap time duration vs the FWHM for the presented peaks 142

7.1 Reference Samples of Microparticles GmbH 156
7.2 Peak Resolution of CFTA 165

List of Abbreviations

AFM	Atomic Force Microscopy, page 14
APD	Avalanche Photodiode, page 72
ARROW	Antiresonant Reflecting Optical Waveguide, page 30
AUC	Analytical Ultracentrifugation, page 23
CFTA	Cavity Fluidic Trapping Analysis, page 6
CWG	Conventional Channel Waveguide, page 32
DBR	Distributed Bragg Reflector, page 66
DCS	Differential Centrifugal Sedimentation, page 24
DI	Deionized, page 68
DLS	Dynamic Light Scattering, page 2
Eo	Electroosmosis, page 172
EV	Extracellular Vesicle, page 21
FCM	Flow Cytometry, page 20
FIB	Focused Ion Beam, page 5
FSR	Free Spectral Range, page 50
FWHM	Full Width at Half Maximum, page 140
LSPR	Localized Surface Plasmon Resonance, page 41
Max	Maximum, page 82
MRI	Magnetic Resonance Imaging, page 1
mRNA	messenger RNA, page 1
NFCM	NanoFlow Cytometry measurement, page 21

NTA	Nanoparticle Tracking Analysis, page 2
P-C	Plano-Concave, page 45
PC	Photonic Crystal, page 38
PDMS	Polydimethylsiloxane, page 68
PID	Portional-Integral-Derivation, page 77
PMMA	Poly(Methyl Methacrylate), page 79
PS	Polystyrene, page 79
Q	Quality, page 5
RoC	Radius of Curvature, page 47
SEC	Size Exclusion Chromatography, page 23
SEM	Scanning Electron Microscopy, page 15
SOI	Silicon on Insulator , page 32
SPR	Surface Plasmon Resonance, page 41
SWG	Slot Waveguide, page 32
TC	Trapping Cross-section, page 153
TEM	Transmission Electron Microscopy, page 2

List of Symbols

L	Cavity length
λ	Wavelength
R_m	Reflectivity of mirrors
$\mathcal{F}$	Finesse
$\delta\lambda$	Line-width
Q	Quality factor
q	Number of antinodes
E	Electric field
ϵ	Permittivity
μ	Permeability
k	Wave vector
ω	Beam waist
I_R	Intensity in realistic optical mode
I_0	Intensity at beam waist ω_0
I_{R0}	Intensity in realistic optical mode at beam waist ω_0
p	Optical power
Z_R	Rayleigh length
R_i	Radius of the beam front curvature for incident beam
R_r	Radius of the beam front curvature for reflected beam
ω_i	Beam width of the incident beam
ω_r	Beam width of the reflected beam
I_c	Intensity in cylindrical model

I_{c0}	Intensity in cylindrical model at beam waist ω_0
$\Delta\lambda$	Optical mode shift
$\mathfrak{U}$	Electromagnetic energy
V	Optical mode volume
α	Polarizability
$\mathfrak{h}$	Planck's Constant
f	Frequency of the incident light
n_{med}	Refractive index of medium
n_p	Refractive index of particle
V_p	Particle volume
ρ	Density
N	Number of particle
a	Radius of particle
D	Diameter of particle
U_{flow}	Flow potential
$U_{Optical}$	Optical potential
$F_{Optical}$	Optical force
F_{Flow}	Flow force
v	Flow velocity
η	Viscosity of fluid
T	Temperature
W_i	Random vector

$\mathfrak{D}$	Diffusion coefficient
v_T	Thermophotetic velocity
k_p	Thermal conductivity of particle
k_l	Thermal conductivity of fluid
k_T	Thermal conductivity
$\dot{Q}$	Heat flow
A	Surface area
σ_{ch}	Surface charges
λ_{DH}	Debye length
I_i	Ionic strength
N_A	Avogadro number
τ	Time filter
u	Flow average velocity
P	Pressure
R_h	Hydraulic resistance
F	Flow rate
F_{ep}	Electrophoretic force
μ_{ep}	Electrophoretic mobility
F_e	Electrical force
Q_{ch}	Particle charge
ζ_p	Zeta potential of particle
ζ_{wall}	Zeta potential of channel
v_{eo}	Electroosmotic velocity

μ_{eo}	Electroosmotic mobility
w	Width of channel
h	Height of channel
r_t	Radius of tube
l_t	Length of tube
A_t	Cross-section of tube
R_e	Electrical resistance
ρ_e	Resistivity of liquid
σ	Standard deviation
σ_{TC}	Nanoparticle Trapping Cross-section
P_{trap}	Trap probability
Γ_{trap}	Trap rate
R_p	Peak resolution

Physical Constants

Permittivity of free space	$\epsilon_0 = 8.85 \times 10^{-12}\ F.m^{-1}$
Permeability of free space	$\mu_0 = 1.256 \times 10^{-6}\ H.m^{-1}$
Speed of light	$c = 2.9979 \times 10^{8}\ m.s^{-1}$
Boltzmann constant	$K_B = 1.38 \times 10^{-23}\ J.K^{-1}$
Avogadro constant	$N_A = 6.02 \times 10^{23}$
Elementary charge	$e = 1.60217657 \times 10^{-19}\ coulombs$
Refractive index of water	$n_w = 1.33$ [24]
Refractive index of PS	$n_{PS} = 1.59$ [24]
Refractive index of PMMA	$n_{PMMA} = 1.49$ [4]
Viscositiy of water at 300K	$\eta = 0.8 \times 10^{-3}\ Pa.s$ [25]
Thermal conductivity of silica	$k_{silica} = 1.4\ W.m^{-1}K^{-1}$ [26]
Thermal conductivity of polystyrene	$k_{PS} = 0.12\ W.m^{-1}K^{-1}$ [27–29]
Thermal conductivity of PMMA	$k_{PMMA} = 0.2\ W.m^{-1}K^{-1}$ [30]
Thermal conductivity of water	$k_w = 0.6\ W.m^{-1}K^{-1}$ [31]
Density of water	$\rho_w = 997\ kg.m^3$ [32]

Chapter 1

Introduction

In the last decades, nanotechnology has appeared in many scientific areas. Nanotechnology is the study and application of targets with nanoscale sizes. At this scale, atoms and molecules have different collective behaviors which can be used in interesting applications such as medical diagnosis, treatment of diseases [33], biodetection of pathogens [34], tissue engineering [35, 36], tumor imaging [37], Magnetic Resonance Imaging (MRI) contrast agents [38], and drug delivery [39, 40]. Drug delivery is a new scientific area that studies pharmaceutical nanocarriers [40–42]. An efficient clinical drug delivery system needs to control drug release and solve the pharmacological limitations [43, 44]. For instance, the measurement of the loading of lipid nanoparticles with messenger RNA (mRNA) is of increasing importance for gene therapy and vaccine development [45, 46].

In nanomedicine, the nanocarriers consist of nanoparticles, nanospheres, nanocapsules, nanoemulsion, and nanovesicular [47–49]. The formulation of the nanodrug loading systems is dependent on the target organ and the desired drug. The ability

of nanomedicine to reach the target organ can be determined by its particle size, surface charge distribution, and concentration. Accordingly, characterizations of nanocarriers such as nanoparticles are crucial to controlling their desired action in vitro as in vivo [50].

Nanotechnology attempts to improve traditional drug delivery and medical diagnostics since the characterization of nanomedicine is essential to uncover the nanomedicine behaviour in a biological system. New devices started to emerge in recent years which allow such manipulations and investigations even in real-time. Medical adjustment of nanoparticles used in medical applications requires accurate characterization techniques. Namely, it is critical to know the physical and chemical aspects of the nanoparticles (size, composition, stability, zeta potential, concentration, etc.) and the media that are needed in such medical applications.

There exist several techniques for characterizing the size, shape and composition of nanoparticles. The most common ones include Dynamic Light Scattering (DLS) [51–53], Transmission Electron Microscopy (TEM) [54, 55], Atomic Force Microscopy (AFM) [6, 56, 57], and Nanoparticle Tracking Analysis (NTA) [10, 54, 55, 57–60]. Many of these methods have a wide detection range of particle size. However, characterizing individual nanoparticles in a fluid is challenging because the particle diffuses rapidly by the Brownian motion. Furthermore, DLS detection resolution for polydisperse nanoparticles is not high enough so that it can not be used for sensitive applications [52]. The TEM and AFM can measure the nanoparticle size and visualize the nanoparticle surface. However, these methods have a number of drawbacks. For instance, TEM technique needs a high-vacuum condition, and that they are time-consuming, and expensive [54, 55].

1.1 Nanoparticle Characterization with Microcavities

Nanoparticle characterization in liquid media is challenging since the particles move rapidly due to their Brownian motion. In this context, our goal is to solve this problem by holding a nanoparticle in place and then measuring the physical parameters of the nanoparticle. Therefore, in this work, optical trapping and manipulation of nanoparticles and biomolecules have been studied due to their capabilities for measuring the size of the nanoparticle and other physical characteristics. Size measurement and size distribution analysis are two important analytical strategies for nanomedicine.

Trapping and characterizing nanoparticles in solution is of great importance for lab-on-a-chip applications in biomedical, environmental, and materials sciences. Devices have been starting to emerge in recent years which allow such manipulations and investigations in real-time. The main principle is that nanoparticles can be trapped and manipulated directly by optical forces. In fact, the optical forces generate a shift in hydrodynamics or electrical conditions around a particle resulting in a change in its path.

There exist several manipulation techniques (e.g. optical tweezers) and techniques involving electrokinetic forces [61] (e.g. electrophoresis, dielectrophoresis, and traveling-wave dielectrophoresis). Arthur Ashkin [62–64] pioneered optical trapping in 1970 by demonstrating that optical forces can move micron-sized dielectric particles in water and air. Ashkin observed the acceleration of microscopic particles and the pulling of transparent particles induced by radiation and gradient forces, respectively. Therefore, characterizing and manipulating nanoparticles and biomolecules have drawn interest due to their capabilities for precise control, delivery, sorting, and analysis of target analytes.

Optical microresonators have become a promising component for the detection and characterization of single-nanoparticles. Electromagnetic field enhancement in resonators is the main principle to optically trap nanoparticles. A Fabry-Pérot microcavity is a well-known optical microresonator, offering a powerful combination of small mode cross-section, high finesse, and open-access (air or vacuum separation) in microcavities [24, 65].

Optofluidic devices constructed based on this type of microcavities have a number of advantages including real-time monitoring, high precision sensing, high resolution, simple fabrication, and single-chip integration. Additionally, this type of optical tweezers reduces any potential biological damage to nanoparticles when being trapped or detected.

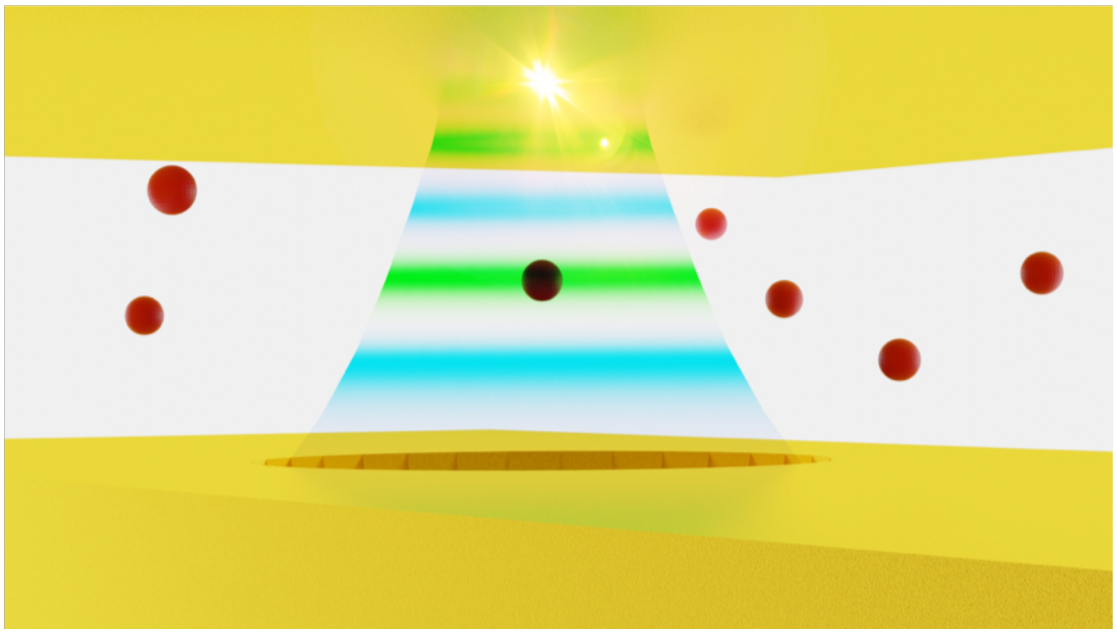


Figure 1.1: A schematic of open cavity as an optical tweezer to trap nanoparticles [4].

Optical microcavities are good candidate devices for detecting and characterizing nanoparticles, because of their small mode volume and high-quality factor. The combination of these two features creates both strong interaction between the confined optical field and nanoscale particles and provides a low limit of detection

measure for small mode perturbations. Figure 1.1 shows a schematic of open-access Fabry-Pérot microcavity.

A nanoparticle can be trapped by a gradient of an electromagnetic field which is created with a focused laser beam [64, 66]. In other words, the interaction between the nanoparticle and the light field creates an optical force. For nanoparticles in a solution, a strong optical force is needed to overcome the random thermal motion that is known as Brownian motion. The Brownian motion can be overcome with low optical power to trap particles with micron size, however, trapping nano-scale particles requires higher optical power.

1.2 Dissertation Overview

This project employs open-access Fabry-Pérot microcavities as a promising technology for lab-on-a-chip applications with the goal of delivering and then trapping nanoparticles in order to detect and to manipulate them. These microcavities show great potential for trapping and manipulating particles, as well as particle identification using refractive index changes and spectroscopic methods [24, 67]. Fabry-Pérot devices incorporating microcavities are good candidates for optical trapping of nanoparticles because of the small mode volume and high-quality factor. The nanoparticles experience a gradient force by the strong electromagnetic field within the Fabry-Pérot device, if the refractive index of the particle is greater than that for the fluid then the field gradient draws them into the optical trap. The small mode shift obtained when a particle is trapped provides a metric for the characterization of the nanoparticles.

This work involves the design of an optofluidic Fabry-Pérot microcavity based on theoretical principles. A stochastic model for the particle dynamics within the microcavity trapping is then simulated to confirm that the design of the optofluidic

system is theoretically correct. We show that this design is suitable for a wide range of particles based on the flow rate of an aqueous medium through the Fabry-Pérot microcavity, the optical laser power, and the optical beam geometry in the microcavity. The ultimate goal is to subsequently detect nanoparticles with high-resolution.

The microcavity parameters, such as Quality Factor (Q), mode volume and device dimensions are subsequently designed and fabricated with high precision. Focused Ion Beam (FIB) milling is used to fabricate a novel mirror substrate in which a series of thin films are deposited to provide optimal mirrors with high Reflectivity (R_m). These mirrors are concave and are aligned with high precision in parallel, facing a planar mirror to create the Fabry-Pérot microcavity, (see Figure 1.1).

Using the open-access microcavity allows us to trap a single nanoparticle and to perform potential subsequent characterization. Also, this allows a deep understanding of the optical trapping of nanoparticles in flowing fluid, which is crucial for trapping and manipulating nanoparticles and biomolecules. By analyzing the trapping rate as a function of the flow rate and the laser power, this project proposes a technique to perform an analysis of the size distribution of the particles in a flowing fluid. In order to do so, optimization of nanoparticle delivery and precise calibration of flow speed through the microcavity is necessary.

A new approach called Cavity Fluidic Trapping Analysis (CFTA) is developed to evaluate the size of nanoparticles, and allows for an assessment of the polarizability. Not only CFTA can measure the size of nanoparticles, but also it is sensitive to the refractive index. Therefore, the method can be used to give a measure of composition such as in drug delivery for nanomedicine. The method is to be developed as a powerful technique to characterize nanoparticles in a solution in applications where we need high-resolution measurements at the single-particle

level.

This dissertation is structured as follows:

- **Chapter 2** A discussion on nanoparticle characterization techniques and the optical biosensor will first take place in Chapter 2, focusing on the key features that enabled the demonstration of nanoparticles characterization. The diversity of applications of the photonic devices will also be briefly mentioned along with other notable advantages of optical resonators. We then discuss alternative strategies for nanoparticle characterization. This will concentrate on optical microcavities for which an optical field is leveraged to manipulate nanoparticles. Also, open-access optical cavities will be discussed as valuable candidates to use as sensors for nanoparticle characterization.

- **Chapter 3** explains the structure of open-access optical cavities along with the physical parameters. We introduce an open-access microcavity and show how the optical beam can be propagated through the cavity and how we can measure the polarizability of nanoparticles by this type of the cavities.

- **Chapter 4** presents the cavity fabrication process. The nanoparticle characterization methods will then also be discussed in this chapter, along with the optical set-up, flow cell, optical cavity mounting, sample preparation, and flow delivery. Finally, there are several experimental aspects of nanoparticle trapping that must be understood, which will be discussed in depth.

- **Chapter 5** discusses the fundamental theoretical elements required to describe the nanoparticle characterization process in a few parts. Then, an overview of how the optical force is generated based on the optical beam is given. According to the introduced flow cell, all presented forces on the particle will be determined by presenting a stochastic model. Since nanoparticles are delivered through the cavity, then the particle behavior will be

studied based on the existing forces in the system. Further, this chapter studies the underlying theory that describes the behavior of particles in an optofluidic microcavity based on the dynamic range and throughput of a given instrument. Additionally, pressure-driven method as one of different methods for delivering nanoparticles through the flow cell will be described. The flowing fluid is crucial for the understanding of the optical trapping of nanoparticles. The pressure delivery will be discussed as the used method for this project and will be analytically and numerically studied.

- **Chapter 6** shows the introduced Fabry-Pérot style microcavity resonator to create the confined optical field for both trapping and measuring nanoparticles with high resolution. The particles will be measured by considering the spectral shift of the mode wavelength. We show that the maximum mode displacement provides an accurate measure of the polarizability of each particle. Polystyrene particles with diameters 50 nm, 75 nm, and 100 nm are measured. The measurements are in water by the distribution of polarizabilities from the solution. Further, we will present the method as a powerful tool for characterizing nanoparticles in solution, for use in applications where high-resolution measurements are required at the single-particle level.

- **Chapter 7** proposes Cavity Fluidic Trapping Analysis (CFTA) as a new technique for analyzing the dynamics of nanoparticles in fluidic systems and studying the potentials of optical trapping. The trapping rate of nanoparticles as a function of the flow rate, trapping laser power, and size of particles are thoroughly discussed in this chapter. This technique will measure the different particle sizes and also the different particle types even with the same size. Thus, the technique will give a deep understanding of the optical trapping of nanoparticles in flowing fluid, which is crucial for trapping and

manipulating nanoparticles and biomolecules.

- **Chapter 8** summarises the dissertation by reviewing the main contributions of this work and outlines directions for future research.

1.3 Publications by the author

The material presented in this dissertation has appeared or is under preparation in international conference proceedings or peer-reviewed journals. The connection between each chapter and the publications is as follows:

- **Chapter 4**

  Kiana Malmir, Trichet Aurelien, Robert Nyman, Benjamin Ash, Matteo Contino, Dean James, Claire Vallance, Jeremy Warren, Jason Smith, "Quantitative Analysis of Nanoparticle Composition using Open Microcavities", International Conference On Nanomedicine And Nanobiotechnology, 2019 [1].

  – The materials presented in Sections 4.4, 4.5, 4.6

  Kiana Malmir, Trichet Aurelien, Jason Smith, "Characterisation of Nanoparticle Size Distributions in a Fluid using Optical Microcavities", Photon, 2020 [3].

  – The materials presented in Sections 4.4, 4.5, 4.6

  Kiana Malmir, William Okell, Trichet Aurelien, Jason Smith, "Sensing Nanoparticles by CFTA", under preparation, 2022.

  – The materials presented in Sections 4.4, 4.5.

  Kiana Malmir, William Okell, Trichet Aurelien, Jason Smith, "Characterisation of Nanoparticle Size Distributions in a Fluid with Open Cavities", under preparation, 2022.

  – The materials presented in Sections 4.4, 4.5.

- **Chapter 5**

  Kiana Malmir, Trichet Aurelien, Jason Smith, "Characterisation of Nanoparticle Size Distributions in a Fluid using Optical Microcavities", Photon, 2020 [3].

  – The materials presented in Sections 5.2, 5.3.

  Kiana Malmir, William Okell, Trichet Aurelien, Jason Smith, "Sensing Nanoparticles by CFTA", under preparation, 2022.

  – The materials presented in Sections 5.2, 5.3.

  Kiana Malmir, William Okell, Trichet Aurelien, Jason Smith, "Characterisation of Nanoparticle Size Distributions in a Fluid with Open Cavities", under preparation, 2022.

  – The materials presented in Sections 5.2, 5.3.

- **Chapter 6**

  Kiana Malmir, William Okell, Trichet Aurelien, Jason Smith, "Characterization of Polystyrene Nanoparticle Size in a Mixture Fluid by Measuring Polarizability.", under preparation, 2022.

  – The materials presented in Sections 6.2

- **Chapter 7**

  Kiana Malmir, William Okell, Trichet Aurelien, Jason Smith, "Characterisation of Nanoparticle Size Distributions in a Fluid using Optical Forces", arXiv preprint, 2021 [4].

  – The materials presented in Sections 7.2, 7.2.1.

Chapter 2

Literature Review

2.1 Introduction

Nowadays, measuring nanoparticle properties and evaluating their structures in a liquid environment are crucial challenges due to the small particle size, Brownian motion, and sample-preparation requirements. Different characterization methods are developed to evaluate different physicochemical properties of nanoparticles. These methods characterize and measure the key parameters of nanoparticles, namely size, shape, and surface charge. A variety of techniques, e.g., optical spectrometry or Raman spectroscopy, can evaluate the material and chemistry of nanoparticles [68]. The characterization of size, shape, and surface charge is an essential stage to understand and anticipate the behavior of particles. However, the small dimension of nanoparticles can affect the behavior of particles. More specifically, the size and the shape of a particle impact its viscous drag in a fluid and thus the rate of diffusion as well as the optical properties [69].

The goal of this chapter is to introduce the use of characterization, manipulation, and optical sensing techniques in microfluidic devices. Firstly, we review the established nanoparticle characterization techniques currently used and describe their advantages and limitations. We illustrate techniques that can improve the drawbacks of common methods. Then, an overview of optical manipulation and trapping of small nanoparticles is provided along with some of the potential new techniques. Further, the concept and various applications of optofluidics are explained. Following this, a number of recent implementations including those that exploit simple waveguides, optical resonators, and plasmonic devices are highlighted in this chapter.

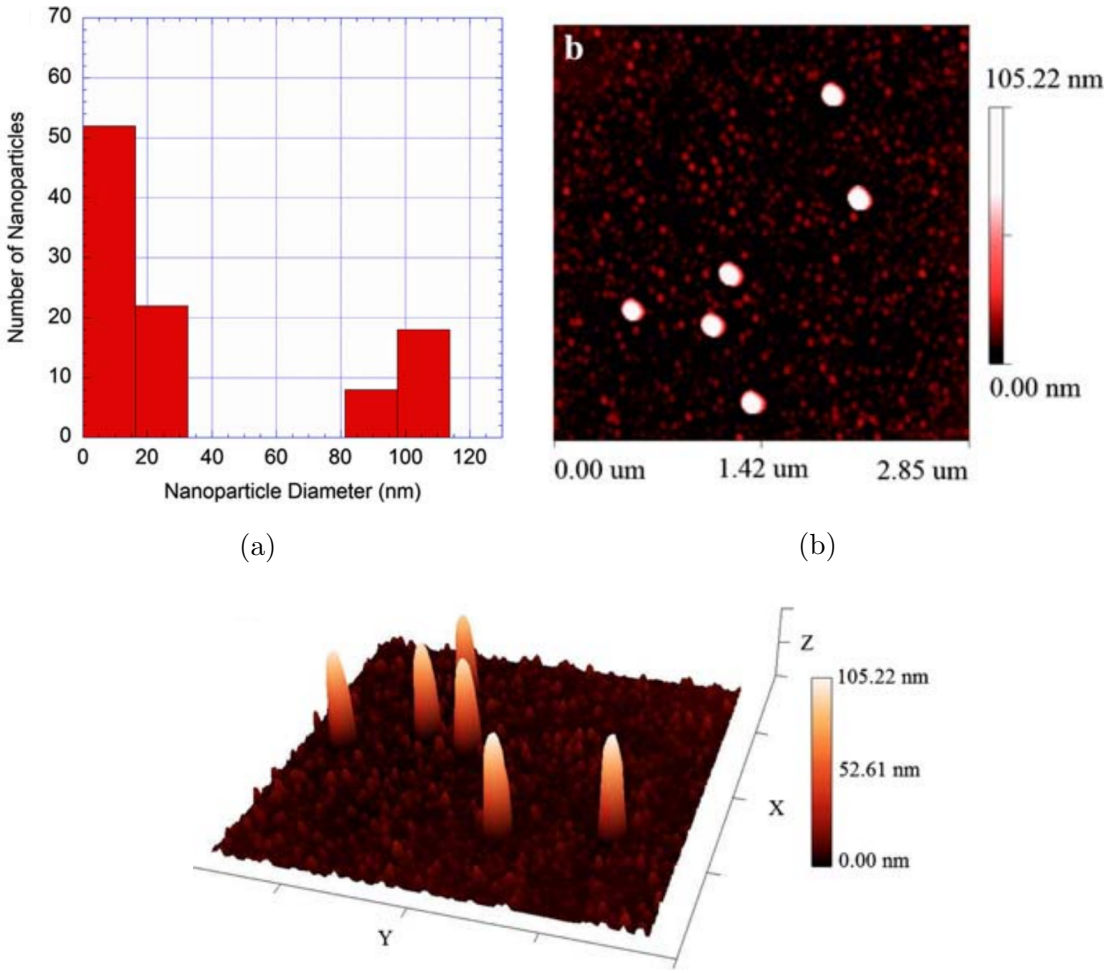
2.2 Characterization Methods

There are a number of methods to characterize nanoparticles at the single-particle level with high resolution. Electron microscopy or scanning probe microscopy can provide accurate information on the shape of the nanoparticles. These techniques use the interaction between the atomic structure and the impinging electron beam or the scanning probe [70]. However, this type of nanoparticle characterization has restrictions. For example, in the scanning probe microscopy technique, the sample needs to be under high-vacuum conditions and deposited on a hard substrate.

Methods based on light-scattering and diffusion have been also developed to characterize the suspended nanoparticles in a fluid. These techniques are the common techniques for determining the size and the shape of nanoparticles. We discuss these methods in this section, and we summarized them in Table 2.1

Table 2.1: Summary of Characterization Techniques

Ref	Method	Situation	Condition	Size	Advantages	Limitations
[57, 71]	AFM	Dry and in liquid	Size, Shape	10 nm to 20 nm	Compatibile with different samples, measurement environments	Needs a hard surface to deposite the samples, limited throughput
[72]	SEM	High vacuum or low pressure	Size, Shape	2 nm to 3 nm	Single-particle resolution, needs low energy beams, user friendly	Limited penetration depth
[54, 55]	TEM	High vacuum	Size, Shape	1 nm to 1 μm	Particle morphology at sub-nm resolution, information on internal structure of nanoparticles	Needs higher energy beams than SEM, very expensive
[51]	DLS	In suspension	Size	5 nm to 10 μm	Fast, shows behavior of nanoparticles in solution	Highly biased toward larger particles in suspension, doesn't provide information on shape of nanoparticles
[10]	NTA	In suspension	Size, Concentration	30 nm to 1 μm	Single-particle resolution, suitable for highly polydisperse samples	Requires sample dilution for highly scattering particles
[73–76]	FCM	In suspension	Size, Concentraion	Larger than 50 nm	Single-particle resolution, quick, reliable result	Noise effect on the performance
[77–79]	AUC	In suspension	Size, shape, stoichiometry	Kilodalton-gigadalton	Non-destructive, sample reusability	Difficult to distinguish similar samples, requires certain optical properties
[80–83]	DCS	In suspension	Size, concentration	10 nm to 50 μm	Fast high-resolution, accurate, inexpensive	Contamination poor recovery



(a) (b)

(c)

Figure 2.1: (a) AFM distribution of 20 nm, and 100 nm polystyrene nanoparticles in an 8:1 mixture. (b) AFM scan of 20 nm, and 100 nm polystyrene nanoparticle mixture, and AFM size distribution data. (c) Three-dimensional AFM image of 20 nm, and 100 nm polystyrene nanoparticle mixture. 20 nm particles can be seen in the background [6].

2.2.1 Atomic Force Microscopy (AFM)

Atomic Force Microscopy (AFM) technique is based on a scanning probe microscopy method to explore and scan the upper surface of a nanoscale object [6, 56, 57, 71, 84]. AFM uses a cantilever with a sharp tip that is rastered across the surface of a sample. Reflection of a laser beam from the cantilever tip onto a photodiode array records the forces which result from the interaction of the tip with the sample.

This technique can characterize nanoparticles with the size range of $1 - 20\ nm$ in a dry and liquid states. Although the AFM has high compatibility with different samples and measurement environments, it is limited in the sample preparation. Namely, the samples need to be deposited on a hard substrate [57].

Hoo and his colleague presented the accuracy of AFM for characterizing size distributions of polystyrene nanoparticles in the size range of $20-100\ nm$. Figure 2.1 demonstrates their results; figure 2.1a illustrates that the analysis of the mixed sample was able to easily produce two distinct distributions with nominal sizes similar to the nominal sizes found for mono-disperse samples. Figure 2.1b and Figure 2.1c show that both the 20 and 100 nm nanoparticles can be easily identified [6].

2.2.2 Scanning Electron Microscopy (SEM)

Scanning Electron Microscopy (SEM) is a technique to image the sample surface by analyzing secondary electrons emitted from the sample after a primary electron beam is pinged [85]. More specifically, secondary electrons are the electrons that are ejected from the specimen surface atoms by the primary beam electrons. Figure 2.2a explains the typical layout of an SEM, which encompasses the electron gun (electron source and accelerating anode), electromagnetic lenses to focus the electrons, a vacuum chamber housing the specimen stage, and a selection of detectors to collect the signals emitted from the specimen [7]. SEM can provide a high-resolution imaging of single nanoparticles with sizes below 10 nm [86]. SEM technique can also characterize the shape of samples although the penetration depth is limited in this method. Additionally, this technique demands a high-vacuum or low-pressure condition to measure the samples [72, 85].

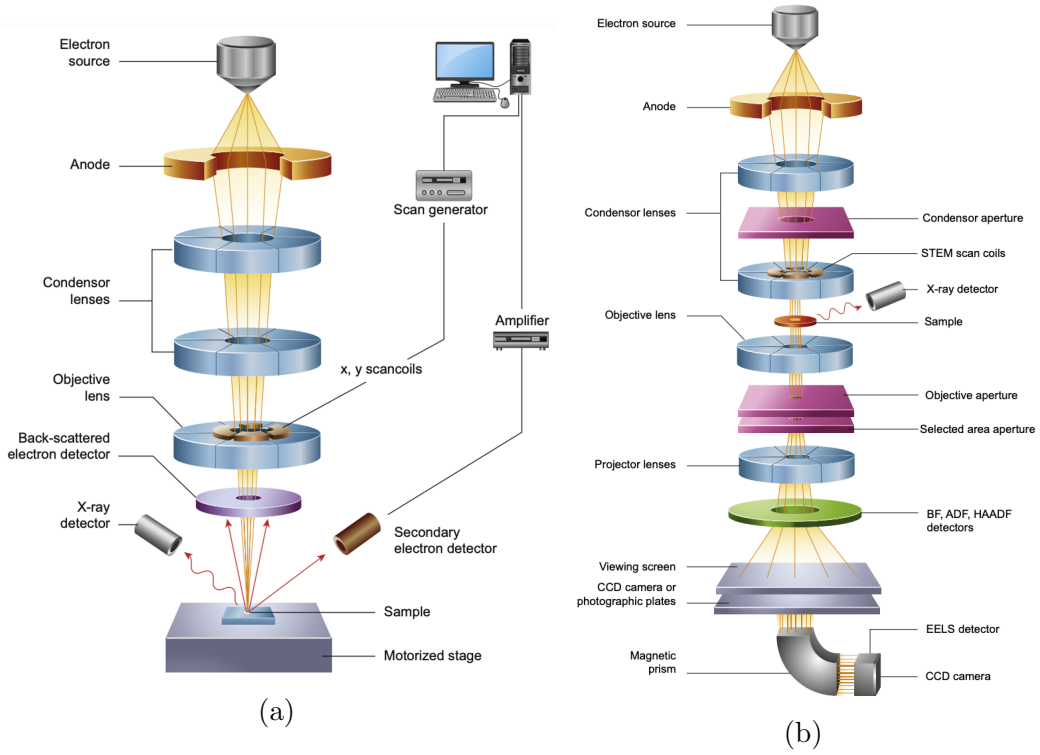


Figure 2.2: Schematic of components of (a) SEM and (b)TEM [7].

2.2.3 Transmission Electron Microscopy (TEM)

One of the most well-known characterization methods is Transmission electron microscopy. TEM technique applies a focused electron beam on a thin sample to build micrographs of the sample with high-resolution [58]. TEM microscopes have many more electromagnetic lenses compared to SEM, arranged sequentially along the electron beam direction as an electron column (Figure 2.2b). Condenser lenses are placed before the specimen to focus the electrons into a beam of controlled diameter and convergence [87]. The objective lens focuses the transmitted electrons to form the diffraction pattern and the first image. Projector lenses then magnify the image or diffraction pattern onto the detection system [7].

TEM resolution can be as high as 0.05-0.1 nm by decreasing image distortion [88]. Although this technique enables the investigation of the size, shape, and structure of crystal at the single level in high resolution, the sample preparation for measurement

and analysis can be difficult. Further, all TEM specimens must have regions of electron transparent material through which the electrons can be transmitted [7]. Furthermore, the specimens need to cope with the high-vacuum condition and the high-energy electron beam during the evaluation [54, 55, 89].

2.2.4 Dynamic Light Scattering (DLS)

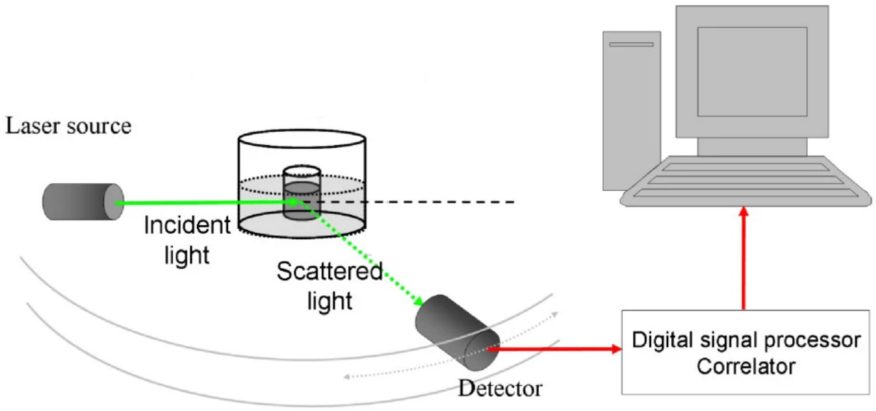


Figure 2.3: The optical configuration of a typical experimental setup for DLS measurements [8].

Dynamic Light Scattering (DLS) detects particle size in liquid suspensions [90–92]. Nanoparticle characterization in DLS can be done with low sample concentration and in a short evaluation time. This technique is based on measuring the free diffusion coefficient of particles [93]. In fact, a laser is directed to the suspended nanoparticle container, and the random thermal motion of particles creates time-dependent fluctuations in the scattered light intensity (Figure 2.3). DLS determines the diffusion coefficient ($\mathfrak{D}$), which is related to the hydrodynamic particle radius (a_h) through the Stokes-Einstein equation:

$$\mathfrak{D} = \frac{k_B T}{6\pi\eta a_h}, \tag{2.1}$$

where K_B is the Boltzmann constant, T is the absolute temperature, and η is the viscosity of the medium.

The fluctuation time depends on the time of diffusion of the scattering nanoparticles through the laser point. The diffusion coefficients of particles can be measured by an autocorrelation evaluation of this time-domain signal. Note that, the particle diffusion is related to the scattering correlation time, therefore this technique can be used for size distribution analysis [93]. DLS can be used to measure the size of nanoparticles with a range of 10 nm to 20 μm in suspension while it is limited for larger particles [51].

2.2.5 Nanoparticle Tracking Analysis (NTA)

Nanoparticle tracking analysis determines the size of particles based on the particle Brownian diffusion in liquid. NTA technique analyzes nanoparticle diffusion by tracking the random movement of the suspended nanoparticles with high temporal-resolution video acquisition and enhanced contrast microscopy [10]. NTA can evaluate the nanoparticles with size of 60 nm to 2 μm. The wide application of NTA is limited because of the needed high level of scattering of the particles and also the required sample dilution. However, this method is still used for size characterization of suspended nanoparticles. Additionally, because of the high dependence of scattering intensity on the particle size, size measurement is typically biased toward the larger population components [51].

Figure 2.4.a shows a schematic of NTA by Nirmalkar and his colleagues [9] to obtain particle size distributions of samples in a liquid suspension. A laser beam is transmitted through a glass flat (optical flat) within the sample chamber. Particles in the path of this beam, scatter light then they can be seen via a microscope

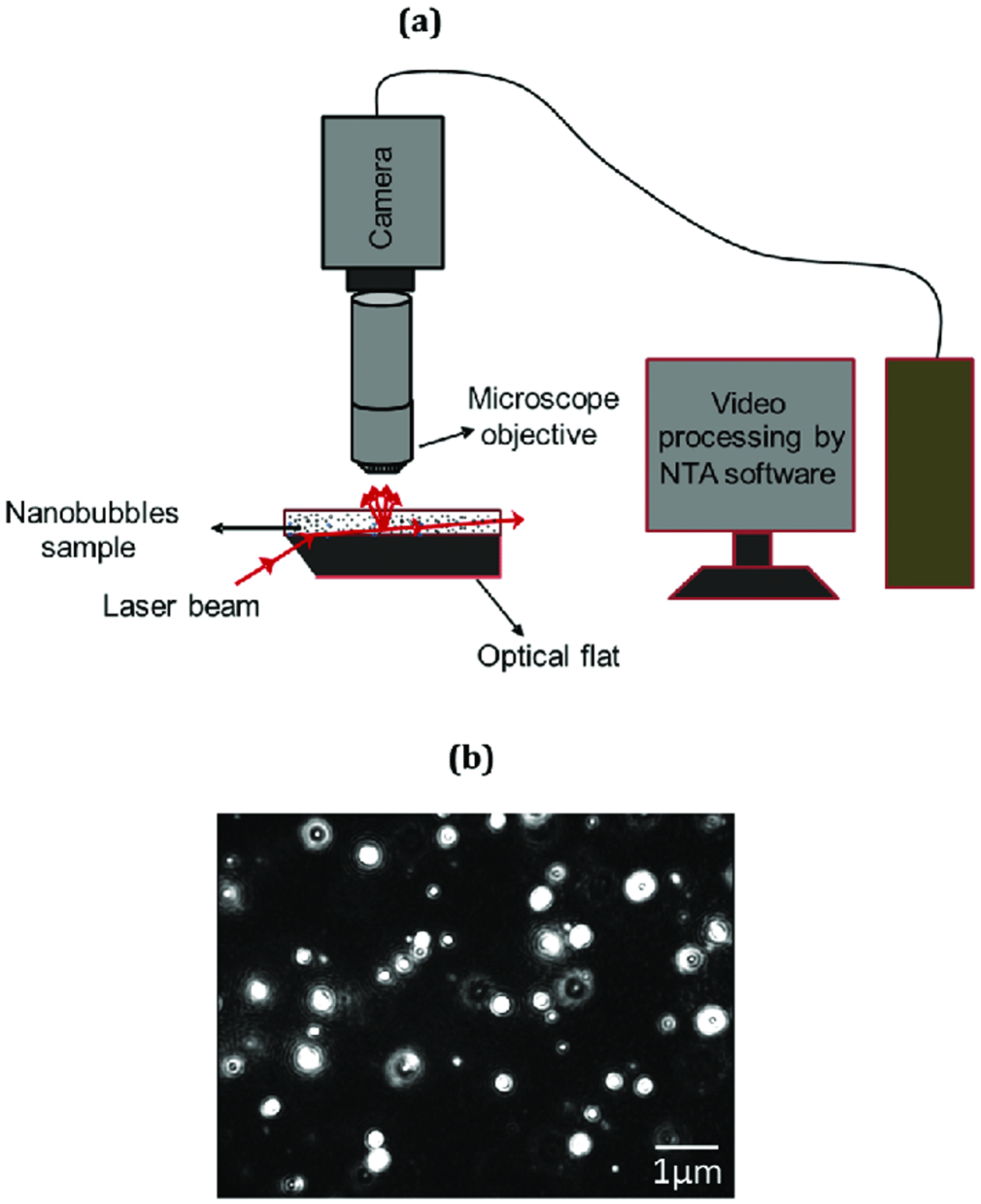


Figure 2.4: NTA characterization system: (a) schematic diagram; (b) typical micrograph showing bulk nanobubbles [9].

objective which is mounted on a CCD. With this set-up, they could capture a video file of particles or nanobubbles moving under Brownian motion. A typical micrograph of nanobubbles is shown in Figure 2.4(b).

Filipe et al. [10] evaluated the NTA technique for monodisperse and polydisperse nanoparticles, and then they make a comparison between NTA and DLS. They

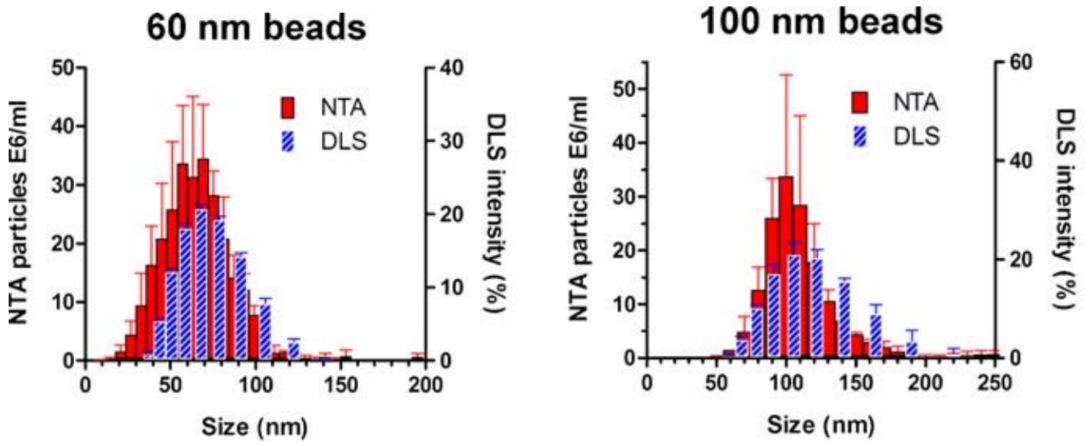


Figure 2.5: Size distribution from NTA and DLS measurements of monodisperse polystyrene beads with size of 60 nm and 100 nm. Error bars represent standard deviations obtained from three measurements of the same sample [10].

also tested the performance of their technique in characterizing the delivery of nanoparticles and protein aggregates. A heat-stressed IgG formulation and a metal-oxidized insulin formulation is used as protein aggregates. Figure 2.5 shows the size distribution of monodisperse polystyrene beads with NTA and DLS techniques. In their work, they showed that NTA is more accurate than DLS for sizing samples and has a substantially better peak resolution [10]. Namely, NTA provides a distribution with a lower deviation.

2.2.6 Flow Cytometry (FCM)

Flow cytometry (FCM) is another well-established method to characterize individual cells and particles [94, 95]. FCM is a based-flow method to detect nanoparticle size and concentration by measuring the properties of scattered light or fluorescence associated with cells. FCM can analyze complex populations according to user-defined cell characteristics, with typical analysis rates approaching 10000 cells/s. In fact, FCM is a fast and reliable method to characterize nano samples but the operation of this method can be disturbed by noisy signals from buffers, optics, or electronics [73, 74, 96, 97].

Figure 2.6 illustrates a schematic of FCM analysis. Here a concentration of 8.5×10^{10} N/ml (N is the number of particles per ml) of 200 nm polystyrene nanoparticle, generates a distinctive side scattering signal from the background. This concentration agrees with 3000 nanoparticles existent in the quartz capillary of the apparatus under laminar flow, of which 150 nanoparticles are illuminated simultaneously by the laser at each event generation [11].

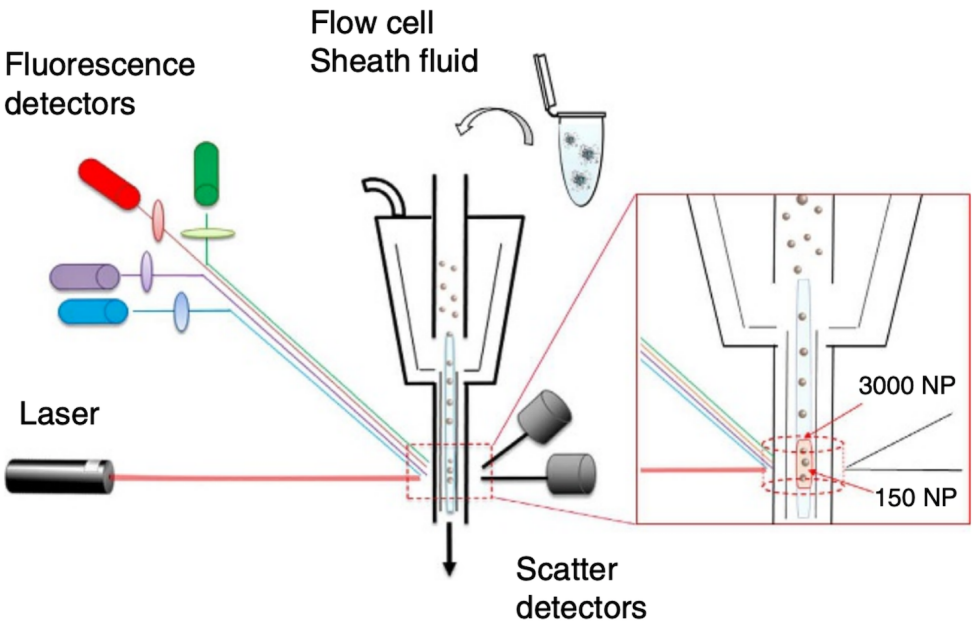
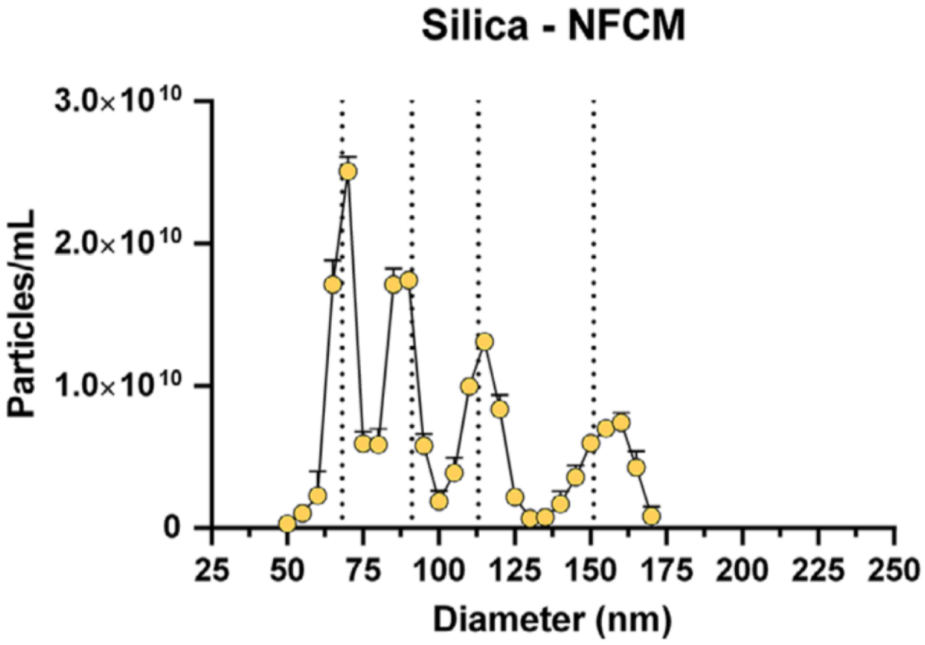
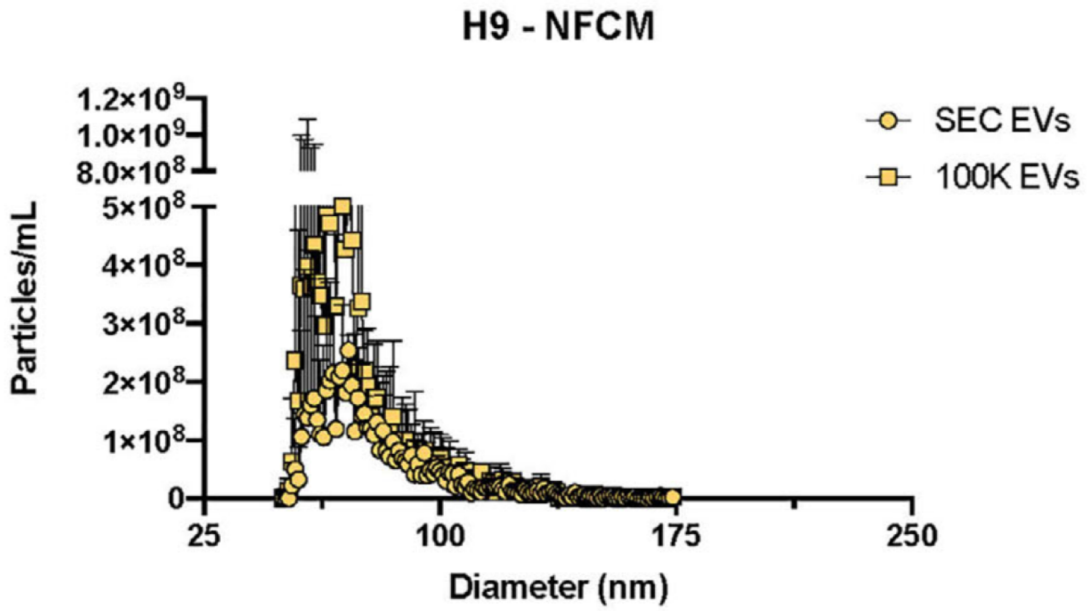


Figure 2.6: Graphical representation of the FCM analysis (NP: nanoparticle) [11].

FCM can provide information on size, shape, and morphology of the particle by measuring the scattered light. Biochemical characteristics, such as enzymatic activity and nucleic acid content, can be evaluated via fluorescent labeling. Although FCM has difficulty measuring nanoparticles smaller than 200 nm based on light scattering [75], there are significant improvements to characterize small single-nanoparticles and viruses by FCM [76, 98, 99]. For instance, Steen could detect the polymer nanoparticle with a diameter of 74 nm by FCM based on the light scattering [99]. Recently, Arab and her colleagues [12] characterized size, count and phenotype of artificial particles and Extracellular Vesicles (EVs) as biological



(a)



(b)

Figure 2.7: Results of Nano-Flow Cytometry (NFCM): (a) silica spherical particles size distribution as an artificial sample (b) particle size distribution for a biological sample [12].

samples by Nano-Flow Cytometry (NFCM) . NFCM was able to detect silica particles with nominal diameters of 68 nm, 91 nm, 113 nm and 151 nm as synthetic samples with concentration of 10^{12} N/ml where N is the number of particles per ml. Figure 2.7a shows the resolved four populations of silica spherical particles with specific peaks at diameters of 66 nm, 85 nm, 112 nm and 154 nm.

Furthermore, they also measured EVs as biological particles. They prepared EVs from H9 (T-lymphocytic) and U937 (pro-monocytic) cell supernatants [100] by ultrafiltration and size exclusion chromatography (SEC EVs) or by differential ultracentrifugation ($100K$ EVs where 100K equals to the speed of ultracentrifugation) [12]. For $H9$-derived materials, NFCM technique identified particles at smaller diameters for the $100K$ EVs compared with the SEC EVs as shown in Figure 2.7b.

2.2.7 Analytical Ultracentrifugation (AUC)

Analytical Ultracentrifugation (AUC) is another technique for the quantitative analysis of macromolecules in a solution. AUC is based on the principal property of mass and the fundamental laws of gravitation [101]. AUC can provide information of size, shape, and stoichiometry of macromolecular and synthetic polymers in a solution state environment by detecting the sedimentation properties of the samples when subjected to a centrifugal force [78, 79]. This analysis is attained by two complementary views; sedimentation velocity provides first-principle, hydrodynamic information about the shape and size of molecules [102, 103]. Sedimentation equilibrium provides first-principle, and thermodynamic information about the solution molar masses, stoichiometries, association constants, and solution nonideality [102, 104].

The apparatus is comprised of a high-speed centrifuge equipped with a transparent cell and a detector to observe the change of the dynamic concentration profile of

the particles along the cell axis during centrifugation (sedimentation velocity), and the final thermodynamic equilibrium (sedimentation equilibrium) [105]. During sedimentation, particles of different sizes and molecular weight separate and sediment at different rates, therefore multimodal sample distributions can be detected. AUC is highly sensitive to variations in density and mass of the nanoparticles thus it makes this technique appropriate for investigating particle surface coverage [106].

There is also a possibility to integrate multiwavelength optical characterization during sample sedimentation. This significantly increases the range of AUC application in nanoparticle characterization such as studying nanoparticle-protein interaction [107] or shape of the particle and optical behavior of polydisperse sample populations in an experiment [108].

There are three optical systems for the AUC technique: absorbance, interference, and fluorescence [104]. Although these optical systems allow precise and selective observation of sedimentation in real-time, these systems make several restrictions on the sample or the solvent. For instance, the sample has to have an optical property that distinguishes it from other solution components, and also it needs to sediment or float at an appropriate rate at an experimentally achievable gravitational field [104]. Also, data translation of sedimentation parameters into size and shape information is not easy because several factors, such as sample concentration or sample interactions can affect the results. Furthermore, the high cost of the instrument is another limitation of this technique [70].

2.2.8 Differential Centrifugal Sedimentation (DCS)

Differential centrifugal sedimentation (DCS) is another characterization method to evaluate high-resolution size distributions of the nanoparticles. DCS measures the time it takes for nanoparticles to sediment through a fluid since exposed to a centrifugal field [13]. DCS technique is based on the capability to separate

nanoparticles of the same density by mass [109]. Further, the method relies on light attenuation, the structure and shape of the nanoparticles which provide deep information to evaluate the relative concentration of particles in different populations [82].

This technique is able to measure the size of nanoparticles with a range of 10 nm to 50 μm however it can be extended with some types of materials. It provides a narrow particle distribution differing in diameter by less than 2% to be resolved, therefore, it enables to detect and measure small differences in particle size as it can be seen in figure 2.8 [13, 81]. This technique has a few restrictions for nanoparticle characterization due to the heterogeneity in biological particles. Furthermore, the DCS method suffers from contamination and poor sample recovery [80].

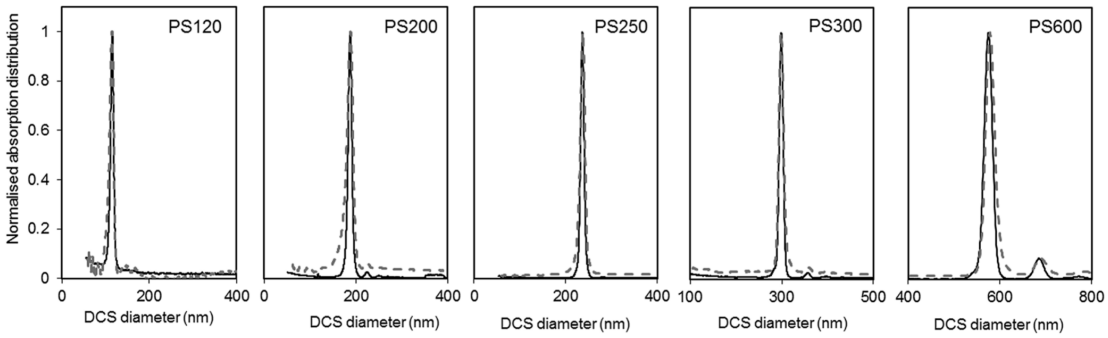


Figure 2.8: Normalized light extinction weighted size distributions of the PS NPs as measured by DCS in sedimentation (continuous black line) and flotation (dash grey line) modes [13].

2.3 Sensors for Nanoparticle Characterization

Characterization of nanoparticles in a solution is of great importance for lab-on-a-chip applications in biomedical, environmental, and materials sciences [110,111]. In the last decade, there has been considerable interest in developing biosensors with high sensitivity that are capable of real-time characterization. The applications include medical diagnosis [112], toxic metal-ion detection [111], cellular biothiol

monitoring [113], food quality control, environmental monitoring, and security [114]. Biosensors must be able to identify low concentrations of the target analytes. In addition, they must represent specific sensitivity in order to reduce interference from non-target molecules and thus avoid any ambiguity in results.

To this end, a number of biosensing mechanisms have been developed to meet these needs. Of these, many are optical biosensors. One of the main advantages of optical biosensors is their naturally small size which makes them compatible with the microfluidic volumes that are often dealt with. In addition, multiplexing is easily achieved with wavelength encoding in optical biosensors [115]. These properties mean that integration with other photonic and microfluidic components is feasible for the production of lab-on-a-chip devices [110], which would be small, easily-operated portable devices for in-site biosensing [111].

The fundamental principle behind the development of the lab-on-a-chip is to integrate numerous functions on a single device with the goal of reducing cost and increasing functionality. Recently, many advances have been made to integrate optical elements in the form of lenses [116–118], lasers, waveguides, and sensors with microfluidic devices [67, 119–126]. Characterization and trapping of nanoparticles in solution are of great importance for lab-one-a-chip applications in biomedical, environmental, and materials sciences. Devices are now starting to appear providing such manipulations and investigations in real-time [127–129]. There are several manipulation techniques such as optical tweezers, and electrokinetic force (electrophoresis, dielectrophoresis, and traveling-wave dielectrophoresis) [61].

Nanophotonic trapping and manipulation of particles and biomolecules have attracted considerable attention due to their capability for precise control, delivery, sorting, and analysis of target analytes. These techniques can directly manipulate nanoparticles by light forces and indirectly by light field to trigger a shift in hydrodynamic or electrical conditions around a particle and thereby change its flow

path. Optical manipulation methods employ either gradient or scattering forces. Gradient force acts as a pulling force on a dielectric particle which is proportional to the intensity of light [62, 130]. The scattering force technique is appropriate for stretching and rotating cells. However, the optical scattering force is not as strong as the gradient force to manipulate cells, but this technique is much easier to operate and integrate with microfluidics settings. Therefore it can potentially allow cell manipulation with a higher degree of freedom, and one can find a broader variety of optofluidic designs using the optical scattering force [130].

Using conventional far-field techniques, micrometric particles can be trapped and manipulated, while trapping nanoparticles remains a challenging task due to two reasons; (1) excessive-high laser power and a gradient force are often needed to create trapping forces large enough to overcome the Brownian motion; (2) there is an absence of real-time techniques for identifying the trapping events of such small particles, chiefly nonfluorescent nanoparticles [131–133].

Many of the most powerful optical manipulation techniques are derived from single-beam optical trapping techniques known as optical tweezers. This technique was introduced by Ashkin along with his colleague at AT&T Bell Laboratories [63, 64]. It was created by using a large numerical aperture microscope objective to produce a strong gradient of intensity along the direction of the laser beam near the laser focus as shown in Figure 2.9. This axial gradient makes a light pressure force in the backward direction relative to the beam and of a magnitude that can exceed the forward scattering force. At a definite distance downstream but adjacent to the beam focus center, both the gradient and scattering light pressure forces are equal [14]. This equilibrium point is where a spherical particle was trapped [14, 63, 134].

Far-field-based optical tweezers have been confirmed to be extremely successful for manipulating targets larger than the wavelength of light. Namely, they confront

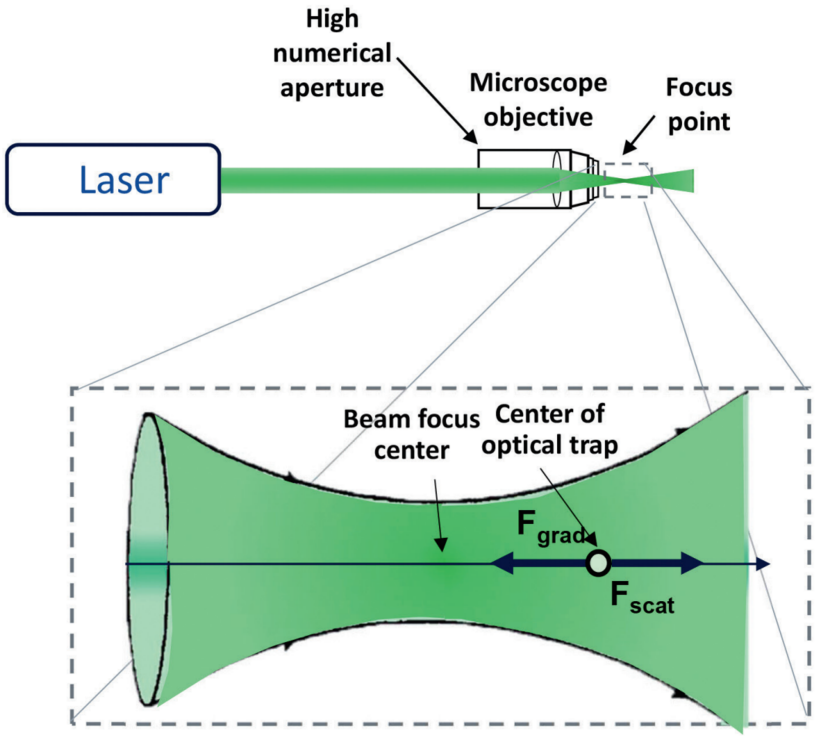


Figure 2.9: The layout of an optical tweezer (above) along with a magnification near the beam focus. A transparent sphere settles on the beam axis just beyond the beam focus where the gradient and scattering forces are equal [14].

obstacles at the nanoscale due to the diffraction-limited focused spot size. This has driven interest in trapping particles with plasmonic nanostructures, as they provide strong fields confined to sub-wavelength dimensions.

Direct measurements of particle surface interactions are important for characterizing the stability and behavior of colloidal and nanoparticle suspensions. Present methods are restricted in their capability to gauge pico-Newton scale interaction forces on nanoscale particles because of signal detection limits and thermal noise. Therefore, a new technique is offered for making measurements in this regime by Schein et al. [135], which they refer to as nanophotonic force microscopy by near-field light to confine dielectric particles as small as 100 nm close to a surface.

In recent years, researchers have exploited devices such as slotted waveguides,

Table 2.2: Summary of Optical Sensors for Trapping and Manipulating Particles

Ref	Structure	Method	Material	Size of Particle	Application
[119]	Planarphotonic Structure	Evanescent Field	Polymer	2,3 μm	Trapping, Transport
[136]	Slot Waveguides	-	Silicon	Sub 100 nm	Trapping, Transport
[137]	Ring Resonator	-	Silicon	1.1, 1.2 μm	Trapping
[138]	Ring of a Whispering	WGM	Silica	140 nm	Trapping
[19]	Photonic Crystal	WGM	Silica	62 nm	Trapping, Transport
[135]	Photonic Crystal	Evanescent Field	Silicon-nitride	100 nm	Optical tweezers
[17]	Slot Waveguide	Near-Field	SOI	320 nm,2 μm	Sorting
[139]	Ring Resonator	Evanescent Field	Silicon	3 μm	Trapping
[136]	Slot waveguide	Near-field	SOI	75 nm	Trapping, Transporting
[140]	Surface Plasmon	Near-field	Gold	4.8 μm	Optical tweezer
[65]	Open Cavity	Far-Field	SOI / TiO_2	300 nm	Trapping, Tracking, Sensing

microcavities, and plasmonic structures to generate high-intensity field gradients for the trapping and manipulation of nanoparticles and biomolecules with small diameters. While this is highly advantageous for nanoscale trapping applications, they are limited for microparticle trapping and propulsion because the length scale that a nanophotonic trap can act over is much smaller. Table 2.2 provides a summary of the published works in recent years, which will be investigated in the rest of this chapter with a detailed discussion on their structures.

2.3.1 Optical Waveguides

Devices based on solid-core waveguide are of special interest due to the advantages they have when integrated with microfluidic systems. These systems are designed to generate optical scattering and absorption forces for propulsion and gradient (trapping) forces for confinement along the waveguide [141]. The result is a kind of optical train tracks for transporting and processing nanoparticles. Additionally, from a practical point of view, when optical waveguides are being integrated into

microfluidic chips, it is relatively easy to couple light into and overlay microfluidic infrastructure without disturbing the optical and fluidic performance [21].

In the past few years, researchers have demonstrated the ability to increase optical trapping forces on particles by using the evanescent field of planar waveguides [142–144]. The evanescent fields (exponentially decaying law of evanescent mode) around planar photonic systems provide strong optical gradient and scattering forces to be exerted on particles in the near-field generated by integrated photonic structures as shown in Figure 2.10 [15, 119]. Planar waveguides are capable of localizing particles near their surface and push them in the direction of the propagated wave.

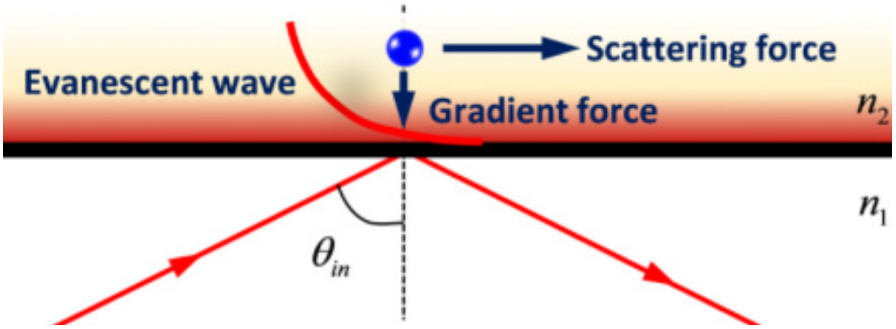


Figure 2.10: Schematic illustration of electromagnetic force in evanescent modes, where the gradient force and scattering force are perpendicular to each other [15].

2.3.1.1 Antiresonant Reflecting Optical Waveguide (ARROW)

Another type of these waveguides is Antiresonant Reflecting Optical Waveguide (ARROW) [136] which demonstrates dielectric reflecting enclosures that enable light guiding in a medium with an index lower than the surrounding material. ARROW relies on optical interference of the light reflected from a multi-layered cladding to confine the light within its core [137]. This structure is particularly attractive when the core is filled with water (or buffer) that usually has a lower refractive index than the cladding, which can significantly reduce the transmission

loss, compared to the case where the regular high refractive index core is used to confine the light. Different from the evanescent interaction, in the ARROW structure, maximal interaction between the light and the analyte inside the liquid channel can be realized. These systems are still limited in optical trapping due to the size of the optical mode (order of a few micrometers). For instance, these devices can be employed for electro-optical trapping of small materials [16] where the guiding properties of the waveguide can be used for the ease of observation and electrokinetic effects can be used for target stabilization along the waveguide axis. Figure 2.11(a-d) shows the suggested overall chip layout of the sample used in [16].

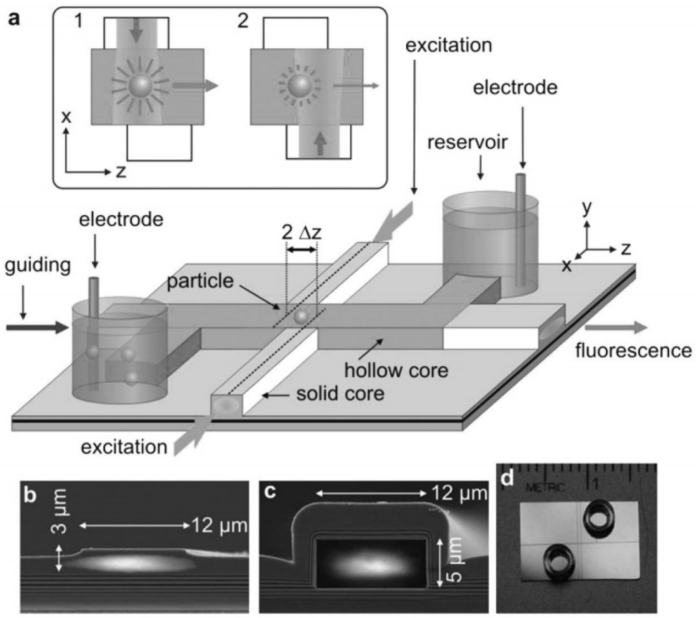


Figure 2.11: (a) Schematic layout of the ARROW optofluidic analysis platform. Inset: Working principle of the particle position sensor showing the illumination during (1) the first and (2) the second half-period of modulation. (b) Solid-core waveguide with overlayed optical mode profile. (c) Same for hollow-core waveguide. (d) Photograph of the actual chip with reservoirs [16].

2.3.1.2 Slot Waveguides

Crozier's group has investigated optical manipulation using various platforms including plasmonics and silicon photonics [20, 145]. Particles with different sizes,

shapes and refractive indexes experience different optical forces and can be separated into output channels based on their intrinsic properties without fluorescent labeling. The movement of several microns is often needed to deliver particles into different microfluidic outlets, which requires a large incident power for optical force to push or drag the particles for such a long distance. This is even more difficult for particles with sub-micron size [121].

In [17] an integrated microparticle passive sorting system is proposed based on near-field optical forces exerted by a 3-dB optical splitter that consist of a Slot Waveguide (SWG) and a Conventional Channel Waveguide (CWG). Polystyrene particles with sizes of 320 nm and 2 μm are sorted and exit along the slot waveguide and the channel waveguide, respectively. Due to applied waveguides, the incident light to the device can interact with the particles over a long distance. The mode keeps its profile and does not diffuse as it would for a laser beam in free space.

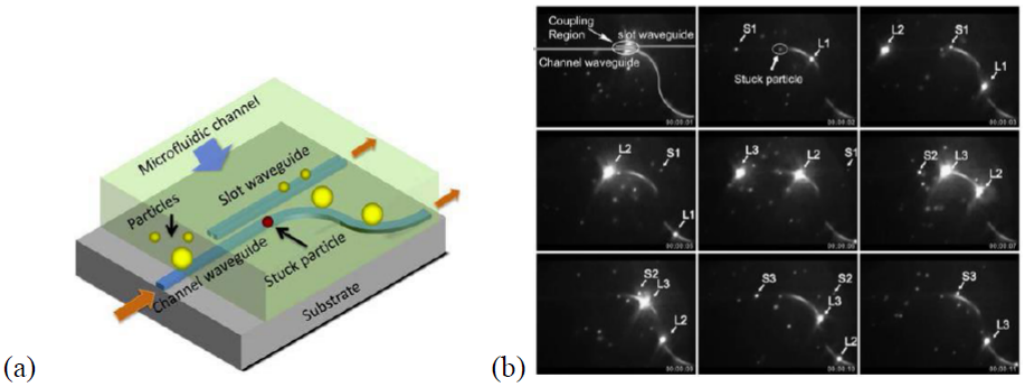


Figure 2.12: (a) Microparticle sorting device. (b) CCD image of the sorting with a guided power of 20 mW. The waveguides are indicated by the gray lines in the first frame. The trapped particles are marked by white arrows with the indicators S and L for the 320 nm and 2 μm particles, respectively. The obstacle particle is marked in the second frame [17].

Particles are classified into various waveguides, rather than into various microfluidic channels. The presented device is fabricated on a Silicon on Insulator (SOI) wafer with a 220 nm top silicon layer and a 3 μm thick buried oxide. A

PDMS chip containing microfluidic channels (50 μm height, 100 μm width) is bonded to the SOI chip (Figure 2.12). Particles with diameter of 320 nm and 2 μm are sorted by using an optical splitter. The particles are pulled onto the CWG by optical gradient forces and pushed to the splitter by optical scattering forces, where they face a perturbation comprising a stuck bead. The particles with a dimension of 2 μm continue to be driven along with the CWG after leaving the splitter, while the 320 nm particles are transferred to the SWG. A sorting rate of 30 particles/min is reported, which can be improved by increasing the density and speed of trapped particles on the waveguide. A structural perturbation is employed to switch them from the CWG to the SWG, while the perturbation doesn't affect the larger particles. In the bending part, the larger particles chase the CWG, as its potential well is deeper. Additionally, position tracking analysis of particles passing through the device shows proof for this sorting mechanism. According to this results, the planar form of this waveguide-based sorting device provides an easy way to implement massive parallel processing and integrate other pre- or post-sorting functionalities into the system.

More recently, other works have been done based on the slot waveguides [125, 136, 146]. Yang et al. presented an approach to optofluidic transport by using subwavelength liquid-core slot waveguides to manipulate small objects. This technique simultaneously employs near-field optical forces to confine matter inside the waveguide and scattering/adsorption forces to transport it. The ability of the slot waveguide to concentrate the accessible electromagnetic energy to nanoscales as small as 60 nm resolve the fundamental diffraction problem.

The authors in [125,136,146] applied the approach to the trapping and transporting of dielectric nanoparticles with size of 75 nm and λ-DNA molecules. Because trapping occurs along a line, instead of trapping at a point as with traditional point traps, this technique creates the capability to directly handle extended

biomolecules. Also, this work achieved a detailed numerical analysis that relates the near-field optical forces to release kinetics. According to these results, this architecture will potentially help to bridge the gap between optical manipulation and nanofluidics [146].

One of the difficulties of the development of active nanodevices is to efficiently deliver objects to and within nanostructures. The proposed architecture by [146] displays the combination of near-field optical and photon scattering forces (such as those used in optical traps) to confine nanoscopic matter inside a liquid core-slot waveguide and to transport them, respectively. The waveguide solves the diffraction limits of conventional optical trapping systems to manipulate small objects down to tens of nanometres in scale. The waveguide has a linear shape and therefore it can additionally manipulate extended biomolecules demonstrated by trapping and transporting DNA molecules. This method enables the capability to handle extended biomolecules directly because trapping occurs along a line, more than at a point as with traditional point traps.

Sub-wavelength slot waveguides such as those used in [146] can be integrated into lab-on-a-chip platforms using existing manufacturing techniques. These structures allow us to manipulate and transport nano-objects with greater precision than is available with existing approaches. Therefore, these techniques could lead to new methods of bioanalysis and directed assembly.

2.3.2 Optical Microcavities

Integrated photonic resonators, based on photonic crystals, and surface plasmon structures have also been used to exert optical forces on particles in suspension. Resonant cavity trapping offers two essential advantages in comparison to a waveguide trapping configuration : (1) high field confinement in a cavity leads to strong optical force enhancement, and (2) cavity perturbation induced by the trapped

object could present as a highly sensitive probe for analyzing the physical properties (size, refractive index, absorption) of the objects.

Optical waves propagating through waveguide devices remain highly confined over larger distances, and are capable of delivering larger optical forces over a larger region. Trapping on planar ring resonators has also been reported recently such as the work in [139]; although, careful analysis of the force enhancement, trapping stiffness, and potential depth has not been discussed yet.

2.3.2.1 Ring Resonators

There are a number of research work that have the guided optical field intensity in a waveguide structure by adopting the geometry of a closed-ring called Whispering Gallery Mode (WGM) resonators [124, 126, 137, 138]. This is an alternative method to increase both the optical gradient and scattering forces. Photons that are coupled to the waveguide resonators from a near bus waveguide can circulate through the ring many times before being absorbed or scattered [122].

If the resonance condition is satisfied by the optical excitation wavelength, coupled photons constructively interfere with each other and reinforce the field intensity in the resonator. In other words, particles that are optically transported along the straight (bus) waveguide can be transferred to a specific ring resonator by tuning the excitation wavelength in the bus waveguide to coordinate with the resonance wavelength of a specific ring.

Lin and Crozier [18] suggested a switchable particle storage chain for on-chip particle trapping. Figure 2.13 shows the proposed chip, comprising two microrings with radii of 5 μm and 10 μm integrated with a waveguide fabricated in the top (silicon) layer of SOI wafer and a PDMS chip containing microfluidic channels which are bonded to microrings for optical manipulation demonstrations (Figure 2.13 (a)). The transmission spectrum in Figure 2.13 shows resonance peaks at 1557.9 nm

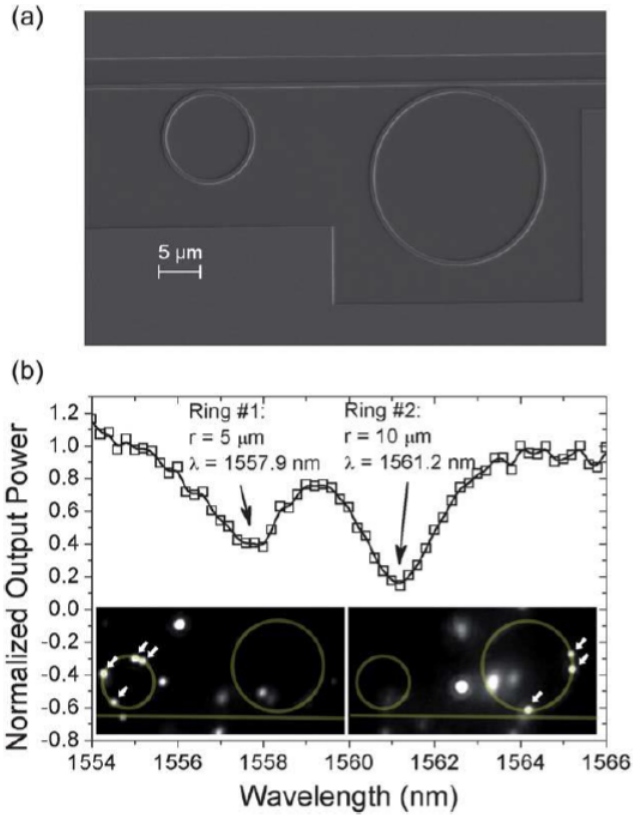


Figure 2.13: (a) SEM image of the double-ring structure, (b) transmission spectrum of a particle storage chain comprised of two microrings with radii of 5 and 10 μm. Dips at 1557.9 nm and 1561.2 nm correspond to the resonance frequencies of small and large microrings, respectively. Lower left inset: CCD image of particles trapped on the small microring at a laser wavelength of 1557.9 nm; Lower right inset: CCD image of particles trapped on the large microring at a laser wavelength of 1561.2 nm. Yellow lines label the positions of micro rings and bus waveguides. The white arrows indicate the trapped particles [18].

and 1561.2 nm that correspond to the microrings with radii of 5 μm, and 10 μm, respectively. With the ability to quantitatively store particles on a microring, to deliver them from one location on the chip to another, and to switch them between rings, the demonstrated particle storage chains could be used as building blocks in the construction of larger systems with additional functionalities.

Particle counting and velocity measurement are illustrated by monitoring the intensity of the output power. The output signal in [18] from the bus waveguide provides monitoring of the trapped objects (particles) without the need for an

external imaging system since the existence of an object (a particle) on a ring varies its resonance frequency. They measured the velocity of the trapped particle from the output power using:

$$v = 2\pi r_r/\tau_p,$$

where r_r is the ring radius and τ_p is the period of the optical power signal, equal to the particle circling period (see Figure 2.14).

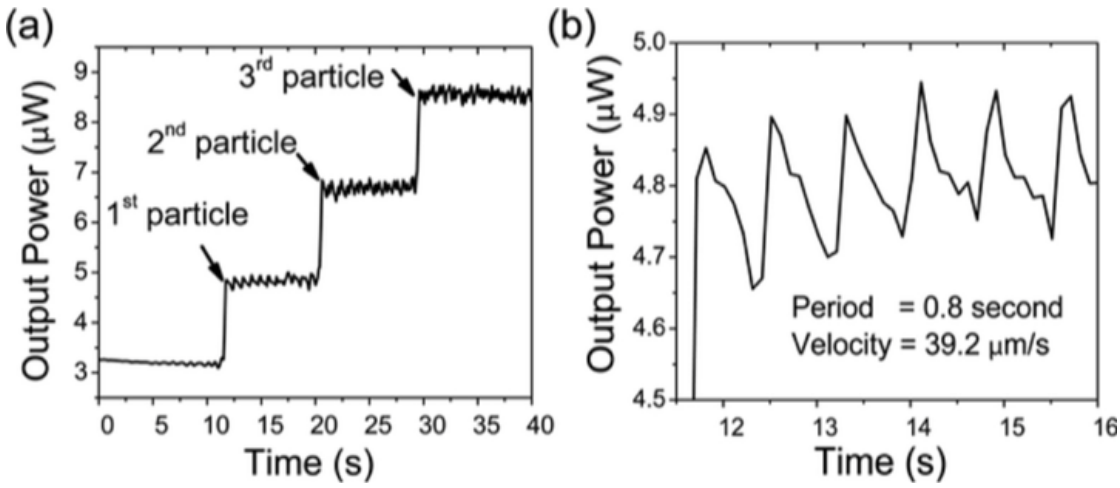


Figure 2.14: (a) Output power as a function of time when particles are trapped. (b) Output power as a function of time, shown in detail [18].

The authors in [18] tuned the input laser to the resonance frequencies of the smaller (left image Figure 2.13.b) and larger (right image Figure 2.13(b)) rings so that particles are only trapped on the resonance ring. When the wavelength of the laser is tuned away from the center of the resonance peak, less power is coupled into the resonator, and the speeds of the trapped particles reduce. Since the wavelength of the laser is shifted beyond the resonant wavelength of the ring, the field intensity in the ring resonator becomes smaller than that in the waveguide. Therefore particles that are in the coupling region are released to the bus waveguide, namely the escaped particles are directed along the waveguide.

Particles that are in the coupling area are therefore released to the bus waveguide. The released particles are pushed along the waveguide. If the laser wavelength

matches the resonant wavelength of the second ring (1561.2 nm), the particles are trapped by it. A trapped particle is delivered from the smaller to the bigger ring by adjusting the incident wavelength from 1557.9 nm to 1561.2 nm. This ability to control the precise position could be useful in various applications. For instance, it allows us to study the response of an individual cell to different solvents. This could be attained by having the first microring placed in a channel containing a specific solvent, and the second microring placed in a channel containing a second solvent. An object can be trapped on the first ring, and then on the second, in a controllable way [18].

While optical microresonators of the mentioned type offer excellent detection sensitivities with selectivity; they are surface-sensitive detectors. This means that they are not well suited for applications that require detection across an entire microfluidic channel. In this respect, bulk sensors such as hollow waveguides offer alternative solutions for microfluidics applications [147]. Leake et al. [148] reported size-based sorting of micro-and sub-micron particles using optical forces on a planar optofluidic chip. Two combinations of optical beam propagations in liquid-core waveguides and fluid flow are shown in [148]. These techniques allow for tunability of size selection and sorting with high efficiencies. Great agreement between experimental results and calculated particle trajectories in the existence of flow and optical forces is also reported. Optofluidic chips based on microring resonators are reusable with ultrahigh sensitivity which provides real-time and on-site detection of low-molecular-weight targets for many applications such as food safety and environmental monitoring.

2.3.2.2 Photonic Crystals

Photonic crystals contain two or more dielectric materials of differing refractive indexes (e.g., water and Si) constructed in a periodic pattern [123]. Photonic

Crystal (PC) -based biosensors use a subwavelength periodic dielectric surface structure, which results in resonance reflection [149] at a narrow wavelengths band. These devices can be engineered to offer localized resonant modes where optical field intensity is highly concentrated at the waveguide, providing a strong optical force to the particle. Several studies from D. Erickson's lab have investigated the use of one-dimensional photonic crystal waveguide structures in near-field optical trapping and analysis, e.g., [19].

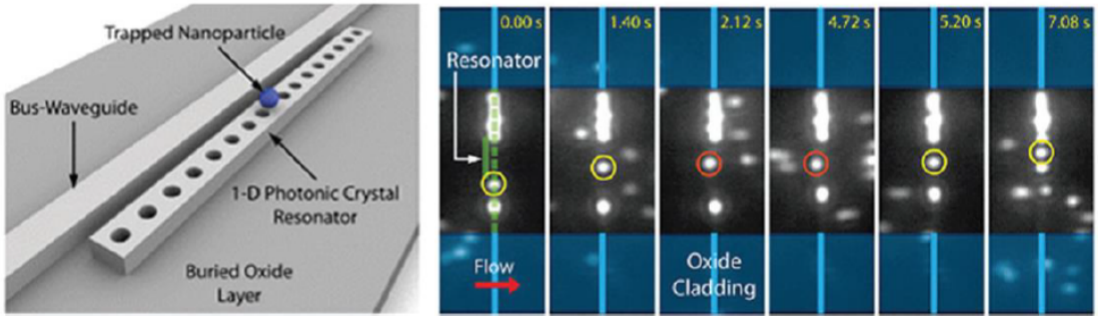


Figure 2.15: Stronger fixed-position traps are achieved with photonic crystal (PC) resonators. A nanoparticle that was transported along a bus waveguide (yellow circles) is trapped at a side-coupled PC resonator (orange circles) before being released and transported along the bus waveguide again [19].

Using silicon devices, [19] presented a new class of nanoscale optical traps using optical resonance in one-dimensional silicon photonic crystals. The trapping of dielectric nanoparticles with sizes of 48 nm and 62 nm is illustrated along with the capability to transport, trap, and manipulate larger nanoparticles. This is obtained by simultaneously applying the propagating essence of the light in a coupling waveguide and its stationary essence within the resonator. This resulted in the capability to optically transport a 500 nm polystyrene particle along with a bus waveguide, transfer the particle to the photonic crystal trap and then release the particle for further optical transport on the bus waveguide (Figure 2.15).

Increasing field intensity within the resonator is displayed to generate an order of magnitude stronger trap force as compared to conventional tweezers and other

near-field methods. This technique lays the foundation for a new type of optical trapping principles that enables complex all-optical single-molecule manipulation and directed assembly of nanoscale material.

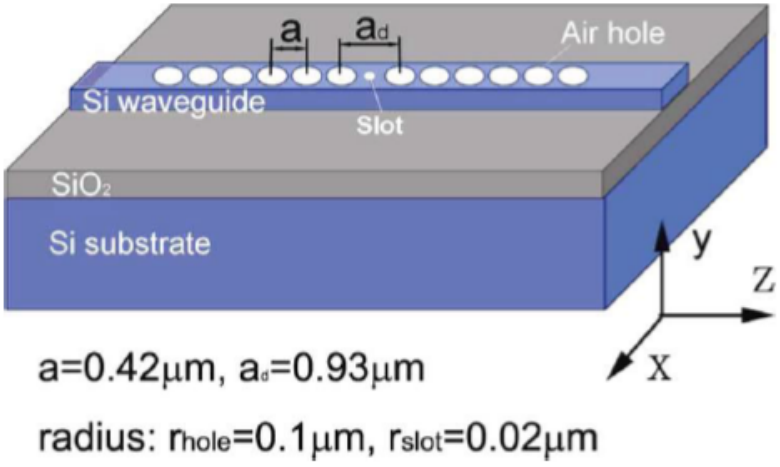


Figure 2.16: Schematic illustration of a nanoslot waveguide photonic crystal cavity [20].

Lin et al. [20] designed an on-chip photonic device to manipulate and detect a single nanoparticle and macromolecule. A unique combination of a photonic crystal waveguide cavity and a nano slot structure generates an optical force that is 1300 times larger than a conventional waveguide trapping device (Figure 2.16). Additionally, they studied this structure by numerical simulations which indicates that the designed device is capable of stably trapping a single-nanoparticle inside the nano slot cavity. Therefore, this method offers an ideal platform for single-particle detection and analysis using cavity-enhanced spectroscopic technologies.

Schein et al. [135] presented a new technique for making measurements as nanophotonic force microscopy. They used a photonic crystal resonator to create a heavily localized region of exponentially-decaying near-field light to confine small particles close to the crystal surface. From the statistical distribution of the light intensity scattered by the particle, they have been able to map out the potential

well of the trap and directly quantify the repulsive force between the nanoparticle and the surface. This technique is also not limited by thermal noise, in other words, the thermal noise cannot affect the performance of their technique. Therefore, they resolved interaction forces smaller than 1 pN on dielectric particles as small as 100 nm in diameter.

2.3.2.3 Plasmonics

Nanoplasmonic devices can provide another approach to concentrate light at dimensions well below the diffraction limit such as photonic crystal cavities, slot waveguides, and other subwavelength waveguiding structures [122, 150]. Nanoplasmonic devices consist of nanoscale metallic features in which resonant surface plasmons, such as collective oscillations of mobile valence electrons in the metal, can be excited by incident light within a particular frequency range [122]. Mie [120] and Ritchie [151] were pioneers in studying the effect of light on metallic nanostructures.

Plasmons make strong electric fields at the metal-dielectric surface boundary that decay rapidly, producing strong optical gradient forces [122]. Therefore, nanoplasmonic devices have been demonstrated effective for trapping particles, bacteria, and yeast [152].

Devices based on nanoplasmonic can be designed in large arrays by using standard nanofabrication techniques. Therefore, they are easily applicable for the optical trapping of arrays of particles. However, since plasmonic field amplification leans to be strongest at the sharp structures and gap junctions, manipulation of an array of trapped objects is generally hard. Despite this difficulty, rotation of trapped objects was achieved by illuminating special trap geometries with circularly polarized light in [145].

Figure 2.17 [21] illustrates a schematic of similar near-field trapping where the

evanescent field is created by a surface plasmon. Surface plasmons are electromagnetic waves that are at the interface between a dielectric and a metal. The effective wavelength of an incoming light beam which is matched to the resonant condition excites these plasmons. It depends on a variety of geometric and physical properties in the system. Since the resonance condition is satisfied, these plasmons can create very large local enhancements of the field strength.

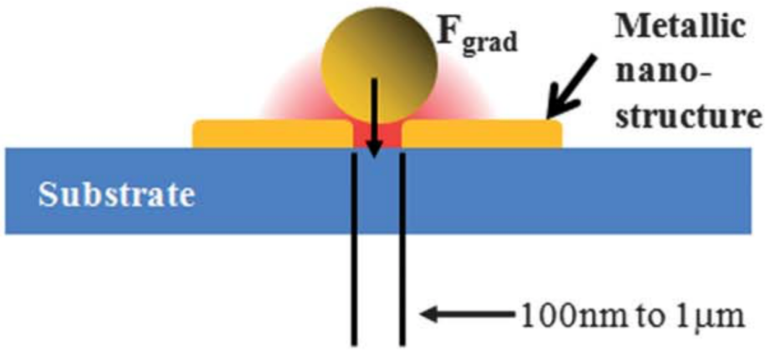


Figure 2.17: Plasmonic near-field optical trap [21].

There are two types of plasmon resonance: (1) Surface Plasmon Resonance (SPR) for flat surfaces, and (2) Localized Surface Plasmon Resonance (LSPR) for nanoscale metal structures. SPR and LSPR can increase trapping force without generating much-unwanted heat. The trapping forces of conventional optical tweezers can be raised around 40 times, at a certain intensity, by SPR according to the study done by Volpe along with his colleague using photonic force microscopy [153].

For trapping nanoparticles based on surface plasmon at a specific location, either a patterned incident light [154] or a patterned metal surface is required to provide additional in-plane field confinement [140]. Optical traps based on surface plasmon can provide enough trapping with non-focused illumination, and the intensity of the needed light is significantly less than that of conventional optical tweezers setup. Righini et al. [140] presented parallel and size-selective trapping of

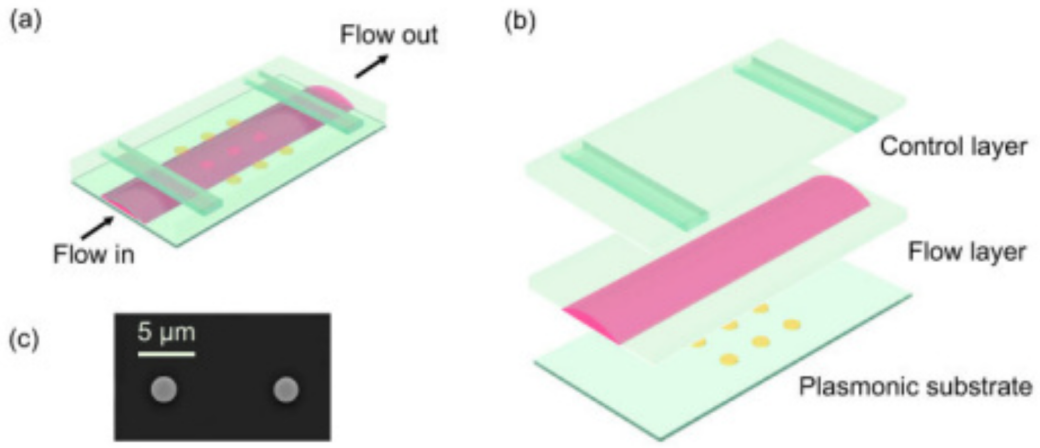


Figure 2.18: Optofluidic lab-on-a-chip: (a) general view; (b) exploded view: the chip is made of three layers: the plasmonic substrate, the flow layer, and the control layer. (c) SEM image of the fabricated gold plasmonic structures on the dielectric substrate [22].

polystyrene particles by exciting surface plasmon on gold discs on top of a glass substrate. Due to the illumination asymmetry in the experimental geometry, the increased local field is also asymmetric, and stable trapping of Rayleigh particles is prevented.

To show the potentials of plasmonic trapping for application of lab-on-a-chip, metallic nanostructures have been integrated with a microfluidic channel to trap yeast cells by Huang et al. [22]. Gold and silver particles has been used to enhance the gradient forces of 3D optical traps which present strong plasmon resonance in LSPR. Figure 2.18 demonstrates the structure of their chip that consists of three layers. The bottom layer exhibits the plasmonic substrate which includes metallic nanostructures. Two disks with diameters of 2 μm and 3 μm are considered, requiring illumination at $\lambda = 810\ nm$. The thickness of the metal is 40 nm and deposited by using the Joule effect and includes a 3 nm thick chromium adhesion layer on the glass substrate.

The work [22] introduces a localized plasmon resonance between two spaced

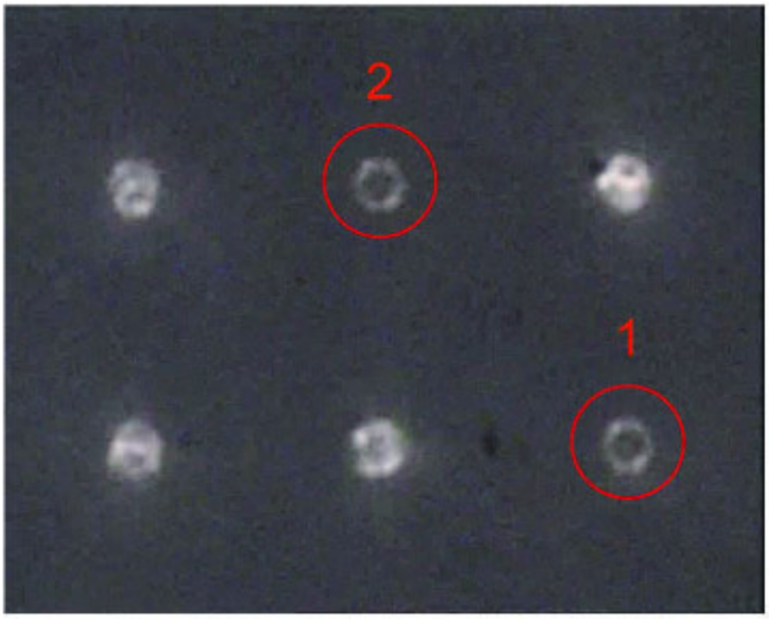


Figure 2.19: Optical plasmonic trapping of yeast cells in a microfluidic channel. The bright structures represent the gold disks with trapped yeast cells on top of them. A free yeast cell is trapped in the bottom right highlighted structure and another cell is trapped by the top highlighted disk about half a minute later [22].

nanodots which generate a strong optical trap that can improve the positioning of particles by about an order of magnitude in comparison with conventional optical tweezers. Figure 2.19 also illustrates the plasmonic trapping integrated with a microfluidic environment to manipulate yeast cells with diameter of 3 μm.

2.3.2.4 Fabry-Pérot Microcavities

Fabry-Pérot interferometers are optical devices that consist of two highly reflecting mirrors in order to form a standing-wave resonator. Fabry-Pérot interferometers have been designed and implemented for biochemical and gas sensing. Fabry-Pérot optical microcavities present a powerful combination of small mode cross-section, high finesse, and open-access. This covers a wide range of topics, containing cavity quantum electrodynamics with cold atoms [155], ions [156], and solid-state-based emitters [157], as well as cavity optomechanics [158] and scanning cavity microscopy [159].

Open-access Fabry-Pérot microcavities generally consist of two separate mirrors facing each other where one mirror can move independently [67, 160–164]. These microcavities are an interesting candidate for detecting optical refractive index in fluid due to their potential such as label-free, high precision, real-time detection and monitoring, low cost, simple fabrication [165, 166], and single-chip integration which have high ability for single-cell measurement [67].

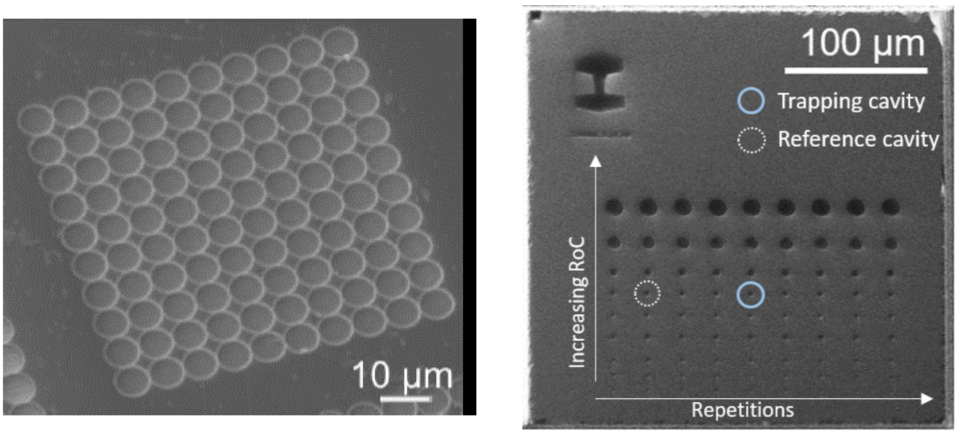
The optical microcavities are able to increase the light-matter interaction, consequently improving the sensitivity [24, 65, 67, 167]. In all types of microcavities, the wavelength of resonance is extremely sensitive to any change in the refractive index in the optical mode field. The refractive index shift is the results of the presence of nanoparticles or bio-targets. However, there are sensing problems that can be solved with a stronger interaction between the optical mode field and the target, along with large target sensing e.g. cells [168] and sensing in weakly absorbing analyte media [169]. For example, hollow-core waveguides are used for bulk sensing. These types of waveguides are able to confine light and a liquid medium within the same volume [147]. However, they need to be long enough, e.g., 2 cm, to have an eligible signal-to-noise ratio for sensing refractive index shift. On the other hand, open-access Fabry-Pérot microcavity sensors create a situation for full interactions between targets and optical fields.

Furthermore, open-access microcavities can be used to trap nanoparticles [24]. Further insights into properties of nanoparticles such as polarizability, scattering cross-section, friction coefficient, antinode location, and potentially its absorption cross-section can also be studied. The nanoparticle can be trapped and sensed with low intracavity power, reducing potential damage to biological samples. Therefore, open-access microcavities are a promising technology for lab-on-a-chip applications.

Recently, a new generation of Fabry-Pérot microcavities based on Plano-Concave (P-C) structure has attracted considerable attention due to higher quality factor

than that of a conventional Plano-Plano Fabry-Pérot microcavities [170,171]. Their high-quality factor increases the sensitivity in biosensors.

The principles of Fabry-Pérot resonators are well understood as such devices were extensively studied in the past decades [172]. Dolan and others [23] demonstrated open-access optical microcavities which is shown in Figure 2.20a.



(a) (b)

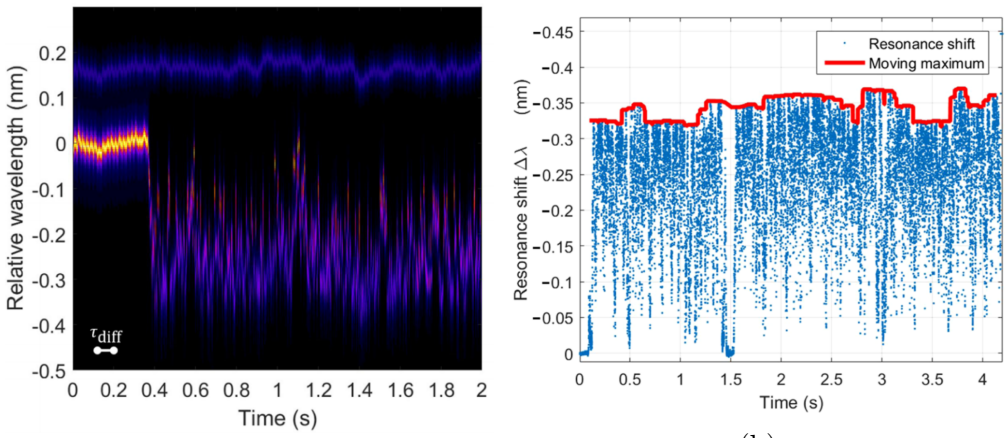
Figure 2.20: (a) SEM image: arrays of cavities FIB milled onto a Silicon substrate [23] (b) SEM image of the chip template displaying different RoC microcavities (vertical axis) and repetitions (horizontal axis) [24].

This type of microcavities is used as label-free lab-on-a-chip optofluidic sensing in [67]. The offered open-access microcavity is used to sense the refractive index of glucose in a femtoliter volume with a sensitivity of 3.5×10^{-4} RIU. The optical resonance cavity mode is shifted by changing the refractive index that comes from the glucose molecules.

Open-access microcavities are good candidates for global refractive index and single-nanoparticles sensing. Vallance et al. [65] investigated the open-access microcavities for refractive index sensing, optical absorption measurements, and optical tracking and trapping nanoparticles with size of 200 nm. Accordingly, the open cavities are promising structures for sensing and trapping nanoparticles.

Additionally, as a new kind of nanotweezers based on open microcavities, Trichet

et al. [24, 167] monitored the cavity mode wavelength shift as the particle diffuses through the cavity. Their experiment has provided a deep understanding of the interaction between the nanoparticle and optical cavity modes. The sensing and trapping of nanoparticles depend on the same physical phenomenon. In other words, they rely on dipolar interaction between the nanoparticles and the resonant optical modes within the cavity. The interaction creates a shift in the mode resonance frequencies which provides a mechanism for particle detection. Owing to the optical force on the nanoparticles in the direction of the maximum mode intensity, this method also offers a trapping mechanism. They used two microcavities with a



(a) (b)

Figure 2.21: (a) Transmission scans as a function of time. The top (or bottom) transmission peak is the reference (or trapping) signal. The parameter τ_{diff} gives the time scale of free diffusion of a 200 nm nanoparticle in the cavity volume. (b) Blue dots: experimental mode shifts versus time during a trapping event. The red line is the moving maximum over 80 ms [24].

Radius of Curvature (RoC) of 4 μm [24]. The finesse of the cavities is 4×10^4. One cavity is selected as a trapping cavity and another one as the reference cavity to detect the vibration noise in the detection. These cavities (Figure 2.20b) are illuminated by a narrow-linewidth continuous-wave 639.6 nm diode laser. The reference cavity has a low optical signal intensity while the trapping cavity has a high intensity to create the optical fields.

Figure 2.21a explains the transmission of the trapping and reference cavities as a function of time when particles with size 200 nm are introduced through the cavity. The mode shift is extracted and its evolution with time is shown in Figure 2.21b. They determined the particle polarizability from the maximum mode shift detected. They observed 18 trap events with a mean maximum mode shift of 390 pm. With this new generation of microcavities, they were able to measure the polarizability along with the trap strength, which gives direct access to the trap properties without a priori knowledge of the particle.

2.4 Summary

In this chapter, the common nanoparticle characterization techniques are reviewed to evaluate different physiochemical properties of nanoparticles. We described the advantages and limitations of the current characterization methods and the alternative methods are discussed to improve the drawbacks of the common methods. Additionally, optical manipulation techniques such as trapping, transport, and handling of nanomaterials are reviewed in microfluidic devices along with some of the new applications.

We also discussed the problems and limitations of common characterization techniques and biosensors that can be solved with Fabry-Pérot microcavities by providing whole-body interactions between the light and particles. Many of these benefits come without problems such as pollution and poor sample recovery, low efficiency in time, and sample preparation. Furthermore, this type of microcavities can overcome the challenges in the fluidic systems by holding nanoparticles and then measuring the trapped particle properties.

This proposed method in this dissertation employs open-access Fabry-Pérot microcavities as a promising technology for lab-on-a-chip applications with the goal

of delivering and then trapping nanoparticles in order to detect and manipulate them. These microcavities show great potential for trapping and manipulating particles, as well as particle identification using refractive index changes and spectroscopic methods. This microcavity sensing allows to measure the maximum mode shift and then optical polarizability of nanoparticles in liquid media. By measuring the nanoparticle polarizability, we can detect the size and refractive index of particles.

Chapter 3

Theory

3.1 Introduction

This chapter presents the theoretical background that is essential to study the open-access microcavity for nanoparticle characterization. The physical characteristics of open-access microcavities are discussed in details. The basic foundation of the Fabry-Pérot resonator is described, followed by a discussion on optical beam propagation through the cavity. Then Gaussian beam is introduced and it is compared with an estimation model and a cylindrical model. We then explain how the open-access microcavity can characterize a nanoparticle.

3.2 Open-Access Cavity

A simple Fabry-Pérot cavity is shown in Figure 3.1. A microcavity consists of two mirrors with a gap of L. Incident light with wavelength λ is transmitted through the cavity to make standing waves or optical resonant modes within the medium

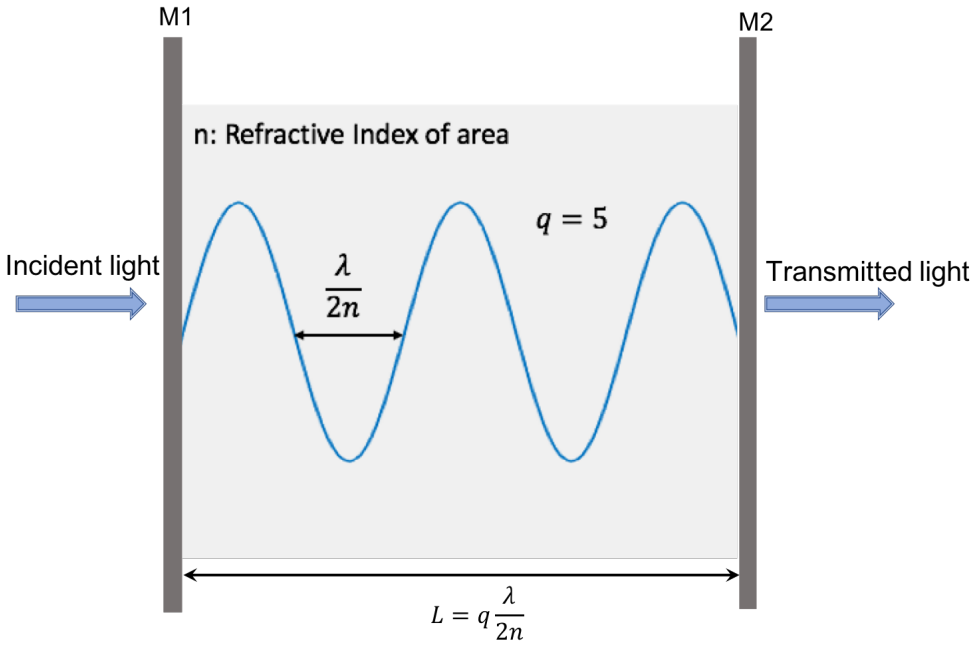


Figure 3.1: A schematic of a simple open microcavity.

of the cavity whose refractive index is n. The resonance occurs when the cavity length is equal to an integer multiplier (number of antinodes) q of half intracavity wavelengths, namely:

$$L = \frac{q\lambda}{2n}. \tag{3.1}$$

When this condition is satisfied, the transmission of light would be maximal because of constructive interference of the waves with the microcavity, given the assumption that there are no scattering and absorption losses within the cavity. Each distinct resonant wavelength has a fixed separation.

By assuming a single-mode laser emitting the incident light of wavelength λ, the spectral spacing of the resonant modes, the Free Spectral Range (FSR), is defined as

$$FSR = \frac{\lambda}{2n}. \tag{3.2}$$

FSR is the spacing in optical frequency or wavelength between two successive

reflected or transmitted optical intensity maximums. Another parameter to explain traits of the microcavity is finesse $\mathcal{F}$, which determines how many round trips light makes within the cavity before exiting. It depends on the reflectivity of both mirrors, (R_{m1} and R_{m2}) and can be calculated as [173]:

$$\mathcal{F} = \pi \frac{(R_{m1}R_{m2})^{\frac{1}{4}}}{1 - \sqrt{R_{m1}R_{m2}}}. \tag{3.3}$$

Note that in practice aligning mirrors perfectly in parallel to each other is impossible. Therefore, the finesse of the optical cavity $\mathcal{F}$ can be determined by an approximation with respect to the line-width $\delta\lambda$ and the FSR in the experimental work:

$$\mathcal{F} = \frac{FSR}{\delta\lambda}. \tag{3.4}$$

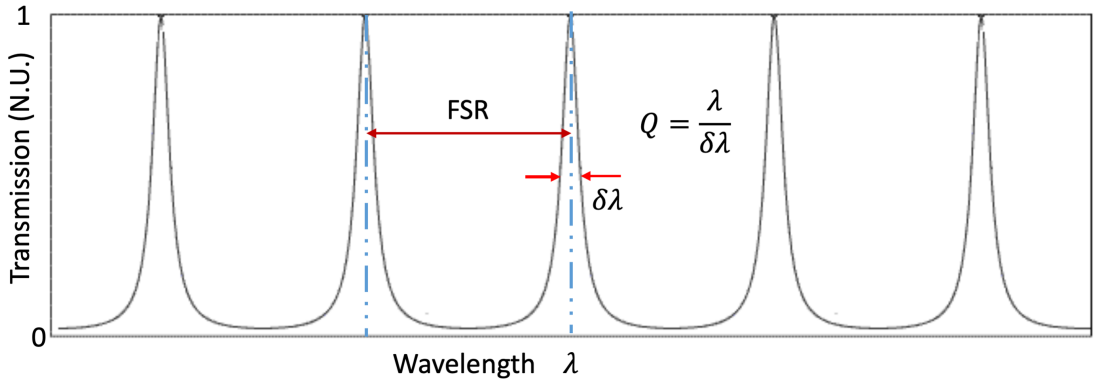


Figure 3.2: The resonant wavelength in terms of FSR and Q factor in a simple Fabry-Pérot resonator.

Another parameter is the quality factor that describes the optical performance of the cavity:

$$Q = \frac{\lambda}{\delta\lambda} = q\mathcal{F}, \tag{3.5}$$

where q is the number of modes. The high-quality factor means the light is confined for a long time, which provides strong light-material interactions and consequently

increases the sensitivity of the (bio)sensor. Figure 3.2 demonstrates FSR and Q factor in a Fabry-Pérot resonator.

3.3 Gaussian Beam

The Gaussian beam is a natural mode of radiation of electromagnetic waves in free space. This radiation mode describes a paraxial wave that is propagated along the beam axis. However, the optical mode has a small divergence in the beam axis, i.e. z-axis in this work. In other words, Gaussian beams are light beams where the electric field profile in a plane perpendicular to the beam axis can be described with a Gaussian function, possibly with an added parabolic phase profile [174]. A Gaussian wave is a solution of a wave equation. The wave equation can be obtained from Maxwell's equations when there is no free currents ($j = 0$) or static charges ($\rho = 0$):

$$\nabla E - \frac{1}{c^2}\frac{\partial^2 E}{\partial^2 t} = 0, \tag{3.6}$$

where E and t are the electric field and time, respectively, also c denotes the velocity of the wave propagation

$$c = \frac{1}{\sqrt{\mu_0 \epsilon_0}}, \tag{3.7}$$

where μ_0 and ϵ_0 are permeability and permittivity in free space, respectively. Note that the polarization of the electric field in (3.6) is ignored. A monochromatic wave is considered as

$$E(x, y, z, t) = \psi(x, y, z)e^{i\omega t}, \tag{3.8}$$

where ω is the angular frequency. The independent part of the electric field ($\psi(x, y, z)$) follows the Helmholtz equation

$$\nabla^2\psi + k^2\psi = 0, \tag{3.9}$$

where k is wave vector.

There are many solutions to the Helmholtz equation, and in this chapter, we study a plane wave case. In the plane wave case, the solution is

$$E = Ae^{i(\omega t - kz)}, \tag{3.10}$$

where the wave vector is independent of x, y and z:

$$k = \frac{\omega}{c}. \tag{3.11}$$

The phase of the wave is constant:

$$\phi(t, z) = \omega t - kz = const. \tag{3.12}$$

The condition $\partial\phi/\partial t = 0$ gives us the phase velocity of $dz/dt = \omega/k = c$. In addition, the condition $\partial\phi/\partial z = 0$ gives us the group velocity $dz/dt = c$.

Note that a paraxial wave is a wave whose wavefront normals are paraxial rays. A paraxial wave can be introduced by starting a plane wave ($E = Ae^{-ikz}$), regard it as a carrier wave, and modifying or modulating its complex envelope A, making it a slowly changing function of the position $A(x, y, z)$:

$$E = A(x, y, z)e^{-ikz}. \tag{3.13}$$

The assumption that $A(x, y, z)$ changes slowly with respect to z implicates that within a distance $\Delta z = \lambda$, the change ΔA is much smaller than A itself [175]. Therefore the condition can be written as $\partial A/\partial z \ll kA$ and $\partial^2 A/\partial z^2 \ll k^2 A$.

Substituting (3.13) into (3.9) we obtain

$$\nabla_T{}^2 A - 2ik\frac{\partial A}{\partial z} = 0, \tag{3.14}$$

where $\nabla_T{}^2$ is the Laplacian operator of transverse

$$\nabla_T{}^2 = \frac{\partial^2}{\partial x^2} + \frac{\partial^2}{\partial y^2}. \tag{3.15}$$

A solution to the paraxial Helmholtz equation creates a paraboloidal wave:

$$A(x, y, z) = \frac{A_1}{z} exp(-ik\frac{\rho_{xy}^2}{2z}), \qquad \rho_{xy}^2 = x^2 + y^2, \tag{3.16}$$

where A_1 is a constant and paraboloidal wave is the paraxial approximation of the spherical wave when $x, y \ll z$.

Another solution of the paraxial Helmholtz equation can be obtained by using a simple transformation that provides the Gaussian beam. When (3.16) can be a solution of (3.15), a shift version of it, using $z - \xi$ instead of z, where ξ is constant yields:

$$A(x, y, z) = \frac{A_1}{q(z)} exp(-ik\frac{\rho_{xy}^2}{2q(z)}), \qquad q(z) = z - \xi, \tag{3.17}$$

In this solution, the wave is centered at the point of $z = \xi$ instead of $z = R$. If ξ is purely imaginary ($\xi = -iz_R$) where z_R is real, (3.17) can be written as:

$$A(x, y, z) = \frac{A_1}{q(z)} exp(-ik\frac{\rho_{xy}^2}{2q(z)}), \qquad q(z) = z + iz_R, \tag{3.18}$$

where z_R is known as the Rayleigh range.

The substitution of (3.18) into (3.13) results an expression for the complex amplitude $E(r)$ of the Gaussian beam:

$$E(x, y, z) = A_0 \frac{\omega_0}{\omega(z)} exp(-\frac{\rho_{xy}^2}{\omega^2(z)}) exp(-ikz - ik\frac{\rho_{xy}^2}{2R(z)} + i\nu(z)), \tag{3.19}$$

where

$$\omega(z) = \omega_0[1 + (\frac{z}{z_R})^2]^{1/2}, \tag{3.20}$$

$$R(z) = z[1 + (\frac{z_R}{z})^2], \tag{3.21}$$

$$\nu(z) = \tan \frac{z}{z_R}^{-1}, \tag{3.22}$$

$$\omega_0 = (\frac{\lambda z_R}{\pi}^{1/2}). \tag{3.23}$$

3.4 Hermite-Gaussian Beam

The Gaussian beam is not the only solution of the paraxial Helmholtz equation. There exist many other solutions including beams with non-Gaussian intensity distributions. Beams of paraboloidal wavefronts are able to match the curvatures of concave mirrors of large radius. They reflect between two concave mirrors that generate a resonator, without being altered. A Gaussian beam of the complex envelope is considered as a modulated version of the Gaussian beam in (3.18).

$$A(x, y, z) = \mathcal{X}[\sqrt{2}\frac{x}{\omega(z)}]\mathcal{Y}[\sqrt{2}\frac{y}{\omega(z)}]\frac{A_1}{q(z)}exp[i\mathcal{Z}(z)]A_G(x, y, z), \tag{3.24}$$

where $A_G(x, y, z) = \frac{A_1}{q(z)}exp(-ik\frac{\rho_{xy}^2}{2q(z)})$, $q(z) = z + iz_R$ and $\mathcal{X}(.)$, $\mathcal{Y}(.)$and $\mathcal{Z}(.)$ are real functions.

Substituting (3.24) into (3.9) yields:

$$\frac{1}{\mathcal{X}}(\frac{\partial^2\mathcal{X}}{\partial u^2} - 2u\frac{\partial\mathcal{X}}{\partial u}) + \frac{1}{\mathcal{Y}}(\frac{\partial^2\mathcal{Y}}{\partial v^2} - 2u\frac{\partial\mathcal{Y}}{\partial v}) + k\omega^2(z)\frac{\partial\mathcal{Z}}{\partial z} = 0, \tag{3.25}$$

where $u = \sqrt{2}x/\omega(z)$ and $v = \sqrt{2}y/\omega(z)$. Note that the left side of (3.25) is a summation of three terms. Each of these terms, is a function of a single variable (u, v, and z), and thus has to be constant. If the first term and the second term

are equal to $-2\mu_1$ and $-2\mu_2$, respectively, we obtain:

$$\frac{1}{2}(\frac{d^2\mathcal{X}}{du^2} - 2u\frac{d\mathcal{X}}{du}) = \mu_1\mathcal{X}, \tag{3.26}$$

$$\frac{1}{2}(\frac{d^2\mathcal{Y}}{dv^2} - 2v\frac{d\mathcal{Y}}{dv}) = \mu_1\mathcal{Y}, \tag{3.27}$$

therefore, the third part boils down to:

$$k\omega^2(z)\frac{d\mathcal{Z}}{dz} = 2(\mu_1 + \mu_2). \tag{3.28}$$

Equation (3.26) and (3.27) show an eigenvalue problem where eigenvalues and eigenfunctions are $\mu_1 = l,\ \mu_2 = m$ and the Hermite polynomials have the following structure:

$$\mathcal{X}(u) = H_l(u),\ l = 0, 1, 2, ...$$

$$\mathcal{Y}(v) = H_m(v),\ m = 0, 1, 2, ...$$

These polynomials can be defined by the revision relation recursively. For instance,

$$H_{l+1} = 2uH_l(u) - 2lH_{l-1}(u), \qquad H_0(u) = 1, \qquad H_1(u) = 2u. \tag{3.29}$$

Thus,

$$H_2 = 4u^2 - 2, \qquad H_3(u) = 8u^3 - 12u, \qquad .... \tag{3.30}$$

Substitution of $\mu_1 = l$ and $\mu_2 = m$ in (3.28) gives us

$$\mathcal{Z}(z) = (l + m)\nu(z). \tag{3.31}$$

According to (3.24), we have finally

$$U_{l,m}(x,y,z) = A_{l,m}[\frac{\omega_0}{\omega(z)}]G_l[\frac{\sqrt{2}x}{\omega(z)}]G_m[\frac{\sqrt{2}x}{\omega(z)}] \times[-ikz - ik\frac{x^2+y^2}{2R(z)} + i(l+m+1)\nu(z)], \tag{3.32}$$

where $G_l(u) = H_l(u)exp(\frac{-u^2}{2})$, $l = 0, 1, 2, ...$ Equation (3.32) is a well-known equation for the Hermite-Gaussian beam of order (l, m). In fact, the Hermite-Gaussian beam of order $(0, 0)$ is a normal Gaussian beam.

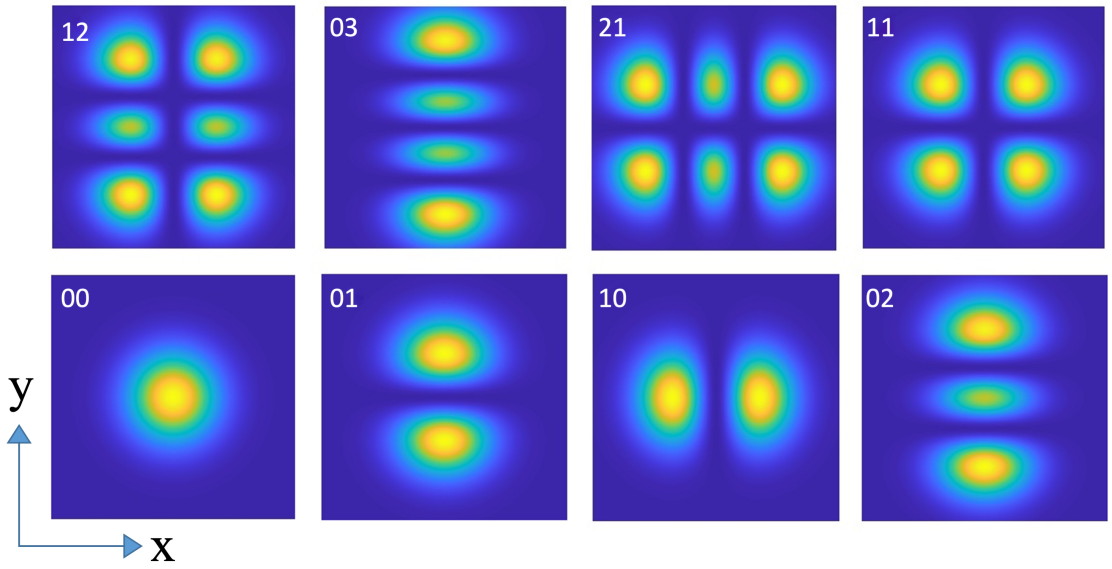


Figure 3.3: The intensity distribution of Hermite-Gaussian beams. The order (l, m) is shown in each case and the intensity is propagated in the z direction.

The electric field of a Gaussian wave is transverse to the z direction, and it is known as $TEM_{l,m}$ (TEM: Transverse Electromagnetic Mode) wave that can be a longitudinal or a transverse mode. Longitudinal mode is a fundamental mode or lowest-order Gaussian mode (TEM_{00}). In this mode, the phase of the electric field changes in the axial direction and the sign of the amplitude does not vary in the directions perpendicular to the resonator axis. However, in the transverse mode or higher-order Gaussian modes, the phase and the sign of the amplitude change in one or two directions perpendicular to the resonator axis.

Figure 3.3 shows the electric field intensity distribution of several low-order Hermite-Gaussian beams in the transverse mode. Beams with higher order have large widths in comparison with those of lower order. In this project, we use the TEM_{00} as a Gaussian beam.

3.5 Optical Modes through the Cavity

This section discusses the theoretical background developed for a Gaussian beam propagated through an open resonator. An open-access resonator consists of two opposed concave and flat mirrors. Figure 3.4 shows the schematic of an open-access resonator when a Gaussian beam is propagated through the cavity on the z-axis.

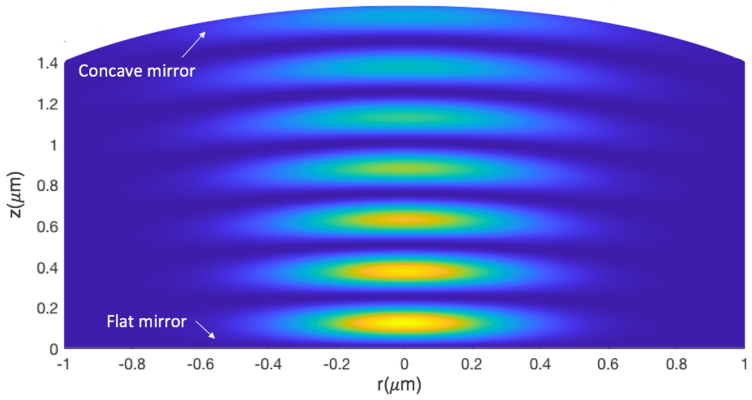


Figure 3.4: A simulation of an open-access microcavity consists of a concave mirror (with radius of curvature of 4 μm) and a planar mirror to create 7 antinodes (optical modes).

According to Figure 3.4, optical modes are placed through the cavity, and subsequently we need to understand how the optical modes help us to characterize nanoparticles. Therefore, we develop realistic optical modes for a Monte-Carlo simulation based on a stochastic modeling of nanoparticle dynamics suspended in fluid subject to a trapping force field. In order to determine the standing wave, retroreflection of the incoming Gaussian beam has to be studied on the mirror.

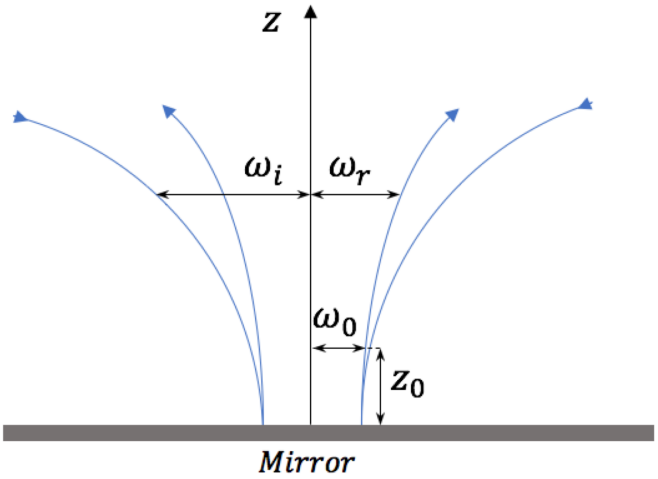


Figure 3.5: An incident beam is reflected by the mirror in the z direction to form a Gaussian beam.

Figure 3.5 shows the incident beam that is reflected by the planar mirror. The z-axis is the direction of the reflected beam and its origin is on the mirror surface. According to (3.19), the electric fields of the incident and the reflected waves are:

$$E_i(z,r) = E_0 \frac{\omega_0}{\omega_i} \exp(\frac{-r^2}{\omega_i^2}) \exp(ikz - \frac{ikr^2}{2R_i} - i \arctan(\frac{z}{z_R})), \tag{3.33}$$

$$E_r(z,r) = E_0 \frac{\omega_0}{\omega_r} \exp(\frac{-r^2}{\omega_r^2}) \exp(-ikz - \frac{ikr^2}{2R_r} + i \arctan(\frac{z}{z_R})), \tag{3.34}$$

where k is the wavenumber. The realistic optical beam intensity (I_R) is related to the electric field and therefore, the intensity distribution can be determined as:

$$I_R(z,r) = \frac{n_w \epsilon c}{2} |E_i(z,r) + E_r(z,r)|^2, \tag{3.35}$$

$$I_R(z,r) = \frac{n_w \epsilon c}{2} (E_i E_i^* + E_i E_r^* + E_r E_i^* + E_r E_r^*), \tag{3.36}$$

$$I_R(z,r) = 2 I_{R0} \frac{\omega_0^2}{\omega^2} \exp(\frac{-2r^2}{\omega^2}) [1 + cos(2kz + \frac{kr^2}{R} - 2 \arctan(\frac{z}{z_R}))], \tag{3.37}$$

where n_w, ϵ, c, and k are the refractive index of water, permittivity, light speed, and wave vector, respectively. Note that r is equal to $\sqrt{x^2 + y^2}$ and I_0 is the optical

intensity at the beam waist ω_0. In the realistic model, I_{R0} can be determined by

$$I_{R0} = I_0 = \frac{2P}{\pi\omega_0^2}.$$

Furthermore, $z_R = k\omega_0^2/2$ is the Rayleigh length as mentioned earlier. The parameter ω_0 is the beam waist at z_0 above the mirror. R_i and R_r are radii of the beam front curvature for the incident and reflected beams, respectively:

$$R_i = -R_r = R = -z(1 + \frac{z_R^2}{z}). \tag{3.38}$$

The beam width of the incident and the reflected beams are denoted by ω_i and ω_r, respectively:

$$\omega = \omega_i = \omega_r = \omega_0\sqrt{1 + \frac{z^2}{z_R^2}}. \tag{3.39}$$

Note that for having the antinodes between the mirrors, the phase of the intensity needs to be shifted by adding a π, and thus the intensity would be:

$$I_R(z, r) = 2I_{R0}\frac{\omega_0^2}{\omega^2}\exp(\frac{-2r^2}{\omega^2})[1 + cos(\pi + 2kz + \frac{kr^2}{R} - 2\arctan(\frac{z}{z_R}))]. \tag{3.40}$$

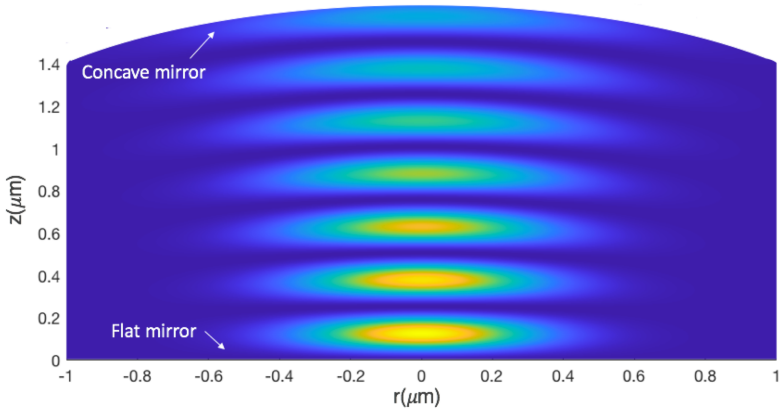
The beam waist can be rewritten by substituting the wavelength with $\lambda = \frac{2L}{q}$ in the Rayleigh length ($z_R = \frac{\pi\omega_0^2}{\lambda}$), therefore the radius of the wave at the length of cavity (L) can be calculated as:

$$R(z)\big|_{z=L} = L(1 + (\frac{\pi^2\omega^4}{\lambda^2 L^2})). \tag{3.41}$$

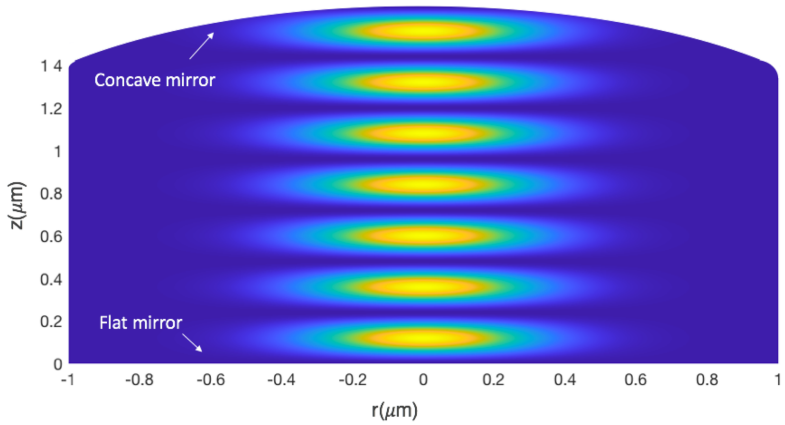
Then the beam waist is proportional to the length of the cavity:

$$\omega_0^2 = \frac{\lambda L}{\pi}\sqrt{\frac{R}{L} - 1}. \tag{3.42}$$

where L and R are the length of the cavity and the curvature radius of the microcavity, respectively.



(a)



(b)

Figure 3.6: The laser beam is propagated through the cavity with radius of curvature of 4 μm, generating 7 antinodes in (a) Gaussian (with small divergence) and (b) cylindrical model (without small divergence).

According to the generated Gaussian wave through the open microcavity, Figure 3.6a shows the normalized intensity that is distributed through the cavity. It is propagated through the z-axis with small divergence, which is called the realistic model in this dissertation.

Additionally, the beam propagation can be estimated by the cylindrical model where the divergence is ignored. Here, this model is studied as well to make a comparison with the realistic model. The cylindrical model is expressed as a

standing wave of a Gaussian beam with cylindrical symmetry where the intensity of each optical mode is identical. The optical intensity in the cylindrical model (I_C) can be rewritten within the paraxial approximation:

$$I_C = I_{C0}\cos^2\left(\frac{2\pi z}{\frac{\lambda}{n_{med}}}\right)e^{\frac{-2(x^2+y^2)}{\omega_0^2}}. \tag{3.43}$$

In order to have the antinodes between the mirrors we need to shift the phase of (3.43) by $\pi/2$:

$$I_C = I_{C0}\cos^2\left(\frac{2\pi z}{\frac{\lambda}{n_{med}}}+\frac{\pi}{2}\right)e^{\frac{-2(x^2+y^2)}{\omega_0^2}} = I_{C0}\sin^2\left(\frac{2\pi z}{\frac{\lambda}{n_{med}}}\right)e^{\frac{-2(x^2+y^2)}{\omega_0^2}}. \tag{3.44}$$

Figure 3.6b shows the optical modes with an identical shape in the optical cavity. We make a comparison between the maximum realistic intensity and the maximum cylindrical intensity with respect to (3.40) and (3.44)

$$\frac{I_R}{I_C} = \frac{\omega_0^2}{\omega^2}\frac{\exp(\frac{-2r^2}{\omega^2})}{\exp(\frac{-2r^2}{\omega_0^2})}, \tag{3.45}$$

where we assume I_{R0} in the realistic model is 4 times greater than cylindrical model I_{C0}. Here I_{C0} is the optical intensity in cylindrical modes at the beam waist ω_0.

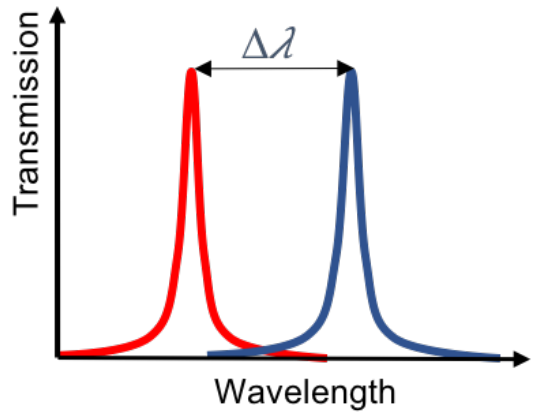


Figure 3.7: Changing the position of resonance wavelength when a particle is placed through the optical mode.

3.6 Optical Mode Shift

When a nanoparticle enters the cavity the optical mode changes. This optical mode shift is determined by the polarizability of the particle in the fluid and the location of the particle within the mode. The red curve in Figure 3.7 shows the nanoparticle is trapped through the cavity, which means the trapped particle caused the mode shift. The wavelength shift of an optical resonance due to the particle presence in the cavity can be calculated as follows. The electromagnetic energy $\mathfrak{U}$ is proportional to the frequency of the incident light f and the Planck's constant $\mathfrak{h}$, i.e

$$\mathfrak{U} = \mathfrak{h}f.$$

On the other hand, the fractional change in resonance frequency $\Delta f/f$ and corresponding the fractional wavelength $\Delta\lambda/\lambda$ can be obtained by comparing the electromagnetic energy it takes to polarize the diffused particle into the cavity at position r_0, i.e.,

$$\Delta\mathfrak{U}_{particle} = \frac{\alpha E(r_0)^2}{2\epsilon_0}$$

to the total energy confined in the microcavity, i.e.,

$$\mathfrak{U}_{total} = \int \epsilon E(r)^2 dV,$$

where α represents polarizability of the particle in a given medium, and V is optical mode volume. This principle of sensing can be applied to any microcavity structure and any biomolecule [24, 176, 177]. The mode volume is $V = \int \epsilon \frac{E(r)^2}{E(r)_{Max}{}^2} dV$, where $E(r)_{Max}$ is the highest field intensity in the cavity. The fractional wavelength can

be determined as

$$\frac{\Delta f}{f} = -\frac{\Delta \lambda}{\lambda} = \frac{\Delta \mathfrak{U}_{particle}}{\mathfrak{U}_{total}} = \frac{\alpha E(r_0)^2 / E(r)^2_{Max}}{2\epsilon_0 V},$$

where $E(r_0)^2/E(r)^2_{Max}$ is equal to the normalized intensity $I_N(r)$, which is derived from the relationship between the electric field and the optical intensity according to (3.35). Therefore, the optical mode shift $\Delta\lambda(r)$ is proportional to the optical mode volume, and the polarizability:

$$\Delta\lambda(r) = -\frac{\lambda\alpha}{2\epsilon_0 V} I_N(r), \tag{3.46}$$

where $I_N(r)$ is the normalized optical intensity which is a function of the particle position in the microcavity and it is equal to 1 for a particle at the maximum intensity. When a particle is trapped, we can make sure that the particle experiences the maximum intensity. The polarizability of a spherical nanoparticle can then be obtained by

$$\alpha = 4\pi a^3 n^2_{med} \epsilon_0 \frac{m^2 - 1}{m^2 + 2}, \tag{3.47}$$

where a is the radius of a spherical particle and m is the ratio of the refractive index of the particle (n_p) to that of the medium (n_{med}). Also, the optical mode volume can be determined by

$$V = \frac{\pi \omega^2 L}{4}, \tag{3.48}$$

where L is the length of the cavity. By measuring the mode shift we can therefore measure the polarizability of the particle.

3.7 Summary

We introduced an open-access microcavity along with the necessary conditions to create optical resonance through the cavity. The key parameters of this type of microcavities were explained in this chapter. The optical Gaussian beam was illustrated and shown as a solution to the Maxwell's equations. We presented the Hermite-Gaussian beam as another solution to the paraxial Helmholtz equation. Then, a realistic model was developed to describe the optical modes through the cavity. We also introduced a cylindrical model where the optical beam is propagated through the cavity as cylindrical symmetry. Namely, the cylindrical model is an estimation of the realistic model where the small divergence in the Gaussian beam has been ignored. Indeed, we can investigate the particle behavior in the cavity by these models based on Monte-Carlo simulations. Furthermore, the optical mode shift was explained when a nanoparticle enters the cavity and also its relationship with the particle parameters and the optical mode volume were studied in this chapter.

Chapter 4

Experimental Method

4.1 Introduction

This chapter explains the requirements to trap nanoparticles and also how they are characterized by the technique proposed previously. The flow cell design is discussed along with the method of nanoparticle delivery. The experimental set-up is further discussed with its various components to deliver fluid to the optical cavities. The function of each component of the experimental setup is explained in this chapter. Furthermore, we present how the optical cavity is stabilized by the phase-locking technique in this work. We show that the proposed technique extracts important information and insights that can be obtained from the raw data and post-processing them.

4.2 Requirements for Nanoparticle Characterization

Nanoparticulate pollutants and microbiological organisms such as viruses have optical characteristic signatures based on their refractive index, size, and polarizability, as well as spectral signatures [178]. As discussed in Chapter 2, characterizing individual nanoparticles in a fluid is challenging since the particle diffuses rapidly by Brownian motion. We overcome this problem using optical tweezers.

This work introduces an optofluidic apparatus for analyzing the dynamics of nanoparticles in fluidic systems and studying the potentials for optical trapping. We can hold a nanoparticle in the place and allow an extended measurement. This optical system allows us to detect and characterize nanoparticles at the single-particle level. Our optofluidics apparatus is based on optical microcavities and, as discussed in Section 2.3.2.4 in Chapter 2, this type of microcavities can create strong interaction between the confined optical field and the particle.

4.3 Optical Microcavity

Nanoparticle characterization in this work heavily hinges on an optical microcavity that is used as a flow cell. The microcavity consists of two facing mirrors (see Figure 1.1). One of them is a flat mirror (planar mirror) that is covered with a dielectric coating with minimum refractivity of 99.9% at an optical wavelength of 640 nm. The planar mirror is essentially a Distributed Bragg Reflector (DBR) that provides the high refractivity from the coating. It is fabricated by LAYERTEC using ion beam sputtering. A fused silica substrate is coated by 10 pairs of alternating layers of silica (11 nm) and titania (6 nm) that the thickness of each

layer is

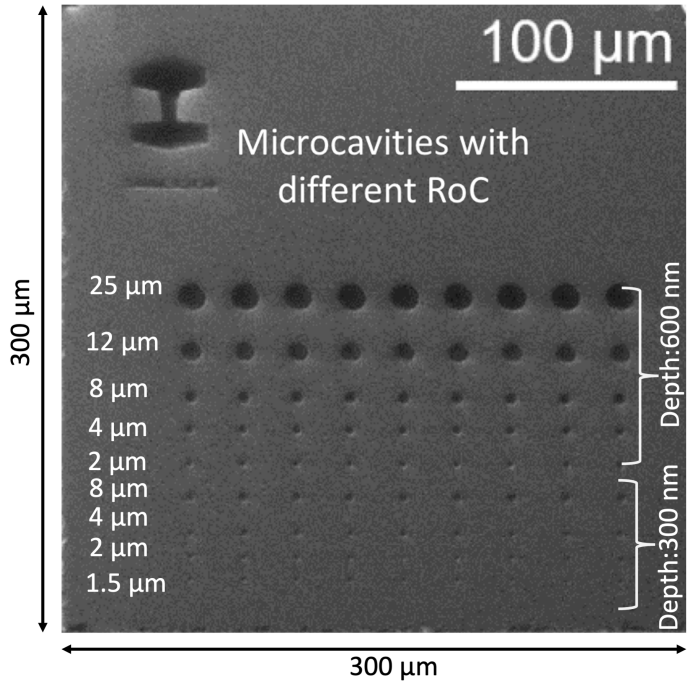
$$\frac{\lambda}{4n}.$$

Here, we use n and λ to denote the refractive index of the material and the desired reflection wavelength, respectively.

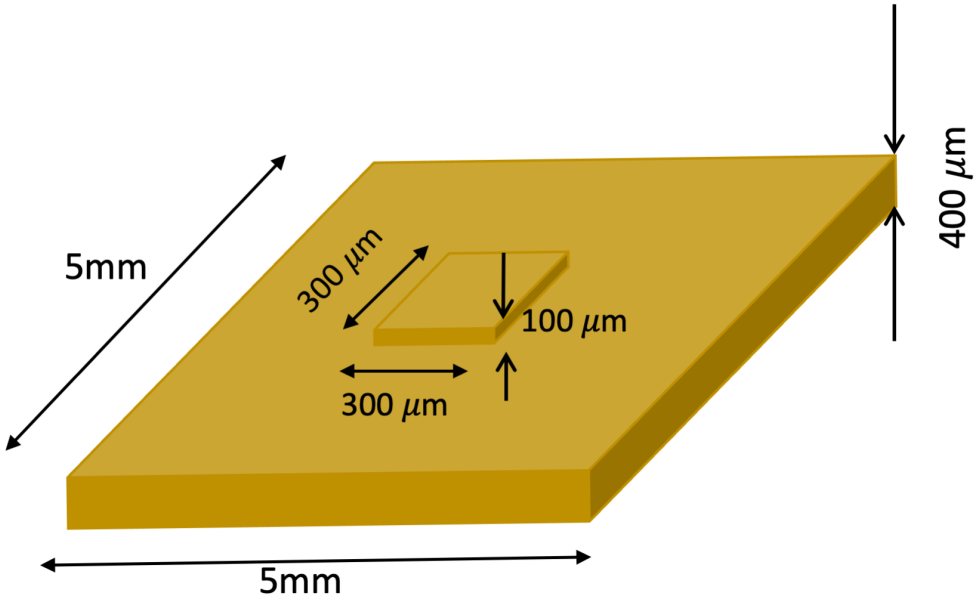
The second mirror is a patterned mirror, it has a square shape with a dimension of 5 $mm \times 5$ mm where a plinth is placed in its center by using dicer. The plinth is square with size of 300 μm and with height of 100 μm (see Figure 4.1a, 4.1b). The plinth facilitates the procedure of bringing the two mirror surfaces within microns of each other. We use the plinth structure when there is no flow through the cavity as explained in Chapter 6.

The patterned mirror has various concave structures with different radii and depths. Figure 4.1a shows the concave mirrors in which the radii of curvature change between 1.5 μm and 25 μm. The patterned mirror can also be a square with the dimension of 5 $mm \times 5$ mm where a ridge is placed in its center (using a dicing machine) and then the cavities are milled on the ridge part instead of the plinth. The ridge (Figure 4.2b.(3)) is rectangular with a length of 5 mm and width of 300 μm with a height of 100 μm. In this work, we use these patterned mirrors where there is flowing fluid through the cavity to facilitate the flow calibration in the cell. It will be discussed in Chapter 7.

These concave mirrors are formed by Focusing Ion Beam (FIB) milling. FIB milling is a technique to create desired surfaces with a resolution of 5 nm. The focused beam of gallium ions sputters tiny content of surface material to fabricate patterned surfaces. The mirrors are coated with dielectric Bragg reflectors consisting of alternating layers of SiO_2 and TiO_2 to achieve the required reflectivity in the wavelength region of interest. As mentioned before, these concave mirrors are good candidates for sensing and characterizing nanoparticles therefore we use them as flow cells.



(a)



(b)

Figure 4.1: (a) SEM image of an array of concave mirrors on the plinth along with the different RoC and the depth of the cavities, (b) a schematic of the chip where the microcavities are milled on the plinth (the center squar).

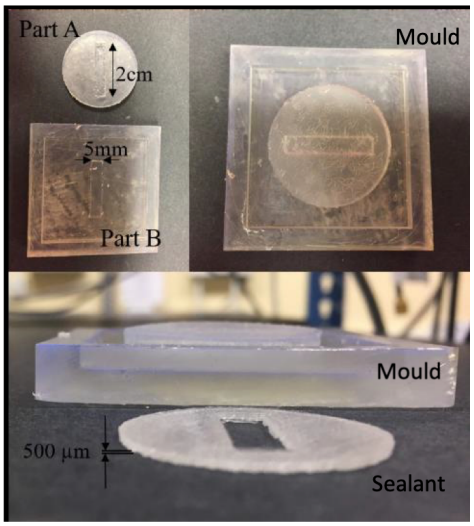
4.4 Flow Cell

The flow cell is the most crucial part of our setup. it consists of microcavity (planar and concave mirrors) and a solution of nanoparticles. The solution can be delivered through the cavity by tubing and pipes as inlet and outlet. In case when we have flowing solution in our setup, the flow velocity is controlled by a pressure-driven system (ELVEFLOW [179]). The ELVEFLOW system is connected to reservoirs of the solution to make a constant pressure-driven flow.

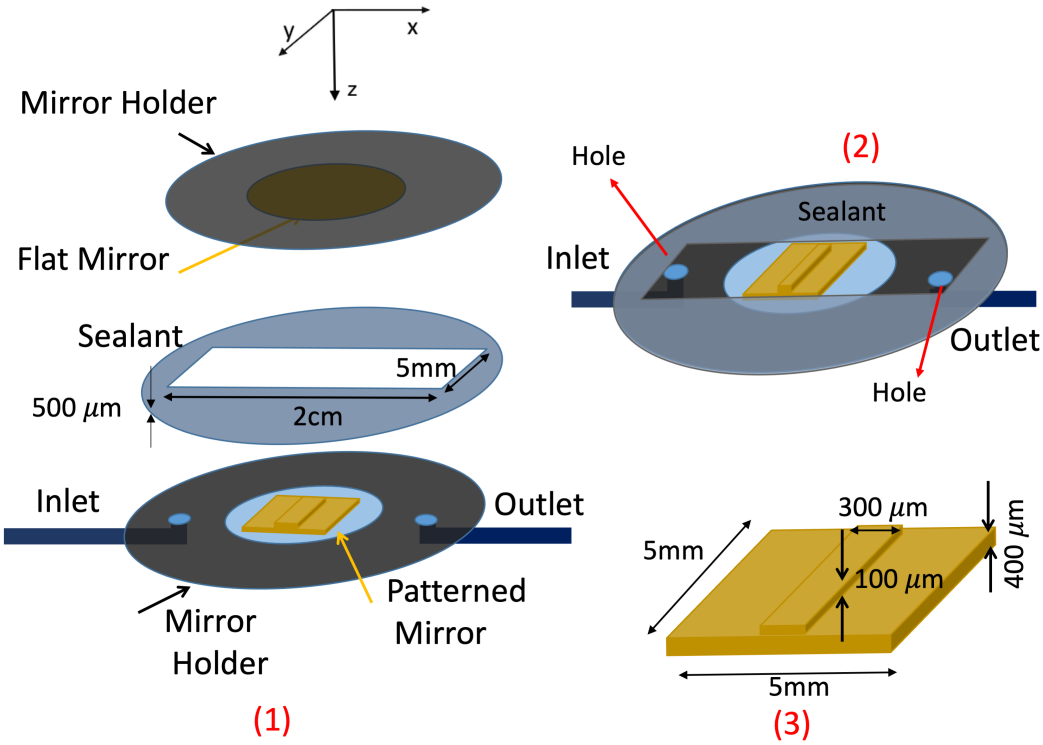
The solution consists of nanoparticles and DeIonized (DI) water. The concentration of nanoparticles can be adjusted by diluting DI water. As discussed before the cavity type is "open", which means a sealant is needed to prevent any leakage from the cavity and to make sure that nanoparticles enter the cavity. When there is a chance to have leakages in the system, the nanoparticles may not reach the center of the channel or plinth. The leakage problem then can be solved with the introduction of the sealant to entirely seal the flow cell.

The sealant is made out of Polydimethylsiloxane (PDMS) and a fabricated mould. Figure 4.2a shows the mould that is designed in AutoCAD and fabricated by a 3D printer. PDMS is mixed in a 1:10 ratio of curing agent and PDMS monomers. In this implementation, a mixture consists of 7 g of curing agent and 70 g of monomer is used (Dow Corning: SYLGARD 184, Silicone Elastomer, Flowable, RT Cure). The PDMS monomers are much more viscous than the curing agents. After making the mixture, by using a vacuum container (over 2 hours), the air bubbles are removed, and then we pour the PDMS into the mould. The PDMS and the mould are placed in a 60 degree Celsius curing oven for one hour. Finally, the sealant has a channel as shown in Figure 4.2b. The size of the channel matches with the width of chip 5 mm and has thickness of 500 μm.

The fluidic channel is connected to two tubes (diameter of 1 mm) as inlet and

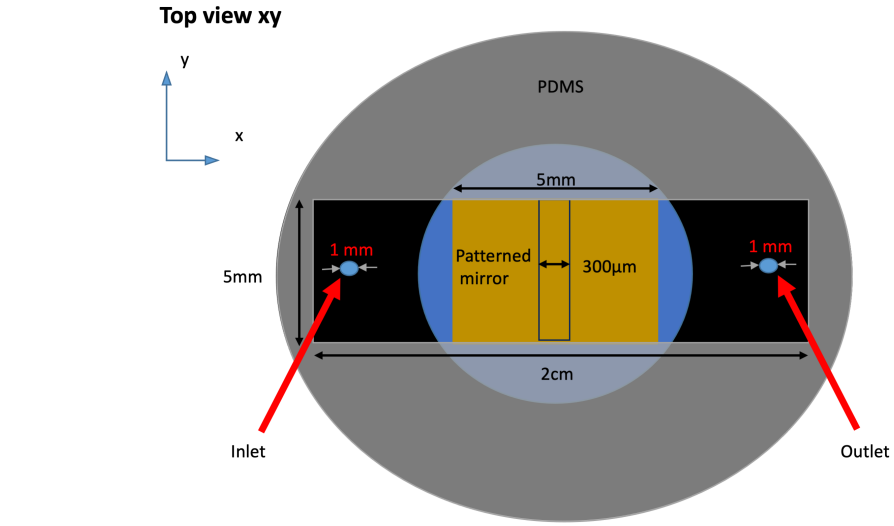


(a)

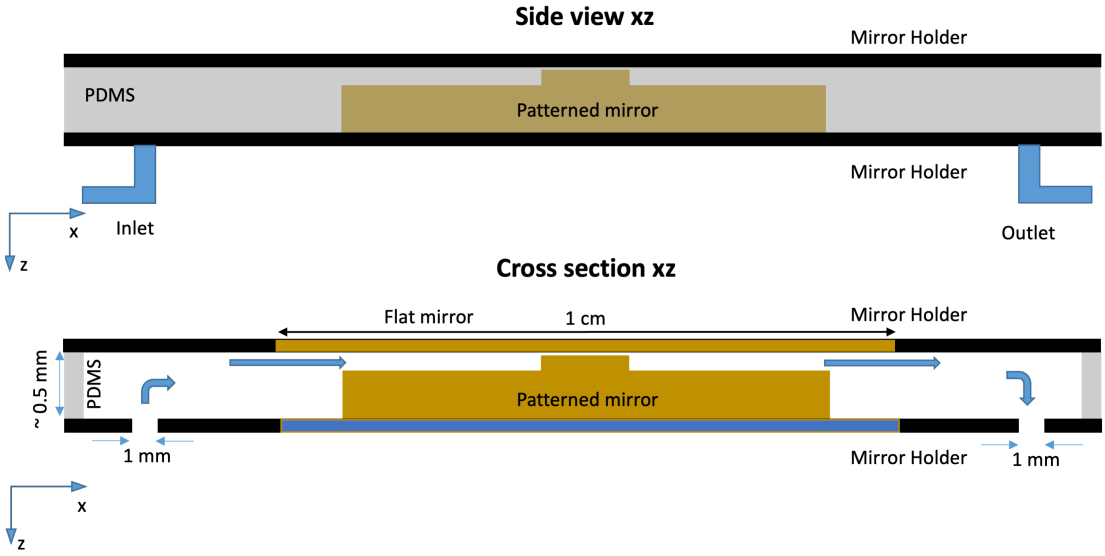


(b)

Figure 4.2: (a) An image of the mould along with the sealant; the mould consists of two parts; part A and B, part A is installed on part B to make the sealant. (b) a schematic of components of the flow cell; (1) the flow cell comprises of patterned mirror on the ridge, sealant, flat mirror, inlet, and outlet tubes (2) the channel shape when the sealant environs the ridge to seal the flow cell and (3) the patterned mirror with the dimension of the ridge (the center rectangular).



(a)



(b)

Figure 4.3: (a) A top-view of the flow cell (the cavities are placed on the ridge) in the xy direction and (b) a side view along with a cross-section of the flow cell in the xz direction to show how the particles are introduced through the cavity.

outlet to deliver the flow through the channel between two mirrors (see Figure 4.2b). The mirrors are glued to two holders. The inlet and outlet are connected to the mirror holders. Therefore, the fluid flows between the mirrors from the top side of the mirror holder (inlet) and leaves the channel through the downside (outlet).

The sealant is placed between the mirror holders. Figure 4.3 presents a top view in the xy direction and a side view in xz along with the cross-section of the flow cell to have a sufficient understanding of the flow cell in detail.

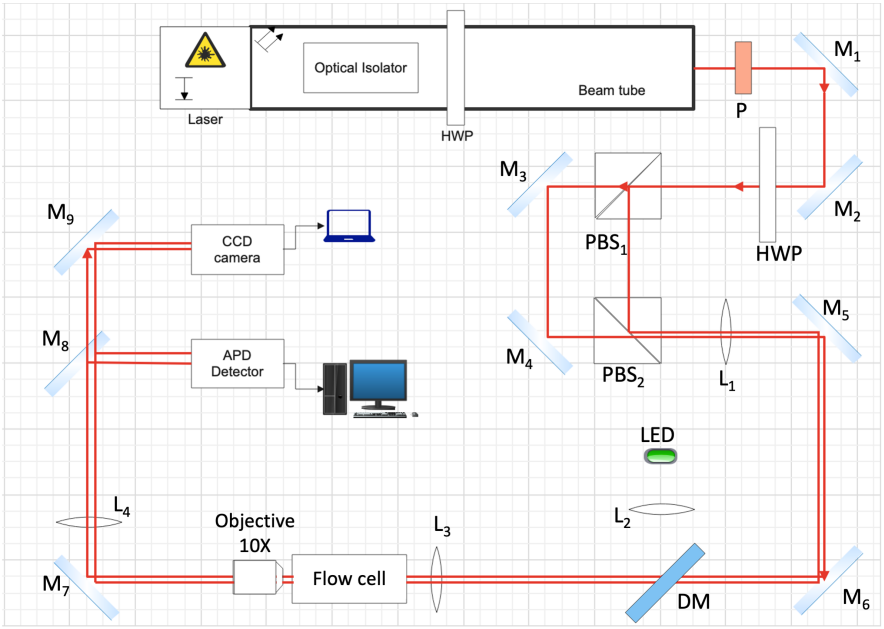
4.5 Optical Set-up

Figure 4.4 illustrates the experimental set-up. There is a CCD camera to monitor the image of the patterned mirror and to help to adjust the angle and the distance between two mirrors. The incident light is from a Lasos laser with a wavelength of 640 nm and linewidth of 5 MHz. Here, the linewidth is the width (typically the full width at half-maximum, FWHM) of its optical spectrum. The polarized laser beam is split into two parts by two polarizing beam splitters (PBS1, PBS2) to have a relative intensity of two cavities that can be independently aligned onto the two cavities. Then two beams are transmitted into two cavities simultaneously which are then collected in transmission by an objective lens with a magnification of 10×. One cavity is used as a sensing cavity with a higher intensity and the other cavity acts as a reference cavity with a lower intensity to eliminate the vibration effect which would affect both cavity modes identically. Note that the laser is propagated through the cavity in the z axis direction.

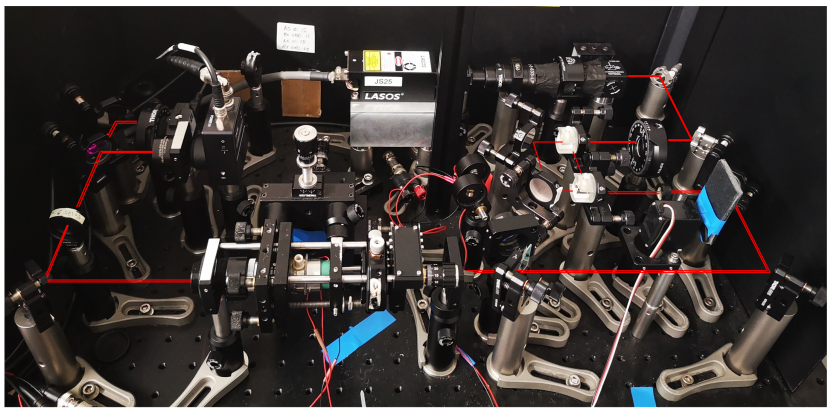
These lights are collected by an Avalanche Photodiode (APD). One cavity is used as the sensing cavity with high intensity and the other one acts as the reference cavity with low signal. Figure 4.5 shows these cavities that are aligned.

There is a kinematic stage (Figure 4.6a) connected to the patterned mirror for aligning the cavities and imaging the mirror through the camera by shining a yellow LED with a wavelength of 593 nm to the optical direction. Figure 4.6a shows a schematic of the flow cell along with the holders and piezo actuator.

To change the length of the cavity, two piezo actuators, long and short, are



(a)



(b)

Figure 4.4: (a) Schematic of the optical setup; P:P-Polarizer, M(1-9): PF10-03-P01-protected silver mirror, M8:Flip mirror, HWP: Half-Wave Plate for adjusting the input light intensity, L(1-4): lenses (Thorlabs), L1:LC1060-B - N-BK7, L2:AC254-075-B-ML, L3, L4:AC254-030-A-ML, DM: Dichroic Mirror (DMLP605R-Thorlabs and angled at 45^o with respect to the LED light beam), Objective lens (10X): Nikon, antireflection, the APD (430-Thorlabs) and CCD camera:(340M-USB-Thorlabs). (b) an image of the experimental set-up.

used to make large and small displacements, respectively. The piezos are attached to the planar mirror whose diameter is 10 mm). The long piezo is employed for adjusting the cavity length, and the short one is used for cavity stabilization. The

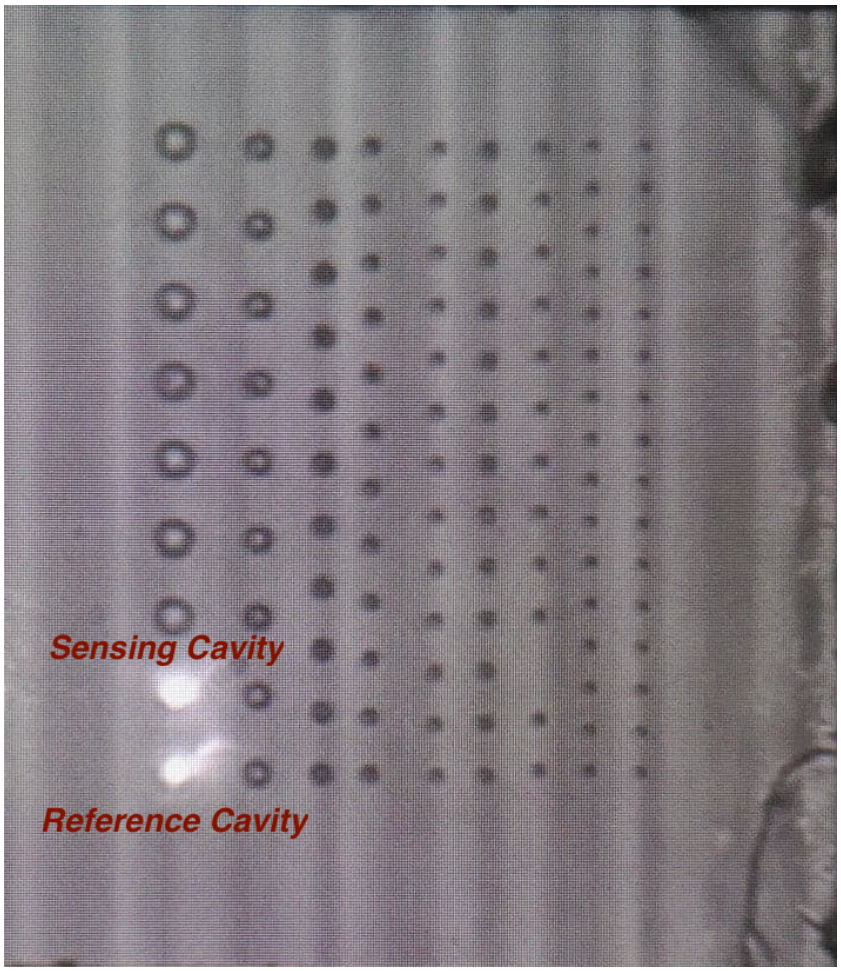
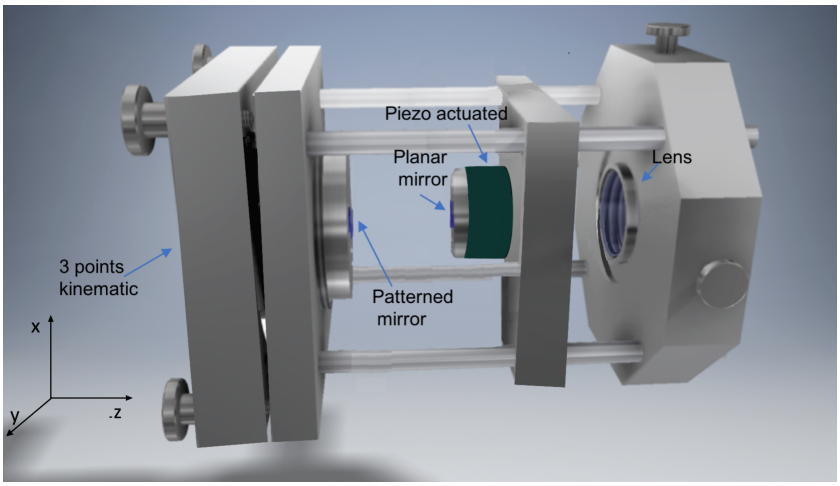


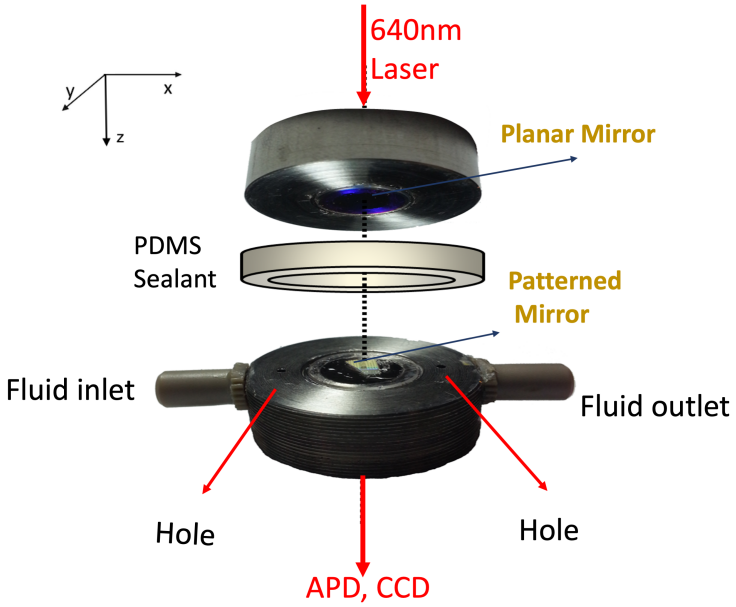
Figure 4.5: An image of the sensing and reference cavities that are monitored by the CCD camera.

optical resonances can be obtained by scanning the cavity length.

For an efficient alignment, a fast oscillating sinusoidal frequency in the range of 500 Hz along with a voltage of 10 V is applied to the long piezo by a signal function generator. Once the laser alignment is done, the short piezo is connected to the function generator to have a sinusoidal frequency in the range of 5 KHz and a voltage of 2 V. This helps to have an accurate length adjustment. In other words, the length of the cavity is determined and locked for the rest of the experiment. This step of the experiment is important since we can determine the length of the cavity for calibrating the experimental data, and furthermore, we lock the cavity to neutralize any vibration that comes from mechanical and thermal changes.



(a)



(b)

Figure 4.6: (a) A 3D image of the flow cell with holders to show where the piezo and the mirrors are placed (b) a close up of the flow cell along with more details in the direction of the incident laser, the sealant, fluid inlet, and outlet.

Our locking technique that uses phase detection is the most practical approach to stabilize the cavity. For locking the cavity, we use a phase-error signal and feedback it to the piezoelectric in the cavity to control the length of the cavity. The controller configuration is presented in Figure 4.7. The principle of the stabilization system is that the repetition frequency of the cavity is phase-locked to a reference

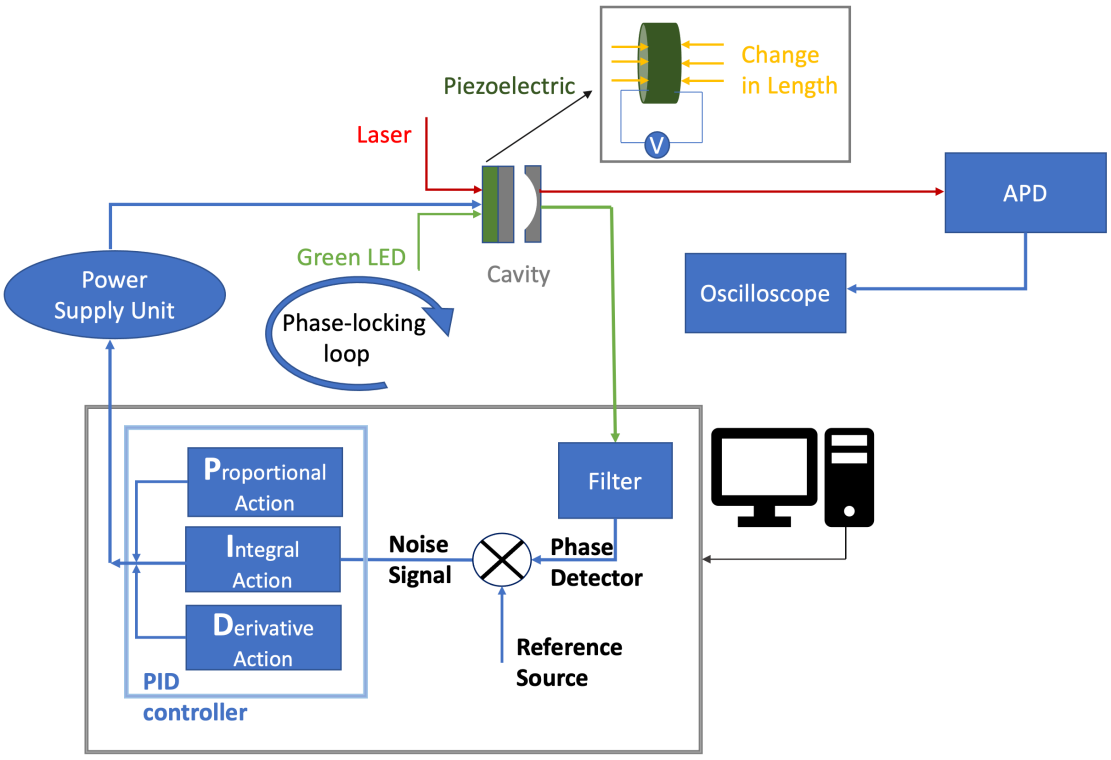
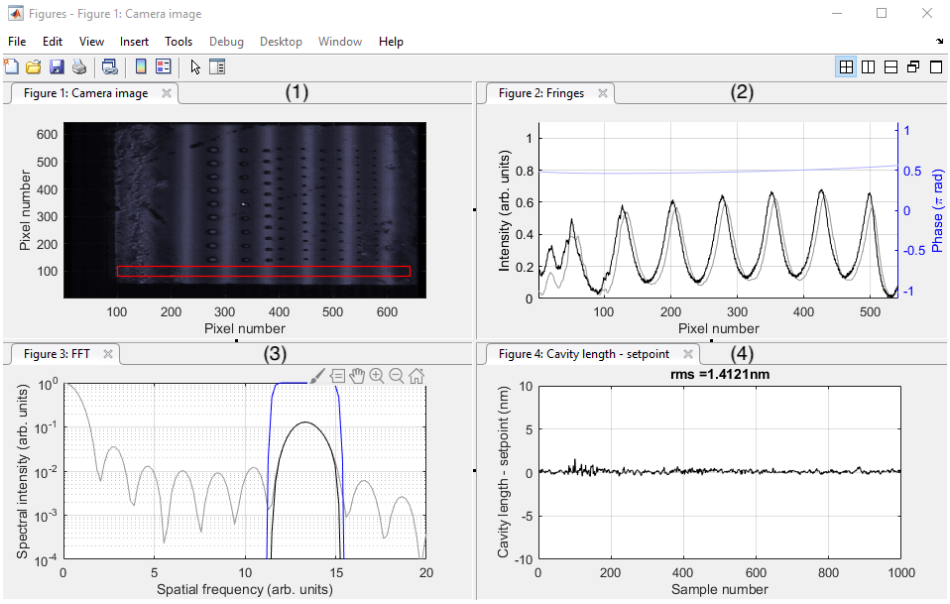


Figure 4.7: Diagram of locking the cavity by the PID controller.

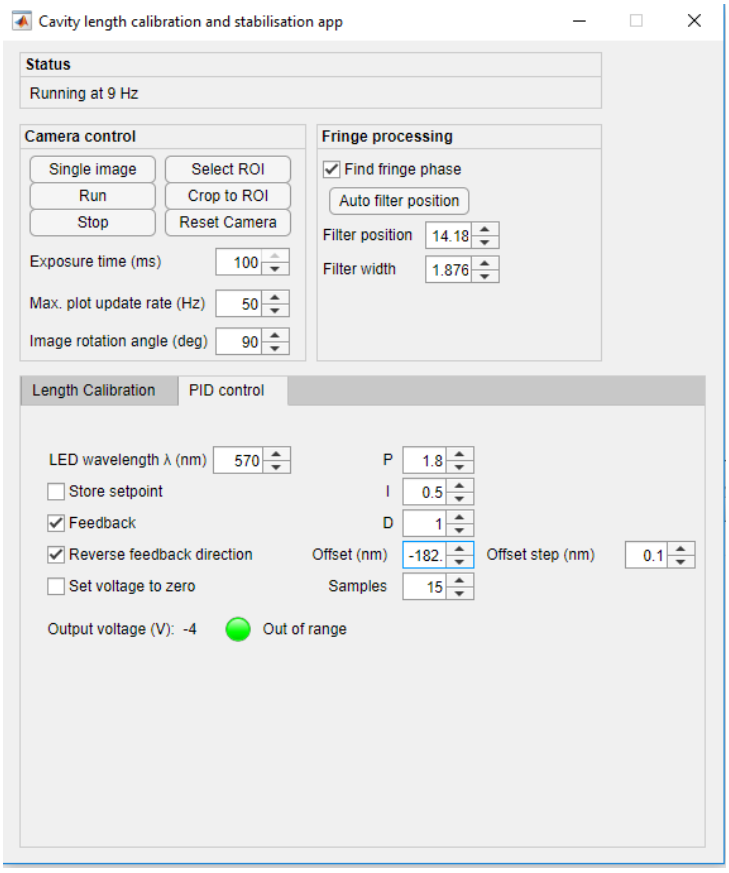
source. Here, the piezo is sinusoidally derived at its mechanical resonance (5 kHz) over a free spectral range of the cavity and analyzes the temporal positions of transmitted fringes through phase detection.

We use the CCD camera for the measurement of fringes and stabilization of the phase of the fringes by a voltage applied to the short piezo. Figure 4.8a.1 shows the fringes made by LED along with the intensity and the phase of fringes. The phase of fringes is stabilized by the voltage applied to the short piezo. For locking the cavity, a green LED with a wavelength of 570 nm is used to calibrate the length of the cavity.

The reason for using this type of LED is that the wavelength of green LED matches with the edge of the stop-band wavelength of the mirrors where the reflectivity reposes around 50%. A relative change of cavity length can be determined concerning the minimum and the maximum transmission through the cavity



(a)



(b)

Figure 4.8: (a) Steps of cavity stabilization process by fringes, (b) PID controller panel.

(planar and patterned mirrors) and the green LED wavelength for observing the transmitted intensity. By making a small angle between two mirrors, the length of the cavity can be measured by the difference of the green LED wavelength (570 nm) on the plinth and the piezo ring actuator displacement that is mounted on the planar mirror. Note that the angle between the mirrors and the green LED creates optical fringes as can be seen in Figure 4.8a.1.

The optical path length between the two end mirrors varies with spatial position due to the angle between them. Recall that consecutive round trips of the light in the cavity interfere with each other. A certain spatial positions where the round-trip optical path is equal to an integer multiple of the illumination wavelength, there is maximum constructive interference. Therefore, one fringe spacing corresponds to a difference in mirror separation of $\frac{\lambda}{2n}$, where λ is the illumination wavelength and n is the refractive index in the cavity. The fringes move laterally as the mirror separation is changed because the spatial position at which maximum constructive interference occurs changes.

The phase of fringes (Figure 4.8a.2) is filtered by a band filter (Figure 4.8a.3) and then mixed with a reference source by a phase detector to produce a phase-error signal at the intermediate frequency. The phase detector is used to measure signals that are synchronous with a reference oscillator. Additionally, any change in the cavity length (Figure 4.8a.4) can be controlled by monitoring the length of the cavity as a feedback loop to adjust the voltage of the piezos and then change the length of the cavity.

A Proportional-Integral-Derivation (PID) controller helps to lock the cavity and stabilize the cavity length while the cavity length is scanned by the short piezo with a sinusoidal frequency generator as shown in Figure 4.8b. In other words, the PID regulator can auto-calculate the regulation voltage signal to drive the piezoelectric incorporated into the plane mirror. The mirror separation is therefore locked by

locking the fringe phase. Therefore, the optical modes are able to be detected on the APD. This cavity stabilization system is implemented by Dr. William Okell in the lab.

In summary, the planar mirror and the plinth are angled away from parallel, giving rise to interference fringes across the planar part of the plinth surface. The phase of the interference fringes gives a relative measure of the cavity length. Drifts in cavity length due to e.g. thermal drift can be corrected by moving one of the end mirrors along the optical axis to maintain a constant fringe phase at a particular spatial position on the plinth. This was achieved by measuring the fringe phase in real-time, comparing to an initial reference fringe phase (it introduces phase error), calculating a correction using a PID controller, and applying feedback to a piezo ring actuator controlling the cavity length. A second piezo sinusoidally scans the cavity length around its actively stabilized mean position, such that an optical mode of the measurement cavity and an optical mode of the reference cavity are fully contained within the scanning range. The angle between the mirrors ensures that the reference and measurement cavity have sufficiently different lengths that there is no overlap between their modes. The reference cavity mode is used to remove residual cavity length changes from the experimental data.

4.6 Sample Preparation

In this project, we use different spherical nanoparticles such as polystyrene (PS) and PMMA particles to show how these particles can be evaluated and characterized by our technique. The concentration of nanoparticles needs to be adjusted because the initial stock of the nanoparticles has a high concentration. We can achieve the desired concentration by diluting nanoparticles with DI water.

We prepare solutions of PS and PMMA particles that are diluted with DI water

to obtain concentration of 10^{11} N/ml, where N is the number of particles per ml. The concentration of each type of particles is defined by the ratio of weight (W) to volume (V), and the number of particles can be calculated by:

$$C_i = \frac{W}{V}\frac{1}{\rho V_p}, \tag{4.1}$$

where ρ and V_p are the density and volume of the particle, respectively. The particles have spherical shapes and thus, the volume of each particle can be easily obtainable. For adjusting the concentration of the sample, we have:

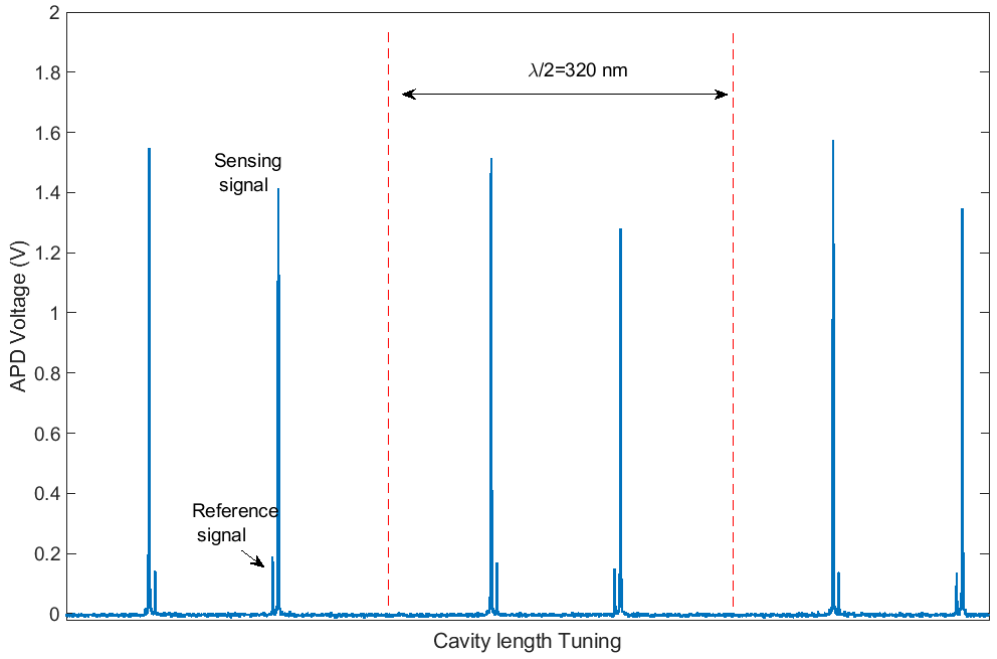
$$C_i V_i = C_f V_f, \tag{4.2}$$

where C_i and V_i are the initial stock concentration and initial volume of the sample, while C_f and V_f are the final concentration and volume of the sample which are desired. Once the required concentration of the sample is achieved, the sample needs to be stirred for 20 minutes by a sonicator. In case when there is flowing fluid in the system, the sample can be delivered to the flow cell by a syringe pump or ELVEFLOW system (both are pressure-driven).

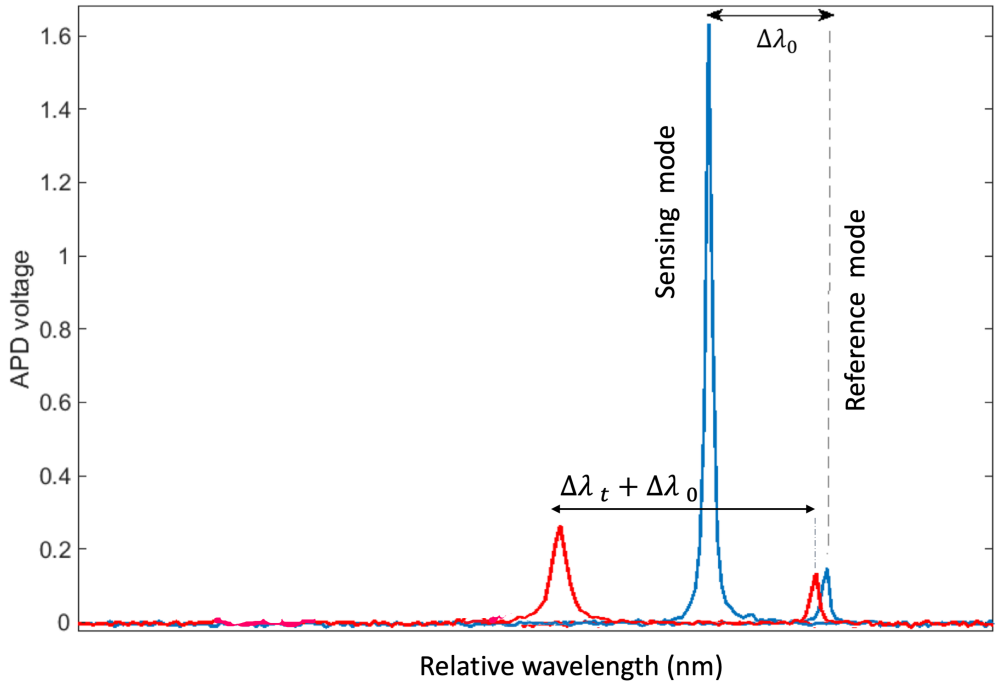
4.7 Measurement

For characterizing nanoparticles, the polarizability of nanoparticles needs to be studied. When a nanoparticle enters through the cavity, the optical mode is shifted which can be determined by the polarizability of the particle in the fluid and the location of the particle within the mode.

Figure 4.9a illustrates the spectrum of two collected signals when the cavity is empty of nanoparticles: the reference signal and the sensing signal are collected by APD. Scanning the cavity mode helps us to optically detect a nanoparticle. Figure 4.9b shows two spectra by scanning the flat mirror when the cavity is locked.



(a)



(b)

Figure 4.9: (a) Transmission scan of experimental data that includes two signals, the strong signal represents the sensing signal and the weaker signal is related to the reference cavity, (b) an example of wavelength shift when the PMMA particle with diameter or size of $196 \pm 4.4\ nm$ is detected by the sensing signal.

The blue spectrum belongs to the cavity that is empty of nanoparticles and the red one is of the cavity when the particle is detected.

Any change in the resonance mode can be acquired by studying these spectra and then calibrated and converted into a wavelength shift axis. Our dynamic calibration is based on a stroboscopic effect on the fringes to find the scan range and the time delay (Dr. William Okell has also implemented this technique in the lab). The $\Delta\lambda_0$ is the constant value of the mode shift before the trapping and $\Delta\lambda_t$ is the disturbance in the cavity mode that is resulted due to the presence of a Poly(Methyl Methacrylate (PMMA) particle with a diameter (size) of 200 nm. Note that by using the self-referencing technique (between a reference and a sensing cavity), the mechanical noise effect is reduced on the mode disturbances and what we obtain is only the disturbance generated by the nanoparticle, i.e., $\Delta\lambda_t$.

The experimental data consists of a series of discrete events as individual nanoparticles diffuse through the cavity mode and are pulled to the center of the optical mode by the trapping forces. The raw data are observed by an Oscilloscope.

Figure 4.10 shows an example of raw data when the nanoparticles are diffused through the cavity. These data belong to a solution of diluted PMMA nanoparticles (from Phosphorex Inc) with a diameter of nominal size 200 nm, actual size of 196 ± 4.4 nm, and concentration of 10^{11} N/ml. In this experiment the radius of curvature of the concave mirror is 25 μm on the plinth structure and the cavity length of around 1 μm . By monitoring any change in mode position in two cavities (reference and sensing cavities), the mode shift can be measured by omitting the noise. According to the sensing intensity, which is much greater than the reference signal, particles are pulled through the sensing cavity.

When a particle enters the cavity the amplitude of the intensity is quenched and the position of the mode is changed as well. By observing mode attenuation over long time scales, we can detect the trapping events. Figure 4.10 displays

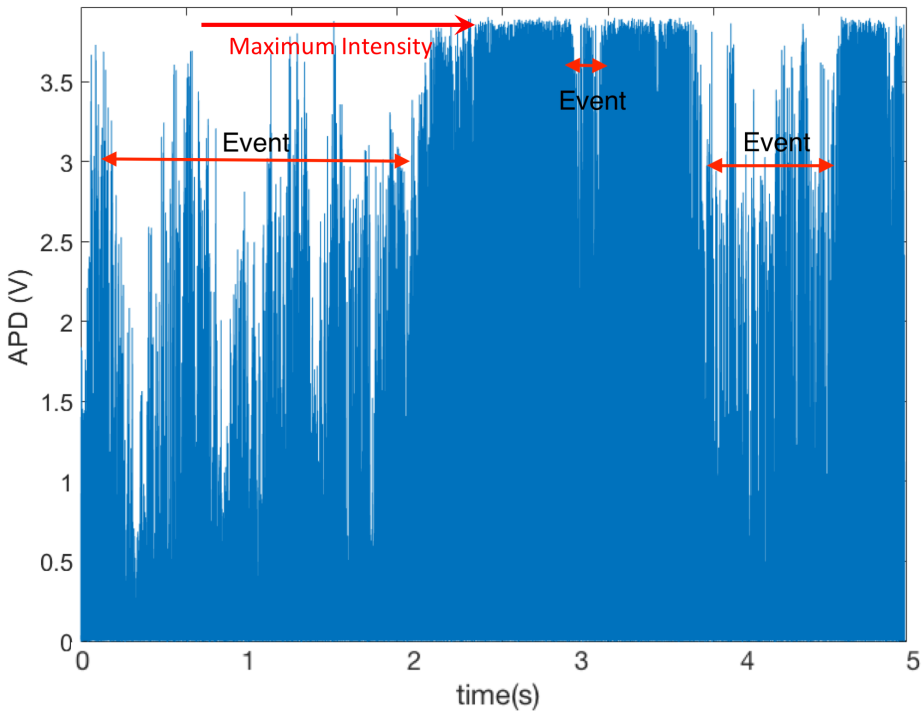


Figure 4.10: An example of raw data from the APD when a solution of PMMA particles with size of 200 nm is introduced through the cavity; the red arrow represents the maximum intensity which indicates that a particle is escaped from the cavity. The events with two-headed arrows indicate that a particle is trapped.

that particles are diffused through the cavity. The two-headed arrows show the trap events as the amplitude of the laser intensity is fluctuated due to the particle presence in the cavity. The x axis is time and the y axis is the intensity of the reference and sensing signals in the scale of voltage. The considerable fluctuations in the mode shift of the sensing cavity shows that the particle is affected by the Brownian motion within the trapping potential. Note that, there is no flowing fluid in this experiment. To ensure the sample is within the microcavities, the solution is derived by pressure. By observing a few drops in the beginning at the outlet, and ensuring that there is no leakage, the particles are guaranteed to be in the flow cell.

Each trapping event is recorded by a trigger in the Picoscope software. The trigger is sensitive to any change in the intensity of the sensing cavity for a defined

time duration. Here, the time duration illustrates how long the particle stays within the cavity. The trigger can be adjusted by the Picoscope software. The raw data are recorded for 5 s and the trigger is set for 200 ms. Namely, if the trigger senses the intensity fluctuation for 200 ms, the data will be automatically saved by the Picoscope. This essentially means the trap events are recorded if the particle stays in the cavity for at least 200 ms.

The raw data needs to be post-processed by observing the changes in the amplitude of the sensing signal as compared to the changes in the reference signal to omit the noise. Therefore, we can determine the mode shift and the changes of the mode position with respect to the initial intensity by using a MATLAB interface. We exhibit an example of post-processed experimental data that consists of a series of discrete events as individual nanoparticles diffuse through the cavity mode and are pulled to the center of the mode by the trapping forces in Figure 4.11. This particle is diffused through antinodes and tried to escape from the cavity due to other forces such as Brownian motion. The fluctuations are caused by the particle movement between antinodes.

Figure 4.11 illustrates an example trace recorded over 5 seconds, where the maximum mode shift of the 200 nm PMMA particle is 700 pm. The expected diffusion time of a particle through the mode is of the order of 10 milliseconds according to $\tau_{diff} = \frac{V^{\frac{2}{3}}}{6\mathfrak{D}}$ where V is mode volume [24]. For instance, the free diffusion time through the cavity mode for a 200 nm diameter particle is about 30 ms. The maximum (Max) shift of 700 pm, and the extended shift for 2.5 s, represent a trapped particle (Figure 4.11). The maximum mode shift provides a measurement of the polarizability of the nanoparticle [180], and the accuracy of polarizability measurement will be discussed in Chapter 6. In this thesis, we show the measured polarizabilities as polarizability volume ($\alpha' = \frac{\alpha}{\epsilon_0}$). The measured polarizability volume for PMMA particles with the size of 200 nm is 11×10^5 $(nm)^3$

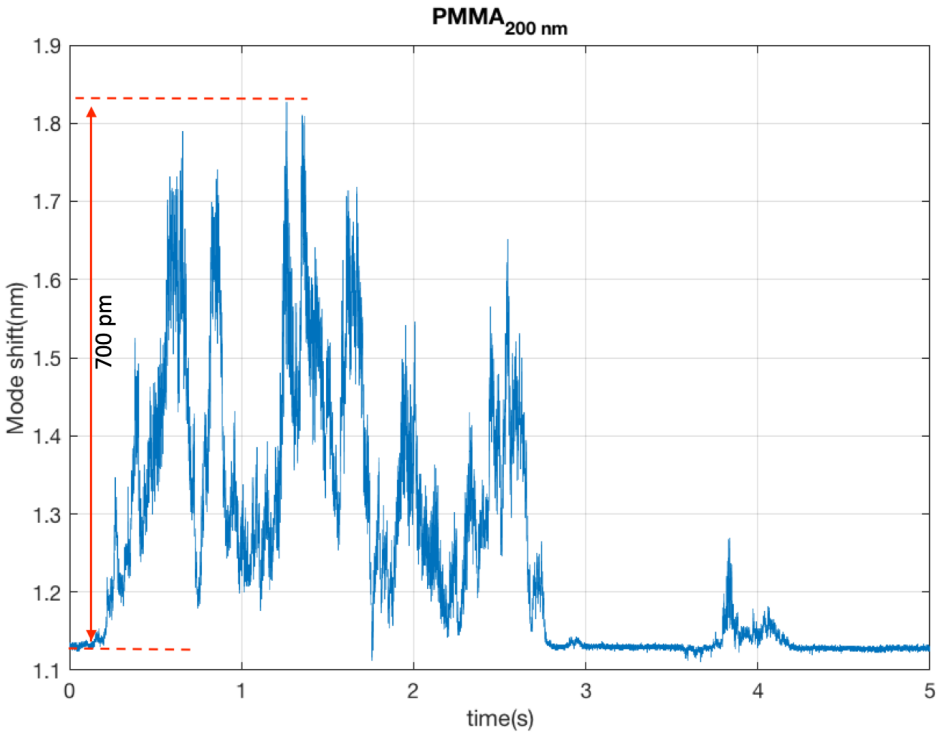


Figure 4.11: The mode shift of a PMMA particle with size of 200 *nm*. The maximum mode shift is 700 *pm*.

according to the measured maximum mode shift. Recall that the relationship between the maximum mode shift and the polarizability is discussed in (3.46) (Chapter 3 in Section 3.6).

4.8 Summary

This chapter discussed the principle of our technique that is the underpinning for the studies to be described in future chapters. We created a Fabry Pérot interferometer incorporating a planar and a concave micromirror with an integrated flow cell for the introduction of suspensions of nanoparticles. This chapter demonstrated an optical and an electronic system with integrated piezoelectric translation stages for adjusting the separation of the two mirrors of the interferometer. We stabilized the open-access microcavity using phase locking. Then we presented our apparatus as an optical tweezer to hold a nanoparticle and measure the properties of the trapped particle.

In this chapter, as part of sample preparation, we explained how the particles are diluted in DI water to achieve the desired concentration of the solution. Furthermore, an example of experimental data for PMMA nanoparticles with size 200 nm was presented as evidence of the performance system. We were able to measure the maximum mode shift of 700 pm and then determined the polarizability of the particle accurately.

Chapter 5

Monte-Carlo Modelling and Simulation

5.1 Introduction

This chapter will present a theoretical point of view on how open-access microcavity is used for nanoparticle characterization. Throughout this chapter we assume that there exists a flow through the microcavity for nanoparticle delivery. The optical force will be evaluated by optical beam propagation theory through the cavity. Then we discuss other forces that can affect the trapping of nanoparticles. Furthermore, the particle behavior will be studied by simulating their trajectory in the cavity under different situations. Then the maximum mode shift will be discussed when a particle is diffused through the cavity.

Further to this, the physical characteristics of the proposed open-access microcavity will be investigated to demonstrate how the optical modes and forces

are impacted by the device size and geometry. Then we will show the maximum mode shift as a key parameter of characterization for different nanoparticles with different optical power and particle velocities. Finally, this chapter will explain how a nanoparticle can be delivered through the system and then the profile of the flowing fluids will be analytically and numerically investigated.

5.2 Optical Nanoparticle Trapping

In this section, we develop the stochastic model of dynamics of a nanoparticle suspended in a fluid that is subjected to the trapping force. This modeling approach essentially simulates the motion of nanoparticles as they flow through an optofluidic system. As such it is a powerful tool to understand the range of behaviors observed and to specify in detail the performance metrics of the instrument. In addition, we further understand how to analyze measured signals more efficiently and extract useful information from the system. Based on this stochastic model, we simulate the particle motion by using a Monte-Carlo approach.

There are various factors that affect nanoparticles and lead to them escaping from a microcavity such as small trapping stiffness and the general randomness in the Brownian motion due to the thermal motion of molecules in a bulk fluid. We investigate these factors to obtain a dynamic trapping range with a desired probability of trapping. Another goal is to find the maximum manipulation flow rate to keep nanoparticles trapped with a determined size, and to determine the optical power needed for a specific time duration.

In the following, we study the physical phenomena that are considered in the theoretical model; optical force [64], drag force [181], Brownian Motion [182] and Thermophoretic Force [183].

5.2.1 Optical Force

Trapping a nanoscale particle is studied through an optofluidic system. The optofluidic system comprises an optical open-access microcavity and the size of the nanoparticle is smaller than the laser wavelength. This type of cavity provides a well-understood tool for nanoparticle trapping and sensing [24]. Specifically, a particle can be trapped by the optical force when the particle spread through the zones which have a high electromagnetic field [62–64].

A nanoparticle experiences a force as a result of a gradient field within a Gaussian beam where the refractive index of the medium is lower than that of the particle. The optical or gradient force is generated by the interaction of incident light with a dielectric particle. In other words, the optical modes generate the optical forces in the cavity. The gradient force $F_{optical}$ applied on a spherical particle with a radius of a (diameter or size of $D = 2a$) in an electric field E can be calculated as follows:

$$F_{optical} = \frac{1}{2}\alpha \nabla E^2, \tag{5.1}$$

where α is the polarizability of the particle in a given medium as determined in (3.47) (Section 3.6 in Chapter 3). The intensity of Gaussian beam I is proportional to the electric field

$$I = n_{med}\epsilon_0 c|E^2|. \tag{5.2}$$

We assume that the electric intensity is propagated as a Gaussian beam through the fluid, according to (5.1), (5.2) and (3.37). The optical forces in the x, y and z directions are:

$$F_{Optical_x R} = \frac{\beta}{\omega^2}[\frac{-4x}{\omega^2}(1 + cos(\pi + \phi)) - \frac{2kx\sin(\pi + \phi)}{R}]e^{\frac{-2r^2}{\omega^2}}, \tag{5.3}$$

$$F_{Optical_y R} = \frac{\beta}{\omega^2}[\frac{-4y}{\omega^2}(1 + cos(\pi + \phi)) - \frac{2ky\sin(\pi + \phi)}{R}]e^{\frac{-2r^2}{\omega^2}}, \tag{5.4}$$

$$F_{Optical_z R} = e^{\frac{-2r^2}{\omega^2}}(1 + cos(\pi + \phi))[\frac{-2\beta\omega'}{\omega^3} + \frac{4\beta r^2\omega'}{\omega^5}] - \frac{\beta\phi' \sin(\pi + \phi)}{\omega^2} e^{\frac{-2r^2}{\omega^2}}, \quad (5.5)$$

where

$$\beta = \frac{\alpha I_0 \omega_0^2}{n_{med}\epsilon_0 c},$$

and

$$\phi = 2kz + \frac{kr^2}{R} - 2\arctan(\frac{z}{z_R}). \quad (5.6)$$

In the following we calculate $\phi', R'(z)$ and ω', which are derivatives of ϕ, R and ω with respect to z, respectively. These parameters are:

$$\phi' = 2k - kr^2\frac{R'(z)}{R^2(z)} - \frac{z}{z_R}\frac{1}{1 + \frac{z^2}{z_R^2(z)}}, \quad (5.7)$$

where

$$R'(z) = (1 - \frac{z_R^2(z)}{z^2}), r = \sqrt{x^2 + y^2}, \quad (5.8)$$

$$\omega' = \frac{\omega_0}{z_R^2}\frac{z}{\sqrt{(1 + \frac{z^2}{z_R^2})}}. \quad (5.9)$$

These optical forces can be derived by considering the laser intensity propagated through the cavity as a cylindrical model according to (3.44). The optical force can then be calculated in x, y and z direction by:

$$F_{Optical_x C} = I_{C0}\frac{-4x\alpha}{2cn_{med}\epsilon_0\omega_0^2}cos^2(\frac{2\pi z}{\frac{\lambda}{n_{med}}})e^{\frac{-2(x^2+y^2)}{\omega_0^2}}, \quad (5.10)$$

$$F_{Optical_y C} = I_{C0}\frac{-4y\alpha}{2cn_{med}\epsilon_0\omega_0^2}cos^2(\frac{2\pi z}{\frac{\lambda}{n_{med}}})e^{\frac{-2(x^2+y^2)}{\omega_0^2}}, \quad (5.11)$$

$$F_{Optical_z C} = I_{C0}\frac{-2\pi\alpha}{2cn_{med}\epsilon_0}sin(\frac{4\pi z}{\frac{\lambda}{n_{med}}})e^{\frac{-2(x^2+y^2)}{\omega_0^2}}. \quad (5.12)$$

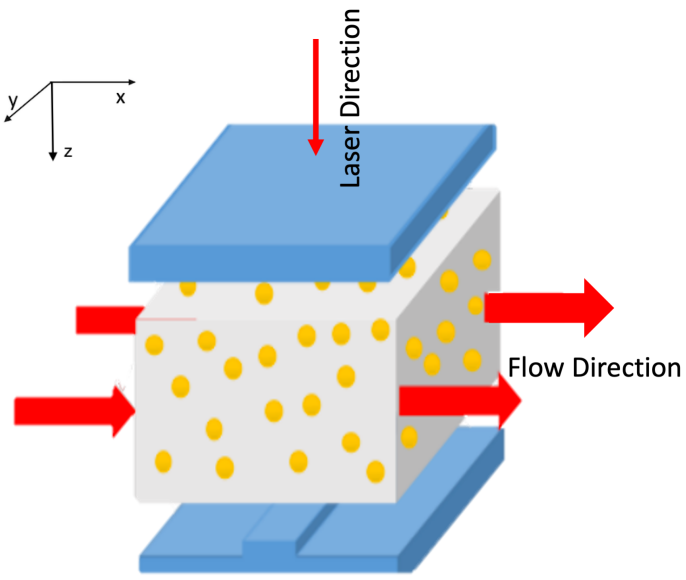


Figure 5.1: A schematic of the flow cell to show flow direction and the propagated laser direction when there is flowing fluid and the cavities are milled on a ridge.

5.2.2 Drag Force

In this section, the theory of optical trapping is extended to flowing fluids with linear potential gradients arising from the frictional drag of the flowing fluid. The drag force is an additional force that results from the viscosity of the surrounding medium. According to Stokes' law, the drag force F_{flow} is proportional to the flow velocity v, the radius of the particle a (particle size $D = 2a$) and the viscosity of the fluid η:

$$F_{flow} = -6\pi\eta a v. \tag{5.13}$$

Note that, here, we initially assume that the optical beam propagates based on the cylindrical model ((Section 3.5 of Chapter 3)), and the flow profile is linear. For now these assumptions simplify the analysis, helping us to gain a clear insight.

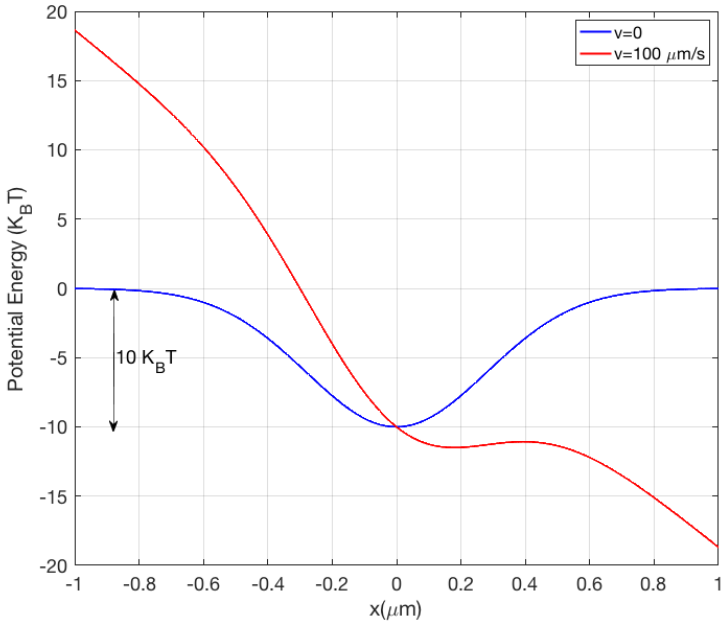


Figure 5.2: Total potential energy with the intracavity power of $10mW$ and beam waist of 560 μm by considering a polystyrene particle (diameter or size of 100 nm) with no flow (blue curve) and with the flow of 100 $\mu m/s$ velocity in the x direction. Note that the laser wavelength is assumed to be 640 nm in our simulations to match the experimental work (see Section 4.5 of Chapter 4).

Later in the chapter we change these assumptions to more realistic ones. Based on the relationship between the force and potential energy, the flow force can be derived by finding the derivative of the flow potential along the flow direction x (see Figure 5.1). The flow potential is calculated as follows:

$$U_{flow} = 6\pi\eta avx. \tag{5.14}$$

The total potential consists of the optical potential and the flow drag potential:

$$U_{total} = U_{flow} + U_{optical}, \tag{5.15}$$

where

$$U_{optical} = \frac{\alpha}{2n_{med}\epsilon_0 c} I. \tag{5.16}$$

If we assume that the optical potential along the y and the z axis is zero, then the optical potential based on the cylindrical model (Section 3.5 of Chapter 3) can be then written as

$$U_{optical} = \frac{\alpha}{2n_{med}\epsilon_0 c} I_0 e^{\frac{-2x^2}{\omega_0^2}} = U_0 e^{\frac{-2x^2}{\omega_0^2}}, \tag{5.17}$$

where

$$U_0 = \frac{\alpha}{2n_{med}\epsilon_0 c} I_0. \tag{5.18}$$

The total potential energy for trapping a nanoparticle depends on several factors such as the beam waist, the laser power, and also particle size, velocity, and refractive index. In order to trap a particle, the potential depth (or potential well) must be larger than the Brownian kinetic energy of the particle. The potential depth is sometimes referred to as the Boltzman factor and is denoted by K_BT where K_B is Boltzman constant and T is temperature. The minimum energy needed for stable trapping is $U_{min} > 10K_BT$ [64].

By considering these forces in the cavity, it is easy to see that by increasing the velocity of the nanoparticle, the potential depth is decreased. As in Figure 5.2, the minimum potential is proportional to K_BT as shown for different flow rates of 0, and 100 $\mu m/s$, particle size of 100 nm, laser beam waist of 560 nm and the laser power of 10 mW. The potential well is almost vanished when the flow speed is more than 100 $\mu m/s$. Note that the laser wavelength is assumed to be 640 nm in our simulations to match the experimental work (see Section 4.5 of Chapter 4).

The optical trapping in a flowing fluid is studied based on the optical trapping potential and the linear potential gradient which arises from the frictional drag of the flowing fluid. The potential energy is investigated by showing a cross-section of the potential energy for a 200 nm diameter spherical particle in flowing water at different flow rates in Figure 5.3. It is evident that by increasing the velocity of the flow, the potential depth is decreased. The potential is proportional to K_BT

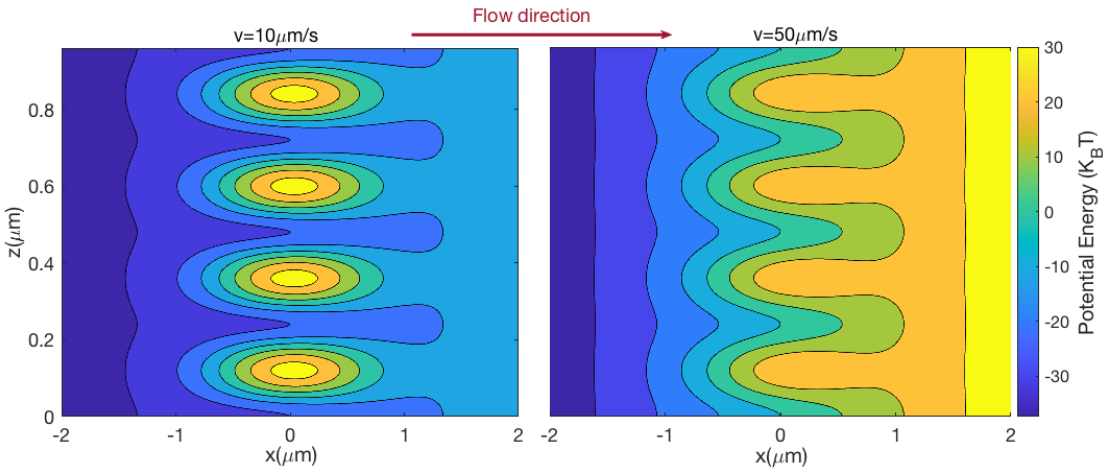


Figure 5.3: Cross-sections of the potential energy versus the position of a 200 nm polystyrene particle which is delivered through the cavity with two different flow rates. The flow profile is assumed to be flat or linear and the optical beam is based on the cylindrical model with the RoC of 25 μm and the intracavity power of 50 mW.

as shown for different flow speeds of 10 $\mu m/s$, and 50 $\mu m/s$, and the intracavity power of 50 mW. Note that the potential well has almost disappeared when the flow speed is more than 50 $\mu m/s$. Consequently, the particle with a velocity of 50 $\mu m/s$ is escaped due to the high flow rate. This essentially means that the flow rate is one of the effective parameters affecting the trapping of nanoparticles. We can then find the maximum flow rate for trapping of the nanoparticle. We call it the critical flow rate, and we determine it by making a balance between the optical trapping force and the flow force:

$$F_{optical} = F_{flow}, \tag{5.19}$$

$$I_0 \frac{-4x\alpha}{2cn_{med}\epsilon_0\omega_0^2} cos^2(\frac{2\pi z}{\frac{\lambda}{n_{med}}}) e^{\frac{-2(x^2+y^2)}{\omega_0^2}} = -6\pi\eta a v. \tag{5.20}$$

Therefore, the closed-form of the critical velocity, i.e., maximum velocity that a

particle can be still trapped, is determined as:

$$v = I_0 \frac{4x\alpha}{2cn_{med}\epsilon_0\omega_0^2} \frac{\lambda}{n_{med}} \frac{1}{6a\pi\eta} cos^2(\frac{2\pi z}{\frac{\lambda}{n_{med}}}) e^{\frac{-2(x^2+y^2)}{\omega_0^2}}. \tag{5.21}$$

Note that an interesting observation from (3.47) and (5.21) is that the critical velocity is proportional to a^2 since in the numerator of (5.21) we have α, where α is proportional to the particle radius cubic (a^3) as shown in (3.47). We also have the particle radius in the denominator of (5.21), and by simplifying these two we can see that the critical velocity is proportional to the radius squared, i.e., a^2.

5.2.3 Brownian Force

When a particle moves freely in a fluid, two other forces affect the motion of the particle: the damping force, which comes from the viscosity of the fluid; and a random fluctuating force due to molecular collisions. The motion of the particle in the presence of an optical field can be modeled by the Langevin equation. The optical potential causes a disturbance to the velocity of the particle, which depends on the Euclidean position of the particle (x, y, z). By making a balance between the optical force, the Brownian motion, drag force, and an external flow force γv_{x0} on the x axis we have:

$$\gamma \frac{dr(t)}{dt} = F_{optical}(t) + \sqrt{2K_B T\gamma}\ W + \gamma v_{x0}, \tag{5.22}$$

where $\gamma = 6\pi\eta a$, the term $\gamma\frac{dr(t)}{dt}$ presents the drag force, and $\sqrt{2K_BT\gamma}\ W$ is the fluctuating force which arises from random impulses of the Brownian motion where W is a time-varying normally-distributed random vector [184]. Recall that K_B is the Boltzmann's constant, and T is the temperature. The corresponding finite difference equation evaluated at regular time steps $t_i = i\Delta t$ if Δt is sufficiently small, is

$$\frac{dr(t)}{dt} = \frac{r_i - r_{i-1}}{\Delta t}, \tag{5.23}$$

where $r(t_i) = r_i$. A set of equations are set up for the movement in each direction during each time step of Δt based on a balance between the driving and frictional forces acting on the particle [184]. We assumed that the acceleration of the particle in Newton's second law of motion is zero as appropriate for a heavily damped system. Therefore, the trajectory of a nanoparticle in three coordinate directions, in the presence of optical trapping force and a flow in the x axis can be calculated as follows:

$$x_i = x_{i-1} + \frac{\Delta t}{\gamma} F_{optical_x} + \frac{\Delta t}{\gamma} \sqrt{2K_B T\gamma}\ W_i + \Delta t v_{x0}, \tag{5.24}$$

$$y_i = y_{i-1} + \frac{\Delta t}{\gamma} F_{optical_y} + \frac{\Delta t}{\gamma} \sqrt{2K_B T\gamma}\ W_i, \tag{5.25}$$

$$z_i = z_{i-1} + \frac{\Delta t}{\gamma} F_{optical_z} + \frac{\Delta t}{\gamma} \sqrt{2K_B T\gamma}\ W_i, \tag{5.26}$$

where

$$W_i = \frac{w_i}{\sqrt{\Delta t}}, \tag{5.27}$$

w_i is a random variable sampled from a Gaussian distribution with zero mean and unit variance [184]. By substituting (5.10), (5.11), and (5.12) in (5.24), (5.25), and (5.26) we can easily show that

$$x_{i+1} = x_i + \frac{\Delta t}{\gamma} I_0 \frac{-4x_i\alpha}{2cn_{med}\epsilon_0\omega_0^2} cos^2\left(\frac{2\pi z_i}{\frac{\lambda}{n_{med}}}\right) e^{\frac{-2(x_i^2+y_i^2)}{\omega_0^2}} + \sqrt{2\mathfrak{D}\Delta t} w_{xi} + \Delta t v_{0x}, \tag{5.28}$$

$$y_{i+1} = y_i + \frac{\Delta t}{\gamma} I_0 \frac{-4y_i\alpha}{2cn_{med}\epsilon_0\omega_0^2} cos^2\left(\frac{2\pi z_i}{\frac{\lambda}{n_{med}}}\right) e^{\frac{-2(x_i^2+y_i^2)}{\omega_0^2}} + \sqrt{2\mathfrak{D}\Delta t} w_{yi}, \tag{5.29}$$

$$z_{i+1} = z_i + \frac{\Delta t}{\gamma} I_0 \frac{-2\pi\alpha}{2cn_{med}\epsilon_0} sin\left(\frac{4\pi z_i}{\frac{\lambda}{n_{med}}}\right) e^{\frac{-2(x_i^2+y_i^2)}{\omega_0^2}} + \sqrt{2\mathfrak{D}\Delta t} w_{zi}, \tag{5.30}$$

where $\mathfrak{D} = \frac{K_B T}{\gamma}$ is diffusion coefficient as discussed in Section 2.2.4 of Chapter 2.

The second and third terms on the right-hand side of (5.28), (5.29) and (5.30) are associated with the optical trapping force and the random Brownian motion, respectively. In (5.28) there is the fourth term which presents the motion of the particle due to the fluid flowing at speed of v_{0x} or the flow velocity in the x direction where the flow profile is assumed flat. Note that in the obtained equations, the trapping of particles depends on the size of the particle, the flow rate, and the electric intensity that is proportional to the laser power.

Additionally, these equations can be calculated using the realistic model or the Gaussian beam with the divergence. With respect to the realistic beam intensity (3.37), the determined optical forces (5.3), (5.4),(5.5) can be used as optical forces in x, y and z direction. In the following chapters, for making a fair comparison between the experimental results and simulation ones, the realistic model is considered for theoretical calculation.

5.2.4 Thermophoretic Force

Further to the above forces, nanoparticles suspended in fluids can be affected by another force that induces the particles to travel towards cold areas. This phenomenon is called thermophoresis. There exist numerous theoretical and experimental studies on thermophoresis in gases, but the thermophoresis effect in liquids is known to be significantly different from those in gases [185]. Specifically, thermophoresis in liquids has been extensively studied in theory [183, 186–189], while experimental data on the movement of a single-particle under thermophoresis is sparse [190].

We investigated the thermophoretic effect on the optical microcavity to see how the thermophoresis alters potential wells. More specifically, we studied two models and made a comparison between the thermophoresis models and no-thermophoresis; the first model is the McNab-Meisen model which is a version of a model for

thermophoresis in gases that has shown the thermophoresis velocity of polystyrene particles with size of $800 - 1000\ nm$ [186] and the second model is the Duhr-Braun ionic-shielding model that is based on the entropy of the particle-solvent system [187].

5.2.4.1 McNab-Meisen Model

As we show later, the thermophoretic force creates a thermophoretic velocity that depends on the position of a particle and the interactivity power. The thermophoresis generates a thermophoretic velocity that compels the particle to cold areas. The cold area is the field out of the cavity and the beam waist. The temperature in the cavity is maximum due to the presence of the laser beam and thus the temperature gradient is zero through the cavity. The thermophoresis is considered in fluids with small particles suspended when a temperature gradient exists. The temperature gradient creates a force F_T in the direction opposite of that gradient, namely

$$F_T = \gamma v_T, \tag{5.31}$$

where v_T is thermophoretic velocity

$$v_T = -D_{TM} \nabla T, \tag{5.32}$$

where, D_{TM} in this model is defined as:

$$D_{TM} = \frac{0.13\eta}{\rho T[1 + (\frac{k_p}{2k_l})]}. \tag{5.33}$$

D_{TM} is proportional to the liquid viscosity (η), the density of fluid (ρ), temperature (T), the thermal conductivity of the particle (k_p) and the fluid (k_l) (water in our case).

The temperature gradient ∇T can be estimated by treating the microcavity

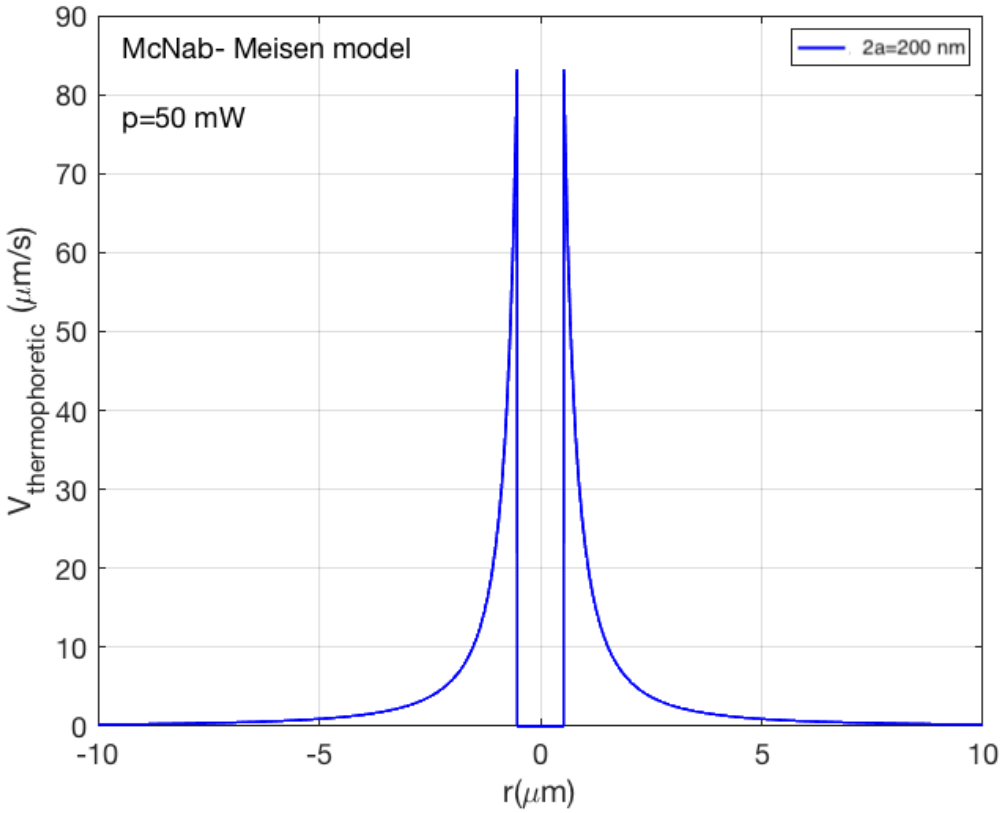


Figure 5.4: Thermophoretic velocity versus the particle position, where the laser power and the particle diameter are 50 mW and 200 nm, respectively.

as a sphere of air at a constant temperature in an infinite block of silica. This is the case when the air in the gap around the microcavity is assumed to be in equilibrium with the silica substrate.

The rate of heat flow, $\dot{Q}$, from the microcavity to the surrounding silica substrate is determined by

$$\dot{Q} = -k_T A \nabla T, \tag{5.34}$$

where k_T is the thermal conductivity of silica and A is the surface area of a sphere:

$$A = 4\pi r_s^2. \tag{5.35}$$

Substituting the expression for A into the expression for $\dot{Q}$ and rearranging for ∇T yields:

$$\nabla T = -\frac{\dot{Q}}{4\pi k_T r_s^2}. \tag{5.36}$$

Note that the laser transmitted into the microcavity is a Gaussian beam. The beam waist ω_0 is the distance from the centre of the beam at which the intensity falls to $\frac{1}{e^2} = 0.135$ of the maximum. The radius of the sphere representing the microcavity can be taken as $\frac{\omega_0}{2}$. The maximum temperature rise $\Delta T_{max} = T(r_s = \frac{\omega_0}{2}) - T_{amb}$, (where T_{amb} denotes ambient temperature) is found by integrating ∇T with respect to r_s from $r_s = \infty$ to $r_s = \frac{\omega_0}{2}$:

$$\Delta T_{max} = \int_{\infty}^{\frac{\omega_0}{2}} \nabla T \; dr_s = \int_{\infty}^{\frac{\omega_0}{2}} -\frac{\dot{Q}}{4\pi k_T r_s^2} \; dr_s = \frac{\dot{Q}}{2\pi k_T \omega_0}. \tag{5.37}$$

For $r_s \geq \frac{\omega_0}{2}$, $\Delta T(r_s)$ is found be integrating ∇T with respect to r_s from $r_s = \infty$ to $r_s = r_s$:

$$\Delta T(r_s) = \int_{\infty}^{r_s} \nabla T \; dr_s = \int_{\infty}^{r_s} -\frac{\dot{Q}}{4\pi k_T r_s^2} \; dr_s = \frac{\dot{Q}}{4\pi k_T r_s}. \tag{5.38}$$

Therefore, the variation of $\Delta T(r_s) = T(r_s) - T_{amb}$ with respect to r_s (the radius of the sphere) is:

$$\Delta T(r_s) = \Delta T_{max} = \frac{\dot{Q}}{2\pi k_T \omega_0}, r_s = 0 \text{ to } r_s = \frac{\omega_0}{2}, \tag{5.39}$$

and

$$\Delta T(r_s) = \frac{\dot{Q}}{4\pi k_T r_s} = \Delta T_{max} \frac{\omega_0}{2r_s}, r_s = \frac{\omega_0}{2} \text{ to } r_s = \infty \tag{5.40}$$

where $\dot{Q}$ can be found by dividing the intracavity power by the finesse, in our microcavity $\dot{Q}$ is around 50 *watts* (the amount of heat that is transferred per unit of time.) According to the temperature gradient and (5.32), the thermophoretic velocity depends on the position of the particle through the cavity.

Recall that the thermophoresis creates a thermophoretic velocity that forces the

particle to cold areas. The cold area is the area out of the cavity. The temperature in the cavity is maximum because of the laser power. Figure 5.4 shows a volcano shape which means we don't have any temperature changes through the antinodes.

According to (5.36), and Figure 5.4, the thermophoretic velocity is zero in the optical waist area. Consequently, the thermophoretic velocity affects the potential energy contour by creating a volcano shape over the boundary of the beam waist and the cavity region. Figure 5.5 describes how the optical potential is changed by considering the thermophoresis model. Note that the temperature gradient is zero through the cavity. The thermophoretic force is proportional to $\frac{1}{r^2}$ (temperature gradient), then by calculating the integral over the position of the particle r, it is evident that the thermophoretic energy is proportional to $\frac{1}{r}$. The potential energy is changed out of the beam waist and the cavity by considering the thermophoretic energy.

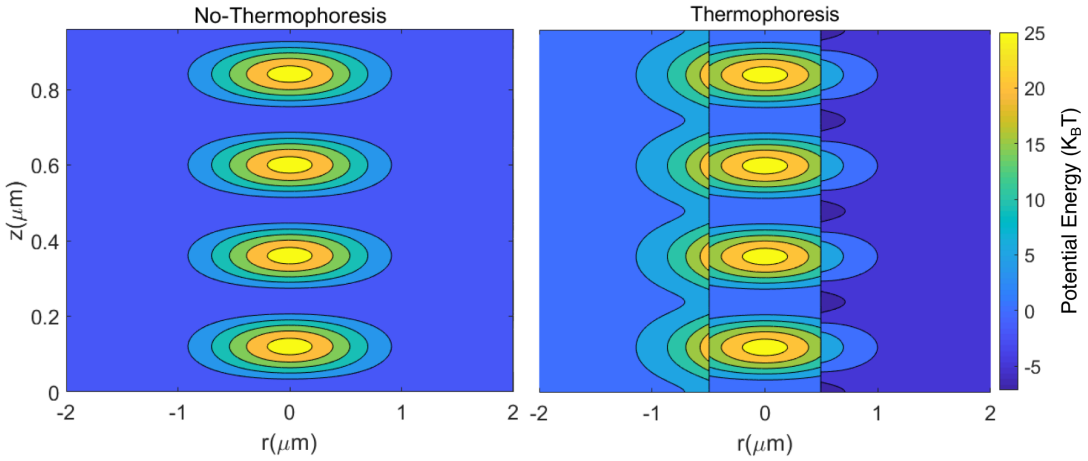


Figure 5.5: Thermophoresis effect on the potential energy (based on cylindrical model) when a polystyrene particle with diameter of 100 nm is in the cavity with RoC of 25 μm.

Finally, the thermophoretic effect on the Monte-Carlo model can be described as:

$$\gamma \frac{dr(t)}{dt} = F_{Opt(t)} + F_{thermophoresis} + \sqrt{2K_B T\gamma}\, W + \gamma v_x \tag{5.41}$$

5.2.4.2 Duhr-Braun Ionic-shielding Model

This model is developed based on the local thermodynamic equilibrium. The Soret coefficient is determined as $S_T = \frac{D_T}{\mathfrak{D}}$, which specifies the magnitude of thermodiffusion (D_T) in the steady-state. The parameter $\mathfrak{D}$ is the diffusion coefficient for sphere particles that is proportional to the radius of the particle however the McNab-Meisen model is independent of particle size. The Soret coefficient is related to entropy as has been mentioned before. The thermodiffusion also depends on the Debye length and the effective surface charge. The Debye length can be expressed as a distance over which a charge is shielded by the ions in a solution [191].

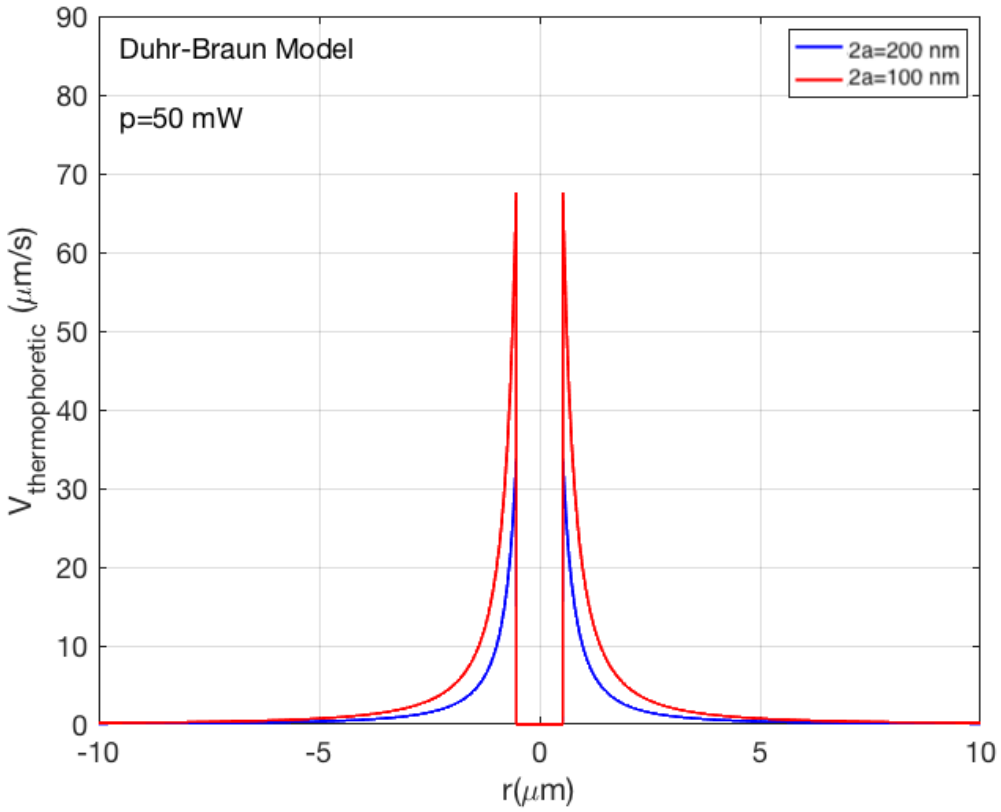


Figure 5.6: Thermophoretic velocity versus the position of two different particle sizes of 100 nm and 200 nm when the intracavity of 50 mW is assumed.

The Soret coefficient can be determined as follows

$$S_T = \frac{A}{KT}\frac{\sigma_{ch}^2 \lambda_{DH}}{4\epsilon_r \epsilon_0 T}, \tag{5.42}$$

where effective surface charge σ_{ch} and Debye length λ_{DH} can be obtained by

$$\sigma_{ch} = \frac{\eta\epsilon_0\epsilon_r(1+\frac{a}{\lambda_{DH}})}{a}, \tag{5.43}$$

$$\lambda_{DH} = \sqrt{\frac{\epsilon_0\epsilon_r KT}{e^2 N_A I_i}}, \tag{5.44}$$

where I_i is the ionic strength of the electrolyte, which the hydronium concentration is 1×10^{-7} M for pure water at room temperature and N_A is the Avogadro number. Therefore, the thermophoretic velocity in this model can be achieved by

$$V_T = -D_T \nabla T. \tag{5.45}$$

The thermophoretic velocity in this model is shown in Figure 5.6. The maximum thermophoretic velocity is about 1.2 times smaller than the thermophoretic velocity in the McNab model. Furthermore, note that the thermophoretic velocity is dependent on the size of the particle in the Duhr-Braun model. By increasing the particle size, the thermophoretic velocity is decreased.

5.3 Particle Trajectory

In this section, the developed model allows to observe and analyze the trajectory of the particle through an open-access microcavity. Figure 5.7 shows three trajectories of a polystyrene (PS) particle with diameter of 200 nm. We firstly determine the behavior of the PS particle when it travels through the flow cell with two velocities; Figure 5.7a displays the path of a particle with a flow rate of 1 $\mu m/s$ where the

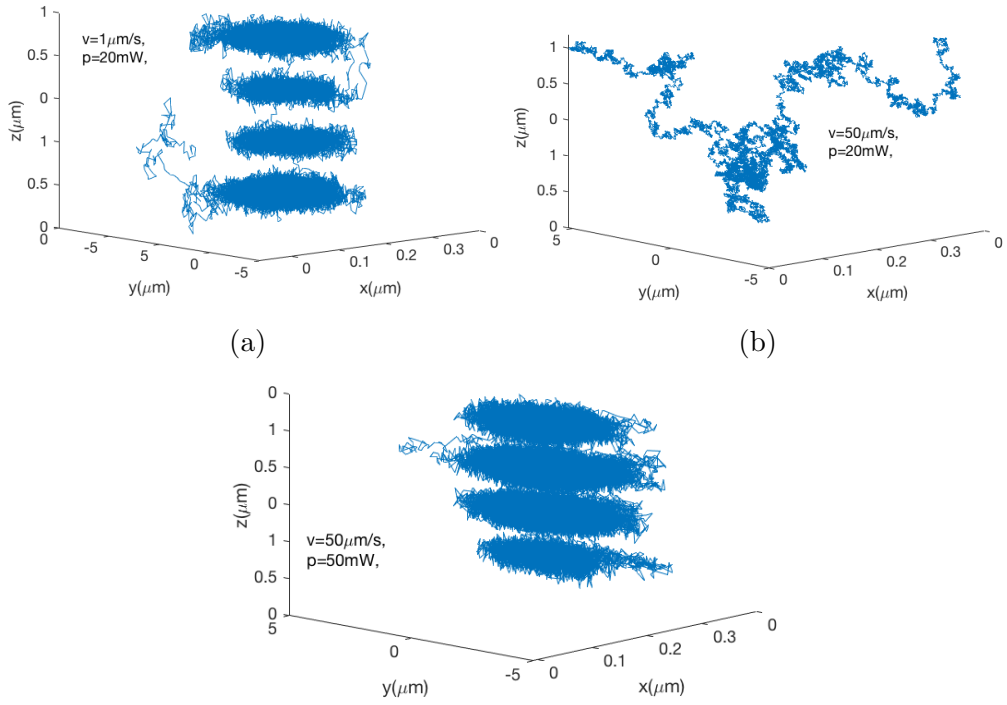
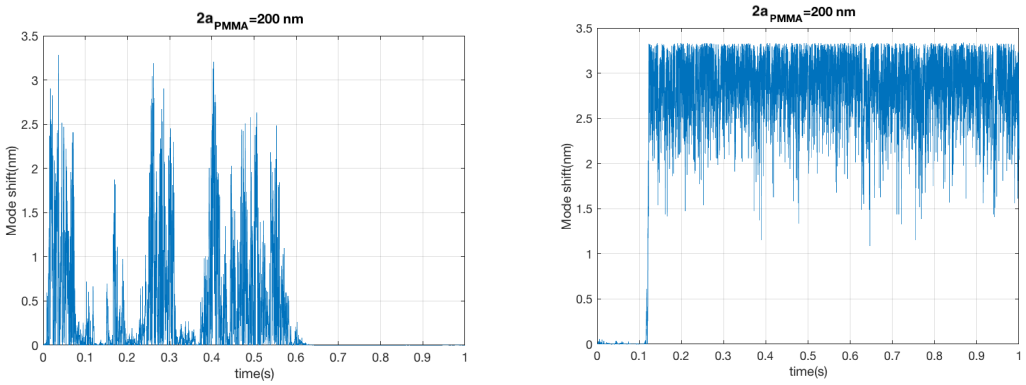


Figure 5.7: The trajectory of a PS spherical particle with diameter or size of 200 nm in an open-access microcavity with the intracavity laser of 20 mW and two flow rates: (a) 1 $\mu m/s$ which the particle is trapped through the antinodes and (b) 50 $\mu m/s$ which the particle has escaped from the cavity, (c) the particle is trapped by increasing the laser power to 50 mW.

laser power is 20 mW, while Figure 5.7b shows the trajectory of the particle with the velocity of 50 $\mu m/s$ in which the particle has escaped from the cavity and is swept rapidly downstream. The assumed laser beam has a Gaussian shape with a beam waist of 560 nm (according to the RoC of 4 μm) and a wavelength of 640 nm. Further, the profile of the flow is linear. Figure 5.7c presents the particle with the same flow rate of Figure 5.7b but the power of the laser is increased to 50 mW which causes the particle to be trapped by the optical antinode when the intracavity power is increased.

The mode shift can be studied by the particle trajectory since the mode shift is proportional to the intensity $I(r)$. We discussed how a nanoparticle creates the optical mode shift through the cavity in Section 3.6 of Chapter 3. Figure 5.8 shows



(a) (b)

Figure 5.8: The mode shift of a PMMA particle with size or diameter, $2a_{PMMA}$ of 200 nm for two intracavity powers of (a) 2 mW with which the particle is diffused and then escaped from the cavity, and (b) 10 mW under which the particle is trapped through the cavity more than 850 ms.

mode shifts of a spherical Poly(methyl methacrylate) PMMA nanoparticle that is diffused through the cavity. The size or diameter of the PS nanoparticle is 200 nm. Two different intracavity powers of 2 mW and 10 mW are assumed here. This figure illustrates how optical power can affect particle behavior through the cavity. By studying the maximum mode shift against the time in this example, we can learn the trap time duration of the particle, namely how long the particle stays through the cavity with respect to these two powers.

Here we study PMMA particles through the cavity to show that the developed Monte-Carlo is able to investigate particles with a different refractive index as we will show the measured PS and PMMA particles in the experimental chapters. Figure 5.8a presents the mode shift of the PMMA particle with the intracavity power of 2 mW. As it can be seen, the particle is diffused through the cavity and then escaped from the cavity because the mode shift has become 0 after 630 ms. When the intracavity power is not enough to hold the particle, then the particle is just diffused through the optical modes (Figure 5.8a). By increasing the intracavity power, the trap chance of the particle is increased. Figure 5.8b shows the mode shift against the time when the intracavity power is 10 mW. According to the

optical mode shift presented, the particle remains in the optical modes for a long time which means the particle is trapped. Note that the power of intracavity is different from the incident laser in the experimental work because the intensity is not passed 100% through the cavity due to losses. The maximum optical mode shift provides important information on the polarizability of the particle as its relationship is shown in (3.47) in Section 3.6 of Chapter 3.

5.4 Diffusivity Particle

As we explained how the existence of a nanoparticle in the cavity can change optical modes in Section 3.6 of Chapter 3, this section demonstrates how a maximum mode shift induced by a particle changes under different conditions such as the physical parameters of the cavity and different laser powers. The maximum mode shift is a statistical estimate of nanoparticle polarizability. We assume that a solution of $10,000$ nanoparticles is delivered through the cavity with the velocity of v. In the following, all of the numerical simulations of maximum mode shift are based on the realistic model (Gaussian optical modes with a small divergence) and by using the stochastic Monte-Carlo model.

The trajectory of each particle is simulated for 1 s and the simulations are based on a small time-step of 10^{-5} s. In other words, the simulation frequency is 100 KHz. However, this value of the time step will be deeply investigated later.

Recall that two models of optical modes can be studied in the Monte-Carlo model to show the particle behavior through the cavity (Section 3.5 of Chapter 3). The maximum mode distribution is compared between these models when 200 nm (diameter) PS particles are introduced in the cavity in Figure 5.9 where the laser power is 20 mW.

In the cylindrical model, the modes have an identical intensity profile while

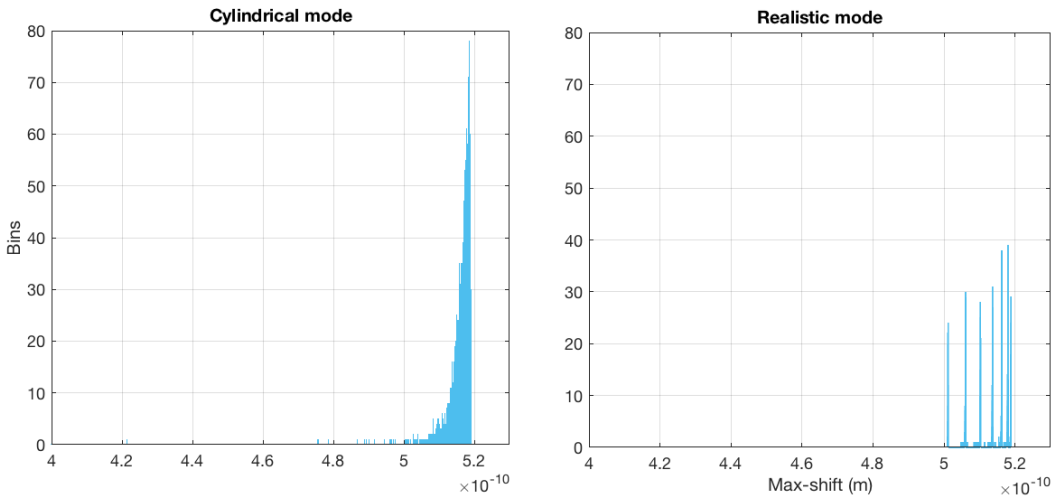


Figure 5.9: Maximum mode distribution of PS particles with the size of 200 nm in cylindrical and realistic models when the intracavity power is 20 mW.

in the realistic model, the optical intensity is gradually decreased by increasing the length of the cavity then it results from a small divergence. The mode shift depends on the optical intensity, therefore, the difference between these models makes the inequality in maximum mode shift distribution. However, note that the value of the mode shift is the same in these models.

Figure 5.10 explains the relationship between the optical intensity with the optical mode shift. Figure 5.10.a shows optical intensity distribution through the cavity and Figure 5.10.b is maximum mode distribution. Figure 5.10.c is zoomed in version of Figure 5.10.b. According to Figure 5.10.d (that is Figure 5.10.a but it is rotated 90 degrees) and Figure 5.10.c, the position of each optical mode matches with the maximum mode shift (refer to (3.46) in Section 3.6 of Chapter 3). Note that, in this example, the optical intensity and the maximum mode shift distribution for the assumed particles are normalized and shown by I_N and $Max\text{-}shift_N$, respectively.

Next, the time step effect is studied as shown in Figure 5.11. We study the maximum mode shift distribution of the PS particles with the diameter of 200 nm, ($D = 2a = 200\ nm$), and three intracavity powers of 0, 5, and 20 mW with a

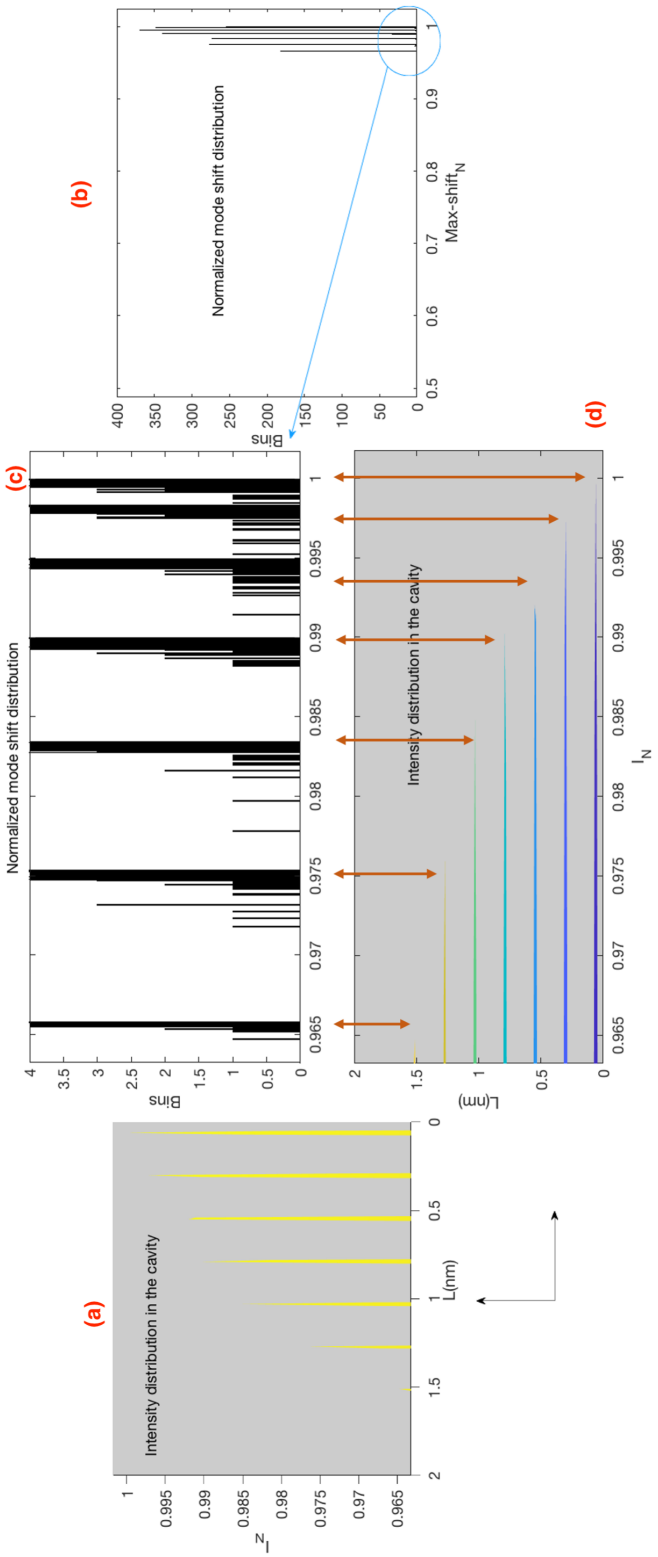


Figure 5.10: Relationship between the optical intensity and the maximum mode shift. The mode shifts of PS particles with the size of 200 nm are calculated here.

microcavity with the radius of curvature of 25 μm. This mirror provides a Gaussian beam with a waist of 1.1 μm (according to the relationship between RoC and beam waist, see (3.42)). In Figure 5.11, the x and the y axes are the maximum mode shift and the number of particles, respectively.

The maximum mode shift distribution is changed by decreasing the time step. In real-word, the time is not discrete, therefore we need to use the possible smallest time step in the simulation. Thus, a reasonable time step is important to see a convergence towards a constant distribution in the simulation. According to Figure 5.11, the maximum mode shift distribution converges towards a constant distribution in the small time steps.

Therefore, a small-time step has more accuracy to simulate the experiment. In the small-time step, the convergence test in maximum mode shift distribution is passed and the histograms seem to all have the same distribution when using a small-time step (Figure 5.11). In this section, the time step of 40 μs is selected due to the limitation on the PC memory.

The maximum mode distribution of particles can be affected by the optical power and particle size changes. In the following, optical beam waist, flow rate, trap time duration, and shape of the cavity are studied to see their effect on diffusive particles through the cavity, the maximum mode shift, and the resolution of the characterization technique.

5.4.1 RoC Effect

Figure 5.12 illustrates the maximum mode shift distribution for PS particles with diameters of 100 nm to 300 nm and the intracavity powers of 0 mW to 8 mW where the RoC of the cavity is 25 μm. In Figure 5.13, the maximum mode shift distribution is normalized to have an easier comparison. This is equal to a beam waist of 1.129 μm. In Figure 5.12 the data for the nanoparticles of different radii are

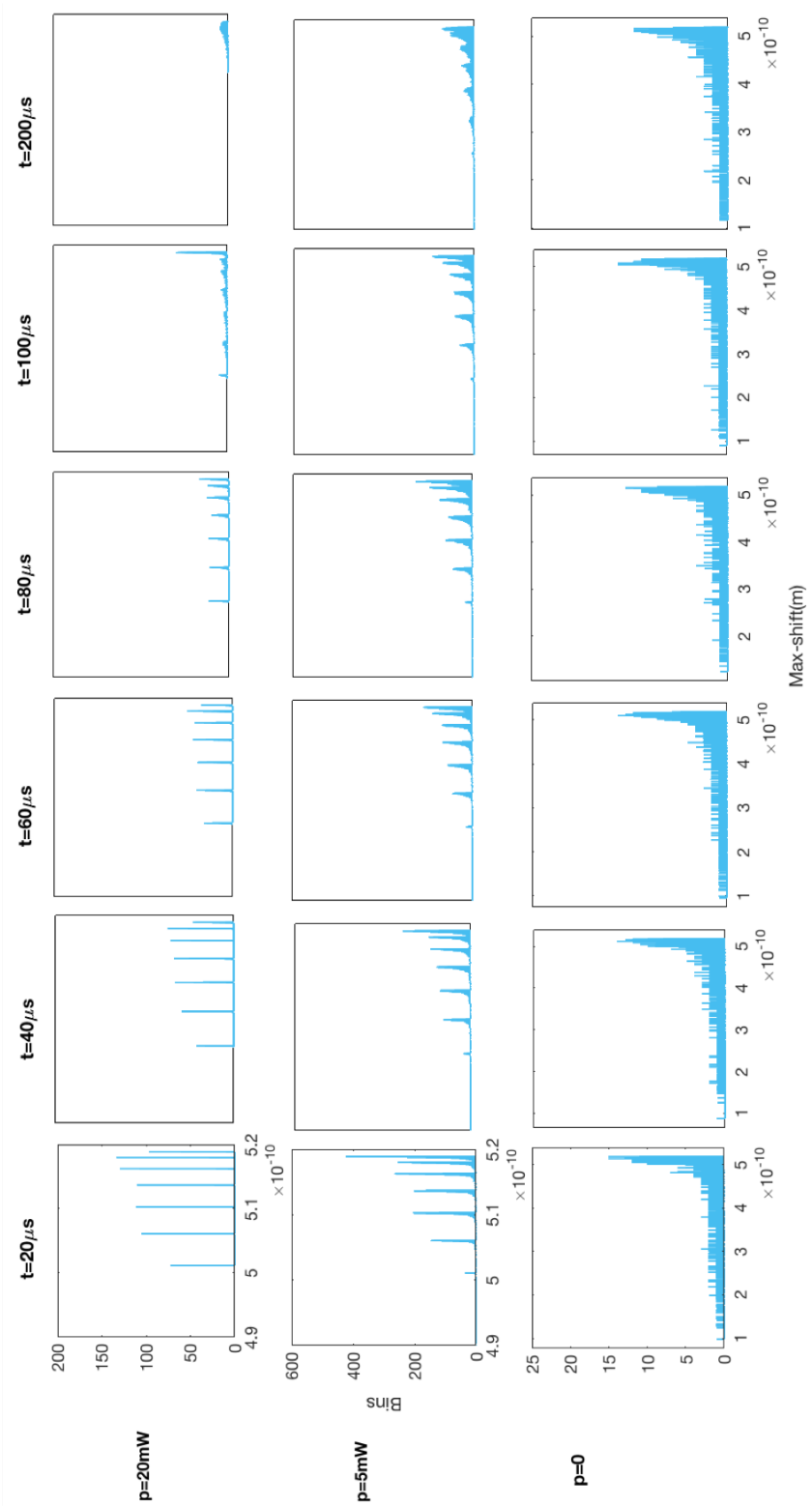


Figure 5.11: Maximum mode distribution simulated for 200 nm PS particles ($D = 2a = 200\ nm$) for different time steps and intracavity powers.

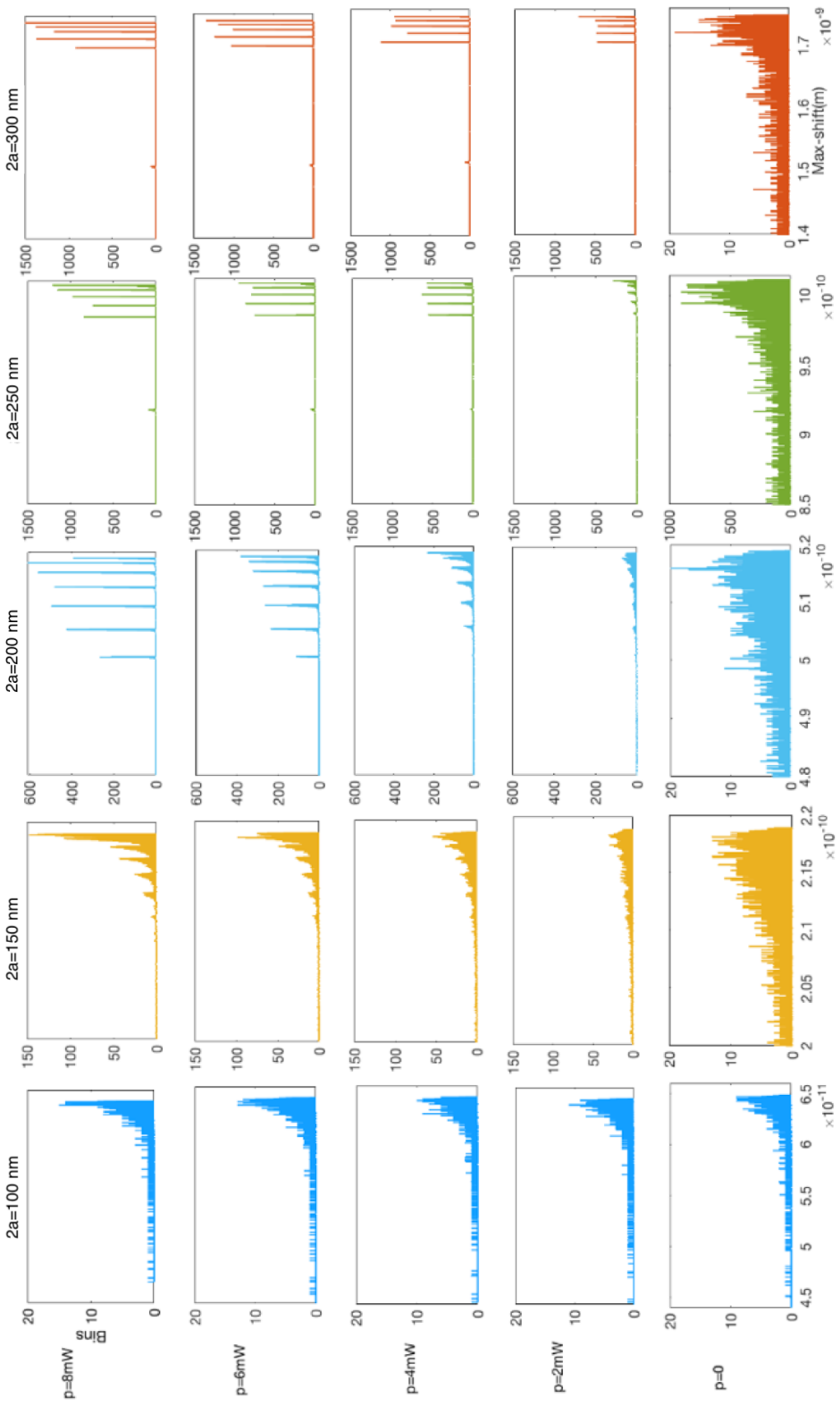


Figure 5.12: Maximum mode distribution with respect to the intracavity power and the size of the particle when the RoC is 25 μm.

now considered. The maximum mode shift (Max-shift) as a function of laser power in the microcavity is illustrated in these experiments. It can be observed from this data that the largest particle studied with a diameter of 300 nm is trapped in the cavity when the laser power is 2 mW. The particles with smaller sizes require higher intracavity powers to be trapped. The maximum mode distribution and shifts vary as a function of the nanoparticle size.

By increasing the laser power and the size of the particle, the number of trap events is increased as it can be observed in the y axis. Graph of the PS nanoparticle with diameter of 200 nm and power of 2 mW shows that the majority of particles are just diffused through the cavity. Although by increasing the laser power (e.g. to 8 mW) the number of the trap events is increased through the optical modes. Note that by increasing the size of the particles, the trap events are increased as well. Consider the same configuration ($D = 2a = 200\ nm$, $p = 2\ mW$), where we observe that by increasing the particle diameter to 300 nm, the power of 2 mW is enough to trap the large particles.

By selecting a concave mirror with a small RoC, it is thus demonstrated that the efficiency for trapping particles in the microcavity is increased. According to (3.42), the beam waist is proportional to the RoC and the length of the cavity, and thus because the RoC impacts the size of the beam waist it will also define the force on the nanoparticle in the microcavity. In Figure 5.13, we present the maximum mode distribution of different PS particle sizes with the various powers when the RoC is decreased to 5 μm. The PS particles with diameter of 200 nm are introduced into the open-cavity Fabry-Pérot interferometer and trapped when the intracavity power is 2 mW or greater. In comparison with Figure 5.12, the number of trapped particles is increased while the power and size are the same in these experiments. As noted before, the RoC of the concave mirror impacts the geometry of the laser beam within the microcavity. This impacts the field gradient

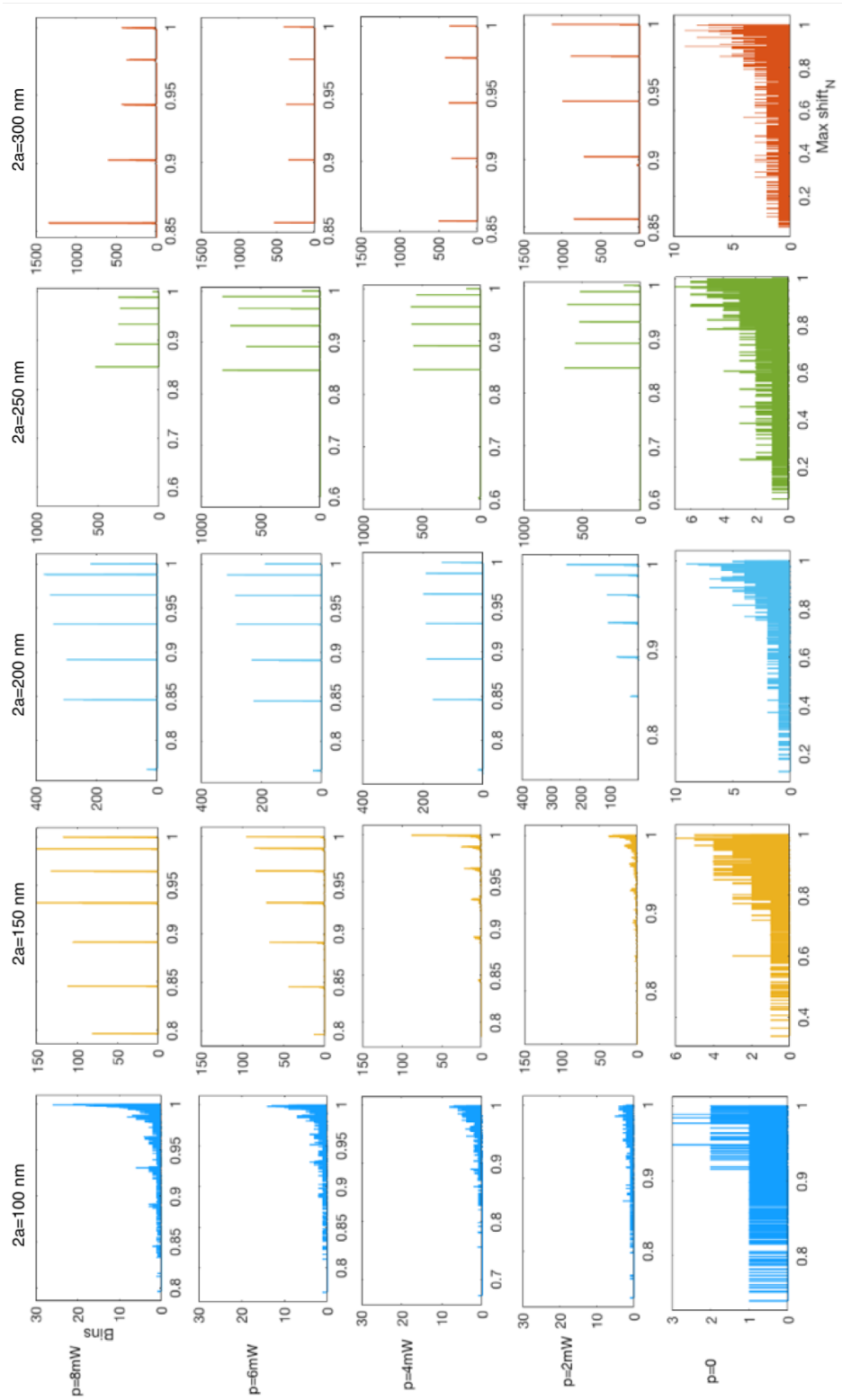


Figure 5.13: The normalized Maximum mode ($Max - shift_N$) distribution for the intracavity power and particle size when RoC is 5 μm or the beam waist is 693 nm.

and thus the trapping of nanoparticles is a function of RoC.

5.4.2 Flow Velocity Effect

Additionally, we study the effect of the flow rate or particle velocity in the cavity (Figure 5.14). The interactivity power is assumed to be set to 8 mW and the RoC is 25 μm. It is evident that a high flow rate causes a decrease in the number of the trap events and then the maximum mode shift distribution gets broader.

The maximum mode shift for particles of diameter between 100 and 300 nm as a function of the flow velocity in the x-direction is shown in Figure 5.14. Recall the $\textit{Max-shift}_N$ in the x axis represents the normalized maximum mode shift in this simulation result. The data when compared illustrates that the nanoparticles are not effectively trapped when the flow velocity is 30 $\mu m/s$. Only particles with diameter of 300 nm are trapped at this velocity and rather inefficiently. From the Figure 5.14 we observe that the maximal mode distribution varies as a function of both the particle size and also the flow velocity in the x-direction. Let us consider particle diffusion when the PS particles have the diameter of 200 nm and the velocity of 30 $\mu m/s$ in comparison with the same size particles but with a lower flow speed of 10 $\mu m/s$. It can be observed that by increasing the flow velocity, the probability of particles being trapped is decreased.

5.4.3 Trap Time Duration

According to the particle size and the intracavity power, the trap time of a particle can change the maximum mode distribution as well. The trap time acts as a filter to limit the number of events. Therefore, the number of the trapped particles can be changed by applying the time filter, denoted by τ.

Figure 5.15 shows two histograms of the normalized maximum optical mode shift for polystyrene particles with diameters of 100 nm, 200 nm and 300 nm where

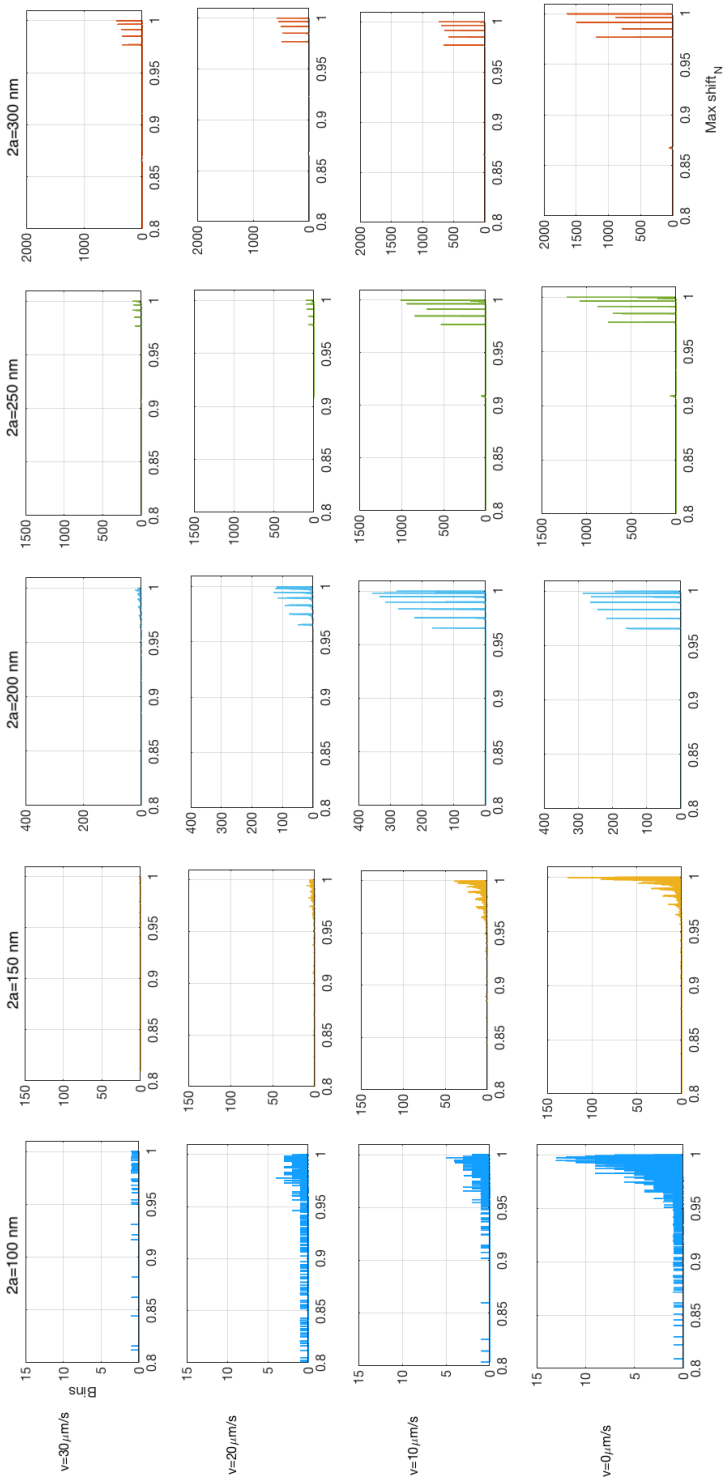
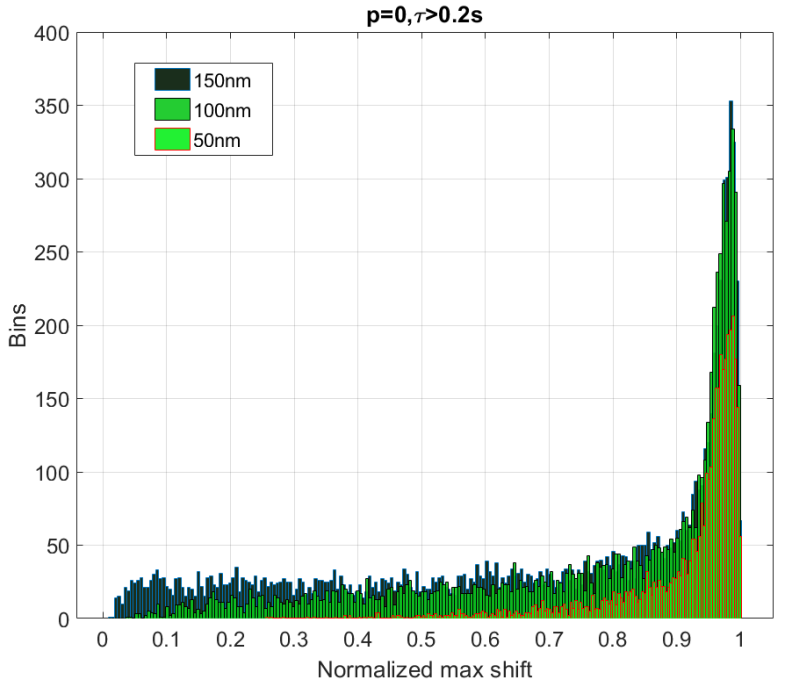
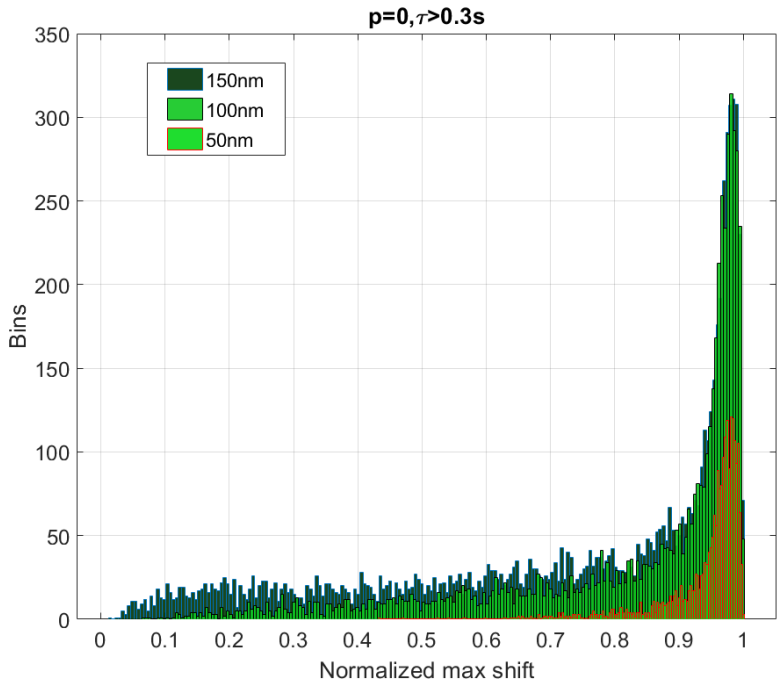


Figure 5.14: Normalized maximum mode shift ($Max - shift_N$) distribution with respect to the flow velocity in the x direction and particle size with RoC 25 μm.



(a)



(b)

Figure 5.15: Simulation results of two trap time durations as a filter; particles diffuse in the cavity more than (a): 200 ms and (b): 300 ms.

the interactivity power (p) is assumed to be negligible, i.e., $p = 0$. The filters (τ) of 200 ms and 300 ms are applied in this simulation. The filter essentially

means the events longer than 200 ms and 300 ms are counted in the figure. In other words, the particles that stay through the optical modes at least for 200 ms (see Figure 5.15a) and 300 ms (see Figure 5.15b) are only considered as trapped. Additionally, the width of the mode shift distribution is expanded due to the short filter. Nanoparticles do not need high optical force to stay in the cavity for a short time. Therefore we expect to have more trap events in the easy trap situation, i.e. when the timer filter is shorter.

5.4.4 Shape of Cavity

The shape of the cavity can also change the mode shift distribution and consequently, the resolution of the characterization technique. We study a flat hat model of microcavity in this section. Note that this model cannot be made in practice at the moment. However, it helps to indicate what is driving the linewidth of the measurement. Figure 5.16 shows the cavity with a different shape in which the optical modes are formed as a rectangular shapes through the cavity. The light intensity is propagated through the cavity as

$$I = I_0 \sin^2(\frac{2\pi z n_{med}}{\lambda})(erfc(\frac{r-\omega_0}{\omega_0^2}) - erfc(\frac{r+\omega_0}{\omega_0^2})). \tag{5.46}$$

False color-scale plot of the normalized optical intensity distribution in the flat hat and the concave microcavities with 7 optical anti-nodes are shown in Figure 5.16. According to this form of intensity, the optical force is acquired by using (5.1) and (5.2). Then the particle diffusion is studied in the flat hat cavity to see the effect of the shape of the cavity on the particle distribution. The linewidth of maximum mode distribution in the flat hat model is narrower than the concave mirror (Figure 5.16.right).

For making a fair comparison, the length of the cavity, the power of the laser, and the beam waist are identical in the flat hat and the concave mirrors (concave

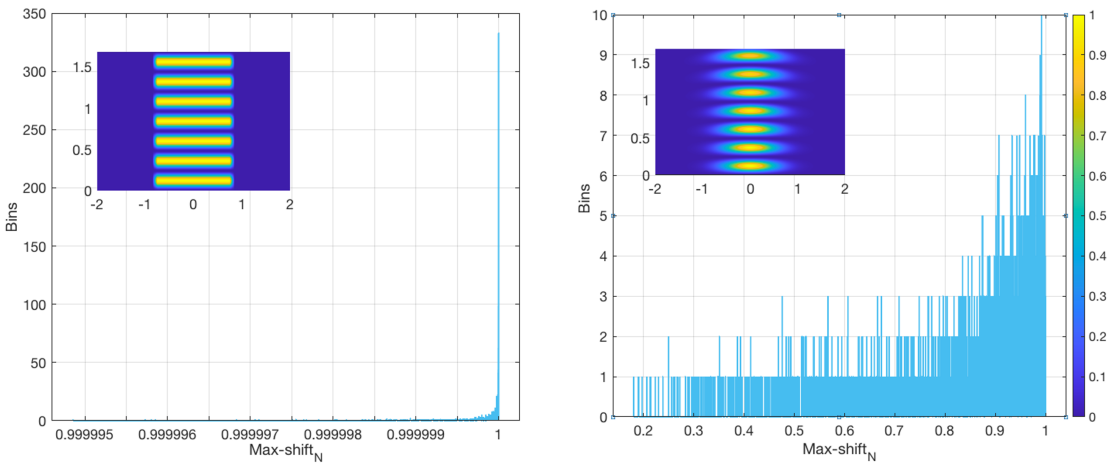


Figure 5.16: The normalized maximum mode shift distribution is compared in the flat hat and the concave cavity for PS particles with diameter of 200 nm where the color scale bar denotes the normalized optical intensity for both cavities.

mirror has RoC of 8 μm which means that the beam waist is 800 nm). Namely, the situation of these two simulations is kept the same. We assume the optical power is below the trapping threshold for particles with diameter ($D = 2a$) of 200 nm. The linewidth of the histograms demonstrates the resolution of the cavities. Figure 5.16.left shows the resolution of the nanoparticle characterization that can be improved by engineering the shape of the cavity as it is compared to the concave mirror.

5.5 Particle Delivery Based on Pressure-driven Method

The flowing fluid can be introduced into the flow cell via pressure-driven method. In this project, the pressure is used as the delivery method however this causes the velocity through the flow cell and microcavity to be non-linear. The velocity is expected to have a parabolic flow profile when the pressure is employed for

delivering the fluid in the flow cell. In the experimental work, the ELVEFLOW system [179] is installed and the initial pressure (input pressure) can be adjusted and by using the hydraulic rules the velocity of flow can be estimated.

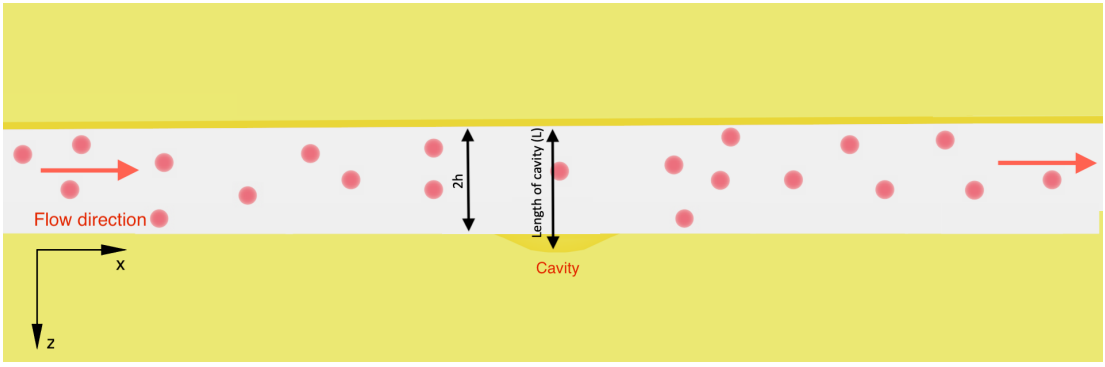
The velocity of the nanoparticle through the cavity with respect to the dimension of the flow cell and the initial parameters such as the input pressure is calculated by COMSOL. Further, we have compared the obtained results from COMSOL simulations to analytical results. Note that for characterizing nanoparticles under the flowing fluid, we use microcavities that are milled on the ridge instead of the plinth. In this section, the pressure-driven flow is investigated and then the particle velocity is studied by using analytical and numerical methods.

Using pressure as the delivery method creates several challenges because of the parabolic flow profile. Nevertheless, in order to have a realistic model, in the following we assumed a parabolic flow. Therefore, for studying the effect of the flow as a Poiseuille flow in this work, we have assumed a steady flow between two parallel plates with a distance of h. One plate is placed at $z = h \approx \frac{L}{2}$ and the other one is located at $z = -h \approx \frac{L}{2}$ where L is the length of the cavity. Note that, for estimating the flow velocity through the cavity, we assume the $2h$ is equal to the length of the cavity (L) see Figure 5.17a.

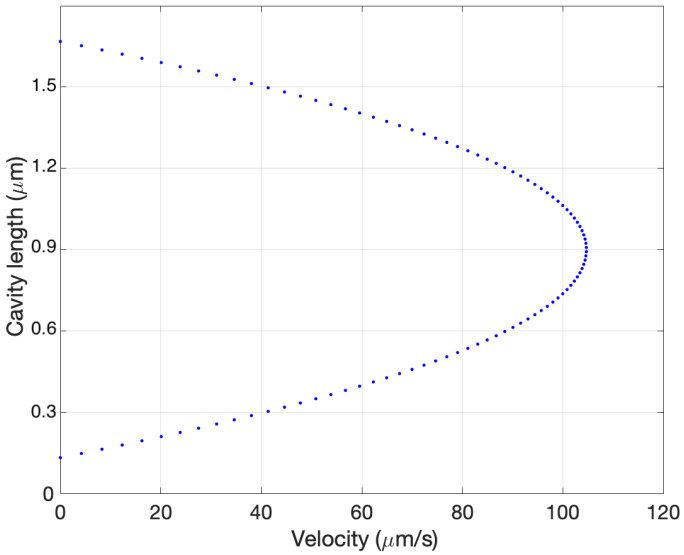
In this delivery method, a gradient of pressure in the x direction creates the flow. We assume that the velocity and pressure are independent of time and the velocity has one component u_x. For the sake of simplicity, we may denote u_x as u. According to Navier-Stokes equations we have [192]

$$\frac{\partial u}{\partial t} + (u.\bigtriangledown)u = -\frac{1}{\rho} \bigtriangledown p + \frac{\eta}{\rho} \bigtriangledown^2 u, \tag{5.47}$$

where ρ, u, and η are fluid density, the fluid flow average velocity, and dynamic viscosity, respectively. For solving this equation we need to apply the boundary



(a)



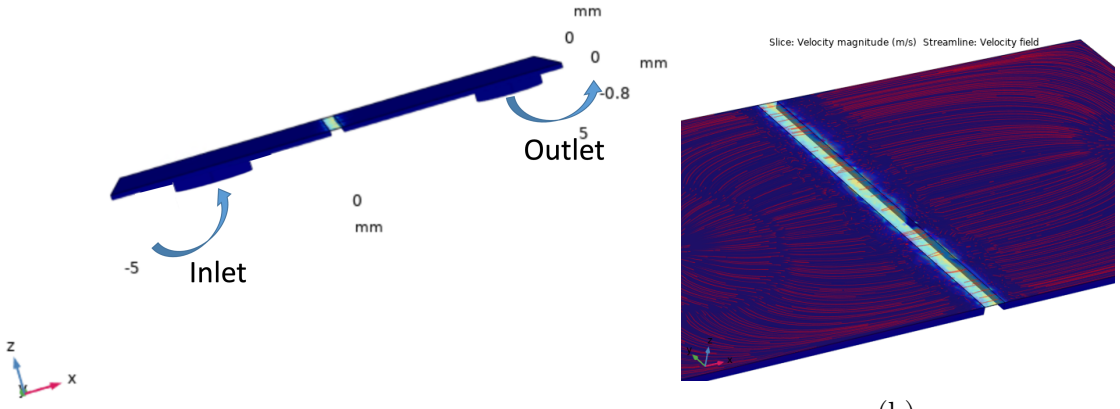
(b)

Figure 5.17: (a) A close-up of the fluidic channel to show the L and $2h$. (b) Profile of parabolic flow according to the length of the cavity when RoC is $25\mu m$ and the pressure is around 4 $mbar$.

condition of $u(z = \pm h) = 0$ by a constant pressure gradient as $\bigtriangledown p = -P$ and consider that the flow is steady, i.e., $\frac{\partial u}{\partial t} = 0$. Due to the constant pressure gradient in the z direction we have

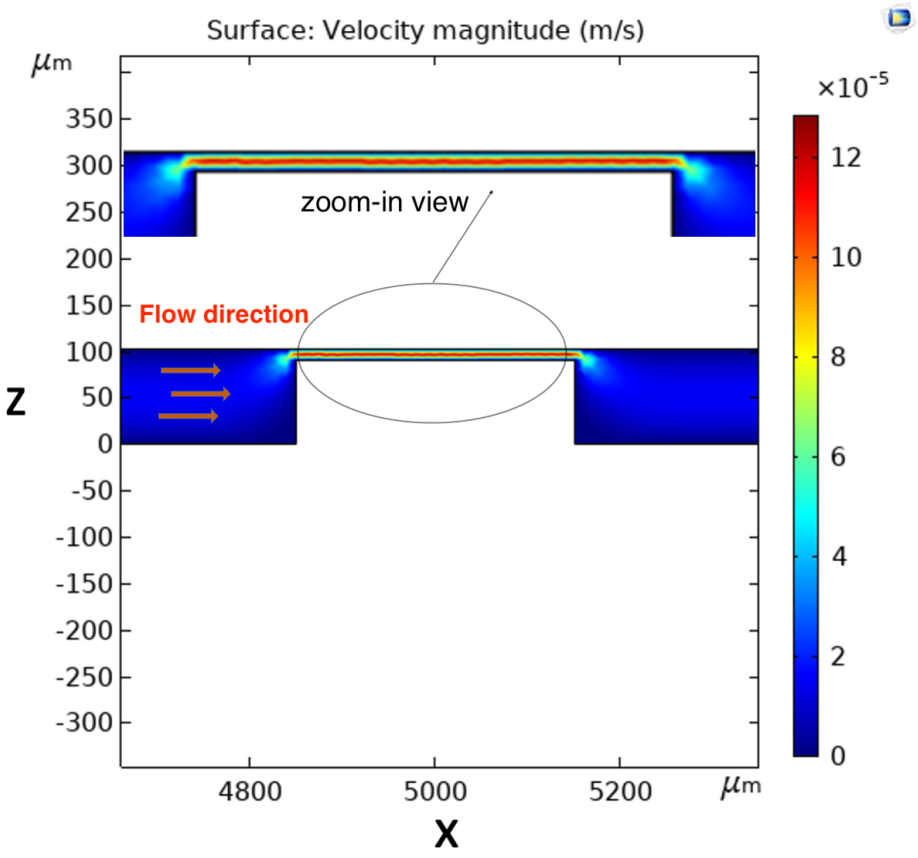
$$u = u(z). \tag{5.48}$$

Note that changes of u in x and y would need a pressure gradient in the x and the y directions. By applying the boundary conditions, the fluid flow average



(a)

(b)



(c)

Figure 5.18: (a) A COMSOL schematic of the flow cell where the cavities are milled on the ridge and the sealant has sealed the channel, (b) COMSOL simulation with the streamline flow through the channel (c) a slice view of the flow profile through the ridge in COMSOL that proves the parabolic flow through the cavity as the velocity in the center of channel is higher (red color) than the walls (light blue) in the zoomed area.

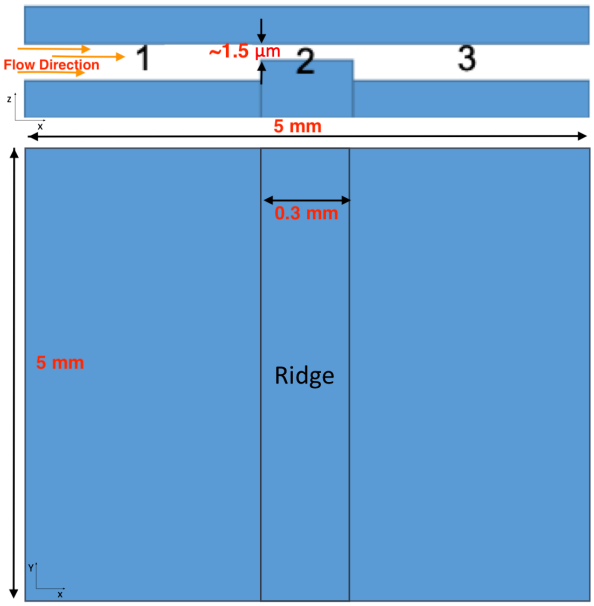
velocity (u) can be determined as

$$u = \frac{P}{2\eta}(h^2 - z^2). \tag{5.49}$$

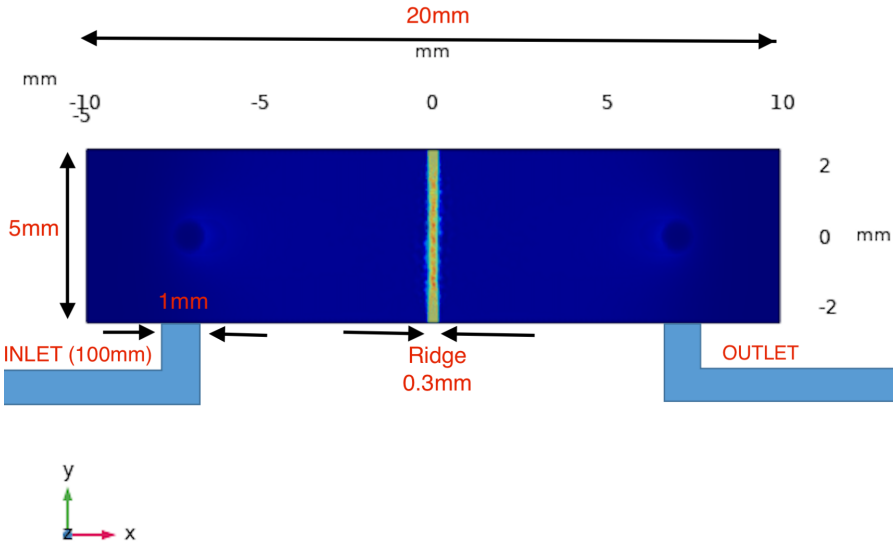
Figure 5.17b shows the parabolic profile through the channel in the x direction where the color scale bar shows the value of flow velocity. Figure 5.18a is the flow cell structure where two holes are connected to the inlet and outlet tubes. In the flowing fluid experiment, the microcavities are milled on the ridge. Figure 5.18c shows the flow velocity through the channel, the color bar is the value of flow velocity on the scale of m/s. Figure 5.18b demonstrates the channel along with the flow velocity and the streamline for the velocity field. As we expected, the velocity in the center of the channel is higher (red color) than close to the walls of the channel when pressure is 3 $mbar$ or 300 Pa. Note that the maximum velocity in the theoretical analysis and the numerical simulations (MATLAB and COMSOL) matches very well as can be seen in Figure 5.17b and Figure 5.18c. Figure 5.19a shows a side view (top figure) of the channel and a top view (bottom figure) of the ridge.

The pressure can be applied in the flow cell by a syringe pump or the ELVE-FLOW system [179] to control the flow rate or the pressure of the inlet. In our experiment, we chose to use the ELVEFLOW system to introduce nanoparticles into the microcavity. Note that the optical microcavities can be milled on a plinth (as shown in Section 4.4 of Chapter 4) and a ridge, where width, length, and height of the ridge are 300 μm, 5000 μm, and 100 μm, respectively. In the following we study the velocity of the flow when the pressure on the ridge is adjusted on 100 Pa and 500 Pa.

The flow speed is affected by hydraulic resistance and the geometry of the channel. The hydraulic resistance of each part in the ridge structure (Figure 5.19a)



(a)



(b)

Figure 5.19: (a) A side view (top figure) and a top view (bottom figure) of the ridge chip, (b) channel dimension along with the tubes size.

can be determined [193] by:

$$R_h = \frac{12\eta l}{wh^3(1 - \frac{0.63h}{w})}, \tag{5.50}$$

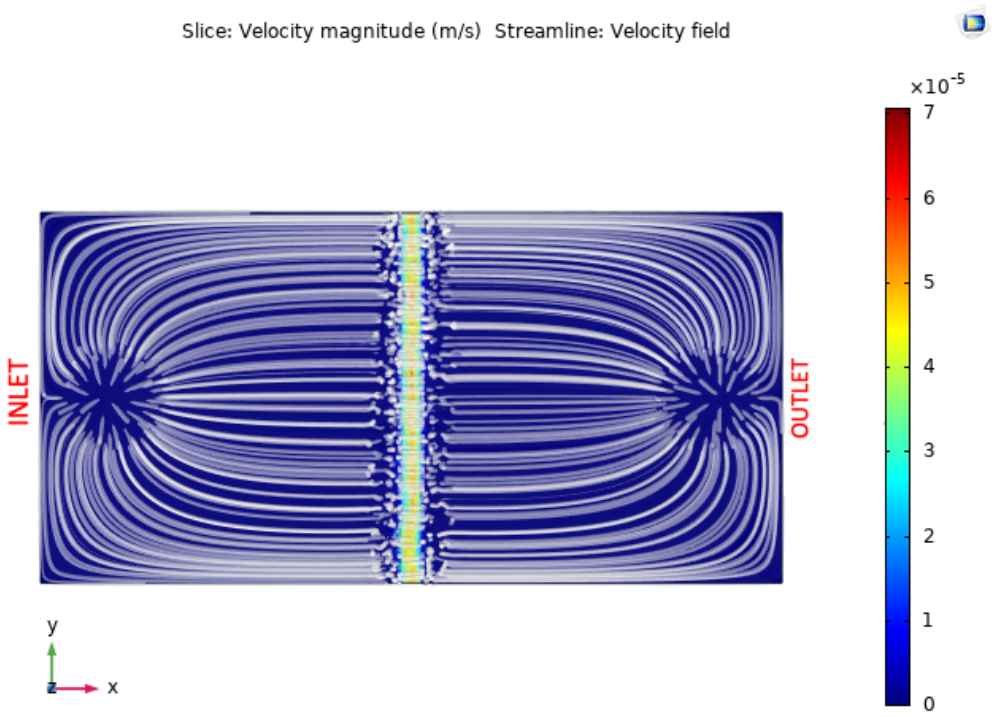


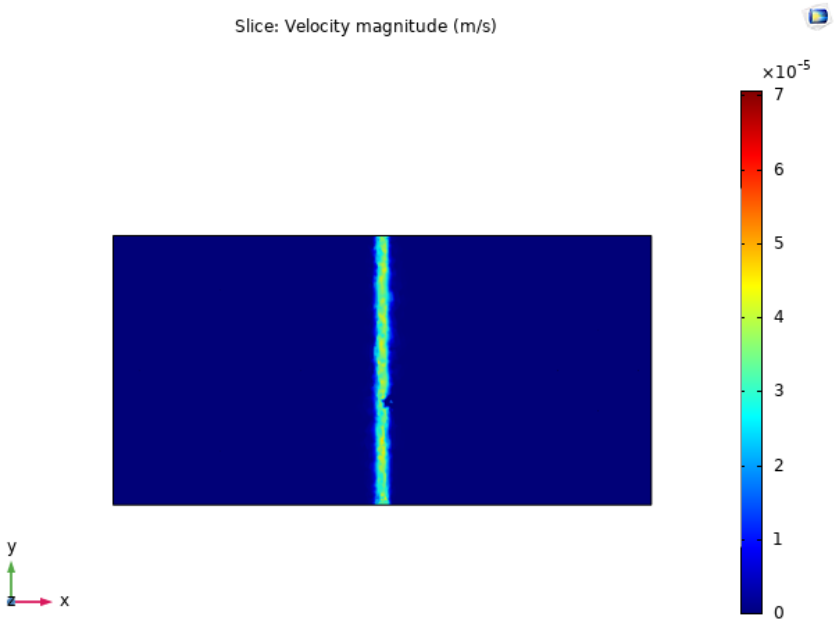
Figure 5.20: A top view of the flow cell to show the flow distribution through the channel by streamlines in COMSOL.

where l is the length of each rectangular, w presents the width of each part of the channel, and h is the height or the cavity length. The inlet and outlet tubes are channels of the circular cross-section with the hydrodynamic resistance of R_{hc}:

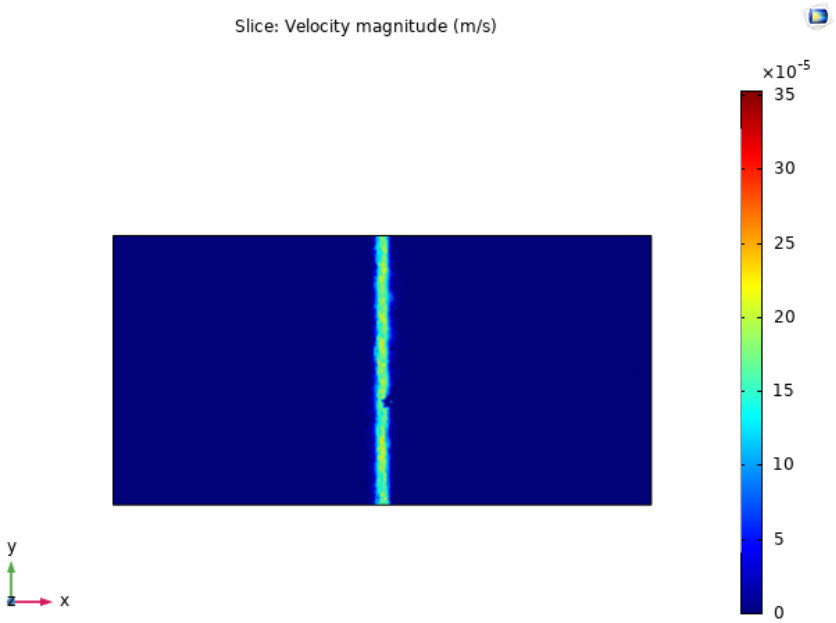
$$R_{hc} = \frac{8\eta l_t}{\pi r_t^4}, \tag{5.51}$$

where r_t is the radius of the tube and l_t is the length of the tube. The radius of the inlet and outlet tubes is 500 μm and the length of inlet and oulet tubes is 10 cm (Figure 5.19b). According to (5.50) and (5.51), we have $R_1 = R_3 = 4.4 \times 10^9(\frac{N.s}{m^5})$, $R_2 = 6 \times 10^{14}(\frac{N.s}{m^5})$ and $R_{hc} = 3 \times 10^9(\frac{N.s}{m^5})$.

Recall that the flow rate is proportional to the hydraulic resistance and the pressure, which means we can estimate the velocity of nanoparticles by obtaining



(a)



(b)

Figure 5.21: The top view of velocity (color-scale bar) through the flow cell when the pressure of (a) 100 Pa and (b) 500 Pa are applied through the ridge according to the mentioned dimension in Figure 5.19a.

the flow rate and the area of the cross-section of each channel:

$$F = \frac{\Delta P}{R_h}, \tag{5.52}$$

where F is flow rate and ΔP is pressure difference through the ridge. Two pressure values of 100 Pa and 500 Pa induce the pressure difference of 100 Pa and 500 Pa across the ridge part, respectively. The flow velocity through the ridge is determined by

$$v = \frac{F}{A_r}, \tag{5.53}$$

where A_r is the cross-section area of the ridge part or the second part of the channel. Therefore when the pressure is 100 Pa

$$F_{ridge} = \frac{\Delta P_{ridge}}{R_h} = 1.7 \times 10^{-13}\ (m^3/s),$$

and

$$v_{ridge} = \frac{F_{ridge}}{A_r} = 27.1\ (\mu m/s),$$

and the inlet flow rate is 1.7×10^{-13} (m^3/s) (principle of mass conservation). Similarly, the flow velocity in the ridge is 135.5 $\mu m/s$ when the pressure is 500 Pa (5 times greater than the velocity that results from 100 pa).

Not only the flow velocity is analytically calculated, but also the numerical results are also presented by COMSOL simulation. With a view to assessing pressures for the delivery of nanoparticles under laminar flow conditions a series of simulations are performed and these will now be described. Here we consider that the particle is traveling at the same velocity as the fluid. Figure 5.20 and Figure 5.21 show the flow velocity in the flow cell with the ridge design and the real dimensions to make a fair comparison with the analytical results. These figures are top views of the flow cell in the COMSOL.

The relationship between the pressure and flow velocity can be seen through the ridge in Figure 5.21. Note that when the inlet pressure is 500 atm or 5 $mbar$ (Figure 5.21b) the velocity is 5 times greater than when the inlet pressure is 100 atm or 1 $mbar$ (Figure 5.21a). The average velocity of nanoparticles through the ridge is 28 $\mu m/s$ and 137 $\mu m/s$, for pressures of 100 Pa and 500 Pa, respectively. The numerical results match with the analytical results.

5.6 Summary

We explained the fundamental theory of optical trapping and established underpinnings that will be used in later chapters. The basic structure of the open-access cavity is discussed to generate the optical modes. Then we explained how the optical modes generate optical forces to trap nanoparticles. The particle trapping is studied in a flowing fluid as other forces such as fluctuating and thermophoresis forces can overcome the optical force. Also, the maximum mode shift is investigated as a key parameter for measuring the nanoparticles. Then the physical parameters are explored to see their effect on the maximum mode shift distribution and the resolution of the characterization technique. Finally, pressure delivery method is described and theoretically studied in this chapter.

Chapter 6

Measurements at Zero Flow Rate

6.1 Introduction

As described in Section 2.2 of Chapter 2 there exists a range of methods to characterize nanoparticles such as microscopy and dynamic light scattering. However, characterizing individual nanoparticles in a fluid is challenging because the particle diffuses rapidly by Brownian motion. In this work, we overcome this problem using optical tweezers. This chapter shows that the confined optical field in a Fabry-Pérot style microcavity resonator can be used as a means for both trapping and measuring nanoparticles with high resolution. We characterize particles by recording the change in the spectral shift of the mode wavelength when the particles diffuse through the microcavity. The maximum mode displacement provides an accurate measure of the polarizability of each particle that is proportional to its volume.

We illustrate the measurement of the distribution of polarizabilities from a

Table 6.1: Summary of Reference Samples of Phosphorex Polystyrene Particles

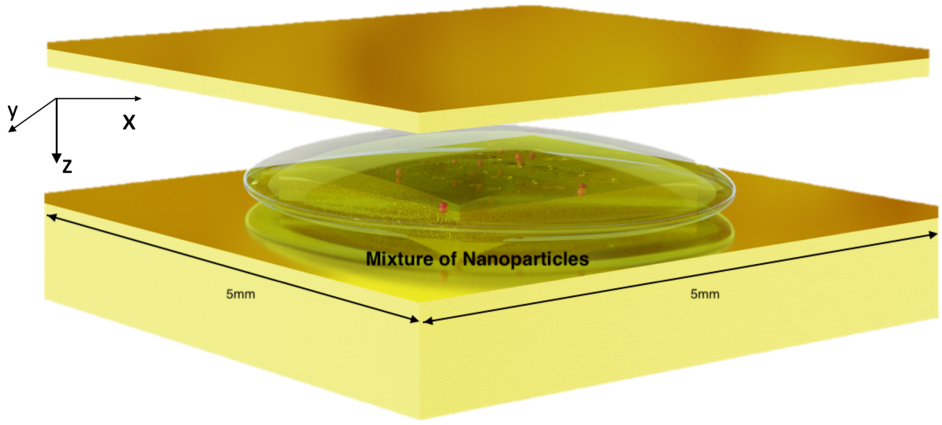
Type of Particles	Batch No.	Nominal Size (Diameter) (nm)	Actual Mean (nm)	Standard Deviation (nm)	Density of polymer ($\frac{g}{cm^3}$)	N/mL
PS	11168	50	41	8	1.05	2.64×10^{14}
PS	3048	75	75	16	1.05	4.31×10^{13}
PS	13033	100	88	11	1.05	2.67×10^{13}

solution containing a mixture of 50 nm, 75 nm, and 100 nm polystyrene particles in water (Table 6.1). As shown later three peaks are clearly visible with the ratio of displacements and in agreement with the expected volumetric scaling. This method provides a powerful tool for characterizing nanoparticles in a solution, for use in applications where high-resolution measurements are required at the single-particle level. In the following, the size distribution is investigated by simulation, and then the experimental results are presented.

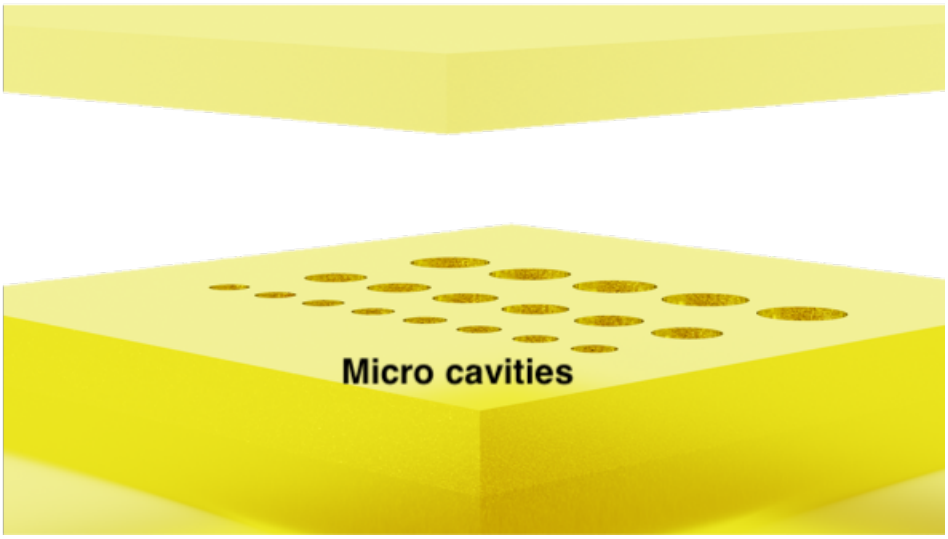
6.2 Simulation and Experimental Data

In the experiment, the designed flow cell (Figure 4.6a) as mentioned in Section 4.4 of Chapter 4 is used to allow us to introduce the sample fluid into the microcavity region whilst monitoring the cavity modes. A schematic of our open-access Fabry-Pérot microcavity is shown in Figure 6.1a where there is no flow. Specifically, the solution is reached the cavity as described in Section 4.6 of Chapter 4. The cavity comprises a planar and a concave mirror separated by a few micrometers to create a confined optical standing wave (see Section 4.3 in Chapter 4). The RoC of 4 μm is selected as the sensing and reference cavities for this experiment. Note that in this experiment, there is no flow velocity (Figure 6.1b) and the concave mirrors are milled on the plinth as shown as a schematic in figure 6.1b.

We monitor the cavity modes by scanning the cavity length through the reso-



(a)



(b)

Figure 6.1: (a) schematic of flow cell along with the mixture of three different PS particles (red spheres), (b) a close up of an array of the concave mirrors on the plinth.

nance with a fixed wavelength laser and recording the difference in mode position between two microcavities to eliminate the effects of vibration as discussed in detail in Section 4.5 of Chapter 4.

In this work, a mixture of three small PS particles with the nominal diameter of 50 nm, 75 nm, and 100 nm is studied (see Table 6.1). The PS nanoparticles are diluted in DI water to create a concentration of 10^{11} N/ml by the method explained in Section 4.6 of Chapter 4. When a nanoparticle enters the cavity the

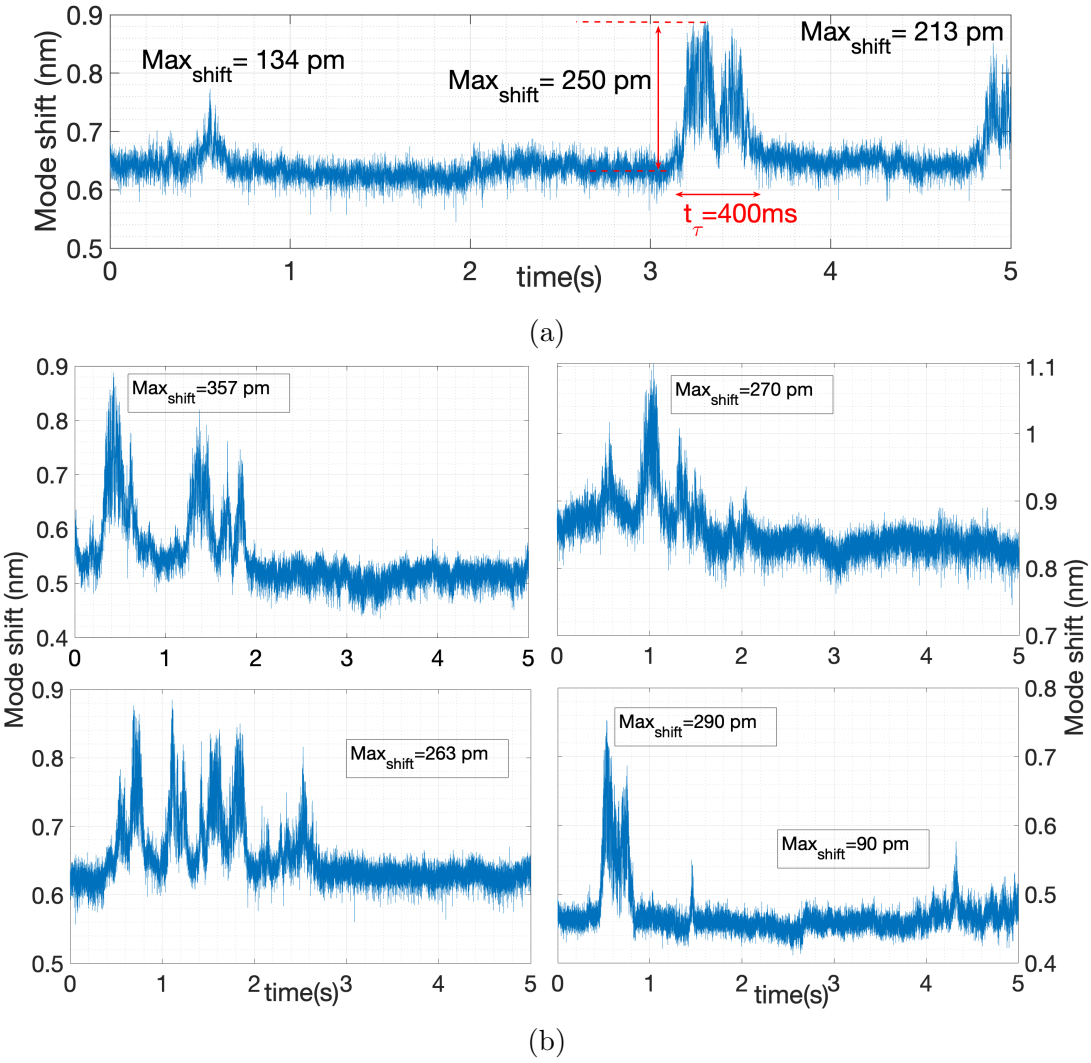


Figure 6.2: The measured maximum mode shifts of the mixture of PS particles with nominal sizes of 50, 75 and 100 nm by the microcavity with the RoC of 4 μm or beam waist of 560 nm with the length of cavity of 702 nm; (a) two different maximum mode shifts of 134 pm and 250 pm, (b) more example of mode shifts that are measured by the flow cell.

optical mode shift is measured by the polarizability of the particle in the fluid and the position of the nanoparticle within the optical mode. By determining the mode shift we can therefore measure the polarizability of the particle. The optical mode shift is proportional to the optical mode volume, and the polarizability as mentioned in Section 4.7 of Chapter 4. Note that we have calibrated the system by measuring the mode shift of PS particles with a size of 75 nm before accomplishing

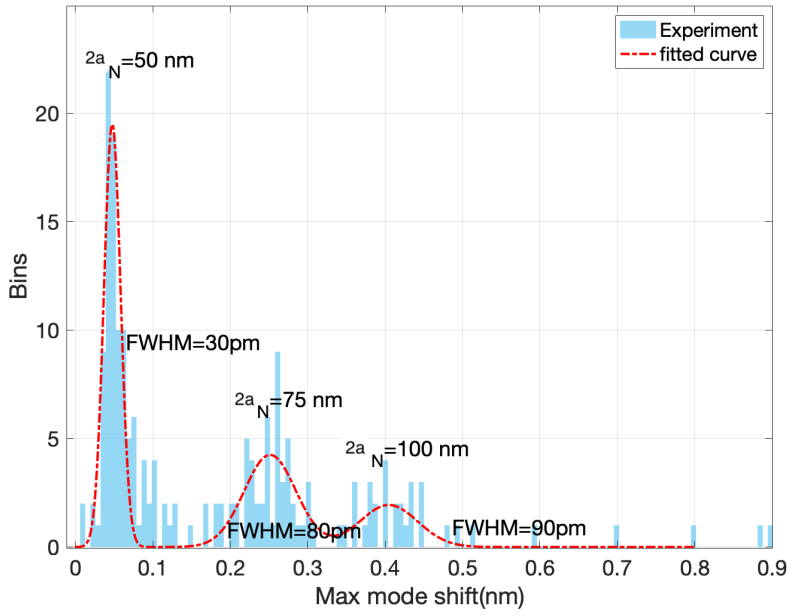
the main experiment.

The experimental data consists of a series of discrete events as individual nanoparticles diffuse through the cavity mode and are pulled to the center of the mode by the trapping forces. Figure 6.2a illustrates an example trace recorded over 5 seconds, where mode shifts of about 133 pm, 250 pm, and 212 pm can be observed. The maximum (Max) shift of 250 pm, the extended shift between 3.2 and 3.6 seconds, represents a trapped particle. The maximum mode shift provides an accurate measurement of the polarizability of the nanoparticle.

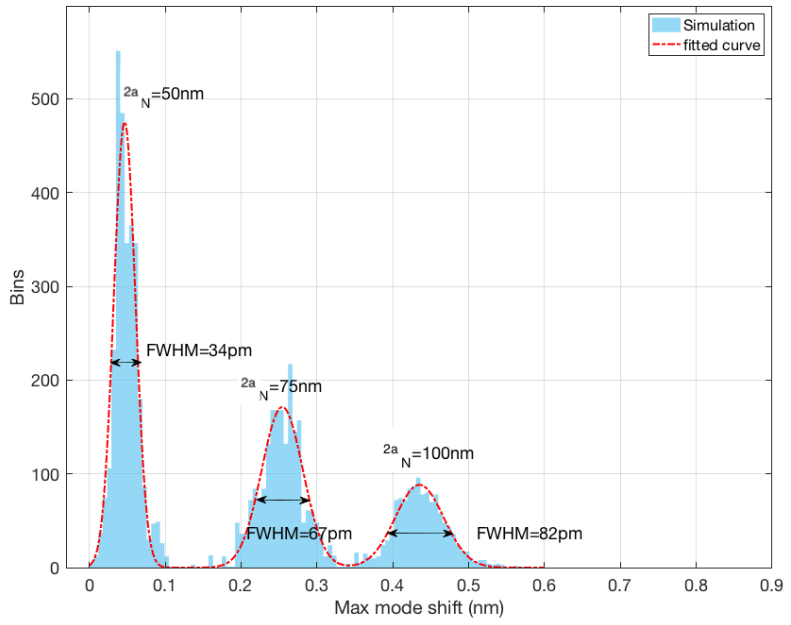
Figure 6.2b shows the examples of the optical mode shifts that arise from the polarizability of these three different nanoparticle sizes (50 nm, 75 nm, and 100 nm). Then the maximum mode shifts are studied for this solution to characterize the nanoparticles. The trap events are counted with respect to the maximum mode shift of each event and the trap time duration.

The events are recorded as the trap event if the particles stay through the cavity for at least 200 ms. It means the trap time filter duration is set to 200 ms and we count the events since the particle is diffused through the cavity at least for 200 ms. With the translated experimental data to maximum mode shift against time, we are able to count the events with the trap time duration of 200 ms. These maximum mode shifts are shown in a histogram as the key result of this chapter. Figure 6.3a illustrates three clear peaks that present the particle size distribution.

The peaks in the histograms are the maximum mode shifts for 50 nm, 75 nm, and 100 nm particles with values of 48 pm, 250 pm, and 400 pm, respectively. Note that the factory specifications for the actual mean of the particles sizes are 41 nm, 75 nm, 88 nm, and these particles are not homogeneous. Figure 6.4 shows a simulation of the manufacturer size distribution with respect to the mean and the standard deviation of each particle as in Table 6.1. It is clear that the nominal particle sizes are different from the actual size.



(a)



(b)

Figure 6.3: (a) Histograms of the maximum mode shift by the experimental data, and (b) the simulation data.

Based on the factory information, the experimental mode shifts follow the relationship between the size and maximum mode shift as predicted by (3.46).

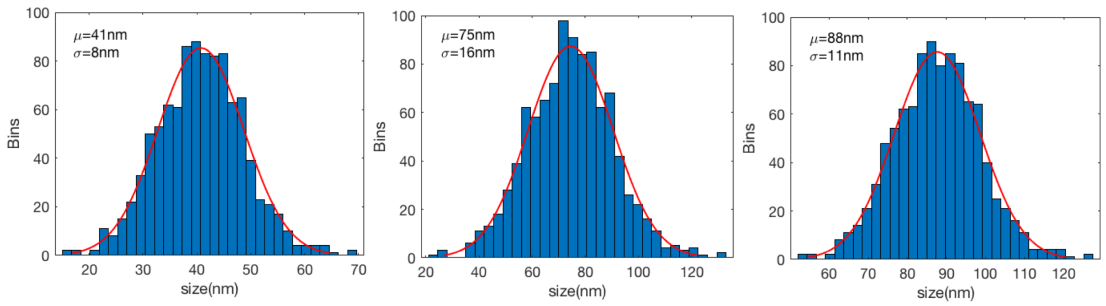


Figure 6.4: Particle size distribution with respect to the mean and the standard deviation from the factory data-sheet for nominal sizes of 50 nm, 75 nm and 100 nm from left to right, respectively.

The maximum mode shift is proportional to the polarizability of the particle, and consequently, it is proportional to a^3, where a is the particle radius. The ratio of displacements of three peaks is in good agreement with the expected volumetric scaling as it can be seen in Figure 6.3a.

A fit curve is applied to the experimental result to make a fair comparison between the experimental and the expected results. In this work we use a Gaussian fit representing normal distributions is shown by a red curve in Figure 6.3.

We conduct the simulation by Monte-Carlo model based on the realistic optical model where nanoparticles are not homogeneous and the standard deviation along with the mean of these particles are considered in our model. Additionally, the same experimental parameters (e.g., RoC of 4 μm, cavity length less than 1 μm) are considered in the simulation. Note that, in the experiment, the length of the cavity is obtained by counting the optical resonance modes through the cavity, see (3.1). For counting the optical modes, the length of cavity is firstly set to zero, namely, the flat mirror touches the patterned mirror. By gradually opening the cavity, the optical modes can be observed via the oscilloscope and the length of the cavity can be measured by (3.1). Three clear peaks can be seen in the histogram of the maximum mode shifts, corresponding to the three particle sizes. The peak positions match those measured by the experiment (Figure 6.3b).

According to the experimental data and the simulation data, we can discuss the sensitivity and resolution of this work compared with other works. To estimate the resolution of the measurements, we determine the value of Full Width at Half Maximum (FWHM) and the standard deviation (σ) of each peak. FWHM of each peak is shown in Figure 6.3. Therefore, the standard deviation (σ) of each peak can be determined by:

$$FWHM = 2\sqrt{2\ln 2}\sigma. \tag{6.1}$$

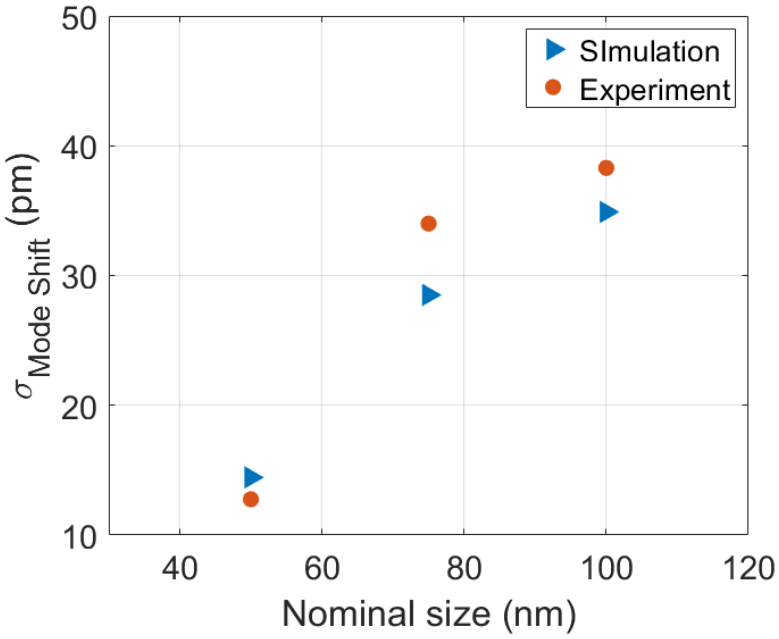


Figure 6.5: A comparison between the standard deviation of the three different particles in the measurement and the calculation of the maximum mode shift.

Figure 6.5 illustrates the standard deviation of the three peaks of the maximum mode shift in the experimental and simulation results (these are obtained from the Gaussian fit in Figure 6.3.) The FWHM of each peak in the experimental results is compared to the simulation results. In the experiments FWHMs are 30 pm, 80 pm, and 90 pm for the 50 nm, 75 nm, and 100 nm PS particles, respectively. In the simulations the widths are determined as 34 pm, 67 pm, and 82 pm for 50 nm,

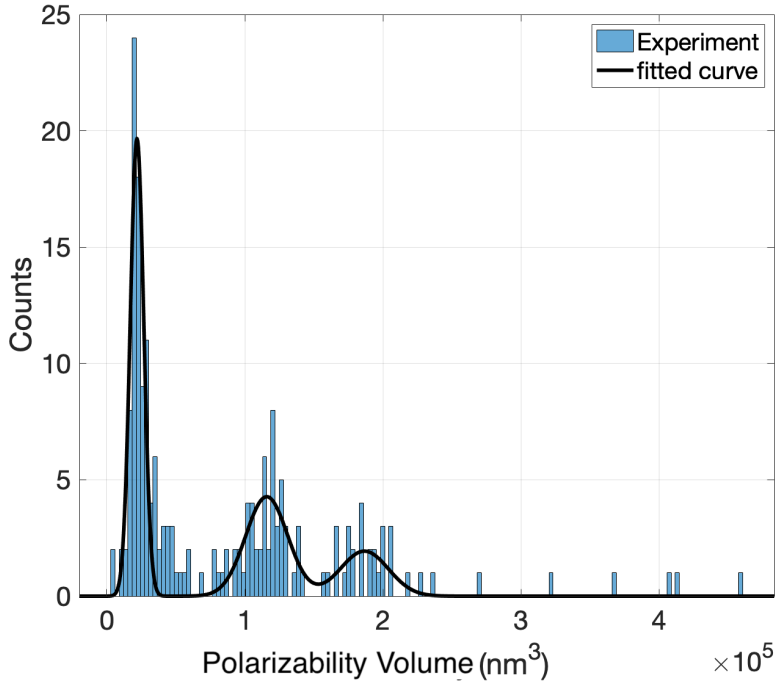
75 nm, and 100 nm PS particles.

Furthermore, the relationship between the size of the particle and the width of each peak in this experiment is investigated. Note that by reducing the size of the particle, the width of each peak becomes narrower. This sensing method provides a new means for speciation of nanoparticles in fluids, or detection of small changes in nanoparticles, such as those resulting from drug loading in nanomedicine applications. Measurement of the distribution of polarizabilities from the mixture of 50, 75, and 100 nm PS nanoparticles in water is shown in Figure 6.6a. The optical mode shift that occurs when a particle enters the Fabry-Pérot Cavity provides a method to determine the polarizability. Namely, by measuring the maximum mode shift we can measure the polarizability with high accuracy (Oxford HighQ Ltd, [180]). Note that the relationship between the maximum mode shift and the polarizability is discussed in Section 3.6 of Chapter 3. Polarizability acts as a fingerprint for nanoparticles as it is proportional to the size of the nanoparticle and its refractive index.

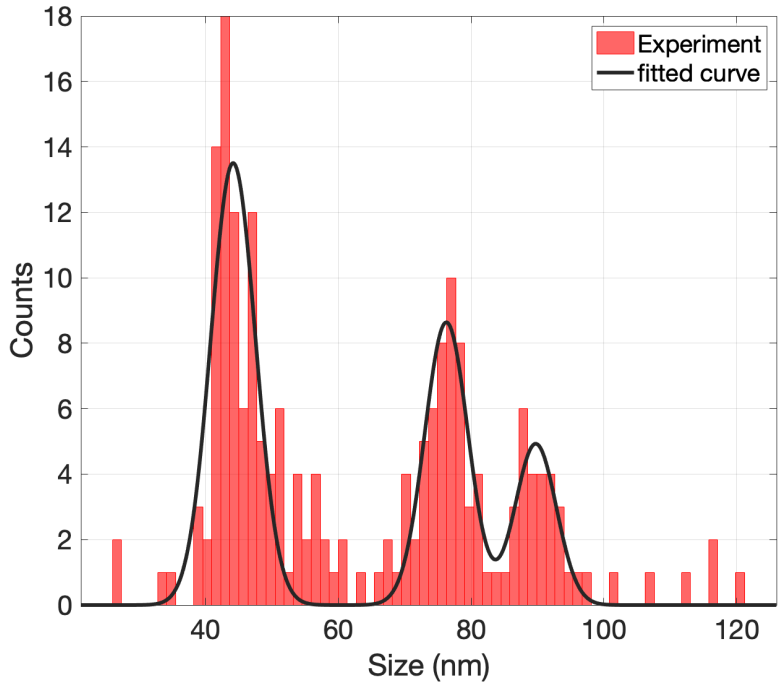
As discussed in the relationship between the polarizability and the size of the nanoparticles, we are able to measure the size of nanoparticles. Figure 6.6b shows the measured particle size by our open-access microcavity. We have applied a Gaussian fit on the particle size distribution, the means of these peaks are 43, 76, and 90 nm, these values match with the actual mean of each particle according to the manufacturer datasheet.

6.2.1 Homogeneous Particles

The results in the previous section encouraged us to investigate the simulated homogenous particles in the cavity and study the difference between inhomogeneous and homogenous particles. More specifically, to study the effect of particles inhomogeneity on the resolution of the characterization method.



(a)



(b)

Figure 6.6: (a) Measured polarizability volume and (b) the measured size distribution with the proposed flow cell.

Figure 6.7 illustrates the distribution of the maximum mode shifts in the cavity when the homogenous particles are delivered to the cavity. The position of each

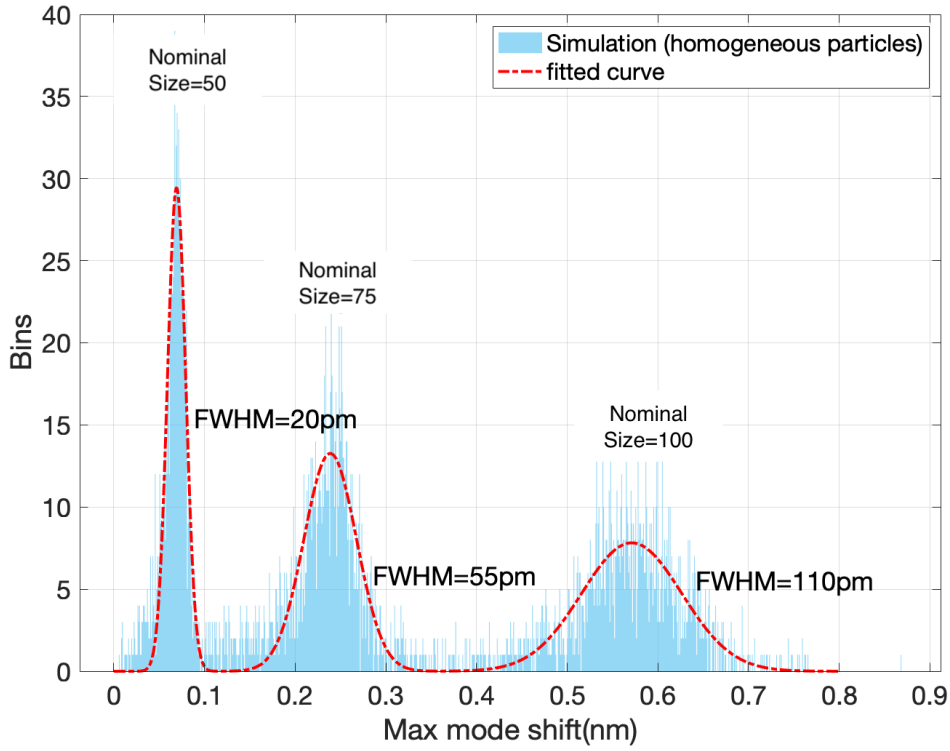


Figure 6.7: Maximum mode shift distribution of a homogeneous mixture of PS particles where the diameters of 50 nm, 75 nm, 100 nm are considered in the simulation.

peak represents the particle size. Peaks of 69 pm, 240 pm, and 572 pm belong to particle sizes of 50 nm, 75 nm, and 100 nm. In the homogeneous simulation, we considered the nominal size for the particles. Furthermore, the Gaussian fit curve is applied to the simulated results to determine the FWHM for each peak.

By comparing Figure 6.7 and Figure 6.3b, we observe that the widths of the peaks corresponding to each particle size are not identical. In the case of homogeneous particles, the widths of the peaks are narrower in comparison to the inhomogeneous ones. This essentially means that the resolution of this method can be improve with homogeneous particles.

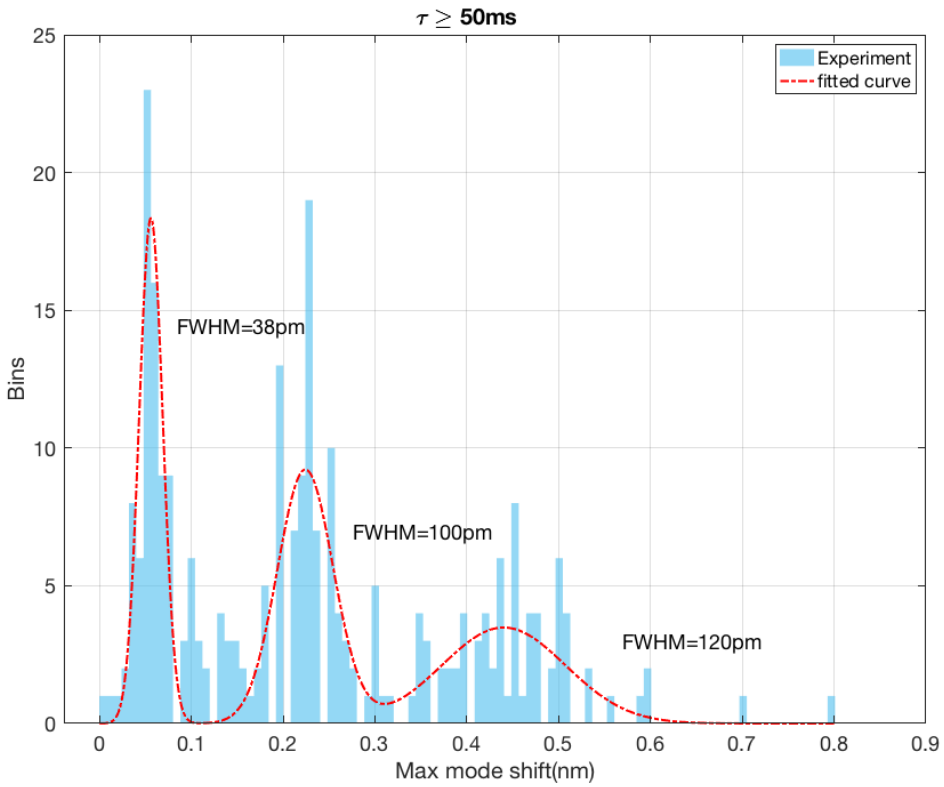


Figure 6.8: Experimental results of trap events when the trap time duration of 50 ms is set for the mixture of 50 nm, 75 nm, and 100 nm PS particles.

6.2.2 Trap Time Duration

As discussed earlier in Section 5.4.3 of Chapter 5, the resolution of nanoparticle size distribution changes by the trap time duration. The trap time duration effectively acts as a filter. In this section, we present this effect in the experiment. The trap time duration is decreased from 200 ms down to 50 ms. A low trap time filter is expected to have more trap events in comparison with the case when the trap time duration is fixated at 200 ms. The experimental results are presented in Figure 6.3 for 200 ms trap time and Figure 6.8 shows the experimental results when the filter of 50 ms is applied. The width of each peak is expanded as expected. Table 6.2 shows the experimental trap time duration versus the full width half maximum for the peaks fitted to the data, as shown in Figure 6.3a and Figure 6.8 for the

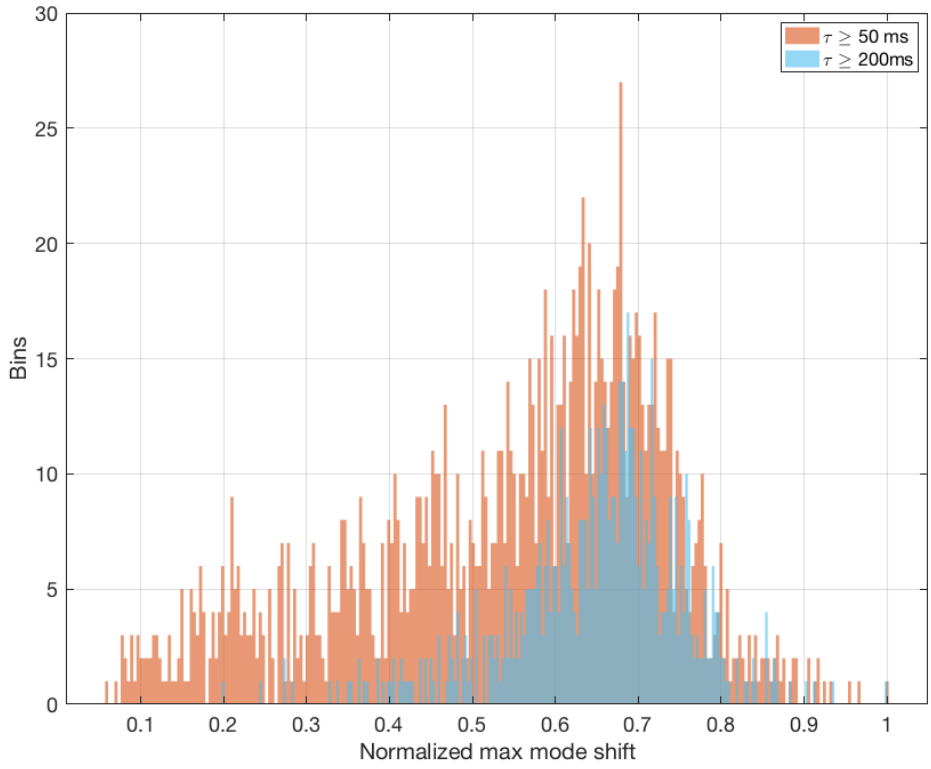


Figure 6.9: Simulation result of the time effect on the resolution of the characterization method for measuring 150 nm PS particles.

trap time duration of 200 ms and for 50 ms, respectively. In this table, $FWHM_{50}$, $FWHM_{75}$, and $FWHM_{200}$ describe the value of FWHM for PS particles with the nominal size or diameters of 50 nm, 75 nm, and 100 nm, respectively for the filter of 50 ms, and 200 ms. The number of the trap events is increased by reducing the trap time duration due to the easier criterion for considering mode shifts as the trap events.

In the following we show the trap time duration effect on the resolution of

Table 6.2: Experimental trap time duration vs the FWHM for the presented peaks

Trap Time Duration	$FWHM_{50\ nm}$	$FWHM_{75\ nm}$	$FWHM_{100\ nm}$
200 ms	30 pm	80 pm	90 pm
50 ms	38 pm	200 pm	120 pm

the method by simulation as well. Figure 6.9 illustrates the simulation results of particle distribution with two filters of 200 ms and 50 ms when the optical force is present in the cavity. PS particles with diameter of 150 nm are considered and the maximum mode shift of particles is determined as a normalized shift in this example. It is clear that the resolution of particle distribution is changed by the filter. τ presents the trap time duration or the filter in this figure. The orange histogram displays the trap events when the time duration of 50 ms is applied and the blue histogram belongs to the trapped particles that stay in the cavity at least for 200 ms. The blue histogram is narrower than the orange one. In other words, the resolution is better when the long trap time is employed.

Based on these results on the effect of the time filter on the average size measured, we can observe that a longer trap time has a more bias towards larger particles. The small nanoparticles have a lower chance to be trapped in a long time due to their size, however, trapping the large particles is easier. Therefore, the trap time duration might be a limitation of the technique.

6.3 Summary

In summary, we presented a new approach to the analysis of single nanoparticles using optical microcavities through which minute quantities of fluid can be flowed, allowing accurate quantitative measurements of size at the single-particle level. We showed that the Fabry-Pérot microcavities provide a simple approach for the determination of the size for a range of polystyrene nanoparticles with diameters of 50, 75, and 100 nm in a non-destructive manner whilst suspended in an aqueous medium. Namely, this technique effectively allows us to evaluate the size distribution of particles in a fluid. We presented the experimental results of a mixture of particles of different sizes and showed how this technique can characterize these particles.

We also compared our measurements with the simulation results that are based on the developed theories in the previous chapters. This chapter also investigated the relationship between the method resolution together with the trap time duration and the particle size as shown in Chapter 5. The proposed technique detected PS particles with sizes as small as 50 nm in diameter. Although, there are many techniques for particle characterization such as DLS that can measure particles in the range from 1 nm to 3 mm [51], our technique also provides a good resolution and overcomes several limitations as discussed in Chapter 2.

As a result, this method can be a powerful technique to characterize nanoparticles in a solution in applications where we need high-resolution measurements at the single-particle level, quantitative diagnostics, and convenient analysis of numerous samples. This technique is able to resolve particle sizes with high accuracy. This technique is also sensitive to the refractive index of particles so it can be used to give a measure of composition in many applications such as drug loading for nanomedicine.

Chapter 7

Measurements Using Pressure-Driven Flow

7.1 Introduction

In this chapter, we introduce a technique based on the open-access microcavities to characterize nanoparticles in a pressure-driven flowing fluid. By introducing an optofluidic system based on a Fabry-Pérot microcavity, not only we can measure the size and the refractive index of the nanoparticle but also, we are able to characterize these parameters in a flowing fluid.

Recall that, our optofluidic system acts as an optical tweezer to hold a nanoparticle in place and allows us to measure the properties of the nanoparticle. Nanoparticle trapping is achieved by the polarization of nanoparticles in strong electromagnetic fields which are generated by focused laser beams. The interaction between the nanoparticle and the light field produces an optical force applied to the nanoparticle.

The optical force is essentially required to overcome the random thermal motion, i.e. the Brownian motion, and the flow force.

This chapter establishes the requirements for trapping nanoparticles in a pressure-driven flow. The efficiency of a Gaussian beam and the power of laser to trap a nanoparticle depends on the fluid flow rate (as discussed in Section 5.2.2 of Chapter 5.) The maximum flow rate, beyond which the particle cannot be trapped, is proportional to the particle size squared (see equation 5.21 in Section 5.2.2 of Chapter 5) [4]. Additionally, nanoparticles suspended in fluids can be affected by thermophoretic force which induces the particles to travel towards cold areas of the fluid as discussed in Section 5.2.4 of Chapter 5.

Therefore the effects of the optical, flow, Brownian, and thermophoretic forces are investigated on the efficiency of trapping for different sizes of nanoparticles. Nanoparticles travel to the x direction and the axis of the laser Gaussian beam is z. Then, by analyzing the trapping rate as a function of the flow rate and the trapping force (which depends on beam waist and laser power) we are able to perform analysis of the size distribution of the particles in a given fluid. We call this technique Cavity Fluidic Trapping Analysis (CFTA). Firstly the CFTA is explained in the designed flow cell as well as the theory of optical trapping. We then present the key performance parameters along with the experimental results.

7.2 CFTA Technique

In this work, we simulate a form of stochastic modeling of nanoparticle dynamics suspended in fluid subject to trapping force field. This modeling approach essentially simulates the motion of nanoparticles as they flow through the instrument. As shown later in this chapter, it is a powerful tool in understanding the range of behavior observed and will allow us both to understand in detail the performance

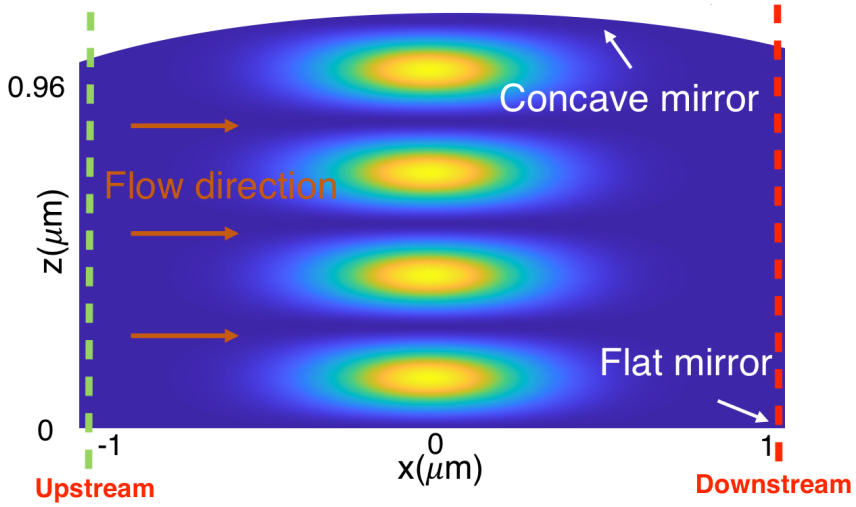


Figure 7.1: Open-access microcavity with 4 antinodes through the concave (RoC of 4 μm) and flat mirrors along with the direction of flowing fluid (antinodes are simulated based on the cylindrical model).

metrics of the instrument and to build our understanding of how to analyze measured signals and extract useful information. Note that to show the concept of CFTA by simulation, the cylindrical optical model are considered through the cavity, and then for making a comparison with our experimental results we use the realistic optical model.

We have developed a MATLAB code to simulate the particle stochastic motion using a Monte-Carlo approach that considers the Brownian motion of nanoparticles as discussed in Section 5.2 of Chapter 5. The trapping event is studied through an optical open-access microcavity with particles whose size is smaller than the laser wavelength (640 nm). This is called the Rayleigh regime. This type of cavity provides a well-understood tool for nanoparticle trapping and sensing [24].

Recall that the flow cell based on optical cavity consists of of two facing mirrors (concave and flat mirrors) in this work. Figure 7.1 shows the structure of the open-access cavity along with the optical modes. The radius of curvature (RoC) of the concave mirror is considered to be 4 μm. The distance between two mirrors is less than 1 μm, which we call the length of the cavity "L".

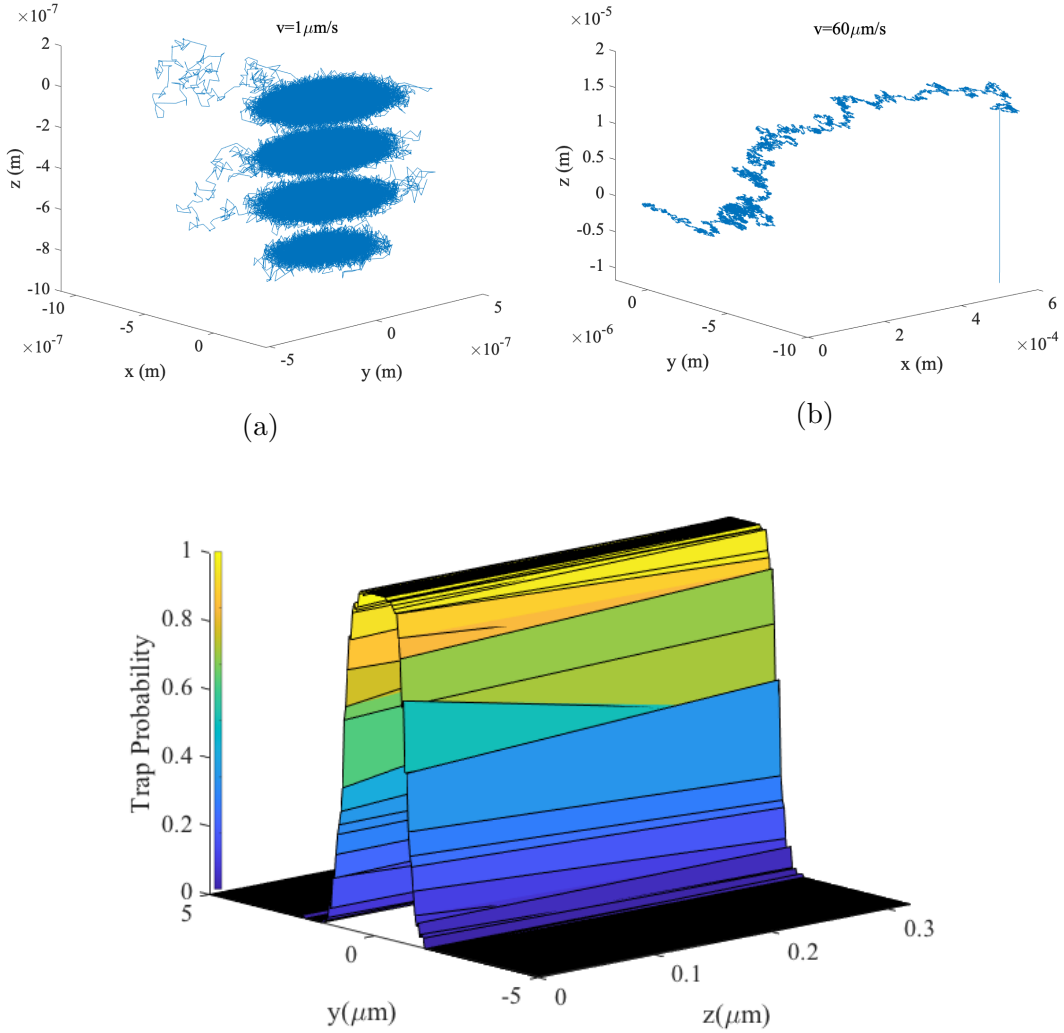


Figure 7.2: The trajectory (based on the cylindrical model with 4 μm RoC of the concave mirror) of a sphere PS particle with a diameter of 200 nm in a flow cell with two flow rates (a) the velocity of the particle is 1 $\mu m/s$ with which the particle is trapped through the antinodes. (b) the particle is escaped from the cavity with a flow rate of 60 $\mu m/s$. (c) Probability of trapping with respect to the position of the particle in y and z direction in the microcavity when the flow velocity is 1 $\mu m/s$.

As mentioned before, for this experiment, the concave mirrors are milled on the ridge. Considering Figure 7.1, the particles can spread through the zones which have a high electromagnetic field. The nanoparticles can be trapped by the gradient force or can be escaped by the flow force. Recall the discussion on the gradient

force over a spherical particle with the radius of a (particle size $D = 2a$) in an electric field in Section 5.2.1 of Chapter 5. The optical or gradient force arises from the interaction of the incident light with a dielectric particle.

The simulation model allows us to study the trajectory of a particle through the open-access microcavity. Figure 7.2 shows two simulated trajectories of a polystyrene (PS) particle with a diameter of 200 μm when the intracavity laser power is assumed to be 10 mW. The length of the cavity is 1 μm (same as Figure 7.1) and the schematic of flow cell is described in Figure 5.19a of Chapter 5 and Figure 7.4 in this chapter. We simulated the behaviour of the particle when it travels through the flow cell with two different velocities; Figure 7.2a presents the path of a particle with the flow velocity of 1 $\mu m/s$. It can be seen that the particle is trapped through the antinodes. On the other hand, Figure 7.2b shows the trajectory of a particle with a higher velocity of 60 $\mu m/s$ in which the particle has escaped the trapping potential and is swept rapidly downstream.

Our model can also determine the probability of trapping for any given size, velocity, and initial particle position. We found out that the particle trapping depends not only on the size, the flow rate, and the laser power but also on the initial position of the particle in the channel. Hence, we investigate the probability of nanoparticle trapping concerning its initial condition on the x, the y, and the z axis. To simulate the measurement method we use a Monte Carlo model based on equations. We define transverse axes x and y and select x as the direction of fluid flow. Particles are 'launched' starting from a position 1 μm upstream of the cavity mode (x = -1 μm) with selected values of position (y, z), fluid flow rate v and optical power p. The particle is said to be escaped if it passes a finish line downstream within a defined time period that is dependent on the flow speed (see Figure 7.1). The time period is long enough such that the particle would certainly have passed the finish line if no trapping has occurred. Namely, to determine a

trapping probability, trapping was defined to have occurred if the particle did not pass $x = 1$ μm within a time equal to 10 μm divided by the flow speed. For a given choice of v and p the initial position (y, z) was varied and the trapping probability (based on 100 repetitions per position) was established to produce a distribution map (Figure 7.2c). It was found that within the range of parameters used the trapping probability was independent of the initial z position and so the trapping cross-section σ_{TC} was defined by integrating the distribution map with respect to y only. Note that, the initial x position is -1 μm upstream of the trap position and is chosen randomly for y and z axis. Note that, here, the flow profile is considered to be linear flow and also we assumed that the optical beam propagation is based on the cylindrical model.

For the initial position of -1 μm in the x direction, Figure 7.2c shows the trapping probability of the PS particle with a diameter of 200 nm for different values of the y and the z. Note that the initial position of the particle on the y axis is critical. If the starting position of the particle is close to $y = 0$, the probability of trap is almost 1. However, changes in the z do not affect the trapping probability.

This probability calculation boils down to an integral over the y axis to give a "trapping cross-section". Similar to the traditional "scattering cross-section" this gives the equivalent range over which the position of the incident particle could vary if the trapping probability is either 1 or 0. We label the nanoparticle trapping cross-section as $sigma_{TC}$ whereby:

$$\sigma_{TC} = \int_{-\infty}^{\infty} P_{trap}(y)dy, \tag{7.1}$$

where $P_{trap}(y)$ is the trap probability on y axis. The unit of σ_{TC} is the unit of length corresponding to the range along the flow channel width. By using this concept, we can show the effect of the nanoparticle material and the optical beam waist or RoC on the trapping events.

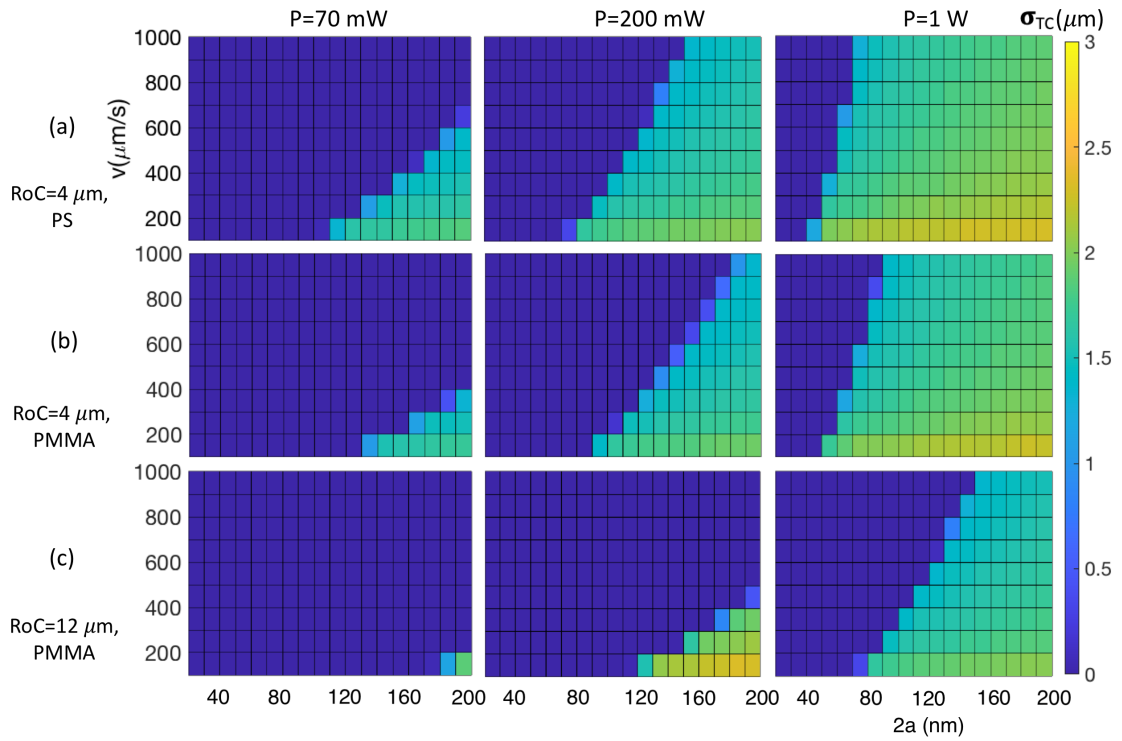


Figure 7.3: Trapping cross-section as a function of diameter ($D = 2a$) in x axis and velocity of the particle (v) in y axis when RoC or the optical beam waist, the laser power, and the refractive index of the particle is changed.

In Figure 7.3, the nanoparticle trapping cross-sections of order 2.5 μm occurs (yellow regions) for the mentioned average intracavity optical power trap and two optical waists $\omega_0 = 546\ nm$ ($RoC = 4\ \mu m$), and $\omega_0 = 741\ nm$ ($RoC = 12\ \mu m$). Note that σ_{TC} in each configuration depends on the radius of the particle a (particle size $D = 2a$) and the flow speed v. The x and the y axes in each subfigure present nanoparticles size ($D = 2a$) and velocity of the particle (v), respectively. Figure 7.3a shows the nanoparticle trapping cross-section (σ_{TC}) for polystyrene particle in the optical cavity with optical waist of 546 nm or RoC of 4 μm for three interactivity laser powers of 70 mW (Figure 7.3a-left), 200 mW (Figure 7.3a-middle), and 1 W(Figure 7.3a-right). Figure 7.3b shows the nanoparticle trapping cross-section (σ_{TC}) of a PMMA particle, which is studied to demonstrate the effect of the refractive index in trapping cross section for three interactivity laser powers of

70 mW (Figure 7.3b-left), 200 mW (Figure 7.3b-middle), 1 W(Figure 7.3b-right). Figure 7.3c shows the nanoparticle trapping cross-section (σ_{TC}) for the PMMA particle with optical waist of 741 nm or RoC of 12 μm for three interactivity laser powers of 70 mW (Figure 7.3c-left), 200 mW (Figure 7.3c-middle), 1 W(Figure 7.3c-right).

The results are studied with three values of average power 70 mW, 200 mW, and 1 W. The first value 70 mW is the intracavity power that can be currently reached by our experimental setup in the lab. The purpose of using the high power in this section is to show the effect of the laser power for trapping the small particles which have encouraged us to consider new ways to increase the power in the experiments.

As mentioned before, the electric intensity is propagated as a Gaussian beam through the microcavity as the cylindrical symmetry. The beam waist is proportional to the length of the cavity and the radius of curvature according to (3.42). Figure 7.3b,c show the nanoparticle trapping cross-section for different RoC of mirrors that makes different optical beam waists. It means the beam waist can be controlled by the RoC. Note that RoC affects the nanoparticle trapping cross-section which is studied for the optical beam waist of $\omega_0 = 546\ nm$, $\omega_0 = 741\ nm$ in this chapter.

Figure 7.3a and Figure 7.3b present the nanoparticle trapping cross-section of the optical microcavity when the beam waist is 546 nm while the type of the nanoparticle is changed. Figure 7.3a-left shows the trapping cross-section of polystyrene particles ($n_p = 1.59$) with the different sizes and various flow rates when the laser power is 70 mW. Note that, if σ_{TC} is 0, it means the probability of trap is 0, and the dark blue colors show particles are escaped from the cavity. The smallest PS particle that can be trapped under this condition is 110 nm in diameter while the flow speed is 100 $\mu m/s$. The presented graphs in Figure 7.3a-middle

and -right (average optical trap powers 200 mW and 1 W, respectively) show that by increasing the power we can trap the small particles even at high speeds. Figure 7.3a-right (average power of 1 W) demonstrates that particles as small as $2a = 40\ nm$ can be trapped at the flow speed of 100 $\mu m/s$.

The type of the particle can also change the nanoparticle trapping cross-section due to fact that the refractive index of the particle is directly related to the polarizability. σ_{TC} is presented in Figure 7.3b for the PMMA particle with the refractive index of $n_p = 1.49$ for powers of 70 mW, 200 mW, and 1 W. As we discussed in (5.1) in Section 5.2.1 of Chapter 5 the optical force is proportional to the polarizability. By increasing the polarizability the optical force will be increased, and subsequently the probability of trapping increases. This essentially shows that by decreasing the refractive index of the particle, the probability of trapping is reduced for the high flow rates and the small size particles. For instance, in the high flow velocity of 1 mm/s the PMMA particles with a diameter or size larger than 180 nm can be trapped in the cavity where the average intracavity power is 200 mW. However, the smallest polystyrene particle which can be trapped is 140 nm with the same flow rate, beam waist, and power (Figure 7.3a) according to the value of the nanoparticle trapping cross-section (σ_{TC}). Recall that the σ_{TC} is obtained by calculating the trapping probability as we discussed in (7.1).

By increasing the RoC or the optical beam waist, the probability of trap drops as in Figure 7.3. With the optical cavity with the beam waist of 740 nm (RoC of 12 μm) and the laser power of 200 mW, the PMMA particle can be trapped for the minimum diameter or size of 120 nm with the lowest flow rate. For flow rates more than 500 $\mu m/s$, we can not see any trapping event even with large particles such as 1 μm.

As we explained before, the nanoparticle trapping cross-section is a function of the power of the laser and the flow rate or the particle velocity. Figure 7.3 shows

that by increasing the power, the probability of the trapping is increased. This means the high power overcomes the flow force and the Brownian force. Therefore, the trap rate or a number of the trap events changes by modifying the interactivity power. Additionally, by increasing the flow velocity, the nanoparticles have a low chance to be trapped because the flow force overcomes the optical force by increasing the flow rate.

Observing this information from CFTA, we can compute the particle size distribution that is the key result of CFTA. To show the size distribution we first determine the trapping rate of particles. The trapping rate is calculated as follows:

$$\Gamma_{trap} = \sigma_{TC}.L.v.N_v, \tag{7.2}$$

where v is the flow velocity, L is the length of the cavity, and N_v is the number of particles per unit volume in the fluid. Using the CFTA technique, we can analyze particle size with the flow velocity and the trap rate and then study a single particle. This technique can precisely and quantitatively recognize the presence of particles of different sizes.

7.2.1 Experiment Results

In the experimental work, nanoparticles are delivered through the cavity with a constant flow rate. To show the size distribution of nanoparticles and the resolution of the CFTA technique, the trap rate is studied with respect to a range of change in the interactivity power, namely we vary the power. The trapping rate is obtained by a counter to poll trap events from the experimental data. The varying technique provides insightful information about the particle size and the type of nanoparticles (or refractive index of nanoparticles). In principle, particle size characterization by the CFTA technique can be done in real-time, which is crucial in a number of applications.

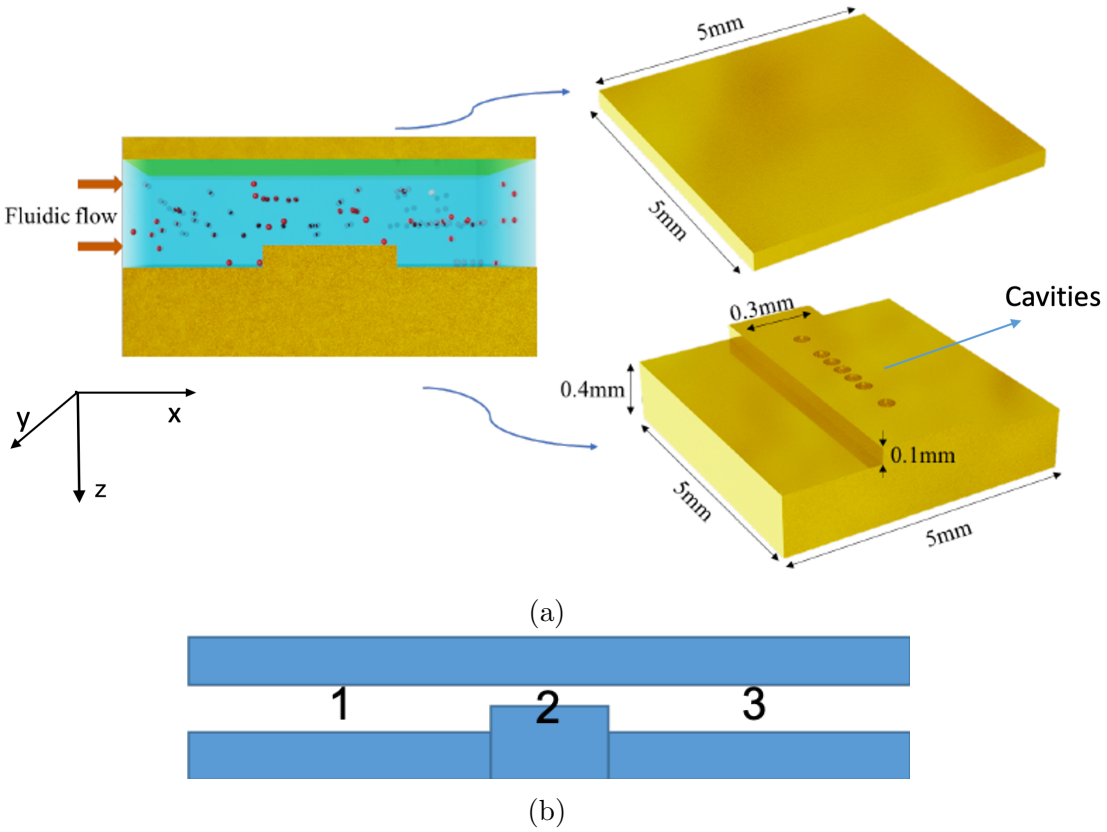


Figure 7.4: (a) A schematic of flow cell along with the flat mirror and the ridge that provides infrastructure for the microcavity. (b) side view of the flow cell.

To carry out the experiment an open-access microcavity flow cell is used to allow us to introduce the sample fluid into the microcavity region whilst monitoring the cavity modes (Figure 7.4a). An array of concave mirrors is employed in the ridge area. The mirrors are coated with dielectric Bragg reflectors consisting of alternating layers of SiO_2 and TiO_2 to achieve the required reflectivity in the wavelength region of interest.

An important consideration for the pressure-driven flow used here is that the flow speed is not uniform but follows a parabolic profile across the flow channel cross-section, with zero flow rate at the mirror surfaces. We select the mirror separation such that five antinodes of the optical field lie within the flow channel, whereby we expect about two-thirds of the recorded events to result from the

Table 7.1: Reference Samples of Microparticles GmbH

Type of Particles	Batch No.	Nominal Size (Diameter) (nm)	Standard Deviation (nm)	Density of polymer ($\frac{g}{cm^3}$)
PMMA	PMMA-R-KM255	196	4	1.05
PS	PS-R-KM248	140	7	1.05
PS	PS-R-KM249	175	5	1.05
PS	PS-R-KM458	187	6	1.05

anti-nodes nearest the center of the flow channel. The parabolic flow profile is included in the simulation to ensure accurate comparison with experimental data.

For this work, we prepared solutions of 4 different nanoparticles (140 nm PS, 175 nm PS, 187 nm PS, and 196 nm PMMA spherical Particles) from Microparticles GmbH, with a constant concentration of 10^{11} N/ml (see Table 7.1). The nanoparticles are delivered through the cavity with constant pressure by the ELVEFLOW system [179]. Particles are delivered to the cavity with the pressure of 2 $mbar$ where the steady pressure creates a constant flow rate.

We estimate the flow speed through the cavity by analytical and numerical calculations. Figure 7.4b shows a simple schematic of the flow cell. It consists of three parts with rectangular cross-sections. Parts of 1 and 3 of the channel are parts that have the same dimension and are also connected to the inlet and the outlet of the flow cell. The middle part presents the cavity section. The gap between the concave mirror and the flat mirror is called the length of the cavity (around 1.5 μm according to the number of modes as discussed in Equation (3.1) of Chapter 3). By using the rectangular geometry the hydraulic resistance can be calculated by Eq (5.52).

According to the dimension of each part, the hydraulic resistance of the first and the third parts is 4.4×10^9 ($\frac{N.s}{m^5}$) and of the cavity part (or the second part) is $7.38 \times 10^{13}(\frac{N.s}{m^5})$ from analytical calculations. The mean flow rate is proportional to the pressure gradient and the hydraulic resistance. Therefore, the flow rate through

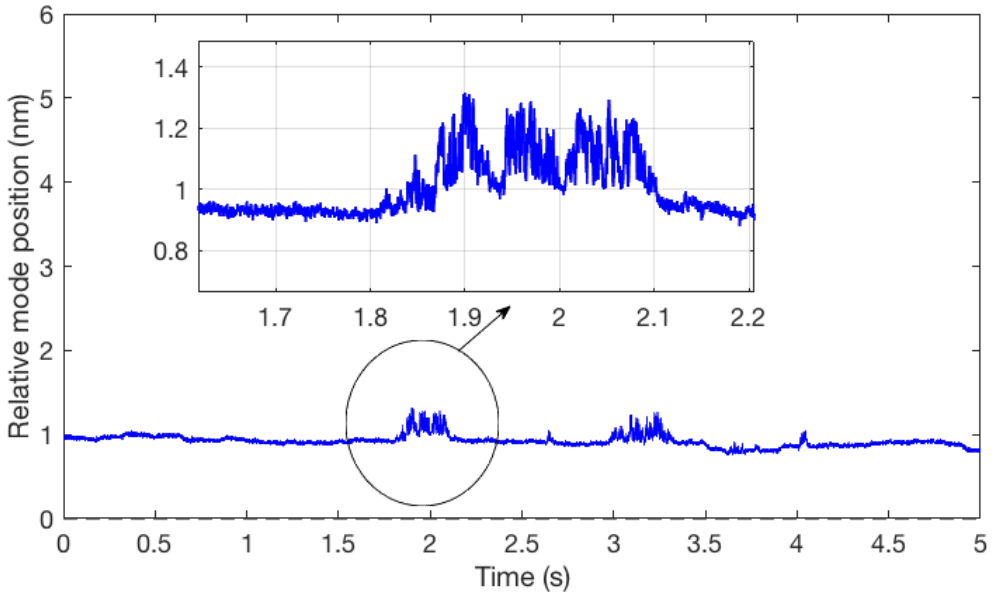
the flow cell can be obtained by (5.50). The particle velocity through the ridge is calculated from the flow rate and the area of the middle channel. The velocity of a particle through the cavity is then $54.2 \times 10^{-6}\ m/s$. According to the numerical (by COMSOL simulation- see Section 5.4.4 of Chapter 5) and analytical calculations (by using the notions of hydraulic resistance), the velocity of the nanoparticle in the flow cell can be determined as 54.2 $\mu m/s$ as we calculated the flow velocity in Section 5.4.4 of Chapter 5. The pressure of 1 $mbar$ gives us the flow velocity of 27.1 $\mu m/s$. According to (5.52) and (5.53), the pressure of 2 $mbar$ produces the flow velocity of 54.2 $\mu m/s$.

Hence, the trapping rate is investigated when the nanoparticles are delivered through the cavity with 2 $mbar$ pressure which generates a particle velocity of 54.2 $\mu m/s$. The size distribution of this technique is introduced by finding the derivative of the trap rate with respect to the power change. Polystyrene particles with a diameter of 175 nm and 140 nm are delivered through the cavity when the concentration of the solution is $10^{11} NP/ml$ and the cavity with RoC of 25 μm is illuminated by a narrow-linewidth continuous-wave 640 nmdiode laser (Lasos RLK DPSS, the maximum power of 150 mW). This size characterization technique is based on a mode shift that results from the polarizability of nanoparticles.

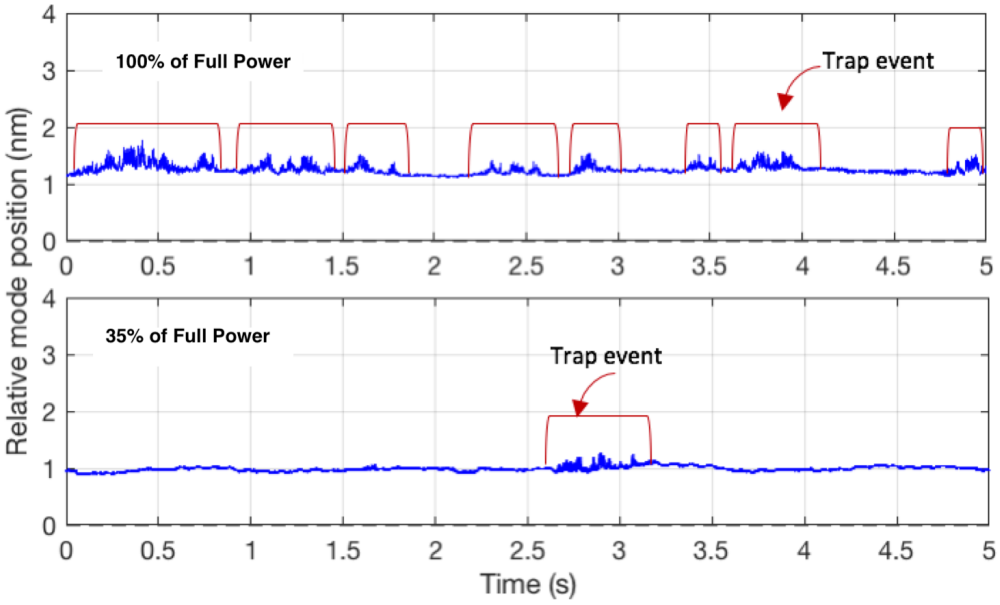
We monitor the cavity modes by scanning the cavity length through the resonance with the fixed wavelength laser and recording the difference in the mode position between two microcavities to remove the effects of vibration.

As mentioned before the data consists of a series of distinct events as single-nanoparticles diffuse through the cavity mode and are dragged to the center of the optical mode by the trapping forces. When a nanoparticle diffuses through the cavity, the polarizability of the particle determines the optical mode shift by considering the location of the particle within the mode (Section 3.6 of Chapter 3).

Figure 7.5a presents an example trace recorded over 5 s, where mode shifts of



(a)



(b)

Figure 7.5: Experimental data of (a) the mode shift when the particle is trapped (b) different laser powers that affect the number of trapping events; the top and the bottom figures represent trap events for 100 % and 35 % of full optical power (20 mW), respectively.

about 300 pm can be observed. The expected diffusion time of a particle through the mode is of order 10 ms, so the extended shift between 1.8 s and 2.1 s represents a trapped particle. The maximum mode shift provides an accurate measurement

of the polarizability of the nanoparticle. The mode shifts in Figure 7.5a results from the polarizability of polystyrene nanoparticles with a diameter of 175 nm. Recall that the constant differential pressure of 2 $mbar$ was established using a hydrostatic flow regulator, resulting in a peak flow speed around 50 $\mu m/s$. Single nanoparticles passing through the microcavity register as discrete "events" the duration of which is our primary indicator for trapping. Based on the flow speed alone we expect events due to particles that flow freely through the cavity mode to display durations of about 20 ms, and so we define a trapping event as one with duration exceeding 200 ms preceded by a period exceeding 100 ms with no observed mode shift. Namely, we call a mode shift with a time duration of more than 200 ms a trap event. For counting the trap events, we need to distinguish two sequential trap events, here we have used time of 100 ms as a threshold value, if the mode position does not have any change for at least 100ms, we can declare the next mode shift to be corresponding to the trap event of the next particle. We have shown this by red brackets in the figure to show the separation between two sequential trap events. Thus, separation of each event would be at least 100 ms. In other words, for the separation, the mode shift is zero for at least 100 ms.

The polystyrene particles with the diameter of 140 nm and 175 nm are delivered through the flow cell by the constant pressure of 2 $mbar$ (200 Pa). The interactivity power is controlled by the internal software of Lasos Laser GmbH. We are able to change the incident laser as a percentage of the maximum power (with increments of 5 %). We observe that the trap rate changes by varying the laser power. Note that the maximum laser power provides the maximum intracavity power of 20 mW.

We present two samples of the mode shifts when the power of the laser is changed. Figure 7.5b shows how the power can affect the number of trap events. The first row shows the trap rate of PS particles when the laser is fired with the maximum power. The number of trap events or mode shifts (8 trap events for 5 s)

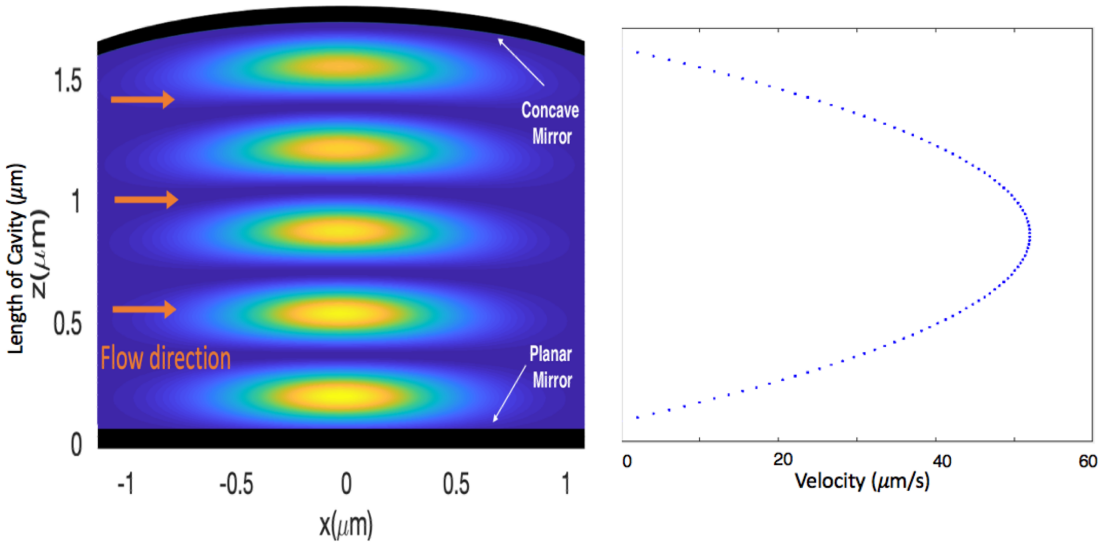


Figure 7.6: Optical modes based on the realistic model in the cavity along with a parabolic flow distribution to show the dependency of speed value on the position of the cavity with RoC of 25 μm.

considering the separation time is more than the bottom row of Figure 7.5b (8 trap events for 5 s). In Figure 7.5b bottom, the power of the laser is decreased to 35 % of the maximum power. Each trap event is marked by a red bracket in Figure 7.5b.

In agreement with the trap rate parameter, we present another parameter to show the nanoparticle distribution and determine the resolution of the technique. This parameter is the derivative of the trap rate with respect to the laser power as

$$\frac{d\Gamma_{trap}}{dp}. \tag{7.3}$$

However, this measurement parameter can be defined as a derivative of the trap rate with respect to any change in the system. For example, if the trap rate is determined by varying the flow velocity, the particle distribution is achieved by finding the derivative of the trap rate with respect to the flow velocity as

$$\frac{d\Gamma_{trap}}{dv}. \tag{7.4}$$

Before presenting the key results of trap rate and particle distribution of this experiment, the type of flow profile is studied. As mentioned in Chapter 5, the particles are delivered through the cavity by the pressure that makes a parabolic profile. This means the velocity of all particles is not identical through the cavity. Figure 7.6 shows a distribution of the parabolic flow in the cavity with three optical modes.

In this type of flow profile, the nanoparticle velocity depends on the position of the nanoparticle in the channel and the maximum velocity is placed in the center of the channel. Namely, Figure 7.6 illustrates that the nanoparticles have a low flow speed in the channel boundary.

According to the trap rate approach and the applied pressure through the system, the trap rate results of PS particles with diameter or size of 140 nm, 175 nm with respect to the power changes are presented in Figure 7.7. (a-b). The trapping rate of each particle is shown by two colors (blue presents the 175 nm PS particles and red shows 140 nm PS particles). By finding the derivative of the trap rates with respect to the power of the laser, two clear peaks of two different particle sizes are generated as in Figure 7.7.b. Note that by analyzing the position of the peaks, we can conclude that the smaller particles need a higher power to be trapped.

The experimental results are also compared with the simulation results (7.7. (c-d)). The positions of peaks in the experimental results match closely with the simulation. To make a fair comparison between the experimental work and simulation, the critical parameters are taken from the experiment. These critical parameters are the RoC, the length of the cavity, and the type and the velocity of the nanoparticle. The maximum intracavity power is assumed to be 20 mW in the simulation. Note that simulations are studied based on the realistic optical model to have a fair comparison between the experimental and the simulation results.

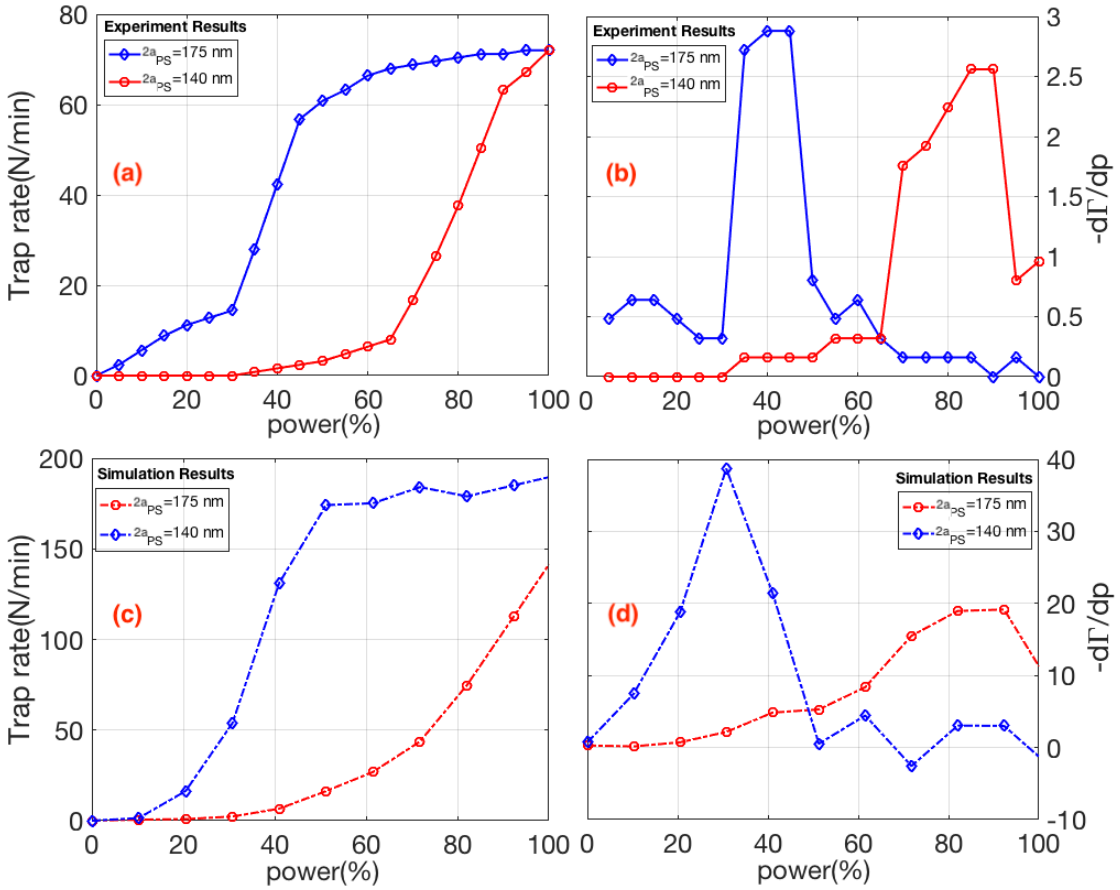


Figure 7.7: Experimental results (a-b) versus simulation results (c-d) when polystyrene nanoparticles with diameters of 140 nm and 175 nm are introduced into the cavity by pressure of 2 $mbar$and when the maximum intracavity power is 20 mW.

In the experimental and simulation results (Figure 7.7), the number of trap events for 175 nm and 140 nm PS particles is slowly changed when the interactivity power is less than 30% and 67% of the maximum power, respectively. We call these percentages of powers 30% and 67% threshold power in this work. This phenomenon results from the parabolic flow effect, when the trap rate is significantly dropped by reducing the power, the number of the trap events is decreasing slowly after dropping power to less than the threshold power. The effect of the parabolic flow can be seen by a small increase in the trap rate at laser powers below the main step, consistent with the lower threshold of trapping for the slower moving particles close to the mirrors. As illustrated before, the velocity of the particle is low when

the particle is placed far from the center of the channel (Figure 7.6). This means that we expect to have trap events with small powers because the slow particle doesn't need high power to be trapped.

As we presented the type of nanoparticle effect on the σ_{TC}, the refractive index of the particles can change the nanoparticle trapping cross-section and subsequently the number of trap events in Figure 7.3. Here we investigated two different types of nanoparticles with almost identical diameters; Polystyrene (size or diameter of 187 nm) and PMMA (size or diameter of 196 nm) nanoparticles. These particles with the concentration of 10^{11} N/ml are delivered through the cavity with RoC of 25 μm by the pressure of 2 $mbar$.

The trapping rate of these particles is studied based on the power changes. The distribution $\frac{-d\Gamma}{dp}$ for particles in the solution is measured by varying over laser power while maintaining the constant flow speed. Figure 7.8 shows broadly how the number of trap events is increased as we increase the laser power. Figure 7.8.(a-b) displays the experimental results in the first row and the particle distribution (Figure 7.8.b) is derived from the trap rate. It shows how the trap rate is changed by a small change in the refractive index of the material of nanoparticles. This means the CFTA technique is also sensitive to the refractive index of nanoparticles.

Additionally, these experimental results are also compared with simulation (Figure 7.8.(c-d)). Note that, the simulation parameters are chosen according to the real parameters that come from the experimental set-up in the lab. According to the obtained experimental results, the peak positions of nanoparticles match with those predicted by the simulation. The flow parabolic profile effect is seen in this experiment as well. In powers less than the threshold power of 35% and 55% for PS and PMMA particles, we have still the trap events due to the low speed of flow around the boundary of the channel, and the trap rate is smoothly decreased

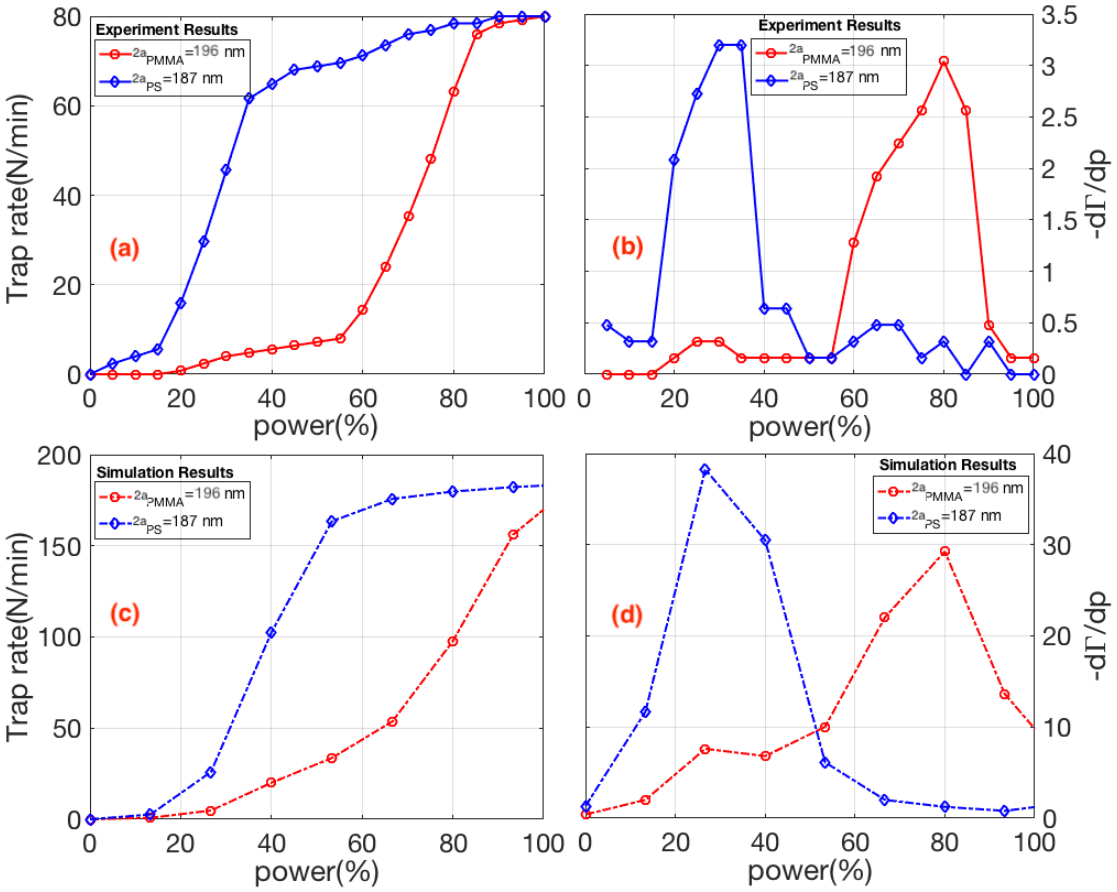


Figure 7.8: Experimental results (a-b) versus simulation results (c-d) when 187 nm PS and 196 nm PMMA nanoparticles are introduced into the cavity by the pressure of 2 $mbar$ and when the maximum intracavity power is 20 mW.

by reducing the power of the laser.

To estimate the resolution of our measurements, we used Gaussian fits representing the particle distributions. FWHM of the peaks in Figure 7.9.left reveals a sizing resolution of about 10 nm. Figure 7.9.right shows similarly that PS particles with size 187 nm and PMMA particles with size 196 nm can be easily distinguished. The PMMA particles require a high laser power from trapping despite being slightly smaller. The FWHM of the peaks in 7.9.right reveals a refractive index resolution of about 0.03 RIU [4].

Additionally, peak resolution can be a key parameter, acting as a separation factor to show resolvability of size distribution or peaks that present the size and the

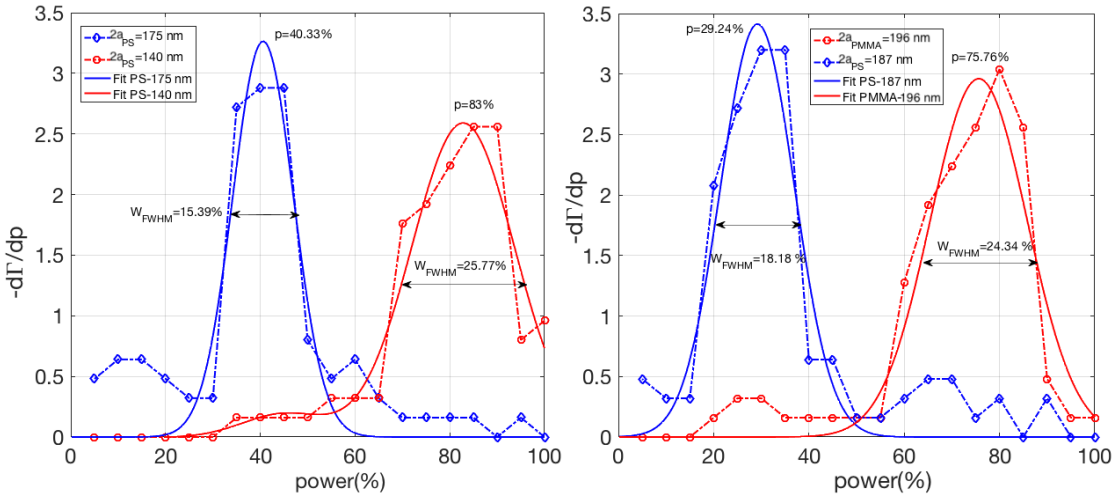


Figure 7.9: The Gaussian fit is applied to the experimental result to show the resolution of the method.

Table 7.2: Peak Resolution of CFTA

Particle Size	P (peak)	FWHM	R_P
$PS_{140\ nm}$	83%	25.77%	1.2
$PS_{175\ nm}$	40.33%	15.39%	
$PS_{187\ nm}$	29.24%	18.18%	1.2
$PMMA_{196\ nm}$	75.76%	24.34%	

material of the particle in our work. In each experiment, two peaks are presented, then the peak resolution is determined as

$$R_p = 1.18\frac{\Delta P}{\Sigma FWHM}, \tag{7.5}$$

where R_p presents the peak resolution that is proportional to the difference of two adjacent peaks (ΔP) and their summation of FWHM of each peak. The peak resolution of this method is 1.2 in both experiments (see Table 7.2). We have also calculated the standard deviation of each peak $PS_{140\ nm}$, $PS_{175\ nm}$, $PS_{187\ nm}$ and $PMMA_{196\ nm}$ particle are 11%, 6%, 7%, and 10%, respectively.

7.2.2 Linear vs Parabolic Flow

The pressure-driven method creates a parabolic flow so that the velocity in the whole channel has no uniform profile. The maximum flow is always placed in the center of the channel. Hence, it is almost impossible to have a linear flow with the pressure-driven method. In this section, the effect of a linear flow and parabolic flow are investigated on the CFTA technique based on electroosmosis.

Figure 7.10 shows the trap rate versus power changes for PS particles with the size of 175 nm where both types of flows (linear and parabolic flows) are considered in the simulation. In both studies, we used the realistic model for propagated laser beams through the cavity. Recall the trap rates are calculated by using the Monte-Carlo model which is coded in MATLAB. The flow velocity is assumed 120 $\mu m/s$. In the parabolic flow, the trap rate is increased slowly as is seen in the

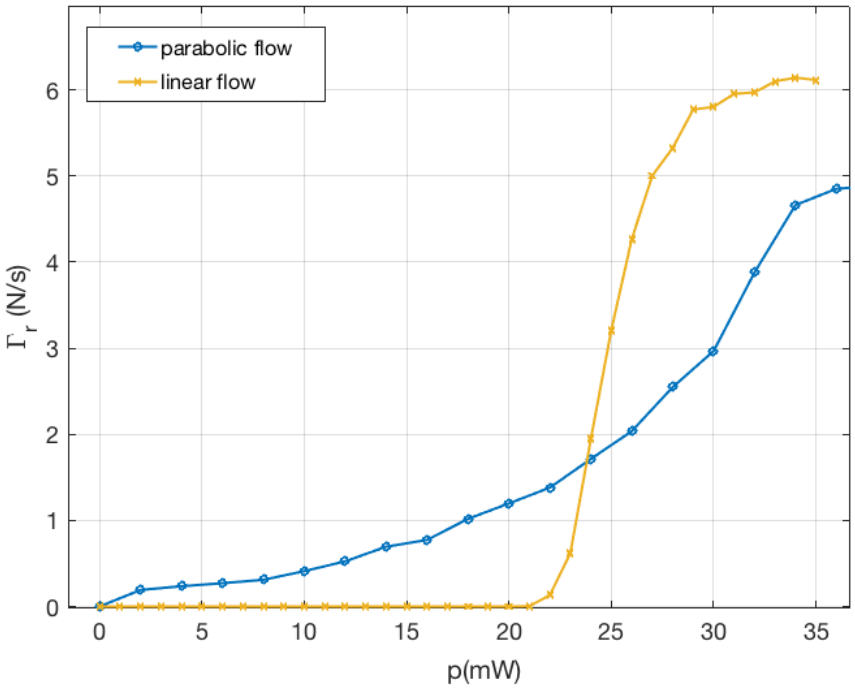


Figure 7.10: A comparison between the effect of linear and parabolic flow on the trap rate of PS particles with size of 175 nm in the simulation when the maximum interactivity is 35 mW.

experimental work (Figure 7.7 and Figure 7.8).

Interestingly, the pattern of the trap rate change against the power is completely different in the linear flow as compared to the parabolic flow. In the linear flow, all the particles have an identical velocity through the channel. According to the trap rate diagram in the linear flow, for the powers less than 21 mW, the trap rate is zero (see the orange curve in Figure 7.10). While in the parabolic flow, nanoparticles can be trapped with lower powers due to the flow velocity and its profile through the cavity. Namely, the number of traps for the laser powers less than 21 mW is gradually dropped (see the blue curve in Figure 7.10), it shows lower velocity particles will be trapped at different points within L. Recall that the trap rate in the simulation is obtained by calculating the nanoparticle trapping cross-section and (7.2) that is discussed earlier in this chapter.

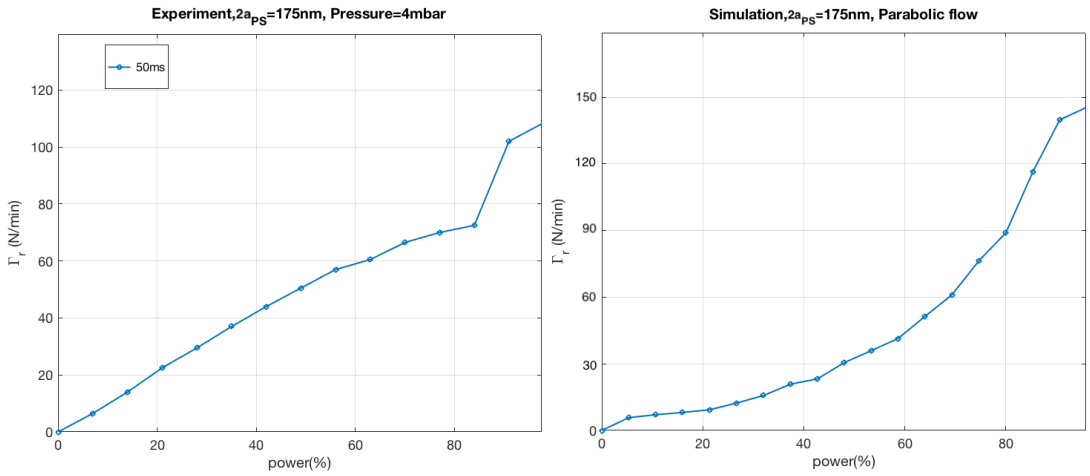


Figure 7.11: Experimental (left) and simulation (right) results of the trap rate when 175 nm PS particles are delivered to the cavity by the pressure of 4 $mbar$ or the average flow velocity of 108 $\mu m/s$. The maximum intracavity power (100%) is 15 mW.

Additionally, the effect of parabolic flow on the trap rate is particularly studied by delivering a solution of 175 nm PS particles through the flow cell in the lab when the nanoparticles are delivered to the cavity by the pressure of 4 $mbar$. The trap events with the trap time duration of 50 ms are counted in different laser

powers by varying power in this experiment, the trap time duration is chosen by considering the size of particles and the flow velocity.

Figure 7.11 exhibits the experimental results of the trap rate against the simulation results to make a comparison. In this experiment, the power percentage is changed with 5% increments when the maximum intracavity power is 15 mW to study the trap rates. According to Figure 7.11, the threshold power is 85% of the maximum power, and for powers less than this threshold power the trap rate is gradually changed. As stated in the simulation results, the trap rate is slowly reduced by reducing power. Note that in the simulation results the trap rate variation is slow when the power of the laser is less than 80%. This essentially means that with respect to the threshold power, the behavior of the trap rate in the experiment matches with the expected results from the simulation.

Furthermore, we demonstrate the trap rate of 175 nm PS particles when the nanoparticles are delivered by two different pressures. The pressures of 3 $mbar$ and 5 $mbar$ are applied by ELVEFLOW to deliver nanoparticles into the cavity. As explained before, two different pressures generate two different flow velocities. Recall from Section 5.4.4 in Chapter 5, the velocity has a linear relationship with the presure. The power of the laser is swept in this experiment as the prior experiment. The number of the trapped particles is counted for each power of the laser.

Figure 7.12 displays the results of the trap rate and the derivative of the trap rate with respect to the power in this experiment. Two peaks are distinguishable in the figure, which means this method is sensitive to the flow velocity as well. As an interesting point, the power peak ratio of particle distribution for 3 $mbar$ and 5 $mbar$ is almost identical to the pressure ratio. According to Figure 7.12.right, the peak positions of the orange (3 $mbar$) and the blue (5 $mbar$) curves are 40% and 70%, respectively. The ratio of the pressure is 1.66 which is almost identical to the peak ratio of 1.7. This experiment confirms the effect of the pressure or the

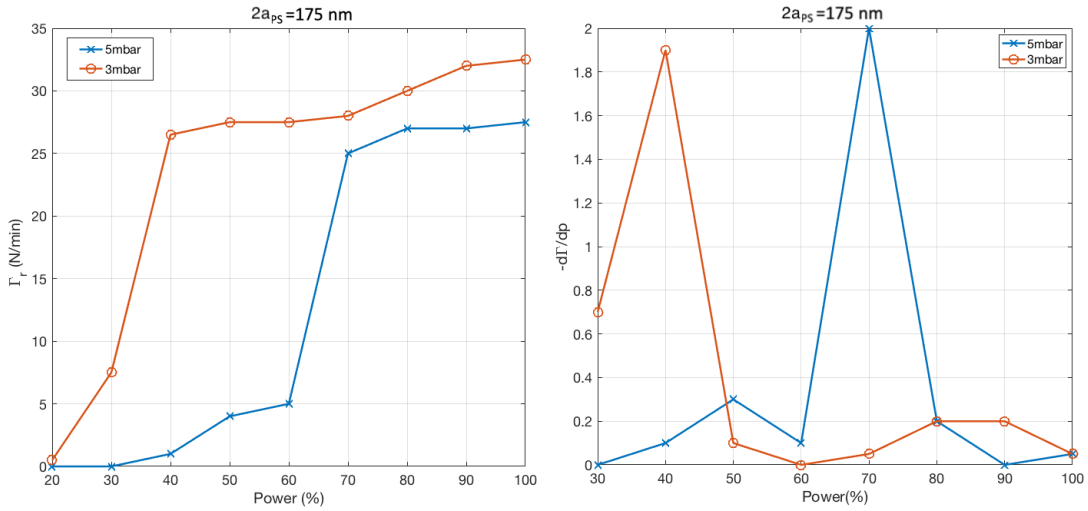


Figure 7.12: Experimental results of changing the trap events in two different pressures of 5 $mbar$ or the average flow velocity of 135 $\mu m/s$ and 3 $mbar$ or the average flow velocity of 81 $\mu m/s$ for the PS particle with the diameter of 175 nm when the maximum intracavity power is 20 mW.

flow velocity on the trapping rate. It means that if the velocity of the particle is multiplied by a factor (~ 1.7) then the peak positions of $\frac{-d\Gamma}{dp}$ follow the same factor as well. Namely, the peak positions shift with the same factor (in this experiment ~ 1.7) of the multiplied velocity or pressure. Note that the power increment step is larger than the presented experimental result in Figure 7.11 since the maximum intracavity power is larger.

7.2.3 Time Effect on Trap Rate

The trap time duration can affect the number of events and consequently the resolution of this technique as we discussed in Section 5.4.3 of Chapter 5.

Figure 7.13 denotes the trap rate when two criteria of trap time duration are considered. The blue curve presents trap events when particles stay through the cavity more than 100 ms and the red curve displays the number of particles kept in the cavity for at least 50 ms. Note that the particles are delivered through the cavity by the constant pressure through the cavity. The peak of the trap rate

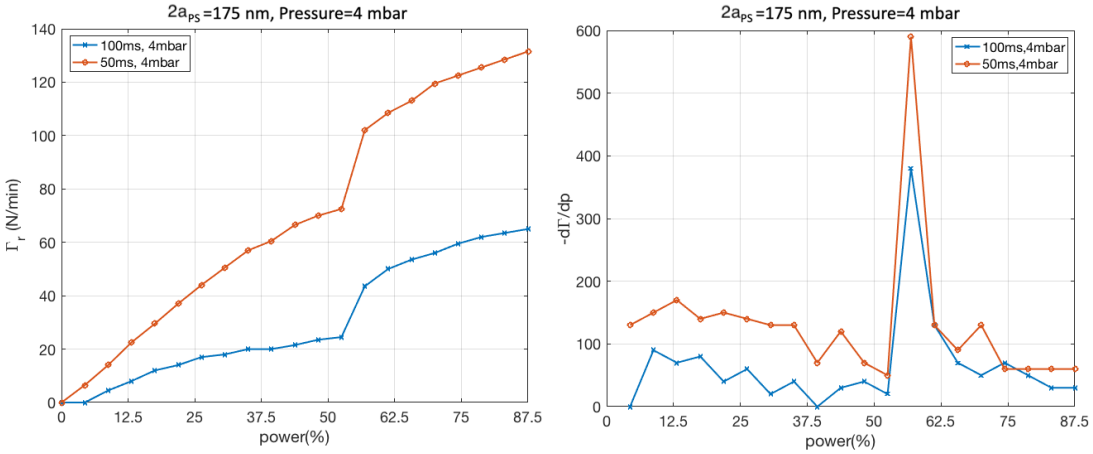
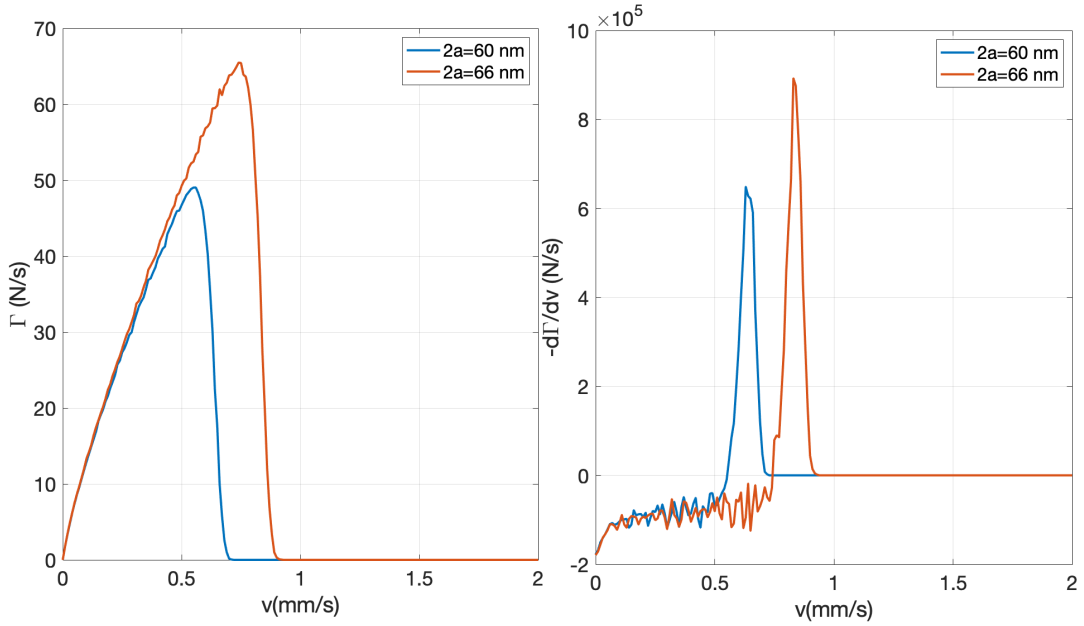


Figure 7.13: Experimental results where particles (more than 800 particles) are delivered throught the cavity with pressure of 4 $mbar$ or the average flow velocity of 108 $\mu m/s$ - Trap rate (left) and the derivative of trap rate (right) for two different filter times of 100 ms and 50 ms when the maximum intracavity power is 20 mW.

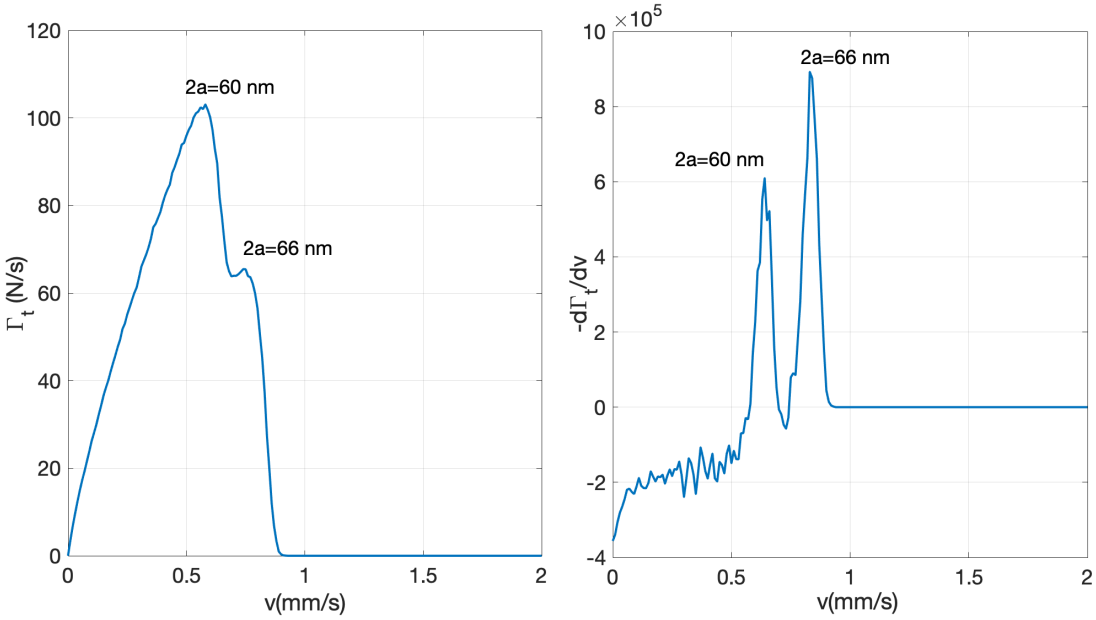
derivative in both experiments is identical, which means the time duration of the trap solely affects the number of events. In this experiment, the resolution of these peaks is changed by changing the trap duration as we expected according to Section 5.4.3 in Chapter 5. Note that, we have the same behavior of growing trapping rate in this experiment as we studied the parabolic flow effect on the trap rate in Section 7.2.2 of this chapter. In both experiments, the number of trap events is slowly increased before 53%, then the trap rate is suddenly increased for powers larger than 53%.

7.3 CFTA based on Velocity Changes

The CFTA can be performed by studying the trap rate with respect to the velocity of the flow. In this case, the trap rate is theoretically investigated by varying the flow velocity. It is however challenging in pressure-driven flows due to the parabolic flow. Nonetheless, it can be performed when a linear flow is applied through the flow cell.



(a)



(b)

Figure 7.14: Results of (a) the trap rate calculation for two PS particles with diameters of 60 nm and 66 nm (left) and size distribution based on the derivative of trap rate with respect to velocity (right) (b) trap rate calculation for a mixture of two PS particles with sizes of 60 nm and 66 nm (left) size distribution based on the derivative of trap rate with respect to velocity (right).

Electroosmosis can be an alternative to pressure-driven flow. By regularizing the distribution of nanoparticles, an orthogonal measurement involving particle

surface charge can be performed. Electroosmosis (Eo) is a promising type of micropump to deliver nanoparticles through the cavity [194–203, 203–205]. The nanoparticles are purely driven by an electric field to make a linear flow through the cavity. Using Eo, we can analyze particle size by CFTA based on the velocity of flow as well, which we call CFTA-Eo. In this way, the trap rate is determined by varying the velocity and then measuring the trap rate. Namely, the trap rate is studied by changing the particle velocity where the flow profile is linear. This technique can precisely and quantitatively recognize the presence of particles of different sizes. In this section, we present the CFTA simulation results based on the velocity changes.

For showing the CFTA-Eo, two different PS particle sizes are separately considered in the cavity ($RoC = 4\ \mu m$) with the same concentration of $10^{11}\ N/ml$. The radii of nanoparticles are 30 nm and 33 nm. We assume that nanoparticles are delivered through the cavity with a linear flow profile where the intracavity power of the laser is 100 mW. This simulation is done for determining the number of the trap events for a velocity range of 0 to 2 mm/s. Figure 7.14 demonstrates the trap rate changes with respect to the velocity of particles.

According to Stokes' Law and considering the optical force, the velocity of the particle is proportional to the square of the particle size as it is shown in (5.21) in Section 5.2.2 of Chapter 5. Figure 7.14a displays particles with a diameter of 66 nm is trapped 1.2 times faster than the 60 nm particle.

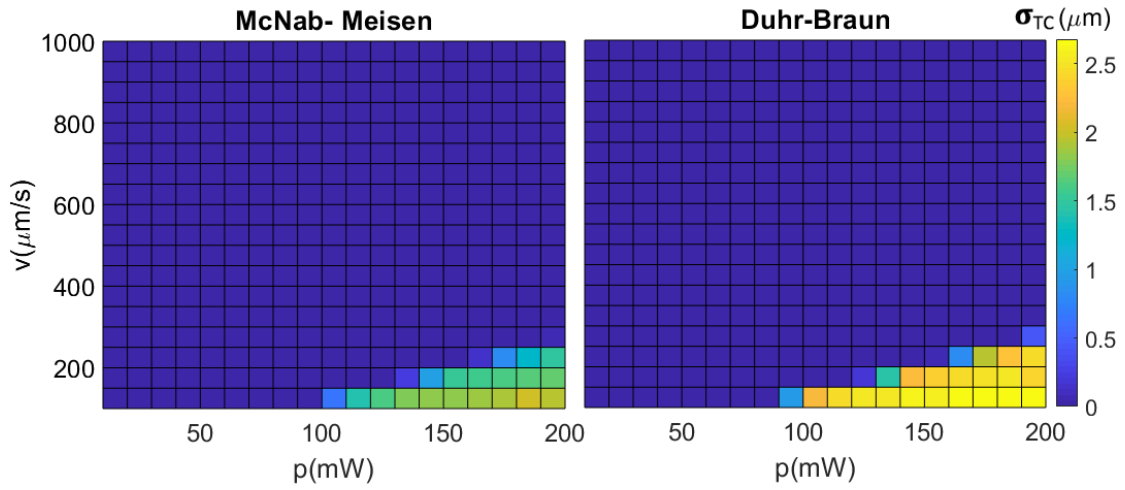
As it can be seen the number of trap events is firstly raised for each size particle since by increasing the velocity the number of delivered particles is increased. After the particles pass the critical velocity or the maximum velocity (as discussed in Section 5.2.2 of Chapter 5), the number of the trap events is decreased (Figure 7.14a). To present the resolution of the size measurement, we find a negative derivative of the trap rate with respect to the velocity (Figure 7.14a, right).

Figure 7.14b presents the trap rate and the size distribution of a mixture of the above-mentioned particles. The trapping rate and size distribution are calculated by varying the flow velocity where the intracavity power, the length of the cavity and the RoC are kept the same as in the previous simulation. The intracavity power ($100\ mW$) is considered constant for all velocities. According to the individual measurements, the trap rate result of the mixture is a summation of two trap rates of these particles where are studied separately. It shows this technique is able to detect small differences in the size of nanoparticles in a mixture and provides high-resolution measurements.

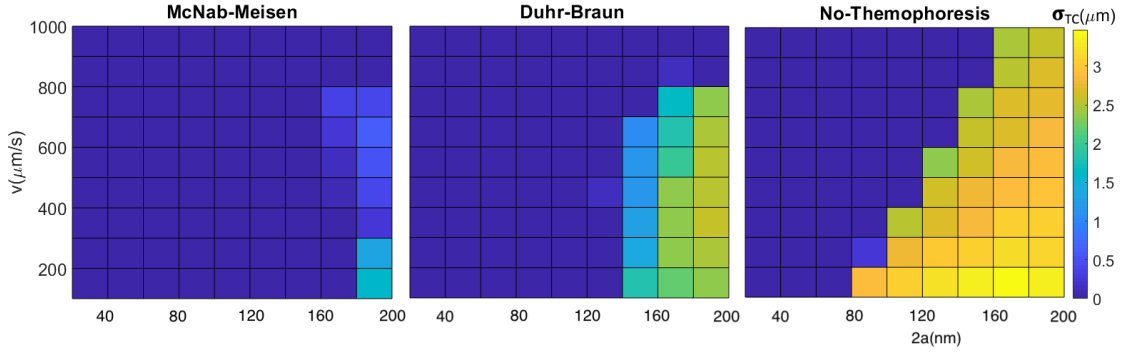
7.4 Effect of Thermophoresis on CFTA

As mentioned before, thermophoresis is a force in fluids with small particles suspended due to the presence of thermal gradients. Two models are introduced in Chapter 5, McNab-Meisen and Duhr-Braun. We make a simulation-based comparison between the mentioned thermophoresis models in this section. Two experiments are studied in the cavity by the CFTA technique. A polystyrene particle with a diameter of 200 nm is studied under different flow rates and laser powers. The beam waist is 989 nm which equals the RoC of 25 μm. Figure 7.15 shows the result of nanoparticle trapping cross-section for PS particles with disparate sizes and diverse flow rates and laser powers. Figure 7.15a shows the behavior of the particle in various velocities and laser powers.

As mentioned before (Section 5.2.4 of Chapter 5), the thermophoretic velocities are not similar in the two models (recall that thermophoretic velocity in McNab-Meisen model is 1.2 times larger than one in Duhr-Braun). Therefore, the probability of trapping in Figure 7.15b.left is less than that of Duhr-Braun. Further, the σ_{TC} is calculated when the size and velocity of the nanoparticle are



(a)



(b)

Figure 7.15: Nanoparticle trapping cross-section for different velocities against different interactivity powers in (a) McNab-Neisen and Duhr-Braun Models. (b) Thermophoretic effect on trapping nanoparticles in McNab-Meisen (left column), Duhr-Braun (middle column), and no thermophoresis (right column) models when interactivity power and RoC are $1\ W$ and $25\ \mu m$, respectively.

changed when the interactivity power is $1\ W$.

Figure 7.15b.left shows the action of the particle through the cavity concerning the size and velocity of particles in the McNab-Meisen model. It can be seen that the slow particles never reach the cavity by the thermophoresis effect. In McNab-Meisen model, a particle with a size of $180\ nm$ cannot reach the cavity with the small velocities due to the thermophoretic velocity that forces the particle to the cold side. Note that the thermophoretic velocity is proportional to the interactivity power that it caused to force the particle out of the cavity even with

the small flow velocity.

Figure 7.15b.left shows that a slow particle (100 $\mu m/s$) is escaped from the cavity while the same particle can be trapped with the speed of 700 $\mu m/s$. This means particles with small speeds can not be delivered through the cavity since the thermophoresis exists. The particle should have a proper flow rate to be driven through the cavity. Figure 7.15b.middle displays the dynamic behavior of particles through the cavity by the thermophoresis model of Duhr-Braun. According to these results, we expect to have a low chance of trap when it is compared with Figure 7.15b.right. It shows the same experiment in which we have not considered any thermophoretic force in the system. Figure 7.15b.right is presented to express the thermophoresis effects on suspended particles in liquid with these two models.

7.5 Summary

In summary, we introduced the CFTA technique for studying the nanoparticle dynamics in the optical cavity and analyzing the trapping rate as a function of the laser power, the size of the nanoparticle, and the flow rate. The CFTA measures the changes in the trapping rate of nanoparticles versus the laser power and the flow speed.

This technique allows us to effectively evaluate the size distribution of particles in the fluid if particles of known composition are taken with different sizes, then these can be distinguished. Thus, the CFTA model is a promising method to find the range of needed power and flow rate to overcome the Brownian force, and to trap nanoparticles. However, this result has motivated us to study other methods to increase the average interactivity power, e.g., by illuminating the cavity with a light source that provides constant optical injection.

CFTA can overcome the current problems in the common characterization

techniques. Common particle sizing techniques such as NTA and DLS can measure small particles in the range of $1 - 1000\ nm$. We also provided a resolution of $10\ nm$ in our method according to the experimental results of Chapter 7. As a result, this method can be a powerful technique to characterize nanoparticles in a solution in applications where we need high-resolution measurements at the single-particle level.

Not only this method can measure the size of particles but also it is sensitive to the refractive index of particles so that we can measure the polarizability of particles (Section 3.6 of Chapter 3 and experimental results of Chapter 6). The magnitude of the resonance shift reveals the particle polarizability, providing a useful fingerprint that is sensitive to the material composition of the nanoparticle. The technique, therefore, allows the differentiation of particles of similar size, as we showed by the distinction of polystyrene and PMMA particles. Therefore, our method can be used to give a measure of composition such as those used in drug loading for nanomedicine.

We also introduced CFTA-Eo as the upgraded technique to characterize nanoparticles with high resolution. In this technique, an electroosmotic flow is generated by the electric field without applying any pressure. Electroosmosis (Eo) is used as a promising type of micropump to deliver particles through the cavity that is purely driven by the electric field. As shown in the results, we can recognize small differences in particle sizes by the CFTA-Eo.

Chapter 8

Conclusions and Future Work

This chapter summarizes the dissertation by discussing key contributions and also the research directions that are currently under investigation.

8.1 Conclusions

In this work, we have developed a nanoparticle characterization method to characterize nanoparticles with a high sizing resolution in comparison with other techniques such as DLS. The flow-cell-based optical Fabry-Pérot is introduced as an optical tweezer to evaluate the size distribution of particles in the fluid. However, there are many techniques such as dynamic image analysis and laser light scattering that can detect small particles. However, these techniques provide limited resolution for polydisperse samples where larger particles dominate the scattered signal [52, 53].

As a result, this method can be a powerful technique to characterize nanoparticles in a solution in applications where we need high-resolution measurements at the single-particle level, quantitative diagnostics, and convenient analysis of

numerous samples. According to the results on the resolution of this method, we can overcome the current problems in the common characterization techniques. This technique is also sensitive to the refractive index of particles. Thus, the method can be used to give a measure of composition such as in drug loading for nano-medicine.

Also, we introduced the CFTA technique based on the stochastic modeling of nanoparticle dynamics suspended in a fluid subject. It is presented as a powerful means of understanding the range of behavior observed. This technique provides details of the instrument performance metrics and allows us to analyze signals and extract useful information.

CFTA technique analyzes the physical properties of nanoparticles in fluids by studying the competition between viscous drag and optical forces. By flowing particles through a microfluidic device containing an optical microcavity that acts as a combined optical trap and sensor, the variation of the rate of trapping events with the different forces can be established. By this concept, we were able to evaluate size and type distributions in the fluid. Further, the power of laser and speed of particles can be controlled to overcome the other forces and the particles are eventually able to be trapped. A clear threshold behavior is observed which provides a measure of a parameter combining the dielectric polarizability and the hydrodynamic radius. This technique could be applied in combination with other analytic techniques to provide a detailed physical characterization of particles in a given solution.

- Optical open-access cavity

  Advantages of the Technique:

  - The proposed characterization technique is useful for small quantities of nanoparticles.

  - This method reduces any potential biological damage to nanoparticles when being trapped or detected.
  - This method can be used where recovery of the samples is crucial.
  - Sample preparation is simple and the channel can be easily cleaned and thus, there is no contamination.
  - This method provides high peak resolution in the measurements.
  - Rapid assessment is another advantage of this technique.

- Optical open-access cavity

  Improvements of the Technique:

  - Additional improvements might be achieved by pumping the particles through the cavity using dielectrophoresis, which is capable of establishing a uniform flow rate across the flow channel.
  - The technique might also be used to measure thermophoretic effects that result from particle heating and can provide information on particle thermal conductivity [185, 186] or ionic shielding [187].

In summary, we showed

- Nanoparticle Size Characterisation

  Impact:

  - Detect the small PS particles (50 nm, 75 nm, and 100 nm)
  - Measure their mode shift and then polarizability of the particles
  - High resolution at the single-particle

- CFTA

  Impact:

- Powerful means in understanding the particle behavior
- Introducing the trap rate as particle distribution in a solution
- Evaluate size (140 nm, 175 nm) and material of particles (PS and PMMA)
- Evaluate differentiation of particles of similar size, as shown by the distinction of PS and PMMA particle with the size of 200 nm
- High resolution in sizing particle

- All the experiments are compared with the theory and the simulation results that are calculated by numerical and analytical methods

8.2 Future Work

There are a number of possible directions towards which the work in this dissertation can be developed further.

8.2.1 CFTA-Eo

The CFTA is limited to pressure-driven flows. Creating a uniform flow rate through the cavity is a non-trivial challenge in our flow cell. Electrophoretic flow is an alternative to pressure-driven flow, therefore, the CFTA can be improved by CFTA-Eo. It makes the problem of flow rate calibration easier to solve, as the flow profile is flat and linear. In future work, we suggest an electroosmotic pump to deliver nanoparticles through the cavity. Namely we can use an electroosmotic flow by the electric field without applying any pressure to deliver fluid in the channel. The trapping rate can be obtained by varying the flow velocity instead of the power of the laser. The resolution of the technique will be significantly improved as was expected by simulation results.

8.2.2 Different RoC

As shown in the simulation work, the RoC and the shape of the cavity can affect the resolution of particle size distribution. It would be worth doing experiments and making a comparison to what we simulated in this project.

8.2.3 Sorting Nanoparticles by CFTA

Optical manipulation of nanoparticles has drawn significant attention recently owing to its functional and noninvasive characteristics and significant value in biological and physical applications [206, 207], such as virus trapping [208], DNA stretching [209], and drug delivery [210]. Biomedical applications are in tremendous need of a setup that could not only trap small nanoparticles but also sort those nanoparticles up to the precision of single-nanometer resolution [211, 212]. Therefore, optical sorting is of increasing importance for applications in biomedical, environmental, and materials sciences [213]. The studied open-access microcavity in this work has the potential to sort nanoparticles.

As learned from CFTA, trapping nanoparticles is proportional to the power of the laser, flow velocity, and the beam waist of the laser. With understanding the particle behavior we can use this technique as a sorting technique as well. Figure 8.1 shows a schematic of the flow cell. A mixture with two different particle sizes can be introduced through the cavity with a constant flow.

Additionally, using the flow velocity concept can be the way to sort nanoparticles as seen in the CFTA technique. Namely, we can use one microcavity and the critical flow velocity for the small particles. The mixture of nanoparticles is delivered into the flow cell by an electroosmotic pump (to have a flat profile in the flow) to create a velocity greater than the critical velocity of the small nanoparticles and smaller than the critical velocity of the large particles. According to the CFTA, the large

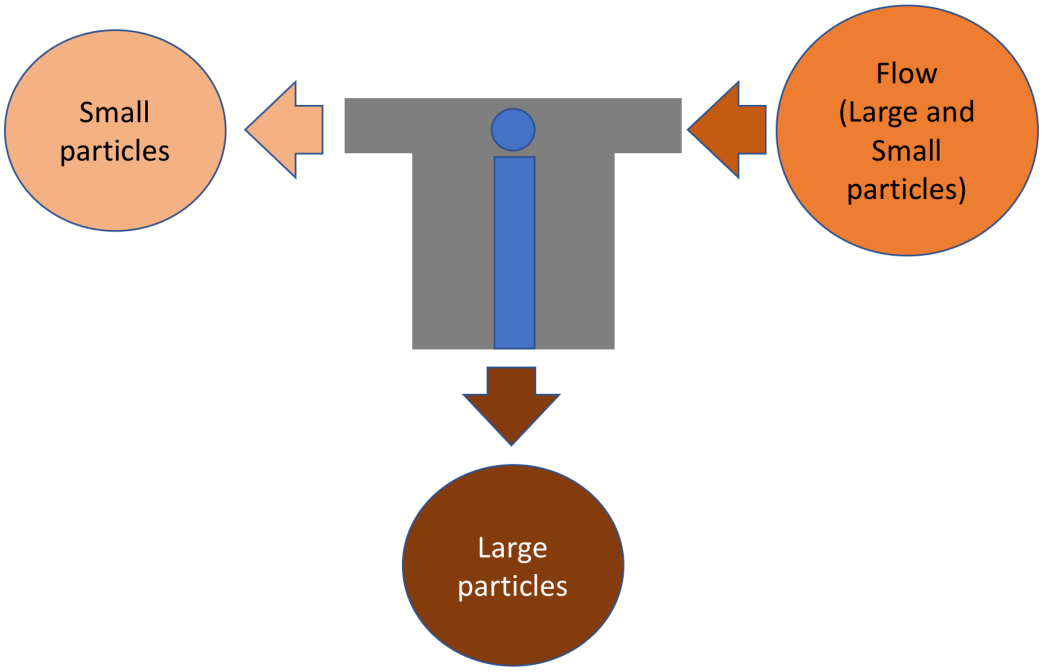


Figure 8.1: CFTA method as a sorting technique by using the cavity, an optical waveguide, and applying an external flow.

particles can be diffused through the optical antinodes due to their size, and the optical force can overcome the flow force. The optical waveguide helps the trapped nanoparticles to keep track by the scattering force and then depart from the flow cell. However, the small particles are escaped from the cavity because of the flow velocity.

8.2.4 Real Nanoparticles

We measured the PS and PMMA particles and showed the high resolution of the designed flow cell. The next step will be looking into a real-world nanoparticles solution as nanoparticle delivery such as the nano cups [214].

Bibliography

[1] K. Malmir, A. Trichet, R. Nyman, B. Ash, M. Contino, D. James, C. Vallance, and J. M. Smith, "Quantitative analysis of nanoparticle composition using open microcavities," in *International Conference On Nanomedicine And Nanobiotechnology*. SETCOR, 2019.

[2] A. Trichet, W. Okell, D. James, K. Malmir, C. Vallance, and J. M. Smith, "Nanoparticle sensing and analysis using open microcavities," in *S3IC*, 2019.

[3] K. Malmir, A. Trichet, and J. Smith, "Characterisation of nanoparticle size distributions in a fluid using optical microcavities," in *Photon*. IOP, 2020.

[4] K. Malmir, W. Okell, A. A. Trichet, and J. M. Smith, "Characterisation of nanoparticle size distributions in a fluid using optical forces," *arXiv preprint arXiv:2111.14989*, 2021.

[5] ——, "Characterization of polystyrene nanoparticle size in a mixture fluid by measuring polarizability," *arXiv preprint*, 2022.

[6] C. M. Hoo, N. Starostin, P. West, and M. L. Mecartney, "A comparison of atomic force microscopy (afm) and dynamic light scattering (dls) methods to characterize nanoparticle size distributions," *Journal of Nanoparticle Research*, vol. 10, no. 1, pp. 89–96, 2008.

[7] B. Inkson, "Scanning electron microscopy (sem) and transmission electron microscopy (tem) for materials characterization," in *Materials characterization using nondestructive evaluation (NDE) methods*. Elsevier, 2016, pp. 17–43.

[8] J. Lim, S. P. Yeap, H. X. Che, and S. C. Low, "Characterization of magnetic nanoparticle by dynamic light scattering," *Nanoscale research letters*, vol. 8, no. 1, pp. 1–14, 2013.

[9] N. Nirmalkar, A. Pacek, and M. Barigou, "Interpreting the interfacial and colloidal stability of bulk nanobubbles," *Soft matter*, vol. 14, no. 47, pp. 9643–9656, 2018.

[10] V. Filipe, A. Hawe, and W. Jiskoot, "Critical evaluation of nanoparticle tracking analysis (nta) by nanosight for the measurement of nanoparticles and protein aggregates," *Pharmaceutical research*, vol. 27, no. 5, pp. 796–810, 2010.

[11] M. C. L. Giudice, L. M. Herda, E. Polo, and K. A. Dawson, "In situ characterization of nanoparticle biomolecular interactions in complex biological media by flow cytometry," *Nature communications*, vol. 7, no. 1, pp. 1–10, 2016.

[12] T. Arab, E. R. Mallick, Y. Huang, L. Dong, Z. Liao, Z. Zhao, O. Gololobova, B. Smith, N. J. Haughey, K. J. Pienta *et al.*, "Characterization of extracellular vesicles and synthetic nanoparticles with four orthogonal single-particle analysis platforms," *Journal of extracellular vesicles*, vol. 10, no. 6, p. e12079, 2021.

[13] C. Minelli, A. Sikora, R. Garcia-Diez, K. Sparnacci, C. Gollwitzer, M. Krumrey, and A. G. Shard, "Measuring the size and density of nanoparticles by

centrifugal sedimentation and flotation," *Analytical Methods*, vol. 10, no. 15, pp. 1725–1732, 2018.

[14] A. Ashkin, "Nobel prize in physics"optical tweezers and their application to biological systems," *Nobel Prize in Physics*, 2018.

[15] T. Zhu, M. Mahdy, Y. Cao, H. Lv, F. Sun, Z. Jiang, and W. Ding, "Optical pulling using evanescent mode in sub-wavelength channels," *Optics express*, vol. 24, no. 16, pp. 18 436–18 444, 2016.

[16] S. Kühn, B. Phillips, E. Lunt, A. Hawkins, and H. Schmidt, "Ultralow power trapping and fluorescence detection of single particles on an optofluidic chip," *Lab on a Chip*, vol. 10, no. 2, pp. 189–194, 2010.

[17] S. Lin and K. B. Crozier, "An integrated microparticle sorting system based on near-field optical forces and a structural perturbation," *Optics express*, vol. 20, no. 4, pp. 3367–3374, 2012.

[18] ——, "Planar silicon microrings as wavelength-multiplexed optical traps for storing and sensing particles," *Lab on a Chip*, vol. 11, no. 23, pp. 4047–4051, 2011.

[19] S. Mandal, X. Serey, and D. Erickson, "Nanomanipulation using silicon photonic crystal resonators," *Nano letters*, vol. 10, no. 1, pp. 99–104, 2010.

[20] S. Lin, J. Hu, L. Kimerling, and K. Crozier, "Design of nanoslotted photonic crystal waveguide cavities for single nanoparticle trapping and detection," *Optics letters*, vol. 34, no. 21, pp. 3451–3453, 2009.

[21] D. Erickson, X. Serey, Y.-F. Chen, and S. Mandal, "Nanomanipulation using near field photonics," *Lab on a Chip*, vol. 11, no. 6, pp. 995–1009, 2011.

[22] L. Huang, S. J. Maerkl, and O. J. Martin, "Integration of plasmonic trapping in a microfluidic environment," *Optics express*, vol. 17, no. 8, pp. 6018–6024, 2009.

[23] P. R. Dolan, G. M. Hughes, F. Grazioso, B. R. Patton, and J. M. Smith, "Femtoliter tunable optical cavity arrays," *Optics letters*, vol. 35, no. 21, pp. 3556–3558, 2010.

[24] A. Trichet, P. Dolan, D. James, G. Hughes, C. Vallance, and J. Smith, "Nanoparticle trapping and characterization using open microcavities," *Nano letters*, vol. 16, no. 10, pp. 6172–6177, 2016.

[25] L. Korson, W. Drost-Hansen, and F. J. Millero, "Viscosity of water at various temperatures," *The Journal of Physical Chemistry*, vol. 73, no. 1, pp. 34–39, 1969.

[26] R. A. Serway and J. W. Jewett, *Principles of physics*. Saunders College Pub. Fort Worth, TX, 1998, vol. 1.

[27] C. V. Vo, F. Bunge, J. Duffy, and L. Hood, "Advances in thermal insulation of extruded polystyrene foams," *Cellular Polymers*, vol. 30, no. 3, pp. 137–156, 2011.

[28] A. Simpson, I. Rattigan, E. Kalavsky, and G. Parr, "Thermal conductivity and conditioning of grey expanded polystyrene foams," *Cellular Polymers*, vol. 39, no. 6, pp. 238–262, 2020.

[29] E. Algaer, "Thermal conductivity of polymer materials-reverse nonequilibrium molecular dynamics simulations," Ph.D. dissertation, Technische Universität, 2010.

[30] M. Assael, S. Botsios, K. Gialou, and I. Metaxa, "Thermal conductivity of polymethyl methacrylate (pmma) and borosilicate crown glass bk7," *International Journal of Thermophysics*, vol. 26, no. 5, pp. 1595–1605, 2005.

[31] Y. S. Touloukian and E. Buyco, "Thermophysical properties of matter-the tprc data series. volume 4. specific heat-metallic elements and alloys.(reannouncement). data book," Purdue Univ., Lafayette, IN (United States). Thermophysical and Electronic ..., Tech. Rep., 1971.

[32] M. Tanaka, G. Girard, R. Davis, A. Peuto, and N. Bignell, "Recommended table for the density of water between 0 c and 40 c based on recent experimental reports," *Metrologia*, vol. 38, no. 4, p. 301, 2001.

[33] R. Rezaei, M. Safaei, H. R. Mozaffari, H. Moradpoor, S. Karami, A. Golshah, B. Salimi, and H. Karami, "The role of nanomaterials in the treatment of diseases and their effects on the immune system," *Open access Macedonian journal of medical sciences*, vol. 7, no. 11, p. 1884, 2019.

[34] A. Mokhtarzadeh, R. Eivazzadeh-Keihan, P. Pashazadeh, M. Hejazi, N. Gharaatifar, M. Hasanzadeh, B. Baradaran, and M. de la Guardia, "Nanomaterial-based biosensors for detection of pathogenic virus," *TrAC Trends in Analytical Chemistry*, vol. 97, pp. 445–457, 2017.

[35] R. Toy and K. Roy, "Engineering nanoparticles to overcome barriers to immunotherapy," *Bioengineering & translational medicine*, vol. 1, no. 1, pp. 47–62, 2016.

[36] A. Hasan, M. Morshed, A. Memic, S. Hassan, T. J. Webster, and H. E.-S. Marei, "Nanoparticles in tissue engineering: applications, challenges and prospects," *International journal of nanomedicine*, vol. 13, p. 5637, 2018.

[37] S. Chapman, M. Dobrovolskaia, K. Farahani, A. Goodwin, A. Joshi, H. Lee, T. Meade, M. Pomper, K. Ptak, J. Rao *et al.*, "Nanoparticles for cancer imaging: The good, the bad, and the promise," *Nano today*, vol. 8, no. 5, pp. 454–460, 2013.

[38] S. Caspani, R. Magalhães, J. P. Araújo, and C. T. Sousa, "Magnetic nanomaterials as contrast agents for mri," *Materials*, vol. 13, no. 11, p. 2586, 2020.

[39] T. M. Göppert and R. H. Müller, "Polysorbate-stabilized solid lipid nanoparticles as colloidal carriers for intravenous targeting of drugs to the brain: comparison of plasma protein adsorption patterns," *Journal of drug targeting*, vol. 13, no. 3, pp. 179–187, 2005.

[40] Y. Duan, A. Dhar, C. Patel, M. Khimani, S. Neogi, P. Sharma, N. S. Kumar, and R. L. Vekariya, "A brief review on solid lipid nanoparticles: Part and parcel of contemporary drug delivery systems," *RSC Advances*, vol. 10, no. 45, pp. 26 777–26 791, 2020.

[41] E. S. Kawasaki and A. Player, "Nanotechnology, nanomedicine, and the development of new, effective therapies for cancer," *Nanomedicine: Nanotechnology, Biology and Medicine*, vol. 1, no. 2, pp. 101–109, 2005.

[42] R. R. Joseph and S. S. Venkatraman, "Drug delivery to the eye: what benefits do nanocarriers offer?" *Nanomedicine*, vol. 12, no. 6, pp. 683–702, 2017.

[43] N. Kamaly, B. Yameen, J. Wu, and O. C. Farokhzad, "Degradable controlled-release polymers and polymeric nanoparticles: mechanisms of controlling drug release," *Chemical reviews*, vol. 116, no. 4, pp. 2602–2663, 2016.

[44] D. Lombardo, M. A. Kiselev, and M. T. Caccamo, "Smart nanoparticles for drug delivery application: development of versatile nanocarrier platforms in biotechnology and nanomedicine," *Journal of Nanomaterials*, vol. 2019, 2019.

[45] K. L. Swingle, A. G. Hamilton, and M. J. Mitchell, "Lipid nanoparticle-mediated delivery of mrna therapeutics and vaccines," *Trends in Molecular Medicine*, vol. 27, no. 6, pp. 616–617, 2021.

[46] L. Zhang, P. Wang, Q. Feng, N. Wang, Z. Chen, Y. Huang, W. Zheng, and X. Jiang, "Lipid nanoparticle-mediated efficient delivery of crispr/cas9 for tumor therapy," *NPG Asia Materials*, vol. 9, no. 10, pp. e441–e441, 2017.

[47] F. Caruso, T. Hyeon, and V. M. Rotello, "Nanomedicine," *Chemical Society Reviews*, vol. 41, no. 7, pp. 2537–2538, 2012.

[48] R. Wang and O. Farokhzad, "Nanoparticle delivery of cancer drugs," *Annu. Rev. Med*, vol. 10, 2012.

[49] S. Svenson, "What nanomedicine in the clinic right now really forms nanoparticles?" *Wiley Interdisciplinary Reviews: Nanomedicine and Nanobiotechnology*, vol. 6, no. 2, pp. 125–135, 2014.

[50] A. K. Jain and S. Thareja, "In vitro and in vivo characterization of pharmaceutical nanocarriers used for drug delivery," *Artificial cells, nanomedicine, and biotechnology*, vol. 47, no. 1, pp. 524–539, 2019.

[51] J. Stetefeld, S. A. McKenna, and T. R. Patel, "Dynamic light scattering: a practical guide and applications in biomedical sciences," *Biophysical reviews*, vol. 8, no. 4, pp. 409–427, 2016.

[52] S. Soares, J. Sousa, A. Pais, and C. Vitorino, "Nanomedicine: principles, properties, and regulatory issues," *Frontiers in chemistry*, vol. 6, p. 360, 2018.

[53] S. Mourdikoudis, R. M. Pallares, and N. T. Thanh, "Characterization techniques for nanoparticles: comparison and complementarity upon studying nanoparticle properties," *Nanoscale*, vol. 10, no. 27, pp. 12 871–12 934, 2018.

[54] E. Nakamura, N. A. Sommerdijk, and H. Zheng, "Transmission electron microscopy for chemists," *Accounts of chemical research*, vol. 50, no. 8, pp. 1795–1796, 2017.

[55] E. Orlova and H. R. Saibil, "Structural analysis of macromolecular assemblies by electron microscopy," *Chemical reviews*, vol. 111, no. 12, pp. 7710–7748, 2011.

[56] G. Binnig, C. F. Quate, and C. Gerber, "Atomic force microscope," *Physical review letters*, vol. 56, no. 9, p. 930, 1986.

[57] Y. Seo and W. Jhe, "Atomic force microscopy and spectroscopy," *Reports on Progress in Physics*, vol. 71, no. 1, p. 016101, 2007.

[58] A. Surrey, D. Pohl, L. Schultz, and B. Rellinghaus, "Quantitative measurement of the surface self-diffusion on au nanoparticles by aberration-corrected transmission electron microscopy," *Nano letters*, vol. 12, no. 12, pp. 6071–6077, 2012.

[59] C. Troiber, J. C. Kasper, S. Milani, M. Scheible, I. Martin, F. Schaubhut, S. Küchler, J. Rädler, F. C. Simmel, W. Friess *et al.*, "Comparison of four different particle sizing methods for sirna polyplex characterization," *European Journal of Pharmaceutics and Biopharmaceutics*, vol. 84, no. 2, pp. 255–264, 2013.

[60] N. C. Bell, C. Minelli, and A. G. Shard, "Quantitation of igg protein adsorption to gold nanoparticles using particle size measurement," *Analytical Methods*, vol. 5, no. 18, pp. 4591–4601, 2013.

[61] P. Y. Chiou, A. T. Ohta, and M. C. Wu, "Massively parallel manipulation of single cells and microparticles using optical images," *Nature*, vol. 436, no. 7049, p. 370, 2005.

[62] A. Ashkin, "Acceleration and trapping of particles by radiation pressure," *Physical review letters*, vol. 24, no. 4, p. 156, 1970.

[63] ——, "History of optical trapping and manipulation of small-neutral particle, atoms, and molecules," *IEEE Journal of Selected Topics in Quantum Electronics*, vol. 6, no. 6, pp. 841–856, 2000.

[64] A. Ashkin, J. M. Dziedzic, J. Bjorkholm, and S. Chu, "Observation of a single-beam gradient force optical trap for dielectric particles," *Optics letters*, vol. 11, no. 5, pp. 288–290, 1986.

[65] C. Vallance, A. A. Trichet, D. James, P. R. Dolan, and J. M. Smith, "Open-access microcavities for chemical sensing," *Nanotechnology*, vol. 27, no. 27, p. 274003, 2016.

[66] J. Mullins, "How to manipulate nanoparticles with lasers," *Physics*, vol. 5, p. 95, 2012.

[67] A. Trichet, J. Foster, N. Omori, D. James, P. Dolan, G. Hughes, C. Vallance, and J. Smith, "Open-access optical microcavities for lab-on-a-chip refractive index sensing," *Lab on a Chip*, vol. 14, no. 21, pp. 4244–4249, 2014.

[68] H. Bahadar, F. Maqbool, K. Niaz, and M. Abdollahi, "Toxicity of nanoparticles and an overview of current experimental models," *Iranian biomedical journal*, vol. 20, no. 1, p. 1, 2016.

[69] S. G. Elci, Y. Jiang, B. Yan, S. T. Kim, K. Saha, D. F. Moyano, G. Yesilbag Tonga, L. C. Jackson, V. M. Rotello, and R. W. Vachet, "Surface charge

controls the suborgan biodistributions of gold nanoparticles," *ACS nano*, vol. 10, no. 5, pp. 5536–5542, 2016.

[70] M. M. Modena, B. Rühle, T. P. Burg, and S. Wuttke, "Nanoparticle characterization: what to measure?" *Advanced Materials*, vol. 31, no. 32, p. 1901556, 2019.

[71] M. Lanza, *Conductive Atomic Force Microscopy: Applications in Nanomaterials*. John Wiley & Sons, 2017.

[72] S. Rades, V.-D. Hodoroaba, T. Salge, T. Wirth, M. P. Lobera, R. H. Labrador, K. Natte, T. Behnke, T. Gross, and W. E. Unger, "High-resolution imaging with sem/t-sem, edx and sam as a combined methodical approach for morphological and elemental analyses of single engineered nanoparticles," *Rsc Advances*, vol. 4, no. 91, pp. 49 577–49 587, 2014.

[73] C. Chen, S. Zhu, T. Huang, S. Wang, and X. Yan, "Analytical techniques for single-liposome characterization," *Analytical Methods*, vol. 5, no. 9, pp. 2150–2157, 2013.

[74] C. Chen, S. Zhu, S. Wang, W. Zhang, Y. Cheng, and X. Yan, "Multiparameter quantification of liposomal nanomedicines at the single-particle level by high-sensitivity flow cytometry," *ACS applied materials & interfaces*, vol. 9, no. 16, pp. 13 913–13 919, 2017.

[75] E. Van der Pol, F. Coumans, A. Grootemaat, C. Gardiner, I. Sargent, P. Harrison, A. Sturk, T. Van Leeuwen, and R. Nieuwland, "Particle size distribution of exosomes and microvesicles determined by transmission electron microscopy, flow cytometry, nanoparticle tracking analysis, and resistive pulse sensing," *Journal of Thrombosis and Haemostasis*, vol. 12, no. 7, pp. 1182–1192, 2014.

[76] V. Ponath, N. Hoffmann, L. Bergmann, C. Mäder, B. Alashkar Alhamwe, C. Preußer, and E. Pogge von Strandmann, "Secreted ligands of the nk cell receptor nkp30: B7-h6 is in contrast to bag6 only marginally released via extracellular vesicles," *International journal of molecular sciences*, vol. 22, no. 4, p. 2189, 2021.

[77] G. B. Edwards, U. M. Muthurajan, S. Bowerman, and K. Luger, "Analytical ultracentrifugation (auc): An overview of the application of fluorescence and absorbance auc to the study of biological macromolecules," *Current Protocols in Molecular Biology*, vol. 133, no. 1, p. e131, 2020.

[78] D. J. Scott and P. Schuck, "A brief introduction to the analytical ultracentrifugation of proteins for beginners," pp. 1–25, 2005.

[79] J. Cole and J. Hansen, "Analytical ultracentrifugation as a contemporary biomolecular research tool," *Journal of biomolecular techniques: JBT*, vol. 10, no. 4, p. 163, 1999.

[80] J. Graham, *Biological centrifugation*. Garland Science, 2020.

[81] Z. Aziz, J. Behlke, G. Bernardi, L. Bourdillon, P. Butler, N. Carels, O. Clay, H. Colfen, J. Correia, M. Daugherty *et al.*, *Analytical ultracentrifugation: techniques and methods*. Royal Society of Chemistry, 2007.

[82] A. G. Shard, K. Sparnacci, A. Sikora, L. Wright, D. Bartczak, H. Goenaga-Infante, and C. Minelli, "Measuring the relative concentration of particle populations using differential centrifugal sedimentation," *Analytical Methods*, vol. 10, no. 22, pp. 2647–2657, 2018.

[83] Z. Krpetic, A. M. Davidson, M. Volk, R. Levy, M. Brust, and D. L. Cooper, "High-resolution sizing of monolayer-protected gold clusters by differential centrifugal sedimentation," *Acs Nano*, vol. 7, no. 10, pp. 8881–8890, 2013.

[84] A. Rao, M. Schoenenberger, E. Gnecco, T. Glatzel, E. Meyer, D. Brändlin, and L. Scandella, "Characterization of nanoparticles using atomic force microscopy," in *Journal of Physics: Conference Series*, vol. 61, no. 1. IOP Publishing, 2007, p. 192.

[85] J. I. Goldstein, D. E. Newbury, J. R. Michael, N. W. Ritchie, J. H. J. Scott, and D. C. Joy, *Scanning electron microscopy and X-ray microanalysis*. Springer, 2017.

[86] V.-D. Hodoroaba, S. Rades, T. Salge, J. Mielke, E. Ortel, and R. Schmidt, "Characterisation of nanoparticles by means of high-resolution sem/eds in transmission mode," in *IOP Conference Series: Materials Science and Engineering*, vol. 109, no. 1. IOP Publishing, 2016, p. 012006.

[87] G. Hübschen, I. Altpeter, R. Tschuncky, and H.-G. Herrmann, *Materials characterization using nondestructive evaluation (NDE) methods*. Woodhead publishing, 2016.

[88] U. Dahmen, R. Erni, V. Radmilovic, C. Ksielowski, M.-D. Rossell, and P. Denes, "Background, status and future of the transmission electron aberration-corrected microscope project," *Philosophical Transactions of the Royal Society A: Mathematical, Physical and Engineering Sciences*, vol. 367, no. 1903, pp. 3795–3808, 2009.

[89] W. Anderson, D. Kozak, V. A. Coleman, Å. K. Jämting, and M. Trau, "A comparative study of submicron particle sizing platforms: accuracy, precision and resolution analysis of polydisperse particle size distributions," *Journal of colloid and interface science*, vol. 405, pp. 322–330, 2013.

[90] C.-L. Huang, "A study of the optical properties and fabrication of coatings made of three-dimensional photonic glass," *Coatings*, vol. 10, no. 8, p. 781, 2020.

[91] X. Liu, T. K. Ali, P. Singh, A. Shah, S. M. McKinney, P. Ruamviboonsuk, A. W. Turner, P. A. Keane, P. Chotcomwongse, V. Nganthavee *et al.*, "Deep learning to detect optical coherence tomography-derived diabetic macular edema from retinal photographs: a multicenter validation study," *Ophthalmology Retina*, 2022.

[92] A. M. Streets, Y. Sourigues, R. R. Kopito, R. Melki, and S. R. Quake, "Simultaneous measurement of amyloid fibril formation by dynamic light scattering and fluorescence reveals complex aggregation kinetics," *PloS one*, vol. 8, no. 1, p. e54541, 2013.

[93] R. Pecora, "Dynamic light scattering measurement of nanometer particles in liquids," *Journal of nanoparticle research*, vol. 2, no. 2, pp. 123–131, 2000.

[94] P. C. Simons, S. M. Young, M. B. Carter, A. Waller, D. Zhai, J. C. Reed, B. S. Edwards, and L. A. Sklar, "Simultaneous in vitro molecular screening of protein-peptide interactions by flow cytometry, using six bcl-2 family proteins as examples," *Nature protocols*, vol. 6, no. 7, pp. 943–952, 2011.

[95] G. Grégori, V. Patsekin, B. Rajwa, J. Jones, K. Ragheb, C. Holdman, and J. P. Robinson, "Hyperspectral cytometry at the single-cell level using a 32-channel photodetector," *Cytometry Part A*, vol. 81, no. 1, pp. 35–44, 2012.

[96] B. Bisha and B. F. Brehm-Stecher, "Flow cytometry for rapid detection of salmonella spp. in seed sprouts," *ScienceOpen Research*, vol. 1, 2014.

[97] R. K. Robinson, *Encyclopedia of food microbiology*. Academic press, 2014.

[98] S. Zhu, S. Wang, L. Yang, T. Huang, and X. Yan, "Progress in the development of techniques based on light scattering for single nanoparticle detection," *Science China Chemistry*, vol. 54, no. 8, p. 1244, 2011.

[99] H. B. Steen, "Flow cytometer for measurement of the light scattering of viral and other submicroscopic particles," *Cytometry Part A: the journal of the International Society for Analytical Cytology*, vol. 57, no. 2, pp. 94–99, 2004.

[100] A. N. Böing, E. Van Der Pol, A. E. Grootemaat, F. A. Coumans, A. Sturk, and R. Nieuwland, "Single-step isolation of extracellular vesicles by size-exclusion chromatography," *Journal of extracellular vesicles*, vol. 3, no. 1, p. 23430, 2014.

[101] T. M. Laue and W. F. Stafford III, "Modern applications of analytical ultracentrifugation," *Annual review of biophysics and biomolecular structure*, vol. 28, no. 1, pp. 75–100, 1999.

[102] G. J. Howlett, A. P. Minton, and G. Rivas, "Analytical ultracentrifugation for the study of protein association and assembly," *Current opinion in chemical biology*, vol. 10, no. 5, pp. 430–436, 2006.

[103] J. Lebowitz, M. S. Lewis, and P. Schuck, "Modern analytical ultracentrifugation in protein science: a tutorial review," *Protein science*, vol. 11, no. 9, pp. 2067–2079, 2002.

[104] J. L. Cole, J. W. Lary, T. P. Moody, and T. M. Laue, "Analytical ultracentrifugation: sedimentation velocity and sedimentation equilibrium," *Methods in cell biology*, vol. 84, pp. 143–179, 2008.

[105] P. Schuck, H. Zhao, C. A. Brautigam, and R. Ghirlando, *Basic principles of analytical ultracentrifugation*. CRC Press Boca Raton, FL, 2016, vol. 2015.

[106] H. Kim, R. P. Carney, J. Reguera, Q. K. Ong, X. Liu, and F. Stellacci, "Synthesis and characterization of janus gold nanoparticles," *Advanced materials*, vol. 24, no. 28, pp. 3857–3863, 2012.

[107] A. Bekdemir and F. Stellacci, "A centrifugation-based physicochemical characterization method for the interaction between proteins and nanoparticles," *Nature communications*, vol. 7, no. 1, pp. 1–8, 2016.

[108] J. Walter, K. Lohr, E. Karabudak, W. Reis, J. Mikhael, W. Peukert, W. Wohlleben, and H. Colfen, "Multidimensional analysis of nanoparticles with highly disperse properties using multiwavelength analytical ultracentrifugation," *ACS nano*, vol. 8, no. 9, pp. 8871–8886, 2014.

[109] H. Cölfen, "Analytical ultracentrifugation of nanoparticles," *Polymer News*, vol. 29, no. 4, pp. 101–116, 2004.

[110] C. A. Barrios, "Integrated microring resonator sensor arrays for labs-on-chips," *Analytical and bioanalytical chemistry*, vol. 403, no. 6, pp. 1467–1475, 2012.

[111] X. Chen, H. Guan, Z. He, X. Zhou, and J. Hu, "A sensitive and selective label-free dnazyme-based sensor for lead ions by using a conjugated polymer," *Analytical Methods*, vol. 4, no. 6, pp. 1619–1622, 2012.

[112] A. Al-Rashid and S. John, "Optical biosensing of multiple disease markers in a photonic-band-gap lab-on-a-chip: a conceptual paradigm," *Physical Review Applied*, vol. 3, no. 3, p. 034001, 2015.

[113] H. Huang, F. Shi, Y. Li, L. Niu, Y. Gao, S. M. Shah, and X. Su, "Water-soluble conjugated polymer–cu (ii) system as a turn-on fluorescence probe for label-free detection of glutathione and cysteine in biological fluids," *Sensors and Actuators B: Chemical*, vol. 178, pp. 532–540, 2013.

[114] P. Debackere, S. Scheerlinck, P. Bienstman, and R. Baets, "Surface plasmon interferometer in silicon-on-insulator: novel concept for an integrated biosensor," *Optics Express*, vol. 14, no. 16, pp. 7063–7072, 2006.

[115] S. Balslev, A. Jorgensen, B. Bilenberg, K. B. Mogensen, D. Snakenborg, O. Geschke, J. P. Kutter, and A. Kristensen, "Lab-on-a-chip with integrated optical transducers," *Lab on a Chip*, vol. 6, no. 2, pp. 213–217, 2006.

[116] S. Kuiper and B. Hendriks, "Variable-focus liquid lens for miniature cameras," *Applied physics letters*, vol. 85, no. 7, pp. 1128–1130, 2004.

[117] L. Dong, A. K. Agarwal, D. J. Beebe, and H. Jiang, "Adaptive liquid microlenses activated by stimuli-responsive hydrogels," *Nature*, vol. 442, no. 7102, pp. 551–554, 2006.

[118] X. Heng, D. Erickson, L. R. Baugh, Z. Yaqoob, P. W. Sternberg, D. Psaltis, and C. Yang, "Optofluidic microscopy—a method for implementing a high resolution optical microscope on a chip," *Lab on a Chip*, vol. 6, no. 10, pp. 1274–1276, 2006.

[119] B. S. Schmidt, A. H. Yang, D. Erickson, and M. Lipson, "Optofluidic trapping and transport on solid core waveguides within a microfluidic device," *Optics Express*, vol. 15, no. 22, pp. 14 322–14 334, 2007.

[120] G. Mie, "Beiträge zur optik trüber medien, speziell kolloidaler metallösungen," *Annalen der physik*, vol. 330, no. 3, pp. 377–445, 1908.

[121] R. Marchington, M. Mazilu, S. Kuriakose, V. Garcés-Chávez, P. Reece, T. Krauss, M. Gu, and K. Dholakia, "Optical deflection and sorting of microparticles in a near-field optical geometry," *Optics express*, vol. 16, no. 6, pp. 3712–3726, 2008.

[122] J. E. Baker, R. P. Badman, and M. D. Wang, "Nanophotonic trapping: precise manipulation and measurement of biomolecular arrays," *Wiley Interdisciplinary Reviews: Nanomedicine and Nanobiotechnology*, vol. 10, no. 1, p. e1477, 2018.

[123] N. Malmir and K. Fasihi, "A highly-sensitive label-free biosensor based on two dimensional photonic crystals with negative refraction," *Journal of Modern Optics*, vol. 64, no. 20, pp. 2195–2200, 2017.

[124] K. Malmir, H. Habibiyan, and H. Ghafoorifard, "Ultrasensitive optical biosensors based on microresonators with bent waveguides," *Optik*, vol. 216, p. 164906, 2020.

[125] K. Scholten, W. Collin, X. Fan, and E. Zellers, "Nanoparticle-coated microoptofluidic ring resonator as a detector for microscale gas chromatographic vapor analysis," *Nanoscale*, vol. 7, no. 20, pp. 9282–9289, 2015.

[126] K. Malmir, H. Habibiyan, and H. Ghafoorifard, "An ultrasensitive optical label-free polymeric biosensor based on concentric triple microring resonators with a central microdisk resonator," *Optics Communications*, vol. 365, pp. 150–156, 2016.

[127] E. Verpoorte, "Focusbeads and chips: New recipes for analysis," *Lab on a Chip*, vol. 3, no. 4, pp. 60N–68N, 2003.

[128] K. B. Mogensen, H. Klank, and J. P. Kutter, "Recent developments in detection for microfluidic systems," *Electrophoresis*, vol. 25, no. 21-22, pp. 3498–3512, 2004.

[129] D. Psaltis, S. R. Quake, and C. Yang, "Developing optofluidic technology through the fusion of microfluidics and optics," *nature*, vol. 442, no. 7101, pp. 381–386, 2006.

[130] N.-T. Huang, H.-l. Zhang, M.-T. Chung, J. H. Seo, and K. Kurabayashi, "Recent advancements in optofluidics-based single-cell analysis: optical on-chip cellular manipulation, treatment, and property detection," *Lab on a Chip*, vol. 14, no. 7, pp. 1230–1245, 2014.

[131] W. Zhang, L. Huang, C. Santschi, and O. J. Martin, "Trapping and sensing 10 nm metal nanoparticles using plasmonic dipole antennas," *Nano letters*, vol. 10, no. 3, pp. 1006–1011, 2010.

[132] M. Daly, V. G. Truong, and S. N. Chormaic, "Evanescent field trapping of nanoparticles using nanostructured ultrathin optical fibers," *Optics express*, vol. 24, no. 13, pp. 14 470–14 482, 2016.

[133] Y. Liu, G. Sonek, M. Berns, and B. Tromberg, "Physiological monitoring of optically trapped cells: assessing the effects of confinement by 1064-nm laser tweezers using microfluorometry," *Biophysical Journal*, vol. 71, no. 4, pp. 2158–2167, 1996.

[134] D. Goswami, "Nobel prize in physics–2018," *Resonance*, vol. 23, no. 12, pp. 1333–1341, 2018.

[135] P. Schein, P. Kang, D. O'Dell, and D. Erickson, "Nanophotonic force microscopy: characterizing particle–surface interactions using near-field photonics," *Nano letters*, vol. 15, no. 2, pp. 1414–1420, 2015.

[136] A. H. Yang, T. Lerdsuchatawanich, and D. Erickson, "Forces and transport velocities for a particle in a slot waveguide," *Nano letters*, vol. 9, no. 3, pp. 1182–1188, 2009.

[137] S. Lin, E. Schonbrun, and K. Crozier, "Optical manipulation with planar silicon microring resonators," *Nano letters*, vol. 10, no. 7, pp. 2408–2411, 2010.

[138] S. Arnold, D. Keng, S. Shopova, S. Holler, W. Zurawsky, and F. Vollmer, "Whispering gallery mode carousel–a photonic mechanism for enhanced nanoparticle detection in biosensing," *Optics Express*, vol. 17, no. 8, pp. 6230–6238, 2009.

[139] A. H. Yang and D. Erickson, "Optofluidic ring resonator switch for optical particle transport," *Lab on a Chip*, vol. 10, no. 6, pp. 769–774, 2010.

[140] M. Righini, G. Volpe, C. Girard, D. Petrov, and R. Quidant, "Surface plasmon optical tweezers: tunable optical manipulation in the femtonewton range," *Physical review letters*, vol. 100, no. 18, p. 186804, 2008.

[141] G. Testa, Y. Huang, L. Zeni, P. M. Sarro, and R. Bernini, "Waveguide based optofluidics," in *Silicon Photonics V*, vol. 7606. International Society for Optics and Photonics, 2010, p. 76060A.

[142] L. Ng, M. Zervas, J. Wilkinson, and B. Luff, "Manipulation of colloidal gold nanoparticles in the evanescent field of a channel waveguide," *Applied Physics Letters*, vol. 76, no. 15, pp. 1993–1995, 2000.

[143] M. J. N. Sampad, H. Zhang, T. D. Yuzvinsky, M. A. Stott, A. R. Hawkins, and H. Schmidt, "Optical trapping assisted label-free and amplification-free detection of sars-cov-2 rnas with an optofluidic nanopore sensor," *Biosensors and Bioelectronics*, vol. 194, p. 113588, 2021.

[144] T. Wall, J. McMurray, G. Meena, V. Ganjalizadeh, H. Schmidt, and A. R. Hawkins, "Optofluidic lab-on-a-chip fluorescence sensor using integrated buried arrow (barrow) waveguides," *Micromachines*, vol. 8, no. 8, p. 252, 2017.

[145] K. Wang, E. Schonbrun, P. Steinvurzel, and K. B. Crozier, "Trapping and rotating nanoparticles using a plasmonic nano-tweezer with an integrated heat sink," *Nature communications*, vol. 2, no. 1, pp. 1–6, 2011.

[146] A. H. Yang, S. D. Moore, B. S. Schmidt, M. Klug, M. Lipson, and D. Erickson, "Optical manipulation of nanoparticles and biomolecules in sub-wavelength slot waveguides," *Nature*, vol. 457, no. 7225, pp. 71–75, 2009.

[147] S. Campopiano, R. Bernini, L. Zeni, and P. M. Sarro, "Microfluidic sensor based on integrated optical hollow waveguides," *Optics letters*, vol. 29, no. 16, pp. 1894–1896, 2004.

[148] K. D. Leake, B. S. Phillips, T. D. Yuzvinsky, A. R. Hawkins, and H. Schmidt, "Optical particle sorting on an optofluidic chip," *Optics express*, vol. 21, no. 26, pp. 32 605–32 610, 2013.

[149] H. Inan, M. Poyraz, F. Inci, M. A. Lifson, M. Baday, B. T. Cunningham, and U. Demirci, "Photonic crystals: emerging biosensors and their promise for point-of-care applications," *Chemical society reviews*, vol. 46, no. 2, pp. 366–388, 2017.

[150] H. M. Wong, M. Righini, J. C. Gates, P. G. R. Smith, V. Pruneri, and R. Quidant, "On-a-chip surface plasmon tweezers," *Applied Physics Letters*, vol. 99, no. 6, p. 061107, 2011.

[151] R. H. Ritchie, "Plasma losses by fast electrons in thin films," *Physical review*, vol. 106, no. 5, p. 874, 1957.

[152] M. Righini, P. Ghenuche, S. Cherukulappurath, V. Myroshnychenko, F. J. Garcia de Abajo, and R. Quidant, "Nano-optical trapping of rayleigh particles and escherichia coli bacteria with resonant optical antennas," *Nano letters*, vol. 9, no. 10, pp. 3387–3391, 2009.

[153] G. Volpe, R. Quidant, G. Badenes, and D. Petrov, "Surface plasmon radiation forces," *Physical review letters*, vol. 96, no. 23, p. 238101, 2006.

[154] T. Čižmár, M. Šiler, M. Šerỳ, P. Zemánek, V. Garcés-Chávez, and K. Dholakia, "Optical sorting and detection of submicrometer objects in a motional standing wave," *Physical Review B*, vol. 74, no. 3, p. 035105, 2006.

[155] Y. Colombe, T. Steinmetz, G. Dubois, F. Linke, D. Hunger, and J. Reichel, "Strong atom–field coupling for bose–einstein condensates in an optical cavity on a chip," *Nature*, vol. 450, no. 7167, pp. 272–276, 2007.

[156] B. Brandstätter, A. McClung, K. Schüppert, B. Casabone, K. Friebe, A. Stute, P. O. Schmidt, C. Deutsch, J. Reichel, R. Blatt *et al.*, "Integrated fiber-mirror ion trap for strong ion-cavity coupling," *Review of Scientific Instruments*, vol. 84, no. 12, p. 123104, 2013.

[157] J. Miguel-Sánchez, A. Reinhard, E. Togan, T. Volz, A. Imamoglu, B. Besga, J. Reichel, and J. Estève, "Cavity quantum electrodynamics with charge-controlled quantum dots coupled to a fiber fabry–perot cavity," *New Journal of Physics*, vol. 15, no. 4, p. 045002, 2013.

[158] I. Favero, S. Stapfner, D. Hunger, P. Paulitschke, J. Reichel, H. Lorenz, E. M. Weig, and K. Karrai, "Fluctuating nanomechanical system in a high finesse optical microcavity," *Optics express*, vol. 17, no. 15, pp. 12 813–12 820, 2009.

[159] M. Mader, J. Reichel, T. W. Hänsch, and D. Hunger, "A scanning cavity microscope," *Nature communications*, vol. 6, no. 1, pp. 1–7, 2015.

[160] Z. Geng, K. Peters, A. Trichet, K. Malmir, R. Kolkowski, J. Smith, and S. Rodriguez, "Universal power law decay in the dynamic hysteresis of an optical cavity with non-instantaneous photon-photon interactions," *arXiv preprint arXiv:1911.00463*, 2019.

[161] ——, "Universal scaling in the dynamic hysteresis, and non-markovian dynamics, of a tunable optical cavity," *Physical Review Letters*, vol. 124, no. 15, p. 153603, 2020.

[162] K. Peters, Z. Geng, K. Malmir, J. Smith, and S. Rodriguez, "Non-markovian stochastic resonance of light in a microcavity," *arXiv preprint arXiv:2008.11615*, 2020.

[163] ——, "Extremely broadband stochastic resonance of light and enhanced energy harvesting enabled by memory effects in the nonlinear response," *Physical Review Letters*, vol. 126, no. 21, p. 213901, 2021.

[164] K. Peters, Z. Geng, K. Malmir, and R. S. Smith, Jason, "Ultra-broadband stochastic resonance of light enabled by memory effects in the nonlinear response," in *EOSAM*, 2021.

[165] F. Wang, Y. Liu, Y. Lu, L. Zhang, J. Ma, L. Wang, and W. Sun, "High-sensitivity fabry–perot interferometer temperature sensor probe based on liquid crystal and the vernier effect," *Optics letters*, vol. 43, no. 21, pp. 5355–5358, 2018.

[166] J. Tian, Y. Jiao, Q. Fu, S. Ji, Z. Li, M. Quan, and Y. Yao, "A fabry–perot interferometer strain sensor based on concave-core photonic crystal fiber," *Journal of Lightwave Technology*, vol. 36, no. 10, pp. 1952–1958, 2018.

[167] A. Trichet, P. R. Dolan, D. James, G. M. Hughes, C. Vallance, and J. M. Smith, "Nanoparticle trapping and characterization with open microcavities (conference presentation)," in *Frontiers in Biological Detection: From Nanosensors to Systems IX*, vol. 10081. International Society for Optics and Photonics, 2017, p. 100810H.

[168] W. Song, X. Zhang, A. Liu, C. Lim, P. Yap, and H. M. M. Hosseini, "Refractive index measurement of single living cells using on-chip fabry-pérot cavity," *Applied physics letters*, vol. 89, no. 20, p. 203901, 2006.

[169] M. H. Bitarafan and R. G. DeCorby, "On-chip high-finesse fabry-perot microcavities for optical sensing and quantum information," *Sensors*, vol. 17, no. 8, p. 1748, 2017.

[170] W. Lee, W. Wang, G. Lee, S. H. Ryu, X. Fan, and D. K. Yoon, "Electrotunable liquid crystal laser based on high-q fabry-pérot microcavity," *Optics express*, vol. 25, no. 2, pp. 874–880, 2017.

[171] M. H. Bitarafan and R. G. DeCorby, "Small-mode-volume, channel-connected fabry–perot microcavities on a chip," *Applied Optics*, vol. 56, no. 36, pp. 9992–9997, 2017.

[172] A. E. Siegman, "Laser beams and resonators: beyond the 1960s," *IEEE Journal of selected topics in quantum electronics*, vol. 6, no. 6, pp. 1389–1399, 2000.

[173] G. Grynberg, A. Aspect, and C. Fabre, *Introduction to quantum optics: from the semi-classical approach to quantized light*. Cambridge university press, 2010.

[174] R. Paschotta, "Gaussian beams," *Encyclopedia of Laser Physics and Technology*, 2011.

[175] B. E. Saleh and M. C. Teich, *Fundamentals of photonics*. john Wiley & sons, 2019.

[176] K. Wilson and F. Vollmer, "Whispering gallery mode resonator biosensors," pp. 2837–2849, 2012.

[177] S. Arnold, M. Khoshsima, I. Teraoka, S. Holler, and F. Vollmer, "Shift of whispering-gallery modes in microspheres by protein adsorption," *Optics letters*, vol. 28, no. 4, pp. 272–274, 2003.

[178] N. Y. Kiang, J. Siefert, and R. E. Blankenship, "Spectral signatures of photosynthesis. i. review of earth organisms," *Astrobiology*, vol. 7, no. 1, pp. 222–251, 2007.

[179] Datasheet, "Ob1-4 channels microfluidic flow controller."

[180] K. Malmir, A. Trichet, R. Nyman, B. Ash, M. Contino, D. James, C. Vallance, J. Warren, and J. Smith, "Quantitative analysis of nanoparticle composition using open microcavities," *International Conference On Nanomedicine And Nanobiotechnology*, 2019.

[181] Z. Gong, Z. Wang, Y. Li, L. Lou, and S. Xu, "Axial deviation of an optically trapped particle in trapping force calibration using the drag force method," *Optics communications*, vol. 273, no. 1, pp. 37–42, 2007.

[182] T. Davis, "Brownian diffusion of nano-particles in optical traps," *Optics express*, vol. 15, no. 5, pp. 2702–2712, 2007.

[183] H. Brenner, "A nonmolecular derivation of maxwell's thermal-creep boundary condition in gases and liquids via application of the lechatelier–braun principle to maxwell's thermal stress," *Physics of Fluids*, vol. 21, no. 5, p. 053602, 2009.

[184] G. Volpe and G. Volpe, "Simulation of a brownian particle in an optical trap," *American Journal of Physics*, vol. 81, no. 3, pp. 224–230, 2013.

[185] R. T. Schermer, C. C. Olson, J. P. Coleman, and F. Bucholtz, "Laser-induced thermophoresis of individual particles in a viscous liquid," *Optics express*, vol. 19, no. 11, pp. 10 571–10 586, 2011.

[186] G. McNab and A. Meisen, "Thermophoresis in liquids," *Journal of Colloid and Interface Science*, vol. 44, no. 2, pp. 339–346, 1973.

[187] S. Duhr and D. Braun, "Why molecules move along a temperature gradient," *Proceedings of the National Academy of Sciences*, vol. 103, no. 52, pp. 19 678–19 682, 2006.

[188] A. Parola and R. Piazza, "Particle thermophoresis in liquids," *The European Physical Journal E*, vol. 15, no. 3, pp. 255–263, 2004.

[189] M. E. Schimpf and S. N. Semenov, "Mechanism of polymer thermophoresis in nonaqueous solvents," *The Journal of Physical Chemistry B*, vol. 104, no. 42, pp. 9935–9942, 2000.

[190] H. Brenner, "Navier–stokes revisited," *Physica A: Statistical Mechanics and its Applications*, vol. 349, no. 1-2, pp. 60–132, 2005.

[191] F. F. Chen *et al.*, *Introduction to plasma physics and controlled fusion*. Springer, 1984, vol. 1.

[192] H. Schlichting *et al.*, *Boundary layer theory*. Springer, 1960, vol. 960.

[193] C. J. Morris and F. K. Forster, "Oscillatory flow in microchannels," *Experiments in Fluids*, vol. 36, no. 6, pp. 928–937, 2004.

[194] R. Nave, "Dc-circuit water analogy," *Internet: http://hyperphysics. phy-astr. gsu. edu/hbase/electric/watcir. html.[October 14, 2012]*.

[195] Y.-C. Tung and C.-Y. Wu, "Pressure sensors and electrical circuits made with liquids."

[196] A. Riad, B. Khorshidi, and M. Sadrzadeh, "Analysis of streaming potential flow and electroviscous effect in a shear-driven charged slit microchannel," *Scientific reports*, vol. 10, no. 1, pp. 1–14, 2020.

[197] R. Padidhapu, S. Bathul, and V. Brahmajirao, "Electrical potential, mass transport and velocity distribution of electro-osmotic flow in a nanochannel by incorporating the variation of dielectric constant of aqueous electrolyte solution," *arXiv preprint arXiv:1602.06971*, 2016.

[198] R. Sarma, N. Deka, K. Sarma, and P. K. Mondal, "Electroosmotic flow of phan-thien–tanner fluids at high zeta potentials: An exact analytical solution," *Physics of Fluids*, vol. 30, no. 6, p. 062001, 2018.

[199] W. Morf, O. Guenat, and N. De Rooij, "Partial electroosmotic pumping in complex capillary systems: Part 1: Principles and general theoretical approach," *Sensors and Actuators B: Chemical*, vol. 72, no. 3, pp. 266–272, 2001.

[200] C. L. Rice and R. Whitehead, "Electrokinetic flow in a narrow cylindrical capillary," *The Journal of Physical Chemistry*, vol. 69, no. 11, pp. 4017–4024, 1965.

[201] M. Smoluchowski *et al.*, "Versuch einer mathematischen theorie der koagulationskinetik kolloider lösungen," 1917.

[202] B. J. Kirby and E. F. Hasselbrink Jr, "Zeta potential of microfluidic substrates: 1. theory, experimental techniques, and effects on separations," *Electrophoresis*, vol. 25, no. 2, pp. 187–202, 2004.

[203] M. Van den Heuvel, M. De Graaff, S. Lemay, and C. Dekker, "Electrophoresis of individual microtubules in microchannels," *Proceedings of the National Academy of Sciences*, vol. 104, no. 19, pp. 7770–7775, 2007.

[204] A. Brask, "Principles of electroosmotic pumps," 2003.

[205] Y. Takamura, H. Onoda, H. Inokuchi, S. Adachi, A. Oki, and Y. Horiike, "Low-voltage electroosmosis pump for stand-alone microfluidics devices," *Electrophoresis*, vol. 24, no. 1-2, pp. 185–192, 2003.

[206] J. J. Saenz, "Laser tractor beams," *Nature Photonics*, vol. 5, no. 9, pp. 514–515, 2011.

[207] S. Sukhov, V. Kajorndejnukul, R. R. Naraghi, and A. Dogariu, "Dynamic consequences of optical spin–orbit interaction," *Nature Photonics*, vol. 9, no. 12, pp. 809–812, 2015.

[208] Y. Pang, H. Song, J. H. Kim, X. Hou, and W. Cheng, "Optical trapping of individual human immunodeficiency viruses in culture fluid reveals heterogeneity with single-molecule resolution," *Nature nanotechnology*, vol. 9, no. 8, pp. 624–630, 2014.

[209] D. G. Grier, "A revolution in optical manipulation," *nature*, vol. 424, no. 6950, pp. 810–816, 2003.

[210] J. E. Curtis, B. A. Koss, and D. G. Grier, "Dynamic holographic optical tweezers," *Optics communications*, vol. 207, no. 1-6, pp. 169–175, 2002.

[211] K. M. Douglass, S. Sukhov, and A. Dogariu, "Superdiffusion in optically controlled active media," *Nature photonics*, vol. 6, no. 12, pp. 834–837, 2012.

[212] J. R. Arias-González and M. Nieto-Vesperinas, "Optical forces on small particles: attractive and repulsive nature and plasmon-resonance conditions," *JOSA A*, vol. 20, no. 7, pp. 1201–1209, 2003.

[213] Y. Shi, S. Xiong, L. K. Chin, J. Zhang, W. Ser, J. Wu, T. Chen, Z. Yang, Y. Hao, B. Liedberg *et al.*, "Nanometer-precision linear sorting with synchro-

nized optofluidic dual barriers," *Science advances*, vol. 4, no. 1, p. eaao0773, 2018.

[214] J. J. Kwan, R. Myers, C. M. Coviello, S. M. Graham, A. R. Shah, E. Stride, R. C. Carlisle, and C. C. Coussios, "Ultrasound-propelled nanocups for drug delivery," *small*, vol. 11, no. 39, pp. 5305–5314, 2015.